Dissipative phase transition and duality of the Josephson junction

Nicolas Bourlet

université PARIS-SACLAY

Transition de phase dissipative et dualité de la jonction Josephson

Dissipative phase transition and duality of the Josephson junction

Thèse de doctorat de l'université Paris-Saclay

École doctorale n° 564, Physique en Ile-de-France (PIF)
Spécialité de doctorat: physique
Unité de recherche : Université Paris-Saclay, CEA, CNRS, SPEC, 91191, Gif-sur-Yvette, France
Référent : Faculté des sciences d'Orsay

Thèse présentée et soutenue à Paris-Saclay, le 16/12/2020, par

Nicolas BOURLET

Composition du Jury

Denis BASKO Directeur de recherche, CNRS	Président
Claude CHAPELIER Chercheur (HDR), CEA-Grenoble	Rapporteur & Examinateur
Max HOFHEINZ Professeur agrégé, Université de Sherbrooke	Rapporteur & Examinateur
Julia S. MEYER Professeur, Université Grenoble Alpes	Examinatrice
Julien BASSET Maître de conférence, LPS Orsay	Examinateur

Direction de la thèse

Philippe JOYEZ Chercheur, CEA-Saclay	Directeur de thèse

Thèse de doctorat

NNT : 2020UPASP017

Remerciements

J'aimerais remercier un grand nombre de personnes, en commençant par celles avec qui j'ai travaillé directement pendant ces trois années: Anil, avec qui j'ai partagé mon bureau et qui m'a beaucoup aidé pour mes (nos) expériences, ainsi que pour la fab'; Philippe qui, en tant que directeur de thèse, a toujours été disponible pour répondre de manière très pédagogique à mes questions et a su guider ma thèse malgré les obstacles rencontrés en chemin; Hélène, en tant qu'encadrante non-officielle, qui m'a apportée une aide inestimable sur les manips micro-ondes ainsi que sur nos expériences plus ou moins farfelues, et a (presque) réussi à me transmettre sa rigueur dans la prise de mesures; et enfin Daniel, qui m'a accompagné jour après jour pendant la longue et éprouvante rédaction de ce manuscrit.

J'aimerais aussi grandement remercier tout les autres membres du groupe Quantronique avec qui j'ai passé de très bon moments, et qui m'ont tous aidé à un moment ou à un autre. Tout particulièrement Denis, détendeur des connaissances du groupe et toujours prêt à aider les étudiants, Dan, qui poursuit avec brio mes expériences, et Pascal que j'ai occupé régulièrement avec mes "petites" questions techniques. Aussi, je garderai un souvenir chaleureux des moments de détentes passé avec les autres non-permanents du groupe, au labo ou en dehors (Bartolo, Emmanuele, Fernanda, Vishal, Léo, Eric, Marianne, Cyril, ...).

Je remercie aussi chaleureusement Pief, qui a aussi subi l'assaut de mes "petites" questions techniques, ainsi que Sébastien pour leur aide concernant la nanofabrication des échantillons. De même, j'aimerais aussi remercier les membres de l'atelier de mécanique du SPEC et du laboratoire Cryogénie pour leur support technique sur mes expériences. Je remercie plus globalement tout les membres du SPEC, qui est un environnement dans lequel j'ai pris plaisir à travailler, et en particulier, les membres de l'administration qui permettent à cette ensemble de tourner harmonieusement.

Je remercie toutes les personnes qui m'ont accompagné jusqu'ici, mes amis de tous bords (de PC, de Londres, les HX3 et bien sur les Lillois qui se reconnaîtront) ainsi que ma famille pour leur soutien infaillible. J'aimerais aussi remercier les différents enseignants qui, tout au long de mon éducation, ont fait naître en moi cette passion pour les sciences sans laquelle je n'écrirais pas ces lignes aujourd'hui.

Abstract

More than a century after its discovery, superconductivity is used today in many applications. One of those is superconducting electronics, of which the Josephson junction is a basic building block. This element has enabled the realisation of electronic circuits in the quantum regime, and it has helped redefining the Volt in the SI system around quantum effects. Nowadays, a lot of time and efforts are spent in order to improve Josephson-junction-based circuits to realise state of the art Quantum-bits for quantum computing. One may think that those highly sensitive experiments involving Josephson junctions and conventional superconductivity imply an exquisite understanding of the component and its behaviour.

We show in this thesis work that this is not entirely the case, and we explore two types of superconducting quantum circuits which are in need of clarification. The first one concerns the Josephson junction itself, and a subtle issue regarding its interaction with its electromagnetic environment. Indeed, it has been predicted nearly 40 years ago that a Josephson junction would become insulating when connected to a resistance larger than $R_Q = h/4e^2 \approx 6.45\,k\Omega$. We find no traces of such insulating state in our experiments which measure the admittance of a Josephson junction connected in parallel to a resistance $R > R_Q$.

The second circuit we explore is the supposedly dual circuit to the Josephson junction, the quantum phase slip junction, which consists of a nanowire made of a highly inductive superconductor. In those nanowires, 2π phase slips of the superconducting phase should produce the dual effects of the Cooper-pair tunneling in Josephson junctions. The control of such an effect would then permit the realisation of a new class of superconducting quantum devices. We measured microwaves resonators patterned in a thin film of an highly inductive superconductor. We find no clear signal revealing the presence of quantum phase slips in our devices. However, we find a clear signature of two-level system low frequency noise which may mask the presence of the quantum phase slips, and we explore the implication of this noise in this kind of devices.

Résumé Français

La théorie BCS de la supraconductivité conventionnelle

Découverte en 1991 par H.K. Onnes [1] dans le mercure, la supraconductivité a depuis fait l'objet de recherches intensives. Elle est une des manifestations les plus spectaculaires de la physique quantique à l'échelle macroscopique. La théorie Bardeen-Cooper-Schrieffer (BCS), proposée en 1957 [2], décrit ce phénomène dans les conducteurs métalliques par l'existence d'une force attractive entre électrons proches du niveau de Fermi, provenant d'une interaction électrons-phonons. Cette attraction provoque la formation d'un condensat d'électrons appariés en paires de Cooper, ce qui ouvre un gap d'énergie dans le spectre d'excitation des quasiparticules. Cette transition de l'état normal vers l'état supraconducteur, qui a lieu à une température critique T_C, est une transition de phase du deuxième ordre caractérisée par un paramètre d'ordre complexe local, le paramètre d'ordre supraconducteur Δ. Son module correspond au gap d'énergie dans le spectre d'excitation des quasiparticules, et sa phase est conjuguée au nombre de paires de Cooper dans le condensat.

Dans le cas où cette phase présente un gradient, un courant strictement non dissipatif traverse le matériau. Cette propriété a permis l'application des supraconducteurs dans la réalisation de puissants électro-aimants, utilisés pour l'imagerie médicale, dans des turbines d'éoliennes ou encore dans des installations de recherches sur les hautes énergies (LHC, ITER,...).

Les applications émergentes dans l'électronique supraconductrice impliquent cependant bien plus que simplement transporter des courants sans effet Joule. En effet, la nature du condensat de paires de Cooper permet la réalisation de circuits entièrement nouveaux. Par exemple, l'inductance cinétique intrinsèque des supraconducteurs est maintenant largement utilisée dans des détecteurs micro-ondes pour l'observation astronomique. Un autre composant simple mais très polyvalent est la Jonction Josephson (JJ).

La jonction Josephson est une jonction tunnel entre deux électrodes supraconductrices. Dans l'état normal, cette jonction est un ensemble de courts canaux de conduction, tous caractérisés par une faible transmission causée par l'effet tunnel à travers la barrière isolante. Malgré la faible valeur de l'interaction attractive résiduelle entre les électrons de chaque côté de la barrière, Brian Josephson a montré en 1962 [3] que, dans l'état supraconducteur, cette jonction tunnel peut permettre le passage cohérent de paires de Cooper, et donc de supercourants. Il démontra l'existence des deux relations dites de Josephson. La première relie la tension aux bornes de la jonction V à la différence de phase δ entre les paramètres d'ordres supraconducteurs des électrodes : $V = \frac{\hbar}{2e}\frac{\partial \delta}{\partial t}$. La deuxième définit le courant traversant la jonction I comme étant périodique vis-à-vis de la différence de phase δ: $I = I_c \sin(\delta)$ avec I_c le courant critique de la jonction Josephson. Une JJ est un élément non-dissipatif qui peut être décrit comme une inductance non-linéaire. Cet effet Josephson a largement été utilisé depuis, par exemple, pour réaliser des détecteurs de champs magnétiques ultra-sensibles, les SQUIDs, formés de deux JJ en parallèle (sensibilité jusqu'à $3\,\mathrm{fT}/\mathrm{Hz}^{1/2}$) [4], ou encore dans des standards métrologiques du Volt qui ont aidé à rebaser le Système International

d'unités uniquement sur les effets quantiques en 2019 [5].

Circuits supraconducteurs dans le régime quantique de la phase

Jusqu'à présent, nous avons seulement mentionné des applications dans lesquelles la différence phase δ pouvait être considérée comme classique. Cependant, aux énergies bien inférieures au gap supraconducteur, la différence de phase aux bornes d'une JJ est l'unique degré de liberté de ce système. Cette caractéristique a fait de la jonction Josephson le circuit modèle pour étudier le régime quantique des circuits électroniques supraconducteurs. En effet, l'intérêt porté à ce composant a considérablement augmenté après la prédiction par A.J. Leggett en 1980 [6] de l'effet tunnel de la phase pour une JJ polarisée en courant. Des mesures expérimentales ont ensuite confirmé cette prédiction [7, 8, 9]. Plus tard, il a été montré que des circuits basés sur des JJ peuvent implémenter des bits quantiques (Qubits), c'est à dire des systèmes à deux niveaux [10, 11]. Aujourd'hui, beaucoup d'efforts sont dépensés pour réaliser des processeurs quantiques à plusieurs dizaines de Qubits supraconducteurs, comme démontré par Google, IBM ou Rigetti.

Comprend-on parfaitement la supraconductivité conventionnelle ?

Au vu des connaissances sur les supraconducteurs conventionnels et de l'usage maintenant quasi-industriel des circuits basés sur les JJ, il est normal de supposer que le sujet est parfaitement maîtrisé. La motivation derrière ce travail de thèse est l'existence de prédictions et de phénomènes qui n'entrent pas dans la description actuelle des circuits supraconducteurs, et qui méritent d'être étudiés plus en profondeur.

Par exemple, il est connu que placer une petite JJ dans un environnement d'impédance finie réduit le supercourant qu'elle peut transporter, car l'impédance s'oppose aux fluctuations de charge quantiques présentes dans l'état fondamental supraconducteur. Il a même été prédit qu'une JJ connectée à une résistance supérieure au quantum de résistance $R_Q = h/4e^2 \simeq 6.5\,\mathrm{k}\Omega$, provoquant des fluctuations importantes de la phase à ses bornes, deviendrait isolante via une transition de phase quantique dissipative. Cette prédiction, réalisée il y a près de 40 ans, est en conflit apparent avec plusieurs résultats obtenus sur les circuits supraconducteurs et elle n'a jamais été vérifiée expérimentalement de façon convainquante.

Un autre exemple est la prédiction de l'existence d'un composant dual de la jonction Josephson. En effet, il est prédit que les sauts de phase quantiques prenant place dans un nanofil de supraconducteur fortement désordonné réaliseraient le dual quantique de l'effet Josephson [12]. Dans ce nanofil, la forte inductance cinétique intrinsèque réduit les fluctuations de charge ce qui, selon le principe d'Heisenberg, induit corrélativement la présence de fluctuations quantiques du paramètre d'ordre supraconducteur, permettant par exemple des sauts de phase de $\pm 2\pi$. Mooij et Nazarov [12] ont prédit des relations duales aux relations Josephson pour ces nanofils, avec une tension à ses bornes variant de manière périodique avec le nombre de paires de Cooper transférées par le nanofil. Le contrôle et l'utilisation cohérente de ces sauts de phase pourrait conduire à une nouvelle catégorie de circuits supraconducteurs, sur lesquels s'appliqueraient des relations duales à leurs homologues basés sur des JJ. Ainsi, alors que la JJ est une inductance non-linéaire, le nanofil se comporterait, lui, comme un condensateur non-linéaire. Selon nous, cette perspective mérite une étude approfondie.

Cette thèse explore donc ces deux exemples de circuits supraconducteurs. Dans un premier

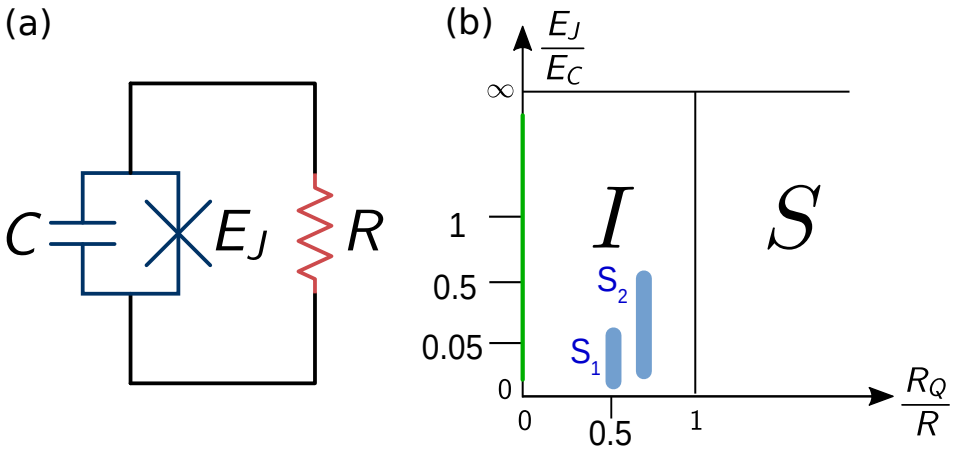

Figure 1. a: Schéma du circuit électrique considéré, avec une jonction Josephson d'énergie E_J en parallèle avec sa propre capacité C et une résistance R. **b:** Diagramme de phase schématique de la transition de phase dissipative prédite dans ce système. Les barres verticales bleues correspondent au paramètres explorés par nos deux échantillons. L'énergie $E_C = (2e)^2/2C$ est l'énergie caractéristique de charge et $R_Q = \hbar/4e^2$. [15]

temps, nous avons mesuré le comportement d'une JJ connectée à une résistance plus grande que R_Q. Dans un second temps, nous avons mis au point et mesuré des résonateurs micro-ondes basés sur des nanofils de supraconducteur fortement désordonné pour essayer d'y observer l'effet de charge non-linéaire des sauts de phase quantiques.

Absence de transition de phase dissipative dans les jonction Josephson

La première partie de cette thèse est donc consacré à la jonction Josephson et à la prédiction de l'existence d'une transition de phase dissipative lorsque celle-ci est connectée à une résistance de valeur R. Il a été prédit par Schmid en 1983 [13], que lorsque $R > R_Q = h/4e^2 \approx 6.45\,\mathrm{k\Omega}$, la jonction deviendrait isolante à température nulle. Cette prédiction a été approfondie dans les années suivantes [14] et a été confirmée et utilisée dans de nombreux travaux théoriques. Cependant, peu de vérifications expérimentales existent sur cette prédiction, et les résultats existants sont critiquables et peu convaincants.

La partie inférieure du diagramme de phase présenté figure 1b a été obtenu initialement par Schmid [13] pour une particule massive dans un potentiel en tôle ondulée (washboard) en présence de dissipation. Le reste du diagramme a ensuite été obtenu grâce à des arguments de dualité position-impulsion. Schmid a suggéré le premier d'utiliser la JJ pour vérifier sa prédiction, en utilisant la phase de la jonction comme analogue de la position de sa particule quantique. Cependant dans cette analogie, certaines limites du diagramme de phase sont contradictoires vis-à-vis des résultats simples et biens connus sur les JJ. En effet, dans la limite où $R \to \infty$, le circuit présenté dans la Figure 1a se réduit à celui d'une jonction Josephson d'énergie Josephson E_J parallèle à sa propre capacité d'énergie $E_C = (2e)^2/2C$. Ce circuit est bien connu sous le nom de boîte à paires de Cooper, et il se comporte comme un résonateur anharmonique. Les résultats obtenus sur ce circuit [16] montrent qu'il existe des fluctuations de charge à travers la jonction quelle que soit la valeur de $E_J \neq 0$. De plus, dans la limite où $E_J/E_C \to \infty$, la non-linéarité de la jonction devient négligeable et ce circuit devient un oscillateur harmonique aux basses énergies et il est connu que ce type d'oscillateur n'a aucune transition pour une quelconque valeur de R.

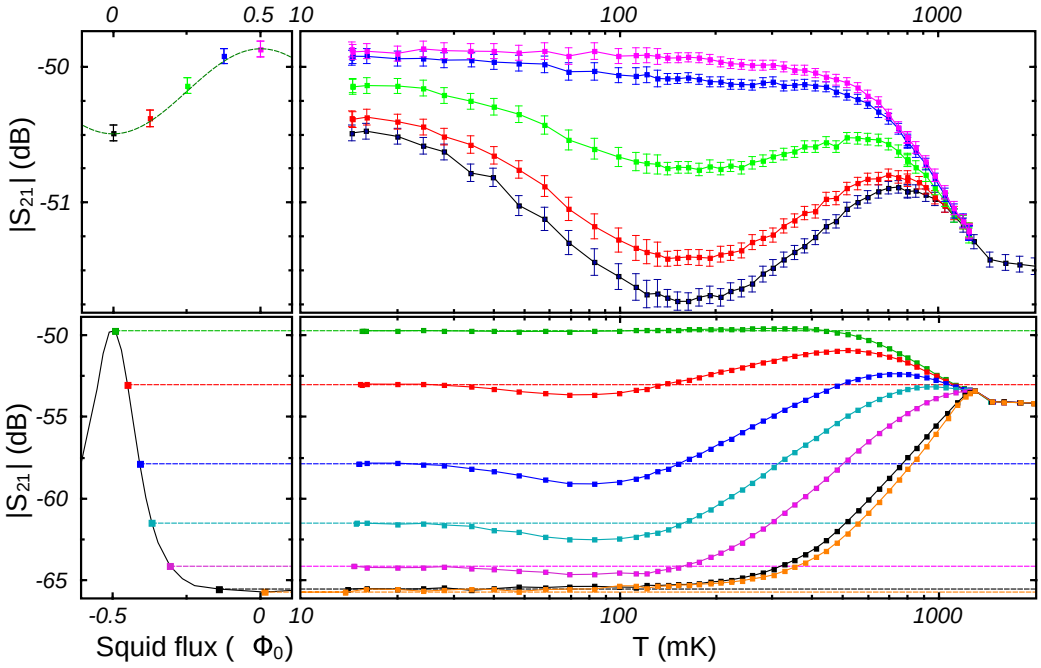

Figure 2. Mesures de la transmission de nos deux échantillons à basse températures [15]. Si la jonction devenait isolante, la transmission mesurée à travers la résistance devrait augmenter aux basses température pour chaque valeur du flux. Ici, nous mesurons une modulation de la jonction en fonction du champ magnétique appliqué qui tends vers une stabilisation à basse température. Cela implique que la jonction est toujours supraconductrice.

Afin de résoudre ces contradictions, nous avons réalisé plusieurs dispositifs contenant une jonction Josephson modulable (un SQUID, deux JJ en parallèle) connectée en parallèle à une résistance en chrome, de valeur $R > R_Q$. Nos dispositifs se placent donc dans la partie isolante du diagramme présenté Figure 1b. Nous avons mesuré la réponse linéaire de ces jonctions dans le domaine des micro-ondes ($\approx$1 GHz) à basse température. Les résultats obtenus (figure 2) indiquent que les jonctions présentent une modulation, indicative d'un comportement supraconducteur, qui sature à basse température. Ce comportement n'est pas compatible avec l'existence d'un état isolant à température nulle. En effet, cet état isolant devrait se manifester par une dépendance de la réponse linéaire en loi de puissance de la température et donc une diminution de la transmission de la jonction et de sa modulation. Ces résultats sont compatibles avec d'autres résultats obtenus sur les JJ dans un circuit contenant une résistance de 32 kΩ [17]. Nous en concluons donc l'absence de transition de phase dissipative dans les jonctions Josephson.

Par la suite, nous explorons des pistes pouvant expliquer la différence entre les prédictions théoriques et nos résultats expérimentaux. Nous montrons que la prédiction de transition dissipative reposait crucialement sur l'hypothèse que la phase de la JJ puisse être traitée comme une variable étendue dans la partie inférieure du diagramme de phase, et que, corrélativement, la théorie négligeait la réponse inductive de la jonction. Nos résultats montrent qu'au contraire il convient d'y considérer une phase compacte, et que la réponse inductive de la jonction la protège contre la transition de phase.

Résonateurs micro-ondes basé sur des nanofils de supraconducteur désordonné

Dans cette deuxième partie, nous explorons le comportement de résonateurs micro-ondes réalisés à partir de couches minces de supraconducteur fortement désordonné, dans l'objectif d'observer les effets des sauts de phase quantiques. Tout d'abord, nous introduisons les particularités de

ces couches minces supraconductrices. Celles-ci présentent une transition supraconducteur-isolant lorsque le désordre de la couche atteint un niveau tel que la résistance par carré dépasse $R_Q \approx 6.45\,\mathrm{k}\Omega$ à l'état normal. Pour des couches minces de résistance légèrement inférieure à cette limite, la résistance à l'état normal se traduit par une forte inductance cinétique dans l'état supraconducteur.

Cette forte inductance permet au paramètre d'ordre supraconducteur d'avoir de fortes fluctuations de point zéro, susceptibles d'induire des sauts de phase quantiques de $\pm 2\pi$ dans des nanofils. Dans l'objectif d'observer de tels sauts de phase quantiques, nous explorons d'abord les caractéristiques micro-ondes de deux supraconducteurs fortement désordonnés avec lesquels nous pourrions fabriquer des nanofils, le diamant dopé au bore et le nitrure de titane. Les résultats obtenus sur le diamant dopé au bore montrent la présence de fortes pertes micro-ondes dans ce matériau, ce qui le rend inadapté pour notre projet. Au contraire, après développement de la fabrication de couches minces de nitrure de titane, celles-ci permettent la réalisation de résonateurs micro-ondes possédant des facteurs de qualité internes allant jusqu'à $Q_{\mathrm{int}} \approx 40k$ (contre $Q_{\mathrm{int}} \approx 10$ pour le diamant dopé au bore). Nous utilisons ensuite ces couches minces de nitrure de titane pour réaliser des résonateurs micro-ondes avec des inductances formées d'un nanofil.

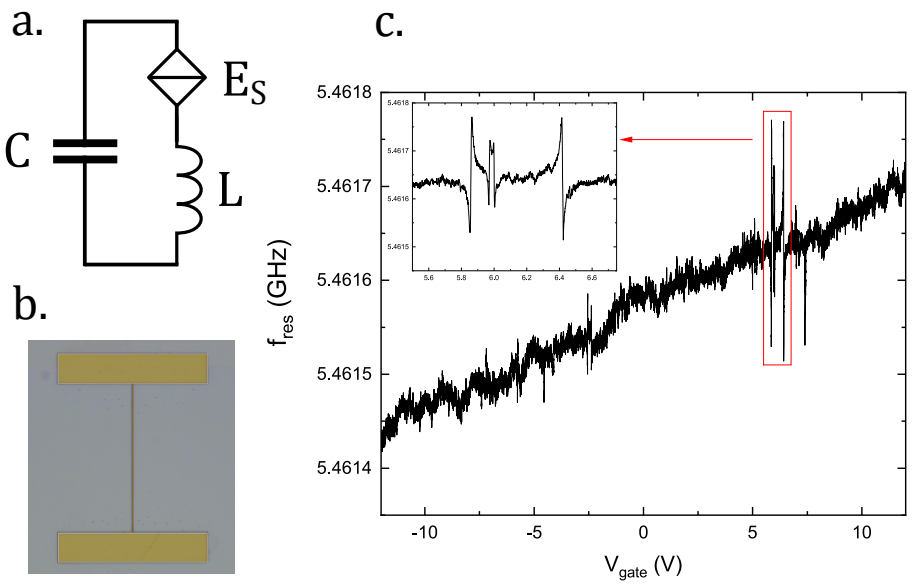

Figure 3. a: Circuit électrique que nous cherchons à réaliser avec une jonction à sauts de phase d'énergie E_S et **(b)** une image d'un de nos résonateurs basé sur un nanofil de nitrure de titane. **c:** fréquence de résonance d'un de ces résonateurs en fonction de la tension appliquée sur une grille locale. En insert, on observe deux doubles anticroisement du résonateur avec deux systèmes à deux niveaux.

Malheureusement, la réponse attendue pour ces dispositifs dans le cas où les sauts de phase prolifèrent, soit une modulation de la fréquence de résonance par l'application d'une tension sur une grille locale [18], n'est pas observée. Cependant, nous observons un fort impact des systèmes à deux niveaux (TLS) sur nos résonateurs (voir figure 3). Dans certaines conditions, nous arrivons même à observer le couplage de TLS individuels avec nos résonateurs, ce qui nous permet de les caractériser. Nous mesurons aussi des fluctuations et un bruit basse fréquence sur la fréquence de résonance de nos dispositifs. Ces effets sont en partie décrits par les théories existantes concernant l'impact de ces TLS dans les circuits supraconducteurs. Cependant, certaines de nos mesures sont

difficilement explicables par ces modèles, telles par exemple les fortes valeurs de couplages TLS-résonateur que nous observons. Nous proposons une approche différente pour décrire le couplage de ces TLS avec nos résonateurs, basée sur une interaction entre le champ dipolaire des TLS avec les canaux de conduction des nanofils. Nous concluons que les fluctuations induites par ces TLS sont un énorme frein à la réalisation de ces dispositifs à sauts de phase quantiques.

Table of contents

Part I

General introduction

1 Motivations

The standard BCS framework of low temperature superconductivity

Superconductivity has been the focus of intense research since its discovery in 1911 by H.K. Onnes [1]. It is one of the most spectacular macroscopic manifestations of quantum physics in condensed matter. The Bardeen-Cooper-Schrieffer (BCS) theory proposed in 1957 [2, 19] explained superconductivity in metals by the existence of an attractive interaction between the electrons near the Fermi surface induced by an electron-phonon coupling. The BCS interaction induces the formation of an electronic paired condensate, the so-called Cooper-pair condensate, with a gap for quasiparticle excitations. The transition from the normal state to the paired state that takes place at a critical temperature T_C is a second-order phase transition described by a local complex order parameter, the superconducting order parameter Δ. Its modulus corresponds to the quasiparticle energy gap, and its phase is conjugated to the number of Cooper pairs in the condensate.

In the presence of a gradient in the phase of Δ, a strictly non-dissipative electrical current flows through the material. This amazing property led to the most widespread application of superconductivity under the form of large-field persistent-current superconducting magnets used for medical magnetic resonance imaging, in wind turbines or in large scale physics research facilities (LHC, ITER, ...).

Applications in low power electronics developed since several decades involve more than wires carrying supercurrents. While the dissipation-less supercurrents can be leveraged to increase the performance of existing circuits, the nature of the Cooper-pair condensate enables novel electronic components not previously possible. For example, the inductive response of superconductors is now widely used in kinetic inductance microwaves detectors for astronomical observations. Another simple and particularly versatile superconducting component is the Josephson Junction (JJ).

This component is a tunnel junction between two superconducting electrodes. In the normal state, a tunnel junction is a parallel combination of weakly transmitted conduction channels thanks to quantum tunneling across the insulating barrier. Despite the smallness of the residual pairing between electrons on both sides of the barrier, Brian Josephson calculated in 1962 [3] that in the superconducting state, a JJ supports the passage of Cooper-pairs, i.e. a supercurrent. He found a periodic relation between the supercurrent through the junction I and the phase difference between the superconducting electrodes δ: $I = I_c \sin(\delta)$ with I_c the Josephson critical current of the junction. This Josephson effect has since been exploited in several ways, for example to realise extremely sensitive magnetometers known as SQUIDs (a SQUID is formed of two JJ in parallel; they can have a sensitivity down to $3\,\mathrm{fT}/\mathrm{Hz}^{1/2}$ of noise) [4] or to make practical Volt standards in the International System of Units [5].

Superconducting devices in the quantum phase regime

So far, we only mentionned applications where the phase difference δ could be describe classically. However, the phase difference across a JJ, conjugated to the number of Cooper-pairs having crossed it, is the only degree of freedom of this system. As such, it became a model for investigating the quantum regime of electrical circuits. A JJ is a non-dissipative component that can be thought of as a non-linear inductor. Interest for JJ rose drastically after the theoretical prediction by A.J. Leggett in 1980 [6] for the quantum tunneling of the phase in a current biased JJ. The experimental observations [7, 8, 9] fully confirmed the quantum nature of the phase across a JJ. Quite later, it was shown that simple JJ circuits can provide Quantum-Bits (Qubits), i.e. two-state systems, suitable for quantum information processing [10, 11]. Nowadays, many efforts are spend towards the realisation of multi-Qubits processors based on JJ circuits, with devices containing several tens of JJ-based Qubits, as demonstrated by Google, IBM or Rigetti [20, 21].

Has a comprehensive understanding of superconductivity been achieved ?

Given the in-depth understanding of low critical temperature superconductors and of devices made with them, one might think that a comprehensive understanding of the whole field has been achieved. The motivation of this PhD research work is the existence of predictions and of phenomena that do not fit in the existing framework, and that deserve further investigations.

For example, it is known that embedding a small Josephson junction in an environment with a finite impedance reduces the maximum supercurrent it can transmit. It has even been predicted that if any Josephson junction is introduced in a highly resistive environment, which induces enough quantum phase fluctuations across it, it would become insulating through a dissipative quantum phase transition. This prediction, made nearly 40 years ago, is in apparent conflict with some results obtained on superconducting quantum circuits, and has never been properly confirmed experimentally.

Another related issue not fully understood in conventionnal superconductors is the prediction of a component that would be the dual of the Josephson junction. More precisely, it has been predicted [12] that nanowires made of highly disordered superconductors would realise the dual of the JJ, the Quantum Phase Slip (QPS) junction. In such a device, the strong quantum fluctuations of the order parameter would produce slips of $\pm 2\pi$ of the superconducting phase in the nanowire. Mooij and Nazarov [12] have predicted for QPS junctions a relation dual of the dc Josephson relation, with the voltage across the nanowire varying periodically with the transferred charge. The controlled use of coherent QPS would open the door to the realisation of new category of superconducting quantum devices, with known JJ circuits mapped to their dual counterparts. This topic has barely been investigated sor far, with mixed results, and we think that its prospects make it worth further investigations.

During this thesis, we explore those two examples of superconducting devices in high impedance environments. In a first part, we investigate the predicted dissipative transition in Josephson junction connected to a large resistor. In a second part, we explore the behaviour of resonators with nanowires made of an highly disordered superconductor, whose intrinsic impedance allows to implement quantum phase slip devices. Before that, we provide some details on superconductivity and quantum circuits.

2 Superconductivity

Superconductivity was initially discovered in 1911 in mercury, and its presence in many other materials was reported in the following years. The first signs observed in superconductors was a zero-resistance state of the material below their superconducting temperature T_C, which allowed the presence of persistent supercurrents. In 1933, Meissner and Ochsenfeld discovered that during the superconducting transition, magnetic fields were expelled from superconductors. This provided the first evidence that superconductors were not simply perfect conductors. Conventional theories of superconductors were devised in the 50s, namely the phenomenological Ginzburg-Landau (GL)theory and the microscopic Bardeen-Cooper-Schrieffer (BCS) theory.

Both those theories describe the superconducting state as a coherent quantum state, and Cooper introduced the description of the charge carriers in superconductors as Cooper pairs, correlated electrons interacting through virtual phonon exchange. In conventional superconductors, this interaction is originating from a second-order electron-phonon interaction, yielding an effective attractive force between electrons of opposite wavevectors and spins. At sufficiently low temperature, this attractive interaction results in a complete reorganisation of the Fermi sea of the normal metal.

2.1 The superconducting state

In the BCS theory, the pairing interaction is treated in the mean field approximation, and the resulting BCS Hamiltonian for the electronic system is [19]:

$$H_{\mathrm{BCS}} = \sum_{k,\sigma} \xi_k c_{k\sigma}^\dagger c_{k\sigma} - \sum_{\substack{k \\ |\xi_k|<\hbar\omega_D}} c_{k\uparrow}^\dagger c_{-k\downarrow}^\dagger \Delta + \Delta^* c_{-k\downarrow} c_{k\uparrow} - \frac{|\Delta|^2}{V_{\mathrm{eff}}} \tag{1}$$

with ω_D the Debye frequency, V_{eff} a constant linked to the effective attractive interaction and $c^\dagger_{k\sigma}$ and $c_{k\sigma}$, the creation and annihilation operators acting on the electrons of wavevector k, spin σ and energy relative to the Fermi level ξ_k. The complex number Δ is called the order parameter or the superconducting gap of the material, which is defined as:

$$\Delta = V_{\text{eff}} \sum_{\substack{k \\ |\xi_k|<\hbar\omega_D}} \langle c_{-k\downarrow} c_{k\uparrow} \rangle \tag{2}$$

where $\langle\rangle$ denotes the expectation value, which depends on Δ, thus calling for a self-consistent solution. The first term in equation (1) is the Hamiltonian of the non-interacting Landau quasiparticles of the normal metal (hereafter simply called electrons) with no external force applied and the other terms describe the attractive interaction between electrons. When $\Delta = 0$, the Hamiltonian reduces to the one of a free electron bath. When $\Delta \neq 0$, electrons within an energy range $\hbar\omega_D \ll E_F$ of the Fermi level, interact and condense into Cooper pairs which reduces the energy of the system. The temperature at which Δ acquires a non-zero value is called the superconducting transition temperature T_C of the material. The condensation removes electronic excitations around the Fermi level, opening an energy gap of $2|\Delta|$ in the single electron excitations density of state. The BCS theory gives the following formula for $|\Delta(T=0)|$:

$$|\Delta(T=0)| = \Delta_0 = 1.76 k_b T_C \tag{3}$$

The complex superconducting gap Δ can vary in space and time, due to fluctuating effects or external influence. Indeed, it is suppressed by temperature, magnetic field or magnetic impurities. Associated with Δ is the characteristic length for the superconductivity called the coherence length, which, in the clean case, is given by:

$$\xi_0 = \frac{\hbar v_F}{\Delta_0} \tag{4}$$

This length corresponds to the distance paired electrons travel during the interaction time $\hbar/\Delta_0$, and it can be viewed as the size of the Cooper pairs or the length scale on which the order parameter Δ can vary. This ideal expression for the coherence length is only valid in perfect crystals, which is usually not the case in metallic thin films. If the electronic mean free path $l_e < \xi_0$, then the diffusive nature of the electrons affects this coherence length which now can be expressed as:

$$\xi = \sqrt{\frac{\hbar D}{\Delta_0}} = \sqrt{\frac{\xi_0 l_e}{3}} \tag{5}$$

where $D = \frac{1}{3} v_F l_e$ the electronic diffusion constant.

2.2 Electromagnetic response of a superconductor

To describe the electromagnetic properties of superconductors, one has to consider spatial non-uniformity of the order parameter $\Delta(\vec{x}) = |\Delta(\vec{x})| e^{i\phi(\vec{x})}$. The phase $\phi(\vec{x})$ of the order parameter is called the superconducting phase. One way to describe this non-uniform system is to use the Bogoliubov-de Gennes equation [22, 23]:

$$\begin{aligned} H_{\text{BdG}}(\vec{x})\Psi(\vec{x}) &= E\Psi(\vec{x}) \\ H_{\text{BdG}}(\vec{x}) &= \begin{pmatrix} H(\vec{x}) & \Delta(\vec{x}) \\ \Delta^*(\vec{x}) & H^*(\vec{x}) \end{pmatrix} \end{aligned} \tag{6}$$

where $H(\vec{x})$ is the Hamiltonian of a single electron:

$$H(\vec{x}) = \frac{1}{2m}(e\vec{A}(\vec{x}) - i\hbar\nabla)^2 - \mu(\vec{x}) \tag{7}$$

This Hamiltonian now encompass electromagnetic fields, and $\mu(\vec{x})$ is the electro-chemical potential. In the case of a constant order parameter and in the absence of any field, this Hamiltonian is equivalent to the BCS Hamiltonian in (1). At sufficiently low fields, the modulus of the order parameter is quasi-constant in space $|\Delta(\vec{x})| \approx \Delta$ and the phase $\phi(\vec{x})$ of the order parameter changes very little over a length ξ, then one can derive the linear-response current density $\vec{J}_s(\vec{x})$ up to the proportionality constant. In the case of a diffusive conductor with $T \ll T_C$ and at frequency $f \ll \Delta/h$, using the "quasiclassical theory of superconductivity" [24, 25], one can even obtain the exact prefactor:

$$\vec{J}_s = \frac{\pi \Delta \sigma_n}{\hbar}\left(\frac{\hbar}{2e}\nabla\phi + \vec{A}\right) \tag{8}$$

where σ_n is the normal state resistivity or the material, and we dropped the $\vec{x}$ for clarity. The (super)current in a superconductor is then proportional to the field $\frac{\hbar}{2e}\nabla\phi + \vec{A}$ instead of the electric field $\vec{E}$ in a normal metal. As an observable physical quantity, $\vec{J}_s$ is gauge invariant. However, the potential vector $\vec{A}$ is gauge dependent. As a result, a gauge transformation $\vec{A} \to \vec{A} + \nabla f$ with f an arbitrary scalar field dictates the following transformation for the superconducting phase: $\phi \to \phi - \frac{2e}{\hbar} f$. In standard electromagnetism, the gauge transformation of the potential vector $\vec{A}$ is linked to the transformation of the scalar potential $V \to V - \partial f/\partial t$. Comparing this with the gauge induced transformation of ϕ, we deduce the following relation between the scalar potential V and the phase ϕ:

$$V = \frac{\hbar}{2e}\frac{d}{\mathrm{dt}}\phi + \text{constant} \tag{9}$$

Using the definition of the electric field $\vec{E} = -\nabla V - \partial\vec{A}/\partial t$, we have:

$$-\int \vec{E}\,\mathrm{dt} = \frac{\hbar}{2e}\nabla\phi + A \tag{10}$$

and combining this result with the time derivative of (8), we have:

$$\frac{d\vec{J}_s}{dt} = -\frac{\pi\Delta\sigma_n}{\hbar}\vec{E} \tag{11}$$

We can draw two conclusions from this result. The first is that contrary to a normal metal where $\vec{J}_s \propto \vec{E}$, we have $\frac{d\vec{J}_s}{\mathrm{dt}} \propto \vec{E}$ in superconductors. This means that supercurrents do not need an electric field in order to exist, and that they increase over time when one is present. This is exploited in superconducting electromagnets, where a supercurrent can circulate in a superconducting coil without losses as long as $T \ll T_C$. The second conclusion relates to the inductive behaviour of superconductors. Indeed, if we consider a linear piece of superconductor and integrate equation (11) across its cross section then along its length, we have (assuming $\vec{A}$ is constant):

$$\frac{dI}{dt} = \frac{\pi\Delta}{\hbar R_n}V_{\mathrm{ab}} \tag{12}$$

where I is the current flowing through the superconducting piece and V_{ab} the potential difference between its ends. Comparing equation (12) to the response of an inductor $V_{\mathrm{ab}} = L\frac{dI}{dt}$, we can conclude that the electromagnetic response of a piece of superconductor is inductive. The corresponding inductance is called the kinetic inductance of the superconductor and, in the linear limits we introduced earlier, writes:

$$L_K = \frac{\hbar R_n}{\pi\Delta} \tag{13}$$

Part II

Josephson junctions in a highly resistive environment

In this first part of this thesis, we explore the behaviour of a Josephson junction (JJ) connected to a resistive environment. When the resistance R of the environment increases, it tends to induces more and more phase fluctuations on the junction. In 1983, it was predicted by Schmid [26] that a quantum particle in a periodic potential in presence of viscous friction would show a dissipative quantum phase transition at a given value of the dissipation strength. He then proposed the JJ as a experimental application of his model, suggesting that a JJ connected to a resistor R would become insulating at zero temperature when $R > R_Q = h/4e^2 \approx 6.45\,k\Omega$. Quite surprisingly, this prediction is supposed to not depend on the JJ characteristics. Schmid's prediction was refined and theoretically confirmed to apply to JJs in the following years [27].

While phase fluctuations surely have an impact on JJs, the existence of this phase transition was not properly investigated experimentally. Moreover, it contradicts experimental results on simple devices, such as in the limit $R \to \infty$ at which point the system is no longer dissipative and one expects to recover the behaviour of a Cooper Pair Box (CPB) [28], where the JJ is superconducting.

We first rapidly summarise key characteristics of Josephson junctions, and then we reproduce here our published article [29] which describes our experiments and their results, as well as theoretical discussions.

1 Josephson junctions

1.1 Description

Josephson junctions are non-linear components named after B.D. Josephson who predicted in 1962 the mathematical relations describing their electrical behaviour in the superconducting regime [3, 30]. They consist of a tunnel junction, i.e. two metallic electrodes separated by a thin insulating layer, where the metal is a superconductor. Both superconducting electrodes have their own superconducting order parameter which can differs in modulus and/or in phase (see figure 1).

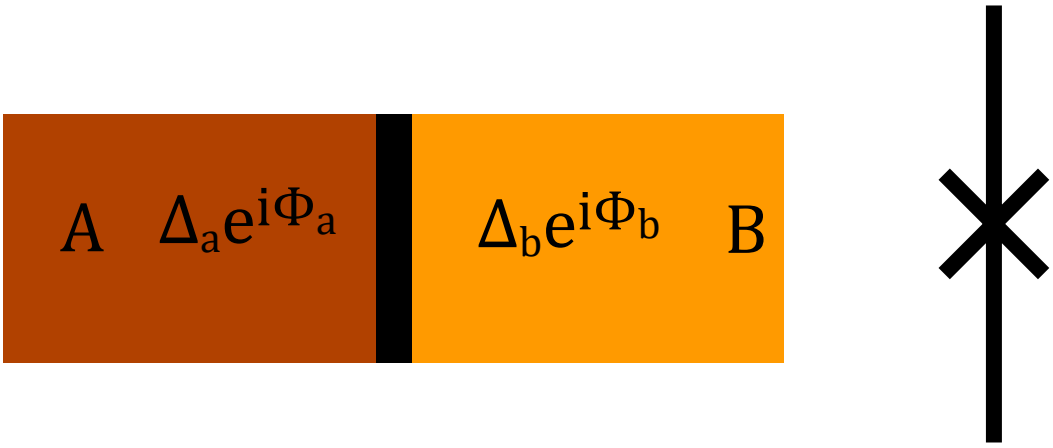

Figure 1. Left is a simple illustration of a Josephson junction, with two different superconducting material A and B, each with their ownsuperconducting order parameter. On the right is the electrical representation of an ideal JJ, i.e. without considering its capacitance.

Typically, a JJ has both electrodes made of the same superconductor. JJ are commonly made of Aluminium, because of the ease of fabrication and the good results obtained with this material. Indeed, such JJ can be made in a single lithography steps, using double angle deposition and the oxidised surface of the first aluminium layer as the insulating material.

1.2 Josephson relations

In the superconducting state, tunneling of Cooper pairs between electrodes enables the passage of supercurrent through the junction. Josephson derived two relations between the supercurrent through the junction I, the superconducting phase difference $\delta = \Phi_a - \Phi_b$ between the electrodes and the voltage across the junction:

$$I(\delta) = I_c \sin(\delta) \tag{14}$$

$$V(\delta) = \frac{\hbar}{2e}\frac{\partial \delta}{\partial t} \tag{15}$$

where I_c is the critical current of the junction. The first relation predicts the presence of a supercurrent even when no voltage is applied, as long as $\delta \neq 0$. The second relation is the same as we derived in section 2.2 of part I and links the voltage across the junction to the derivative of the phase difference; it only proceeds from Maxwell's equations of electromagnetism and has nothing to do with superconductivity, actually.

Within the Landauer formalism [31], JJs can be described as a set of short conduction channels through the insulating material, all weakly transmitting. In the normal state, tunneling of electrons through the insulator yields a conductance:

$$G_T = \frac{2e^2}{h}\sum_n T_n$$

with $T_n \ll 1$ the transparency of the channel n. Using this formalism, one finds:

$$I_c = \frac{e\Delta}{2\hbar}\sum_n T_n = \frac{\pi\Delta}{2e}G_T$$

1.3 Shapiro steps and voltage standard

One of the implications of the Josephson relations is the AC Josephson effect. When a DC voltage V is applied to a JJ, the phase difference increases linearly with time. This produces an alternative supercurrent in the junction of the form:

$$I(t) = I_c \sin(\delta_0 + 2eVt/\hbar) \tag{16}$$

The frequency f of this supercurrent is related to V by the Josephson constant $K_J = \frac{2e}{h} \approx 483\,\mathrm{MHz}/\mu V$, which is fixed by fundamental constants. Taking advantage of this exact voltage to frequency converter, one can realise of perfect voltage reference. If we apply a voltage $V(t) = V_{\mathrm{dc}} + V_{\mathrm{ac}}\cos(\omega t)$ on a JJ, the phase difference writes:

$$\delta(t) = \delta_0 + \frac{2eVt}{\hbar} + \frac{2eV_{\mathrm{ac}}}{\hbar\omega}\sin(\omega t) \tag{17}$$

and the current is:

$$I(t) = I_c \sin\left(\delta_0 + \frac{2eVt}{\hbar} + \frac{2eV_{\mathrm{ac}}}{\hbar\omega}\sin(\omega t)\right) \tag{18}$$

We can rewrite the current using the Bessel functions J_n:

$$I(t) = I_c \sum_{n=-\infty}^{+\infty} J_n(a)\sin((n+\lambda)\,\omega t + \delta_0) \tag{19}$$

with $a = \frac{2eV_{\mathrm{ac}}}{\hbar\omega}$ and $\lambda = \frac{2eV_{\mathrm{dc}}}{\hbar\omega}$. Each time $\lambda \in \mathbb{Z}$, this sum produces a time-independent term. This results in a DC supercurrent when $V_{\mathrm{dc}} = p\frac{\hbar}{2e}\omega$ with $p \in \mathbb{Z}$, producing what is called Shapiro steps in the I-V characteristic of the JJ (see figure 2).

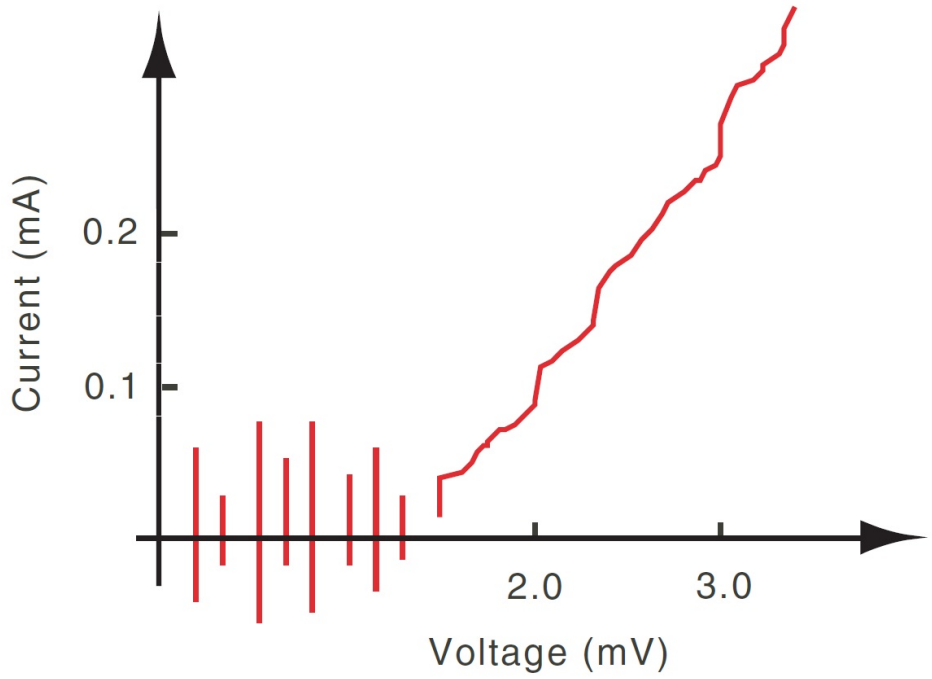

Figure 2. Shapiro steps in a weakly damped Josephson junction. From [5].

Since we can already accurately define frequencies (using atomic clocks), we can now have a precise voltage definition using the exact frequency to voltage conversion of JJs. This effect is used to realise the Josephson voltage standard [5] which is used since 2019 for the International System of Units.

1.4 The Josephson Hamiltonian

Given that the current operator is $\hat{I} = -\frac{2e}{\hbar}\frac{\partial \hat{H}}{\partial \delta}$ and using the first Josephson relation (14) for the current in a JJ, we write the corresponding Josephson Hamiltonian:

$$H_J = -E_J \cos(\delta) \tag{20}$$

with $E_J = \frac{\hbar}{2e} I_c$ is the Josephson energy of the junction. A JJ can be viewed as as behaving as a non-linear inductor. Indeed, the energy of an inductance L is:

$$E_L = \frac{1}{2L}\left(\frac{\hbar}{2e}\delta\right)^2$$

For $\delta \ll 2\pi$, the Josephson Hamiltonian can be approximated as:

$$H_J \approx \frac{\hbar}{2e} I_c \frac{\delta^2}{2} + \text{cst.} \tag{21}$$

which is the energy of an inductor with equivalent inductance

$$L_J = \frac{\hbar}{2e\, I_c} = \left(\frac{\hbar}{2e}\right)^2 \left(\frac{\partial^2 H_J}{\partial \delta^2}\right)^{-1}_{\delta=0} \tag{22}$$

For larger δ, the quadratic relationship between H_J and δ breaks down, but we can generalize the writing of its effective inductance as the inverse curvature of the Josephson Hamiltonian for all values of δ:

$$L_{\text{eff}}(\delta) = \frac{\hbar}{2e I_c} \frac{1}{\cos(\delta)} \tag{23}$$

The Josephson Hamiltonian (20) can be expressed in the basis of the number of Cooper pairs passed through the junction. This number and δ are conjugate variables and we have:

$$[\delta, N] = i$$

$$H_J = -\frac{E_J}{2} \sum \left(|N+1\rangle\langle N| + |N-1\rangle\langle N| \right) \tag{24}$$

The Josephson coupling couples the two superconducting electrodes through the hopping of Cooper pairs back and forth across the junction. Due to its geometry, the JJ also present a capacitive behavior with a capacitance C which we did not accounted for so far. This charging effect has to be added to the bare JJ description presented above, which results in the so-called Cooper-Pair Box (CPB) [32]. The capacitance presents a charging energy quadratic in the capacitor charge. Assuming the junction is only connected to a gate capacitor $C_g \ll C$ with a charge $2e n_g$, for each $N \in \mathbb{Z}$ the charging energy is then $E_c(N - n_g)^2$, where $E_C = 4e^2/2(C + C_g) \simeq 4e^2/2C$ is the charging energy of a single Cooper pair on the capacitance C . The Josephson coupling lift the degeneracy of those charging states at each half integer values of n_g (see figure 3).

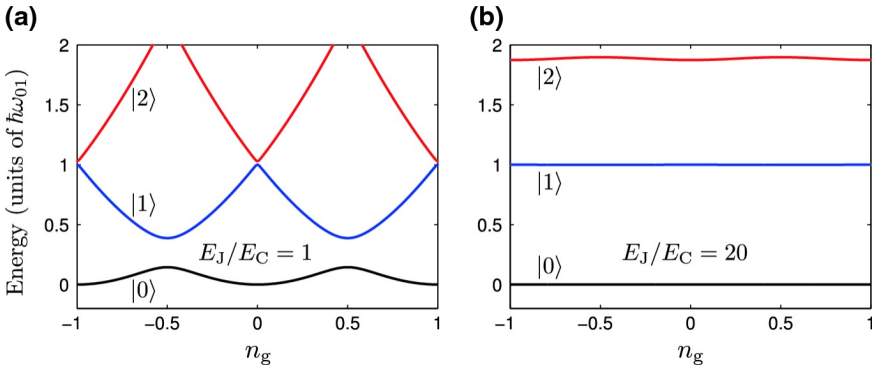

Figure 3. Energy levels of a CPB for two different values of E_J/E_C. From [33].

1.5 Use cases of JJs

Besides their use in Josephson voltage Standards, JJs have many other applications in quantum information, microwave circuits or detectors. We will describe two of those applications in Quantum-Bits (Qubits) and Superconducting Quantum Interference Device (SQUID).

1.5.1 Superconducting Qubit

Theoretical Qubits are perfect two-states systems, used in quantum information for various tasks. JJ Qubits are implementations of those devices using JJ, which are today one of the most promising Qubit realisation. As shown in figure 3, an isolated JJ voltage biased through a capacitor (a CPB) can be considered a good two-states system near half-integer values of n_g, due to the coupling of charge states by the Josephson energy.

1.5.2 SQUID

The SQUID is simply two JJ placed in parallel in a superconducting loop (see figure 4). For simplicity, we assume the inductance of the loop is negligible compared the JJs' inductances.

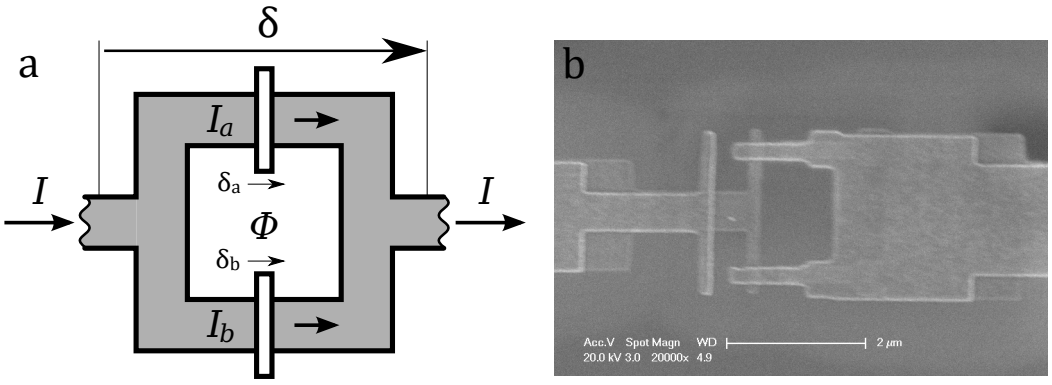

Figure 4. a: Schematic of a SQUID, i.e. two JJs connected in parallel. **b:** SEM image of one of the SQUID used in our devices. It is made using a double angle evaporation technique. A first layer of aluminium is deposited, then oxidised. A second layer is deposited on top of the oxide at a different angle, thus making a JJ.

The current flowing through such device is the sum of the current of each junctions:

$$I = I_a(\delta_a) + I_b(\delta_b)$$

with $I_a(\delta_a) = I_c^a \sin(\delta_a)$ and $I_b(\delta_b) = I_c^b \sin(\delta_b)$. We have:

$$\delta_a + \delta_b = \delta$$

$$\delta_a - \delta_b = \frac{2\pi}{\Phi_0} \oint \vec{A}\, dl = 2\pi \frac{\Phi}{\Phi_0} = \theta \tag{25}$$

with $\Phi_0 = \frac{h}{2e}$ and Φ the magnetic flux threading the loop. The current through the device becomes:

$$I(\delta) = I_a \sin\left(\delta + \frac{\theta}{2}\right) + I_b \sin\left(\delta - \frac{\theta}{2}\right)$$

which can be written as:

$$I(\delta) = (I_a + I_b)\cos\left(\frac{\theta}{2}\right)\sin(\delta) + (I_a - I_b)\cos(\delta)\sin\left(\frac{\theta}{2}\right)$$

In the case of identical junctions $I_a = I_b = I_c$, the current reduces to:

$$I(\delta) = 2I_c \cos\left(\frac{\theta}{2}\right)\sin(\delta) \tag{26}$$

The SQUID then acts as a single JJ with an effective critical current $I_c^{\text{eff}}(\theta) = 2I_c\,|\cos(\theta/2)|$ modulated by the magnetic flux through the loop. This effective critical current vanishes each time the flux Φ reaches half integer values of Φ_0. This effect is used in magnetometers to measure magnetic flux of the order of the flux quantum Φ_0. It is also used to realise JJs whose critical current can be modulated by the application of a magnetic flux, as we use in our experiment.

2 "Absence of a dissipative quantum phase transition in Josephson junctions"

Here we reproduce the article [29] published in Physical Review X

Absence of a Dissipative Quantum Phase Transition in Josephson Junctions

A. Murani,[1] N. Bourlet,[1] H. le Sueur,[1] F. Portier,[1] C. Altimiras,[1] D. Esteve,[1] H. Grabert,[2] J. Stockburger,[3] J. Ankerhold,[3] and P. Joyez[1,*]

[1]Université Paris-Saclay, CEA, CNRS, SPEC, 91191 Gif-sur-Yvette Cedex, France
[2]Physikalisches Institut, Universität Freiburg, Hermann-Herder-Straße 3, 79104 Freiburg, Germany
[3]Institute for Complex Quantum Systems and IQST, University of Ulm, 89069 Ulm, Germany

(Received 7 May 2019; accepted 21 February 2020; published 3 April 2020)

Half a century after its discovery, the Josephson junction has become the most important nonlinear quantum electronic component at our disposal. It has helped reshape the International System of Units around quantum effects and is used in scores of quantum devices. By itself, the use of Josephson junctions in volt metrology seems to imply an exquisite understanding of the component in every aspect. Yet, surprisingly, there have been long-standing subtle issues regarding the modeling of the interaction of a junction with its electromagnetic environment. Here, we find that a Josephson junction connected to a resistor does not become insulating beyond a given value of the resistance due to a dissipative quantum phase transition, as is commonly believed. Our work clarifies how this key quantum component behaves in the presence of a dissipative environment and provides a comprehensive and consistent picture, notably regarding the treatment of its phase.

DOI: 10.1103/PhysRevX.10.021003 Subject Areas: Superconductivity

I. INTRODUCTION

In 1983, Schmid [1] predicted that a dissipation-driven quantum phase transition (DQPT) should occur for any Josephson junction (JJ) connected to a resistance R: When $R > R_Q = h/4e^2 \simeq 6.5\ \mathrm{k\Omega}$, the junction should be insulating at zero temperature, while if $R < R_Q$, the junction should be superconducting (see Fig. 1). The prediction was made more precise shortly after by Bulgadaev [2], and since then, many theoretical works using different techniques [3–12] have further confirmed it. Attempts to investigate this prediction experimentally are scarce [13–15], and these early experiments were all affected by technical limitations (see the Appendix A) that made their interpretation debatable. In this work, we revisit this prediction using well-controlled linear response measurements on the insulating side of the phase diagram, and we find no sign of the junctions becoming insulating. By revisiting the theory, we provide arguments explaining why, actually, no superconducting-to-insulating transition is expected, and we propose an alternative comprehensive physical picture for this system.

Let us first motivate our work by explaining why the predicted phase diagram is problematic. The left axis in the Schmid-Bulgadaev (SB) phase diagram [Fig. 1(b)] corresponds to $R \to \infty$, where we can simply remove the resistor from the circuit. In this limit, we are left with only the junction represented as a pure Josephson element in parallel with the junction's geometric capacitor C defining the charging energy $E_C = (2e)^2/2C$. Such a disconnected junction is known as a Cooper pair box (CPB) in the domain of quantum circuits; it behaves as a nonlinear oscillator and has been extensively investigated theoretically and experimentally [16–19]. In particular, for any junction with a nonzero Josephson coupling E_J, a CPB has finite charge fluctuations through the junction, in contradiction with it being on the insulating side of the phase transition, and it was shown that one can indeed drive finite ac supercurrents through the junction [20]. Furthermore, since the anharmonicity of the CPB vanishes upon increasing the ratio E_J/E_C [18], one expects (at least in the large E_J/E_C range) the effect of a finite parallel resistance R on this nonharmonic oscillator to be similar to that on a harmonic oscillator [21,22]: When R is varied, the phase and charge fluctuations have no abrupt change at $R = R_Q$. Approaches that go beyond considering the junction as a pure inductor [23,24] confirm this intuition down to the moderately large E_J/E_C range: They predict a superconductive junction that smoothly retrieves the "bare" (with no resistor) CPB behavior as the environment impedance gets large and cold. More generally, any Josephson junction connected to a large impedance Z is intuitively expected to smoothly recover the (superconducting) behavior of the CPB in the $Z \to \infty$ limit. This was

*philippe.joyez@cea.fr

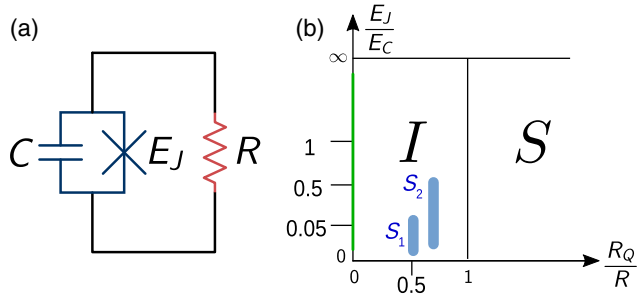

FIG. 1. (a) A Josephson junction connected to a resistor R (abbreviated as JJ + R). The junction's capacitance C determines the charging energy $E_C = (2e)^2/2C$, while the transparency of the tunnel barrier and the superconducting gap set its Josephson coupling energy E_J. (b) Sketch of the Schmid-Bulgadaev phase diagram for the circuit in (a). In the phase I (S), the junction is predicted to be insulating (superconducting) at zero temperature. The insulating phase is paradoxical because the left axis (green line, where $R = \infty$) is the location of the Cooper pair box family of superconducting qubits for which it is well known that the junction is superconducting. Similarly, our samples S_1 and S_2 are found to remain superconducting when lowering the temperature, even though they are supposed to be well inside the insulating phase.

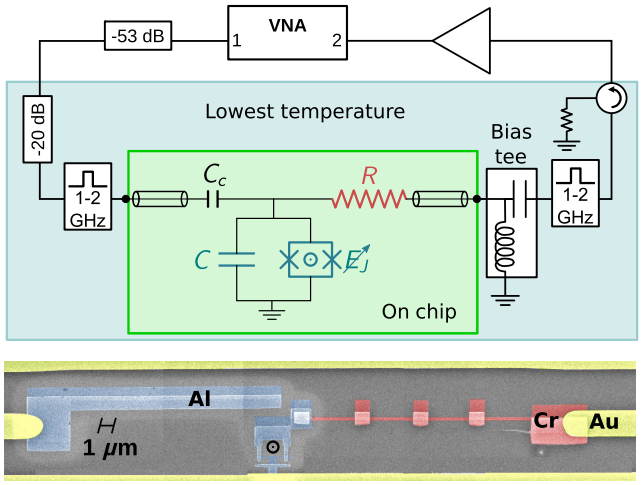

FIG. 2. Top: Simplified schematics of the experimental setup. Bottom: One of the samples measured. Two SEM micrographs are stitched to show the entire central part and colorized to evidence the different metals used (see Appendix B for fabrication details).

confirmed theoretically in the specific case of a purely inductive environment in Ref. [25]. In summary, several known theoretical results [18,21–25], many experimental results [16–18,20], and intuitive expectations in simple limits are consistent among themselves and conflict with the prediction of the insulating phase shown in Fig. 1(b).

II. EXPERIMENT

In order to test the SB prediction, we designed an experiment that closely implements the circuit of Fig. 1(a) while allowing us to probe the linear response of Josephson junctions in ac. A schematics of the experiment and a micrograph of a sample are shown in Fig. 2, and the main sample parameters are given in Table I. Instead of a single junction, we use a superconducting quantum interference device (SQUID) behaving as an effective tunable Josephson junction: By applying a magnetic flux Φ in the SQUID loop, its Josephson coupling energy is tuned as $E_J \simeq E_{J\max}|\cos(\pi\Phi/\Phi_0)|$ with $\Phi_0 = h/2e$ the flux quantum. The input capacitor C_c is chosen small enough that, at the measurement frequency, it essentially converts the input ac signal into a current source for the parallel junction-capacitance-resistance system. This current is split between these components according to their admittance. The fraction of the current flowing through the resistor is routed off chip to a microwave bias tee. The dc port of the bias tee is shorted to ground, closing the circuit in dc and ensuring there is no dc bias applied on the junction. At the high-frequency port of the bias tee, the ac signal coming from the resistor is sent through circulators and filters to a chain of microwave amplifiers with an overall gain of 106 dB. We used microwave simulations of the circuit to check that in this design, the actual impedance seen by the junction is close to $R \parallel C$ up to frequencies well above $(RC)^{-1}$ (note that the impedance to ground of the circuit following the resistor is negligible compared to R at all frequencies). We used a vector network analyzer to perform continuous-wave homodyne measurements of the transmission S_{21} through the sample. Although in this setup we measure variations of the fraction of the ac current flowing through the resistor, they are directly related to the variations of the junction admittance (see Appendix E).

The operating conditions of the experiment are subject to constraints that we now detail. First, in order to improve our sensitivity to the junction's admittance [26], the measurements need to be performed at a frequency well below the "plasma frequency" $\omega_p = (CL_J^{\rm eff})^{-1/2}$ of the junction, so that, as seen from the input capacitance, the ac current through C is negligible. The current is then essentially divided between the resistor and the junction's effective inductance $L_J^{\rm eff}$, should it exist, in proportion of their respective admittance $1/R$ and $1/iL_J^{\rm eff}\omega$. We selected an operating frequency of order 1 GHz in order to simultaneously fulfill this constraint (except in the vicinity of the maximal frustration of the SQUID) and have a reasonably

TABLE I. Main sample parameters. See Appendix B for details on their determination.

Sample	E_c/k_B (K)	$E_{J\max}/k_B$ (K)	R(kΩ)	C_c(fF)
1	2.6	0.12	12	0.3
2	0.64	0.39	8	0.3

good noise temperature for our microwave amplifier. Second, since we aim to probe the linear response of the junction at equilibrium, the ac phase excursion must be $\delta\varphi \ll 2\pi$, so that the junction is properly described by an admittance $1/iL_J^{\mathrm{eff}}\omega$. Assuming the worst case where all the current flows through the resistor, this inequality restricts the ac amplitude at the sample input $V_{\mathrm{in}} \ll \Phi_0/RC_c$ (that is, $P_{\mathrm{in}} \ll -50$ dBm for the values used in the experiment; see below). Correspondingly, all the measurements that we show here are taken in the low-power limit where S_{21} no longer depends on the input power (see Appendix D). The last constraint also restricts the admissible input power: The Joule power dissipated by ac current flowing through the resistor should not raise its temperature significantly. We use the results of Ref. [27] to estimate the electronic heating. Neglecting electron-phonon cooling in the resistor, for the maximum S_{21} value of -50 dB, and at the input power of -70 dBm used for the sample 2 data at the lowest temperature ($T_{\mathrm{ph}} = 13$ mK) in Fig. 3, one predicts an upper bound for the electronic temperature rise of approximately 1.0 mK (0.5 mK for sample 1) close to the junction (see Appendix C). Note that for such a low power level, the signal-to-noise ratio at the input of the first cryogenic HEMT amplifier is such that each data point necessitates averaging for about 20 min. Above about 50 mK, electron-phonon cooling becomes effective (see Appendix C); it is then possible to speed up the measurement by increasing the excitation amplitude (still remaining in the linear regime) without raising the electronic temperature.

In Fig. 3, we show the transmission S_{21} for the two samples we measured, for different flux through the SQUID and different temperatures. On the left panels, we show S_{21} as a function of the flux in the SQUIDs at the lowest temperature. We observe that when the flux is zero in the SQUID, the junction has the highest admittance (S_{21} minimum), whereas its admittance is minimum when the SQUID is frustrated with half a flux quantum in the loop. On the right panels, we show the temperature dependence of S_{21} for several values of the flux in the SQUIDs. We observe that in the low temperature range, for any fixed value of the flux, S_{21} reaches plateaus indicating that the junction admittance saturates to a finite value. In other words, at low temperature, the modulation of S_{21} with the flux proves that the SQUID still carries supercurrent, and it shows no tendency to become insulating at lower temperatures.

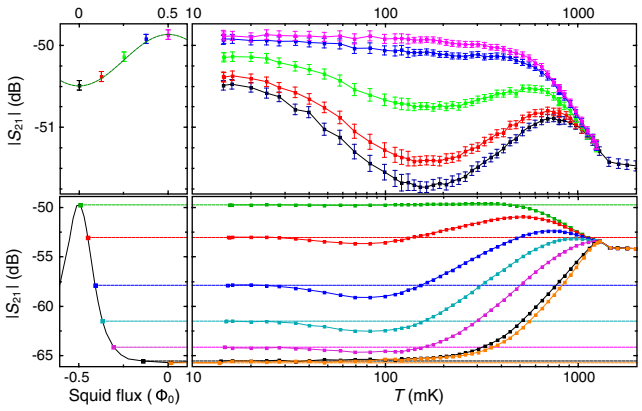

FIG. 3. Measured modulus of the transmission S_{21} (as a power ratio) for sample 1 (top panels) and 2 (bottom panels). Left panels: $|S_{21}|$ as a function of the flux through the SQUIDs at the base temperature. The modulation is periodic with the flux (data not shown), as usual for a SQUID; only half a period is represented. Note that the position of the zero flux is different in the top and bottom panels. Right panels: $|S_{21}|$ for several flux values (using the same colors as on the left panels) as a function of the temperature. For sample 2, the error bars are smaller than the symbols used (note the larger vertical scale).

III. DISCUSSION

Would the predicted insulating phase exist, the junctions would be in the quantum critical regime where one expects the junction admittance to follow a power law of the temperature [28]. This is clearly not the case in our experiments. In a totally independent experiment with a different objective, Grimm *et al.* [29] have recently observed that a SQUID with $E_J^{\max}/E_C \simeq 0.3$ in series with a 32-kΩ resistance ($R_Q/R \simeq 0.2$) had a clear dc supercurrent branch that was modulated with the flux. We consider their observation to support our results.

Together with the known $R \to \infty$ limit of qubits and the observed superconducting junctions at $E_J/E_C \gtrsim 7$ and $R_Q/R \sim 0.6$ in Refs. [14,30] (see Appendix A), we conclude that the experimental observations are consistent with a complete absence of the predicted insulating phase.

We now turn to theoretical considerations. In the first step, we revisit the framework in which the SB prediction of a superconducting-to-insulating phase transition was made. In the second step, we explain the exact nature of the predicted transition and provide arguments according to which JJs are actually not expected to become insulating in any Ohmic environment.

The SB prediction was cast using the model introduced by Caldeira and Leggett (CL) [31], which describes a Josephson junction and its capacitor (forming a CPB) analogous to a massive particle in a washboard potential, coupling the particle position (the junction phase) to a bath of harmonic oscillators that provide viscous damping. The corresponding Hamiltonian is

$$H = E_C N^2 - E_J \cos\varphi + \sum_n 4e^2 \frac{N_n^2}{2C_n} + \frac{\hbar^2}{4e^2}\frac{(\varphi_n - \varphi)^2}{2L_n},$$

where φ (resp. N) denotes the junction's phase (resp. number of Cooper pairs on the junction capacitance) which are conjugate $[\varphi, N] = i$, and the φ_n (resp. N_n) denote the phase (resp. dimensionless charge) of the harmonic

oscillators. H is not invariant upon $\varphi \to \varphi + 2\pi$, so that values of φ differing by 2π are naturally regarded as distinguishable states of the junction, and φ is said to be an "extended phase." Correspondingly, N has its spectrum in $\mathbb{R}$, and we call it an *extended* charge too.

A unitary transformation $H' = U^\dagger H U$ with $U = \exp(i\varphi N_R)$ and $N_R = \sum_n N_n$ (the charge passed through the resistor) yields another Hamiltonian of interest

$$H' = E_C(N - N_R)^2 - E_J \cos\varphi + \sum_n 4e^2 \frac{N_n^2}{2C_n} + \frac{\hbar^2}{4e^2}\frac{\varphi_n^2}{2L_n},$$

where the CPB now couples to the environment through N, here representing the number of transmitted Cooper pairs through the junction. Unlike H, H' is evidently invariant upon the discrete translation $\varphi \to \varphi + 2\pi$ so that the values of φ differing by 2π can be regarded as indistinguishable (wave functions in φ are 2π periodic), and the usual terminology is that φ is a "compact phase." In principle, φ can still be described as an extended variable, in which case the periodicity of the potential implies that wave functions in φ are Bloch functions $\Psi_q(\varphi) = \sum_n a_n(q) e^{i(n+q)\varphi}$. Here, the "quasicharge" q is a conserved quantity fixed by initial conditions. However, a Bloch function with quasicharge q can be transformed to any other Bloch function by a global shift of the bath charge, and the resistance is translationally invariant in both charge and phase (this invariance being respected in the CL model [31]). Thus, in this resistively shunted JJ, states with different quasicharges can be considered degenerate in the sense that no measurement on the circuit can distinguish them after the initial charge shift of the bath has decayed [32]. Thus, one can choose to use only compact phase states ($q = 0 \bmod 2\pi$) for convenience. In this case, N has a discrete spectrum in $\mathbb{Z}$ (even though there is no island in the circuit), and the Josephson coupling term can be written as $E_J \cos\varphi = \frac{1}{2} E_J (\sum_{N\in\mathbb{Z}} |N\rangle\langle N+1| + \text{H.c.})$ as customary for CPBs, which we expect to recover in the $R \to \infty$ limit.

With these provisos, H and H' operate on wave functions with different symmetries; they almost seem to describe different physical systems. This issue was known from the start, and several theory papers considered the suitability of either phase description for the system considered here, but no clear-cut answer emerged (for an overview, see Ref. [33]). However, a unitary transformation cannot break a symmetry of the system, and the contradiction resolves when one properly transforms the boundary and initial conditions together with the Hamiltonian [33,34]. Provided this transformation is carried out properly and barring any spontaneous symmetry breaking, H and H' can be used indifferently to describe the system, and any valid state of the system should thus be representable with either H or H'. As we mention above, in the $R = \infty$ limit of the bare CPB, the phase is known to be compact; hence, by continuity, compact states are also the states to consider at finite R, unless one shows a spontaneous symmetry breaking of the discrete phase translation invariance occurs, a phenomenon also known as the "decompactification" [6,35] of the phase (and which goes along with an "undiscretization" of the charge).

The SB theory is precisely all about dissipation causing spontaneous symmetry breaking; we now describe the core ideas of this theory. Close to the bottom axis of the phase diagram, in the so-called scaling limit where $E_C \to \infty$ (which constrains $N = N_R$), H' becomes equivalent to the tight-binding model used in Refs [3,4] (see Appendix G). In this model, at low friction (low R), the junction's zero-temperature reduced density matrix ρ is completely delocalized in the discrete charge basis, and thus corresponds to a perfectly localized compact phase. For such a state, using an extended description for both charge and phase, the diagonal of ρ is a Dirac comb in both charge and phase representation [Fig. 4(b), bottom right]. For $R > R_Q$, however, the discrete translational invariance symmetry of the charge is broken, and the charge localizes at a given value of $\langle N\rangle = \mathrm{Tr}\rho N$. In ρ, the result of this charge localization can be seen as multiplying the charge Dirac comb by a bell-shaped function b and broadening each peak of the phase Dirac comb by convolving it with the Fourier transform of b [Fig. 4(b), bottom left]. Across the transition, the charge fluctuations (the width of b) vary continuously [4], but the dc charge mobility μ (related to the charge fluctuations according to the standard Green-Kubo relations; see Appendix F) is predicted to

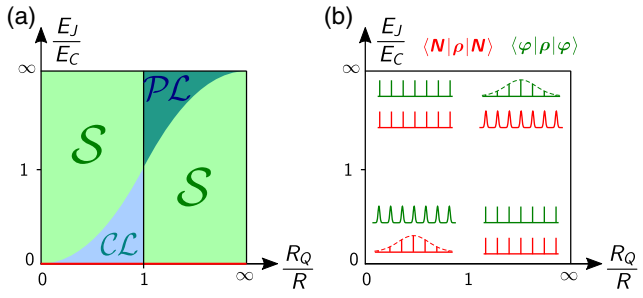

FIG. 4. (a) Reinterpreted Schmid-Bulgadaev phase diagram, in which the junction is superconducting everywhere, except for $E_J = 0$. In the $\mathcal{S}$ parts, the junction is superconducting with a fully delocalized charge and, correspondingly, a fluctuationless (classical) compact phase. Partial charge (phase) localization occurs in the $\mathcal{CL}$ ($\mathcal{PL}$) part. The classical phases $\mathcal{S}$ are artifacts which disappear when improving the model (see text and Appendix G). (b) Final description of the junction's behavior in the parameter space. Drawings are sketches of the diagonal elements of the junction's reduced density matrix in an extended description (red, charge representation; green, phase representation). Close to the left (right) half of the upper (lower) axis, they nearly take the form of Dirac combs where the phase is almost a classical variable. In the lower left (upper right) sector, partial charge (phase) localization occurs, as in (a). The density matrix evolves continuously, interpolating between these limits, without any phase transition.

vanish (resp. diverge) for $R > R_Q$ (resp. $R < R_Q$) at $T = 0$, hence, the prediction of a superconducting-to-insulating transition.

At the time of the prediction, this mobility argument was often associated with the simple picture of infinite polaronic trapping in the insulating phase $R > R_Q$ and the corresponding suppression of the coherence $E_J\langle\cos\varphi\rangle$ between charge states. More elaborate renormalization group (RG) flow arguments [1–3,6,12,36] led to the conclusion that an immobilization of the junction charge indeed occurred in the whole domain where the cutoff frequency of the Ohmic damping is the fastest dynamics in the system, i.e., $E_J/E_C < (R_Q/R)^2$ [see part $\mathcal{CL}$ in Fig. 4(a); note that our experimental parameters are in this zone].

However, works on the closely related spin-boson problem (SBP; the CL model is an infinite-spin generalization of the SBP) have shown that the picture of infinite polaronic trapping is too naive. In this system, the spin and the bath entangle in the ground state, involving an infinite number of bosonic excitations *and* yielding resilient finite coherences (possibly very small) [37–40] that depend algebraically on the UV cutoff of the Ohmic bath. In the CL model itself, perturbation theory in E_J shows as well that, while $E_J\langle\cos\varphi\rangle = 0$ at zeroth order, $E_J\langle\cos\varphi\rangle = \mathcal{O}(E_J^2/E_C)$ (as in the bare CPB) at the next order [41] for any $R > R_Q/2$. Hence, it is no longer believed that the coherences vanish in the "insulating phase," and this has dramatic consequences: (i) It enables a finite supercurrent flow (as evidenced by our experiments), and (ii) previously calculated dc charge mobility does not describe the actual transport properties, because it does not take into account the inductive behavior associated with the supercurrent (see Appendix F). The qualitative explanation for the robustness of the coherence is that the inductive response of the junction shunts the low-frequency modes of the environment that were supposed to fully suppress the coherence [23]. In this new understanding of the (previously believed) insulating phase, the partially localized charge states are similar to those of the bare CPB, and they very naturally coincide with them in the $R \to \infty$ limit. The difference between the resistively shunted junction and the CPB with an island is that in the first case there is a degenerate continuum of localized charge states at all values of $\langle N\rangle$, while in the second case where no dc current can flow, $\langle N\rangle$ is pinned, and the ground state is unique.

Close to the top axis of the phase diagram, one follows similar reasoning in the "dual" picture [42], where charge and phase are interchanged. One then starts from a tight-binding description of Wannier states for the phase located in the different wells of the cosine potential (and where the strength of the friction is inverted [42]). Mirroring what occurs on the bottom axis, this duality predicts that the diagonal of ρ is again a Dirac comb in both charge and phase representations [upper left of Fig. 4(b)] at low friction (large R) and that a smooth spontaneous symmetry breaking transition to partial "phase localization" occurs for $R < R_Q$ [part $\mathcal{PL}$ in Fig. 4(a)]. We thus identify this transition as a *progressive* decompactification of φ. This shows that a generic decompactified phase state is the dual of a CPB state, i.e., a superposition of classical phase states differing by 2π in several adjacent wells of the cosine. To our knowledge, this is the first time the decompactification process is clarified, and it is a key result as it shows this spontaneous symmetry breaking does *not* yield generic extended phase states, contrary to what was generally assumed so far (see Appendix H). In particular, Schmid and subsequent authors treated φ as extended, which led them to attribute an insulating character to the "delocalized phase" in all the wells of the cosine (for $R > R_Q$). However, when considering a compact phase, the junction is insulating only when the phase is completely delocalized within one period (all coherences vanishing: $\langle\cos n\varphi\rangle = 0$, $\forall\, n \in \mathbb{N}^*$), meaning that the diagonal of ρ is completely flat in the phase representation.

In Fig. 4(a), we show our reinterpretation of the SB phase diagram, where the junction is superconducting everywhere, except at $E_J/E_C = 0$, in the so-called *scaling limit*. Note that in actual implementations, E_C is always finite, so that the insulating state of the scaling limit can be achieved only by choosing $E_J = 0$, i.e., trivially, an already fully insulating junction (even in the normal state). This reinterpreted diagram is in agreement with experiments and resolves the conflicts mentioned in the Introduction. At this point, the vertical boundaries at $R = R_Q$ which remain from the SB prediction are continuous transitions from fluctuationless phase states to states having finite zero-point phase fluctuations, i.e., classical-to-quantum transitions. However, one can show these transitions arise from properties of the uncoupled bosonic bath (Ref. [3] and Appendix G), and one expects that a better treatment (taking into account the aforementioned entanglement of the junction with the bath) should restore finite phase fluctuations in the phases S, turning this transition into a crossover.

The emergent understanding of this system is represented pictorially in Fig. 4(b): The junction is superconducting everywhere, and its reduced density matrix evolves continuously as a function of the parameters, interpolating between the limit cases depicted. From this diagram, one sees that when the effective Josephson Hamiltonian is deemed adequate to model a Josephson junction (see Appendix I), the junction phase can be essentially regarded as compact (and one can use the discrete charge basis of a CPB) below the main antidiagonal, while one expects a partial decompactification of the phase above that antidiagonal.

Obviously, generic extended phase states do not have the appropriate symmetries within this understanding. Consequently, assuming an extended phase to describe the low-energy states in such a system is at best approximate or it appeals to (perhaps unspoken) ingredients external to the CL model. Yet, many predictions (besides

the DQPT) were made assuming an extended phase and have been checked to well describe the Josephson physics. This raises the question of when can one safely use such a description? A nonoperative answer is that such a description is fine as long as interference effects that would appear in a proper treatment of the phase (more or less complete) translation invariance play no significant role.

Before closing this discussion, let us comment on the striking dips observed in the temperature dependence of the transmitted power near $T \sim 100$ mK corresponding to a maximum of the junction admittance. They can be understood at a qualitative level using the usual charge description of the CPB (consistent with the above discussion), assuming the resistance is large enough. In the regime $E_J \ll E_C$ and at very low temperature, the state of the CPB is nearly a classical state at the minimum of a charging energy parabola with a given N. This state nevertheless has quantum fluctuations that can be computed by second-order perturbation theory, with virtual transitions through the neighboring charge states. This process results in an effective Josephson coupling for the ground state $E_J^{\mathrm{eff}} = E_J\langle\cos\varphi\rangle \propto E_J^2/E_C$, the energy denominator E_C being the energy of the virtual states. At finite temperatures $k_BT \lesssim E_C$, low-energy modes of the resistance are thermally populated; they can lend their energy to the virtual state, lowering the energy denominator and thus increasing the effective Josephson coupling. At higher temperatures, thermal fluctuations eventually reduce the gap of Al, reducing the Josephson coupling.

IV. METADISCUSSION

Given that the present work contradicts more than 35 years of literature on the understanding of a Josephson junction in a resistive environment, one may rightfully wonder if alternative explanations of our results could exist. One can hypothesize that

(i) we might over- or misinterpret our experimental data and that of Grimm *et al.* [29] when we conclude that the junctions remain superconducting at low temperatures, and

(ii) there could be hidden flaws in our theoretical analysis of the CL model, which leads us to conclude that no insulating phase is expected in JJ + R systems,

such that the original SB prediction regarding JJs could stand. Within these hypotheses, signatures of the insulating state could, for instance, appear only out of the experimental windows for some reason to be worked out, making our experimental data compatible with the original prediction. However, we stress that the inconsistency of the insulating phase with the intuitive limits that we point to in the Introduction would still need to be addressed.

We thus encourage experimental and theoretical work in this domain that could complete, clarify, or correct our findings, in the hope that the community soon reaches consensus on the expected behavior of this key quantum component in the presence of an environment.

V. CONCLUSIONS

Our experimental results show no evidence of the superconducting-to-insulating DQPT in Josephson junctions predicted by Schmid and Bulgadaev, contrary to present widespread expectations. We provide theoretical arguments according to which the superconducting coherence in JJs is actually resilient to dissipation, thereby barring the occurrence of that DQPT in JJ + R systems (the DQPT does occur in *nonsuperconducting* 1D systems, however; see Appendix J). We reach a global and consistent qualitative description of JJs with an environmental impedance that dovetails all well-known limits. As an important by-product, our analysis for the first time clearly exposes how phase decompactification occurs in Josephson junctions. This shows that generic extended phase states are not rigorous solutions for this system, hopefully settling decades of controversies. Our work also highlights that there are presently no comprehensive and quantitative predictions for the effect of dissipation on the CPB able to reproduce our results. Finally, our results prompt for a critical reexamination of the works where the Schmid-Bulgadaev prediction regarding Josephson junctions was used to draw predictions for other systems such as superconducting nanowires proposed to implement quantum phase slip junctions [43–45].

ACKNOWLEDGMENTS

The authors are grateful to M. Devoret, B. Douçot, S. Florens, M. Hofheinz, C. Mora, I. Safi, H. Saleur, P. Simon, and N. Roch for stimulating discussions and suggestions. The technical assistance of Pascal Sénat and SPEC's Nanofabrication lab is acknowledged, and we thank other members of the SPEC's Quantronics group for their constant support. This work is supported in part by ANR Grant No. ANR-15-CE30-0021-01 and ANR-18-CE47-0014-01, the ANR-DFG Grant JosephSCharli, and by the LabEx PALM Project No. ANR-10-LABX-0039-PALM. J. A. and J. S. are supported by the German Science Foundation under Grant No. AN336/11-1 and the Center for Integrated Quantum Science and Technology (IQST). C. A. acknowledges funding from the European Research Council under the European Union's Horizon 2020 program (ERC Grant Agreement No. 639039).

APPENDIX A: FORMER EXPERIMENTAL TESTS

The SB prediction has been researched experimentally [13–15,30], but the scaling laws expected to be the hallmark of the predicted quantum critical regime have not been thoroughly investigated.

In these experiments, the junction and its Ohmic shunt resistance R were typically "current biased" using a voltage

source in series with a large resistor $R_{\rm bias} > R$ and measured using a lock-in technique at frequencies $f_{\rm LI} \sim 100$ Hz or below. Could such a setup properly measure the linear response of the junction?

For junctions with small critical current, it is well known that spurious noise in the setup rapidly reduces the apparent maximum supercurrent [46–48], and particularly so for underdamped junctions, i.e., when $E_J/E_C \gg (R_Q/R)^2$. However, even when the technical noises are completely eliminated, a lock-in measurement has intrinsic limitations when the junction's admittance becomes smaller than $1/R$. In that case, keeping a small phase excursion in these setups requires an ac voltage excitation at the junction $V_{\rm ac} \ll \Phi_0 f_{\rm LI} < 1$ pV which, even taking into account the resistive bridge division $R/(R + R_{\rm bias})$, is several orders of magnitude smaller than required to have a sufficient signal-to-noise ratio in lock-in measurements. Thus, the former experiments aiming to test the DQPT could not properly measure the linear response of junctions with very low admittances: Several periods of the cosine were explored, rapidly averaging any small supercurrent to zero. In contrast, in our setup, measuring at much higher frequencies enables us to use larger excitation voltages while remaining in the linear phase response regime, even when the admittance of the junction becomes very low.

On the other hand, it is easy to observe the supercurrent branch of junctions having a large critical current, even with an imperfect setup, because the junction very effectively shunts noise. Indeed, the authors of Refs. [14,30] found that a superconducting branch was observed for all junctions supposed to be in the insulating phase, provided that $E_J/E_C \gtrsim 7$. At the time of this result, the discrepancy with the DQPT prediction was resolved by arguing that the observed superconducting state was a transient and that the true equilibrium insulating state would be reached only after a possibly cosmologically long time [6,14,30]. The argument given was that when the junction's (extended) phase starts localized in one well of the cosine potential, it will eventually delocalize in all other wells of the cosine by tunneling (and this delocalized state was assumed insulating), but the tunneling rate becomes immeasurably small for large E_J/E_C. However, when timescales become very long and energies very small, one should seriously reconsider all other approximations made in the modeling, such as, for instance, neglecting the level separation in the electrodes. When considering a compact phase, such a slow phenomenon simply does not exist: The phase is always instantly delocalized in all wells of the cosine, and moreover, that state is superconducting. The superconducting state observed in these experiments was then the genuine equilibrium state.

APPENDIX B: FABRICATION DETAILS

The fabrication of the sample starts from a gold 50-Ω coplanar waveguide (CPW) defined by optical lithography and providing the input and output ports for the microwave signals. The central conductor of the transmission line is interrupted on a length of 38 μm, creating a cavity in which the resistor and junctions are fabricated in two subsequent steps, using e-beam lithography and evaporation through suspended masks. The resistor consists of a 8.5-nm-thick, approximately 100-nm-wide and 16-μm-long Cr wire, periodically overlapped with 45-nm-thick, 1×1 $(\mu{\rm m})^2$ Cr cooling pads. One end of the resistor connects to the output transmission line. The junctions are produced by standard double-angle evaporation of aluminum. The SQUID is connected on one side to the ground plane of the CPW, and on the other side to the other end of the Cr resistor. Microwave simulations of the circuit are used to check that in this design the actual impedance seen by the junction is close to $R \parallel C$ up to frequencies well above $(RC)^{-1}$. In order to meet this condition, it is important that the whole SQUID + resistor layout is very compact to avoid stray inductances and capacitances.

1. Determination of the sample parameters

Since the values of E_J and R cannot be independently measured directly on the sample, the values reported in Table I come from the room-temperature measurements of the resistance of several other junctions and resistors having the same dimensions and fabricated at the same time on the sample. From the scatter of these measurements, the values reported are believed to be accurate within ±15%. The value of E_c is estimated from the area of the junction using the commonly used value 100 fF $(\mu{\rm m})^{-2}$ for the capacitance per unit area of aluminum-aluminum oxide junctions. The value of the coupling capacitance is obtained from microwave simulations.

APPENDIX C: JOULE HEATING IN THE RESISTOR

Here we show that for the measurements shown in Fig. 4, the Joule power dissipated in the chromium resistor does not substantially raise the electronic temperature. For this, we rely on the analysis of heating in diffusive wires detailed in Ref. [27], where it is assumed that the electron temperature can be well defined locally, i.e., that the thermalization between electrons occurs faster than their diffusion through the wire and that we can neglect the radiative cooling of the wire. In this reference, the diffusive wire is supposed to be connected to two normal-metal reservoirs at both ends, and these reservoirs are supposed to be large enough so that their electronic temperature is equal to the phonon temperature. In our case, on the junction side the Cr wire is connected to superconducting Al which blocks any heat exchange at very low temperatures. We can nevertheless obtain the electronic temperature at this point by considering the results of Ref. [27] in the middle of a wire with twice the length, twice the resistance, and twice the dissipated power.

We first evaluate the maximum Joule power P_R dissipated in the Cr resistor for the measurements performed at the lowest temperature (13 mK) in Fig. 4. This power is proportional to the power $P_{\rm out}$ at the output of the sample by

$$P_R = \frac{R}{Z_0} P_{\rm out},$$

where $Z_0 = 50\ \Omega$ is the impedance of the microwave circuitry, and

$$P_{\rm out} = P_{\rm VNA} 10^{[(S_{21}-G)/10]},$$

where $P_{\rm VNA}$ is the power at the vector network analyzer (VNA) output, S_{21} is the measured transmission of the setup (in dB), and $G = +106$ dB the overall gain (in dB) of the microwave chain from the sample output to the VNA input. For sample 2, using the maximum value $\mathrm{Max}(|S_{21}|) = -50$ dB, $P_{\rm VNA} = +3$ dBm, and $R = 8$ kΩ, this leads to a maximum $P_R \simeq 80$ aW [for sample 1: $\mathrm{Max}(|S_{21}|) = -50$ dB, $P_{\rm VNA} = -4$ dBm, and $R = 12$ kΩ give a maximum $P_R \simeq 25$ aW].

Looking for an upper bound for the electronic temperature, we consider the simple "interacting hot-electron" limit, where electron-phonon interaction in the wire is neglected, so that cooling occurs only through diffusive electronic exchange with the reservoir (here the gold central conductor of the CPW). In this limit, the maximum temperature (reached in the middle of the wire in Ref. [27] and at the Cr-Al interface in our case) is

$$T_{\rm max} = \sqrt{T_{\rm ph}^2 + \frac{3}{4\pi^2}\left(\frac{e}{k_B}\right)^2 2R2P_R},$$

where $T_{\rm ph}$ is the phonon temperature in the reservoir. At the lowest temperature $T_{\rm ph} = 13$ mK, and for the above values this yields

$$T_{\rm max} \simeq T_{\rm ph} + \begin{cases} 1\ \text{mK for sample 2,} \\ 0.5\ \text{mK for sample 1,} \end{cases}$$

which sets an upper bound for the electronic temperature of the electromagnetic environment in our experiments. These considerations show that in the entire experimental range, Joule heating of the resistor is negligible.

In the above analysis, the thick intermediate pads incorporated in the wire design (see Fig. 2) play absolutely no role. They are meant to increase electron-phonon coupling, but they are effective only at higher temperature, as we now discuss. At the maximum power dissipated in the resistor, we can estimate the electronic temperature $T_\Sigma = (P_R^2/\Sigma\Omega)^{1/5}$ [27] that would be reached if only electron-phonon cooling was taking place. Taking the entire volume of the resistive wire and of the intermediate cooling pads $\Omega \simeq 0.20\ (\mu\mathrm{m})^3$ and assuming the standard electron-phonon coupling constant $\Sigma \simeq 2\ \mathrm{nW}\,(\mu\mathrm{m})^{-3}\,\mathrm{K}^{-5}$ gives $T_\Sigma \simeq 36$ mK (for sample 2). We could thus increase the measurement power at temperatures above 50 mK in order to speed up the measurements while still not heating the electrons.

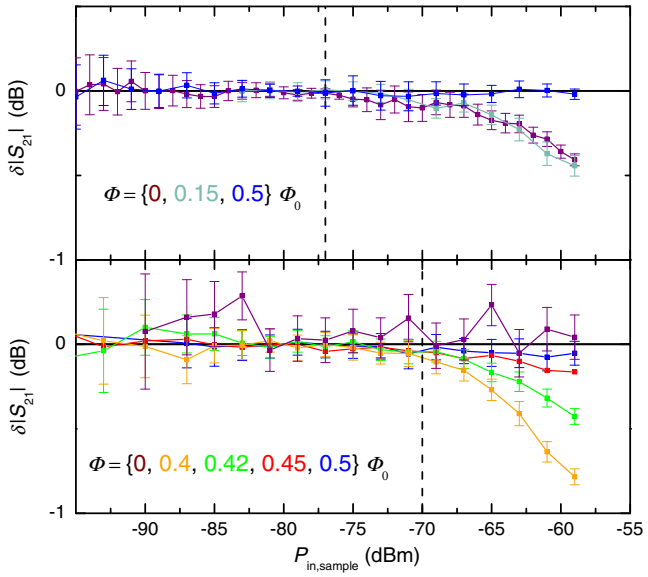

FIG. 5. Variations of the transmission through the samples (top, sample 1; bottom, sample 2), as a function of the power at the sample input, for different values of the flux through the SQUIDs, at the lowest temperature (variations are taken with respect to the value at $P_{\rm in} = -80$ dBm). The size of the error bars does not vary monotonically because the averaging time was increased when reducing the power. The dashed lines indicate the power levels that were chosen to take the data shown in Fig. 3.

APPENDIX D: CHECKING THE LINEARITY OF THE RESPONSE

In order to ascertain that we measure the linear response of the junction properly, we check that S_{21} no longer depends on applied power at low power. In Fig. 5, we show the variations of $|S_{21}|$ as a function of the applied measurement power for various fluxes in the two samples at the lowest temperature (13 mK). We indeed observe that in the low-power range, $|S_{21}|$ no longer changes, confirming that we measure the linear response and that we are not heating the resistor. We used such measurements to choose the operating power for the data presented in Fig. 3, selecting the value at the end of the horizontal plateau (shown as the dashed vertical line in Fig. 5), i.e., −77 dBm for sample 1 and −70 dBm for sample 2.

APPENDIX E: LINK BETWEEN THE MEASURED S_{21} AND THE JOSEPHSON-JUNCTION PARAMETERS

Assuming a probe signal has a low enough amplitude, the circuit between the input port and the output port of

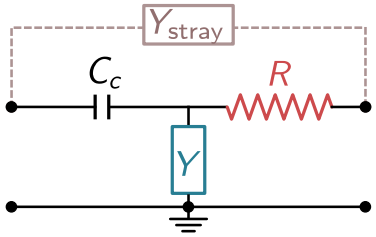

FIG. 6. Quadrupole model of the on-chip components for the calculation of the transmission S_{21}. In the ideal case where the external circuit can be fully calibrated by measuring reference samples, S_{21} would depend only on C_c, R, and Y, the admittance of the junction. In our experiment, this full calibration is not performed, and a weak stray admittance $|Y_{\text{stray}}| \ll |iC_c\omega|$ very likely dominates our measurements at lower values of S_{21}, when the junction admittance is large ($|Y|R \gg 1$).

the sample chip is then a linear quadrupole as depicted in Fig. 6, with the junction described as a linear admittance $Y(\omega)$ corresponding to the parallel combination of the capacitance and the SQUID of Fig. 2. For such a quadrupole, the input and output waves' amplitudes at both ports (assumed to have the standard microwave characteristic impedance $Z_0 = 50\ \Omega$) are related by an S matrix [49]. Considering that at the frequency of the experiment $(iC_c\omega)^{-1} \gg R \gg Z_0$, the S matrix of the sample is approximately

$$S \simeq I + S_{21}\sigma_x,$$

where I is the 2×2 identity matrix, σ_x the Pauli matrix, and

$$S_{21} = \frac{2iC_c\omega Z_0}{1 + RY(\omega)}$$

is the transmission amplitude from the input to the output port.

Thus, in principle, a measurement of the (complex-valued) transmission S_{21} with a vector network analyzer can give access to the complex junction admittance. However, in order to access this ideal on-chip S, one must carefully calibrate the whole microwave setup using several reference devices (e.g., thru, reflect, and line) in place of the sample [49] in order to deembed the effect of the rest of the setup. Such a procedure is needed, in particular, to define a reference for arg S_{21} and to cancel any stray transmission between input and output (Y_{stray} in Fig. 6). As our demonstration involves evidencing only a SQUID modulation that saturates at low temperature, it requires only qualitative measurements, and thus, for simplicity, such a calibration is not performed. The measured (uncalibrated) $|S_{21}|$ variations can nevertheless be qualitatively compared to the ideal prediction

$$|S_{21}|^2 = \frac{(2C_c\omega Z_0)^2}{|1 + RY(\omega)|^2}.$$

Given our choice of parameters $RC\omega \ll 1$, the capacitive contribution in Y can be neglected for the evaluation of S_{21}, and we can consider only the contribution of the Josephson element $Y(\omega) \simeq 1/iL_{\text{eff}}\omega$ (assuming a superconducting character). Under this form, it is clear that larger values of $|S_{21}|$ correspond to small junction admittance (large effective inductance, small supercurrent) and vice versa.

For sample 1, in the low-temperature limit, the modulation of $|S_{21}|$ with flux is small, showing that $|Y|R \ll 1$. Assuming the junction behaves as a usual symmetric SQUID, its inductance depends on the flux Φ as $L_{\text{eff}}(\Phi)^{-1} = 2eI_0^{\text{eff}}|\cos(\pi\Phi/\Phi_0)|/\hbar$, with I_0^{eff} the effective critical current. By adjusting the amplitude of the S_{21} modulation for sample 1 in the low-temperature limit, this gives $I_0^{\text{eff}} \sim 70$ pA, much smaller than the Ambegaokar-Baratoff $I_0 = E_J 2e/\hbar = 5.0$ nA value obtained from the junction's tunnel resistance. This decrease is qualitatively expected, because zero-point phase fluctuations [23,50,51] are known to reduce the effective critical current, or, equivalently, to "renormalize" the apparent Josephson coupling. One can also check that the change of $|S_{21}|$ of approximately -1.4 dB between the maximum frustration of the SQUID at low temperature (where $Y \simeq 0$) and the critical temperature $T_c \sim 1.2$ K of Al (where all lines merge at $Y \simeq 1/R_T$) is consistent with $R_T \simeq 62$ kΩ, the junction normal-state tunnel resistance. This line of reasoning is also true for sample 2: The change of $|S_{21}|$ of approximately -3.6 dB is consistent with $R_T \simeq 19$ kΩ.

For sample 2, however, it is not possible to correctly reproduce the shape of the variations of S_{21} in the bottom left panel of Fig. 3 by assuming the SQUID behaves as a standard one with $L_{\text{eff}}(\Phi)^{-1} = 2eI_0^{\text{eff}}|\cos(\pi\Phi/\Phi_0)|/\hbar$ and adjusting the effective I_0^{eff} as done for sample 1. Given the shape of the modulation, it seems very likely that a weak stray transmission in our setup (as Y_{stray} in Fig. 6) causes $|S_{21}|$ to saturate at a minimum value of approximately -65.7 dB. Note that even if this were not the case, we expect the modulation curve could still not be accurately fitted using $L_{\text{eff}}(\Phi)^{-1} = 2eI_0^{\text{eff}}|\cos(\pi\Phi/\Phi_0)|/\hbar$, because in this sample, the $|S_{21}|$ measurements show that the junction admittance is modulated from $|Y| \lesssim$ or $\ll 1/R$ at the maximum frustration to $|Y| \gg 1/R$ at minimum frustration, such that the total effective impedance at the junction and the corresponding zero-point phase fluctuations (which determine I_0^{eff}) vary much with Φ. This variation of admittance should lead to a strongly flux-dependent $I_0^{\text{eff}}(\Phi)$, and hence, an overall non-abs(cos) modulation of the inverse inductance [23].

Finally, the striking nonmonotonic dependence of the transmission on the temperature is explained qualitatively in the main text before the Conclusion.

Our experiment demonstrates that when quantitative predictions become available for the junction inductance in high-impedance Ohmic environments, calibrated S_{21}

measurement in such a setup should allow a quantitative comparison.

APPENDIX F: LINEAR RESPONSE AND MOBILITY IN THE CALDEIRA-LEGGETT MODEL

Considering the Hamiltonian H' of the main text

$$H' = E_C(N-N_R)^2 - E_J\cos\varphi + \sum_n 4e^2\frac{N_n^2}{2C_n} + \frac{\hbar^2}{4e^2}\frac{\varphi_n^2}{2L_n},$$

the operator for the current flowing through the junction is

$$I = \frac{2e}{\hbar}\frac{\partial H'}{\partial\varphi} = \frac{2e}{\hbar}E_J\sin\varphi = I_0\sin\varphi.$$

Now we consider a thought experiment where the junction phase φ is given a time dependence $\varphi \to \varphi + \delta\varphi(t)$, so that the Hamiltonian acquires a time dependence too, $H' \to H'(t)$. We can obtain the corresponding change in the current by using the general response formula of Ref. [52] [Eq. (1) with $X(t') \equiv \varphi(t')$ and $\hat{O}(t) \equiv I(t)$],

$$\frac{\delta I(t)}{\delta\varphi(t')} = \frac{-i}{\hbar}\theta(t-t')\left\langle\left[I(t), \frac{\hbar}{2e}I(t')\right]\right\rangle + \delta(t-t')\frac{2e}{\hbar}E_J\langle\cos\varphi\rangle(t),$$

where $\langle\ldots\rangle = \mathrm{tr}[\rho(t)\ldots]$ with the time-dependent density matrix $\rho(t)$. This result expresses the exact Hamiltonian evolution, making essentially no assumption on the system or on the drive $\delta\varphi(t)$. However, it involves the time-dependent density matrix $\rho(t)$. The linear response of the system is obtained from this general formula by considering vanishingly small $\delta\varphi(t)$, in which case, we can use the equilibrium density matrix in the above expression (with the last term becoming time independent and the first one depending only on $t-t'$).

Using the fact that the voltage fluctuations across the junction are $\delta V = (\hbar/2e)(d/dt)[\delta\varphi(t)]$, and going to the frequency domain, the above result yields the junction's linear admittance

$$Y(\omega) = \frac{\delta I(\omega)}{\delta V(\omega)} = \frac{1}{\hbar}\int_0^{+\infty} 2\langle[I(t), I(0)]\rangle\frac{e^{i\omega t}-1}{\omega}\frac{dt}{2\pi} + \left(\frac{2e}{\hbar}\right)^2\frac{E_J\langle\cos\varphi\rangle}{i\omega}. \tag{F1}$$

In the first term, one recognizes the standard linear susceptibility of the usual Kubo formula. The second term is due to the (change in the) current carried by the ground state, yielding a purely inductive response of the junction. Even if we do not know what the equilibrium density matrix is in our system (because the junction is entangled with the bath), this term is nonzero as long as $E_J\langle\cos\varphi\rangle \neq 0$.

Using the fact that $2e\dot{N} = I$, the first term in the above expression can also be formulated in terms of the junction's charge correlator

$$Y(\omega) = \frac{4e^2}{\hbar}\int_0^{+\infty} 2\langle[N(t), N(0)]\rangle\omega e^{i\omega t}\frac{dt}{2\pi} + \left(\frac{2e}{\hbar}\right)^2\frac{E_J\langle\cos\varphi\rangle}{i\omega}.$$

The impedance defined by this thought experiment is an equilibrium property of the junction coupled to its environment. In practice, when one wants to measure this linear response, indirect driving of the junction phase can be realized in several ways, say, by threading an ac magnetic field in the circuit loop or by using a capacitive bias as in our experimental setup. As long as the probing circuitry does not alter the impedance seen by the junction, the measured linear response is (and it *must be*) independent of the biasing scheme chosen. We further stress that the linear response theory naturally embraces finite frequencies so that $Y(\omega)$ is a genuine equilibrium property of the system, even at finite frequency. In this regard, our probing of the system at approximately 1 GHz poses no problem of principle.

1. dc mobility vs full linear response

In the entire literature on the Schmid-Bulgadaev transition, the transport quantity that was focused on is the so-called dc charge mobility,

$$\mu = \frac{\delta I_{\mathrm{dc}}}{\delta V_{\mathrm{dc}}} = \mathrm{Re}\,Y(\omega=0),$$

which entirely comes from the first term of the admittance (F1) and that is obtained considering only the equilibrium charge (or current) correlator. Note that, by definition, μ describes *dissipative* transport.

However, if the inductive term in $Y(\omega)$ is nonzero (i.e., if the system can sustain a supercurrent), the zero-frequency limit of Eq. (F1) considered in μ is disregarding a diverging term, and, given that there are never strictly zero-frequency measurements, one may wonder about the relevance of this quantity for describing transport. Indeed, we now show that no experimental measurement protocol gives access to μ in a superconducting system. Let us, for instance, consider the initial unbiased equilibrium state with $\langle\varphi\rangle = 0$ in which there is no current flowing [$I(t\leq 0) = 0$] and assume that at $t = 0$, a voltage step $\delta V(t)$ is applied, ending on a plateau $\delta V \neq 0$ after a time τ. If mobility were appropriately describing the linear dc response, one would expect that after a transient, $\delta I(t \gg \tau) \to \mu\delta V$. However, this is clearly not the case for a linear superconducting inductor because the inductive response to the voltage pulse is a linearly

increasing current, not a transient. It is also incorrect for a Josephson junction and its nonlinear inductance because the interplay of the Josephson nonlinearity and the non-Markovianity due to the retarded response of the RC circuit results in a complex dynamics of the system involving potentially many harmonics of the Josephson frequency $\omega_J = 2e\delta V/\hbar$. There is presently no general theory that is able to predict the resulting dc current for all parameters and, in particular, when phase fluctuations are large. Here we assume a voltage bias scheme, but one can similarly show that the inductive response cannot be ignored in other biasing schemes and that this cannot be fixed by changing the frequency, the amplitude, or the temperature at which the measurement would be performed. In a nutshell, the linear mobility simply does not properly describe transport in a system that can sustain a supercurrent (i.e., where $E_J\langle\cos\varphi\rangle \neq 0$ in the case we consider) because it ignores the dominant effect of the supercurrent.

Consequently, finding a vanishing dc mobility (as in Refs. [1–6,9,11,12]) is not by itself a correct way of proving the system is insulating. For being an acceptable proof, it requires, in addition, that the coherences are suppressed in the ground state. Note that interestingly, Schmid [1] also considered the renormalization of the coherence factor $E_J\langle\cos\varphi\rangle$ (see the following section), but he regarded this as an *independent* proof of his mobility result, and not a condition for it.

2. Insulating state in the Caldeira-Leggett model?

From the above material, it emerges that for an insulating state to exist in this Caldeira-Leggett model, it is *necessary* (and sufficient) that the environment fully suppresses the coherences between charge states in the ground state.

As explained in the main text, RG flow analysis on the Josephson coupling initially indicated that coherences also vanished in the insulating phase, seemingly validating the mobility calculation (on the insulating side). However, results on the spin-boson problem, as well as perturbation theory in E_J in the CL model contradict the RG analysis and indicate that finite coherences always survive in the ground state of the CL model (as long as $E_J/E_C > 0$). Hence, from the theory point of view, it is clear by now that within the CL model, a dissipative environment can reduce the coherence only to a certain point. So, a remaining finite supercurrent is to be expected, and that is indeed what we and Grimm *et al.* [29] observe. Beyond our experiment, this behavior is expected for the entire parameter space: The junction is superconducting everywhere. This resolves the conflicts evoked in the Introduction.

Note that our conclusion that mobility calculations do not correctly describe transport in the CL model (and therefore cannot be used to predict a superconducting-insulating transition) is independent of whether one considers a compact or extended phase description; it applies also to old works which explicitly considered an extended phase for evaluating the mobility. The compact phase symmetry put forward by our analysis is still very important because it enables us to reach a simple consistent picture in all known limits, and, through the self-duality of the model, it clarifies how decompactification occurs.

APPENDIX G: THE PREDICTED PHASE TRANSITION IN THE $P(E)$ THEORY

In Ref. [4], Aslangul *et al.* use a tight-binding model to describe junctions coupled to a linear environment in the so-called scaling limit, and they confirm Schmid's prediction of a phase transition. Here we go over their derivation using the notations more commonly used at present for Josephson circuits.

First we express the Hamiltonian $\tilde{H}$ considered in Ref. [4] as

$$\tilde{H} = \frac{E_J}{2}\left(\sum_{N\in\mathbb{Z}}|N\rangle\langle N+1|e^{i\tilde{\varphi}+2ieVt/\hbar} + \text{H.c.}\right) + H_{\text{bath}},$$

where N is the number of charges passed through the junction, and $\tilde{\varphi}$ is the fluctuating phase across the (disconnected) environment (in the notations of Ref. [4], $B_+ = e^{i\tilde{\varphi}}$, $\hbar\Delta = E_J$). For more generality, we consider the case where a voltage source is present (the results of Ref. [4] are recovered taking $V = 0$). This Hamiltonian is also considered in Ref. [53]. Note that when using this tight-binding description of discrete charge states, it implies the junction phase is considered compact.

The current operator through the junction is

$$\hat{I} = i\frac{2e}{\hbar}\frac{E_J}{2}\left(\sum_{N\in\mathbb{Z}}|N\rangle\langle N+1|e^{i\tilde{\varphi}+2ieVt/\hbar} - \text{H.c.}\right).$$

We now evaluate the current correlator

$$S_{II}(t) = \langle\hat{I}(t)\hat{I}(0)\rangle,$$

assuming that the backaction of the junction on the environment is weak enough to not modify the equilibrium properties of the bath. At first view, this assumption can be justified if the junction impedance at its plasma oscillation is much larger than the environment resistance (i.e., $\sqrt{E_C/E_J} \gg R/R_Q$), in which case the environment imposes its phase fluctuations onto the junction. This condition is indeed fulfilled in the scaling limit considered in Ref. [4]. Within these hypotheses, the correlator evaluates to

$$S_{II}(t) = \left(\frac{2e}{\hbar}\frac{E_J}{2}\right)^2 \left[\left(\sum_{N\in\mathbb{Z}} \langle N|\rho|N\rangle \right) (\langle e^{i\tilde{\varphi}(t)} e^{-i\tilde{\varphi}(0)}\rangle e^{2ieVt/\hbar} + \langle e^{-i\tilde{\varphi}(t)} e^{i\tilde{\varphi}(0)}\rangle e^{-2ieVt/\hbar}) \right.$$
$$\left. - \left(\sum_{N\in\mathbb{Z}} \langle N|\rho|N+2\rangle \langle e^{i\tilde{\varphi}(t)} e^{i\tilde{\varphi}(0)}\rangle e^{2ieVt/\hbar} + \langle N|\rho|N-2\rangle \langle e^{-i\tilde{\varphi}(t)} e^{-i\tilde{\varphi}(0)}\rangle e^{-2ieVt/\hbar} \right) \right], \tag{G1}$$

where ρ is the reduced density matrix of the junction. Considering that the linear environment remains in equilibrium, its fluctuations are Gaussian, and one has

$$\langle e^{\pm i\tilde{\varphi}(t)} e^{\mp i\tilde{\varphi}(0)}\rangle = e^{J(t)}$$

and

$$\langle e^{\pm i\tilde{\varphi}(t)} e^{\pm i\tilde{\varphi}(0)}\rangle = e^{-J(t)+2J(\infty)}$$

with

$$J(t) = \langle [\tilde{\varphi}(t) - \tilde{\varphi}(0)]\tilde{\varphi}(0)\rangle = \int_{-\infty}^{+\infty} \frac{d\omega}{\omega} \frac{\mathrm{Re}Z(\omega)}{2R_Q} \frac{e^{-i\omega t} - 1}{1 - e^{-\beta\hbar\omega}},$$

with Z being the total environment admittance as seen from the Josephson element, including the junction capacitance [i.e., $Z(\omega) = (R^{-1} + iC\omega)^{-1}$]. For an Ohmic environment $\mathrm{Re}J(\infty) = -\infty$, so that the terms in the second line of Eq. (G1) vanish, and using $\mathrm{tr}\,\rho = 1$, the correlator finally reduces to

$$S_{II}(t) = \left(\frac{2e}{\hbar}\frac{E_J}{2}\right)^2 e^{J(t)} \cos\frac{2eVt}{\hbar},$$

or, in the frequency domain,

$$S_{II}(\omega) = \left(\frac{2e}{\hbar}\frac{E_J}{2}\right)^2 [P(\hbar\omega + 2eV) + P(\hbar\omega - 2eV)],$$

where

$$P(E) = \frac{1}{2\pi\hbar} \int_{-\infty}^{\infty} \exp[J(t) + iEt/\hbar] dt$$

is the usual $P(E)$ function considered in dynamical Coulomb blockade. For the RC environment considered here, at zero temperature one has [53]

$$P(E) \propto E^{2R/R_Q - 1}. \tag{G2}$$

1. Charge transport

The *standard* Green-Kubo relations link the admittance Y_{GK} to S_{II},

$$\mathrm{Re}Y_{GK}(\omega, V) = \frac{1}{2\omega}[S_{II}(\omega) - S_{II}(-\omega)]. \tag{G3}$$

Note that, even after applying Kramers-Kronig relations to get the imaginary part, this admittance Y_{GK} corresponds only to the first term in Eq. (F1) and therefore lacks the inductive response of the junction, which we know is important (see Appendix F). If we nevertheless proceed, from Eq. (G3) one predicts a differential conductance

$$\frac{dI}{dV}(V) = \mathrm{Re}Y_{GK}(\omega \to 0, V) = \frac{2e^2}{\hbar} E_J^2 [P'(2eV) + P'(-2eV)],$$

and the $I - V$ characteristics are obtained by straightforward integration

$$I(V) = \frac{e}{\hbar} E_J^2 [P(2eV) + P(-2eV)]. \tag{G4}$$

The above results are already found in Ref. [53]. They describe *inelastic* tunneling processes of Cooper pairs with real transitions in the environment modes. The $I - V$ characteristic (G4) is known to quantitatively describe experiments [50,54] at finite voltages when the Josephson coupling is small enough that the environment modes remain in equilibrium.

From the above results, one predicts the junction zero-bias conductance

$$G = Y_{\mathrm{GK}}(\omega \to 0, V = 0) = \frac{2e}{\hbar} E_J^2 P'(0), \tag{G5}$$

which corresponds to the dc charge mobility calculated by Aslangul *et al.* [4]. Thus, for the RC environment considered here, at $T = 0$, using Eqs. (G2) and (G5), one recovers the "superconducting-to-insulating" phase transition at $R = R_Q$, as found by Aslangul *et al.* [4] (Schmid [1] and Bulgadaev [2] obtained the same results for the mobility by mapping the problem onto a log-gas). However, as noted above, the charge-transfer processes described here are inelastic, and it is therefore not correct to describe this type of process as *superconducting* transport for $R < R_Q$.

2. Conclusions on the phase transition

(i) As shown in Appendix F, Y_{GK} is not the full linear admittance; it entirely misses the inductive response

of the junction and cannot properly describe charge transport (and notably the supercurrent branch in the I-V characteristics) because of that. This perturbative tight-binding approach does predict a transition in the charge correlator (a partial charge localization), but it is incorrect to infer from this result that a superconducting-insulating transition exists.

(ii) The predicted transition in the junction charge correlator arises entirely from the $P(E)$ function, i.e., from the equilibrium fluctuations across the RC environmental impedance not connected to anything. It has nothing to do with the junction. This is already noted in Ref. [3].

(iii) As we mention in the main text, for $R < R_Q$, the charge is predicted to be fully delocalized, and correspondingly, the junction phase is fluctuationless (and its dynamics is that of a classical quantity).

The last two points seem odd and most likely too sketchy. Just as it is now understood that the coherence factors do not actually vanish in this system, it is quite clear that taking into account the backaction of the junction on the environment (causing their entanglement) would suppress the above sharp transition in the charge correlator and turn it into a smooth crossover with finite but small phase (resp. charge) fluctuations in the (resp. dual of the) delocalized charge state. Actually, we know this is the expected behavior when $E_J \gg E_C$ and $R \gg R_Q$ [upper left corner of the diagram in Fig. 4(b)]: At low temperatures, such a junction behaves essentially as a linear inductor, and it is well known that parallel RLC circuits have finite charge and phase fluctuations for all parameters. Then, using the duality argument, the presence of finite charge and phase fluctuations should also be true for $E_J \ll E_C$ and $R < R_Q$. Finally, by continuity, this should be also true in the entire diagram.

The continuous crossover that emerges from our analysis contrasts with the results of the Monte Carlo simulations performed assuming an extended phase in Ref. [11], where an abrupt transition in the phase correlator at $T = 0$ and $R = R_Q$ is found. This discrepancy illustrates that considering an extended phase can lead to results inconsistent with our analysis (see Appendix H).

In conclusion, we expect no DQPT transition in the CL model: neither a superconducting-insulating transition nor a transition in the charge or phase correlator.

APPENDIX H: COMPACT VS EXTENDED JUNCTION PHASE

The analysis of the CL model conducted in the main text is based on symmetry considerations and leads to a "phase diagram" [Fig. 4(b)], which is theoretically consistent (including at its boundaries) and consistent with experiments. In this phase diagram, the junction phase is compact below the antidiagonal and it progressively decompactifies above the antidiagonal in a smooth crossover.

We stress that when this decompactification does not occur, compact phase solutions are dictated by the symmetry of (the effective Josephson Hamiltonian in) the CL model; this symmetry is *not* for the physicist to *choose*. As a corrollary, *choosing* to use an extended phase in many earlier works on the CL model cannot be rigorously justified theoretically because there are no known mechanisms within that model that would break the system's fundamental symmetry in this way. The only established symmetry breaking for the phase is the partial decompactification we describe in the main text (but it cannot be found starting from an extended phase).

Since it cannot be justified within the model, making use of an extended phase implicitly and forcefully adds poorly controlled hypotheses or ingredients to the model, with essentially unknown consequences. (In practice, it adds an additional variable indexing the wells of the cosine and enabling us to distinguish all of them in all circumstances, which is not possible in the original model.) For sure, this can be done theoretically—it works. But does such a treatment still yield fully relevant predictions for the real-world system that the model was originally meant to describe? Clearly not. It is certain that predictions will differ in circumstances where interferences between the wells matter, and this difference is unavoidable in a system with superconducting coherences such as the one we consider. In other words, in the parameter space where we now know the phase discrete translational symmetry is not spontaneously broken, there exists mathematically correct extended phase solutions for H that cannot be unitarily transformed to a suitable (i.e., compact) solution for H'. Such solutions do not respect the intrinsic system symmetry, but it is nearly impossible to figure this inconsistency by considering only the extended phase hypothesis.

This subtle point on the junction phase symmetry and its spontaneous breakage has never been properly understood so far. We think that bringing this point up and clarifying it is a significant achievement of the present work.

1. Retrospective on the compact vs extended phase debate

Prior to this work, it was intuited that phase decompactification must take place somehow (at least for some parameters), but it was not understood how it was occurring, and this resulted in a lot of ambiguities and confusion. Here, we try to put into perspective why the situation was so confusing.

An extended phase description contains the compact phase solutions as solutions of higher symmetry (periodic solutions in phase representation), so that, in principle, it should be the only description ever needed. Indeed, when starting from a Hamiltonian such as H in the main text, for which an extended phase is the "natural" point of view, one can obtain the compact phase solutions by considering highly nontrivial initial and boundary conditions [33,34].

However, in the existing literature based on using H, this was not done, and, as a consequence, compact phase solutions (which are of utmost importance as our work shows) were not found or not recognized as such.

Until now, this seemed not too problematic, and it was even rationalized that compact phase states were irrelevant in systems that are most conveniently described using H (essentially, systems where a dc current can flow). The rationale was that in these systems, a "full decompactification" process (i.e., yielding only nonperiodic extended phase states solutions of H) would always occur for all parameters and all temperatures. At first, this was just argued for qualitatively [55]. Soon after, Zwerger *et al.* [56] showed that such a full decompactification process should indeed always occur for Ohmic environments, but their derivation can no longer be considered conclusive as it did not take into account the entanglement of the junction with the environment, which we now know is key. Later, Apenko proposed another justification [35], but in his derivation, the identification of different phases in the circuit was not rigorous (similar to what we discuss about the Hamiltonian of the fluxonium circuit in Appendix H 4).

Hence, schematically, for a very long time, it was broadly considered that the symmetry of the phase and the Hamiltonian used were somehow tied: ($H \Leftrightarrow$ extended phase assumed to be a decompactified phase) XOR ($H' \Leftrightarrow$ compact phase).

To support this dichotomic view, several arguments or criteria were used to favor using a compact or an extended phase description, depending on the problem considered. For instance, it was frequently argued that a compact junction phase is suitable only in circuits having an "island" connected to the junction, as it would be a manifestation of the charge quantization in the island or of the tunneling of individual Cooper pairs through the junction. In other words, a compact phase should not be appropriate in a circuit where the charge can flow continuously (and thus, considering H' to describe the Ohmic shunted junction was not considered appropriate). Although the general discussion of the main text already shows such arguments are not relevant, in the following subsections of this Appendix we nevertheless specifically discuss why these arguments do not hold.

2. Phase compactness is not due to the tunneling of individual Cooper pairs through the junction

If instead of a Josephson junction one considers a superconducting ballistic (or nearly ballistic) weak link, then the current-phase relation is still periodic with the phase, so that one can again use a discrete charge basis to describe the state of the weak link. In that case, this apparent "charge discretization" obviously cannot be directly linked to an underlying charge quantization due to the tunneling of charge carriers.

3. Is charge quantization due to the presence of islands?

As we discuss in the main text, using the discrete charge basis of the CPB (equivalent to considering a compact phase) arises from the symmetries of the system. It does not require the presence of "an island" in which the charge is "naturally quantized." The simplest argument against this is that in a CPB the mere presence of the Josephson junction destroys this charge quantization (the ground state of the CPB consists of a coherent superposition of charge states, with finite zero-point fluctuations). This "charge quantization" is not observable, it is only a mathematical illusion, actually.

Our statement is further supported by the fact that the form of the Caldeira-Leggett Hamiltonian is independent of whether the circuit has an island or not. This can be shown using the explicit decomposition of the total circuit impedance into oscillators according to the rules in Ref. [22].

Finally, one can show that the Hamiltonian of a circuit with an island has a smooth limit to the islandless case by taking the limit where the capacitance defining the island becomes infinite. Correspondingly, all the finite-frequency linear response functions of the system have smooth limits too. However, as the system is nonlinear, the linearity range may vanish at low frequency (see, e.g., Appendix A), depending on the type of response probed. This agrees with the obvious expectation that at strictly zero frequency no dc current can flow when there is an island, while it can if there is no island. As we explain in the main text, the absence of dc current in a circuit with an island results from having a single ground state, while there is a continuum of them in the islandless case permitting a dc current flow.

As a conclusion, whether one considers a CPB with an island or a galvanically shunted junction does not radically change the way the system is modeled.

4. The junction's phase in the fluxonium

It is frequently argued that one *must* use an extended phase description for describing the fluxonium circuit [57] where a Josephson junction is connected in parallel with a inductor (instead of a resistor in this paper).

Indeed, for the fluxonium, the Hamiltonian proposed in Refs. [25,57] is

$$H_{f1} = \frac{q^2}{2C} - E_J \cos\varphi + \frac{(\Phi_{\text{ext}} - \frac{\hbar}{2e}\varphi)^2}{2L}, \qquad \text{(H1)}$$

where $(\hbar/2e)\varphi$ and q denote the branch flux and charge of the junction, and Φ_{ext} is the magnetic flux enclosed by the loop formed between the junction and the inductor considered as an external control parameter, i.e., a fixed real number. In this model, obviously not invariant upon $\varphi \to \varphi + 2\pi$, the junction's phase clearly appears as extended. However, the eigenstates of the system have current fluctuations that, in addition to vacuum flux

fluctuations, cause fluctuations of the flux in the loop, which contradicts the assumption that Φ_{ext} is a fixed parameter. Thus, the model is not fully consistent.

Another fluxonium Hamiltonian is derived in Ref. [45]. It reads

$$H_{f2} = \frac{(Q+q)^2}{2C} - E_J \cos\varphi + \frac{\Phi^2}{2L}. \tag{H2}$$

In this writing, Φ and Q denote the branch flux and charge of the inductor, while $(\hbar/2e)\varphi$ and q still denote the branch flux and charge of the junction. This Hamiltonian thus has 2 quantum degrees of freedom (each with fluctuations), and the flux in the loop is given by Kirchhoff's law

$$\frac{\hbar}{2e}\varphi - \Phi = \Phi_{\text{loop}}$$

so that Φ_{loop} fluctuates too (as expected) and has an expectation value related to the externally applied flux Φ_{ext}. It is only by suppressing one of the quantum degrees of freedom, turning it into a classical one, that Eq. (H2) becomes Eq. (H1) (and, strictly, φ can no longer be considered as a degree of freedom describing the sole junction). The junction's phase appearing as extended in Eq. (H1) thus results from an approximation (perhaps a very good one); it is not an obligation.

The inconsistency pointed out above is a general problem of the circuit quantization scheme proposed in Ref. [22], where loop fluxes are always assumed constant. It can be easily fixed though. Other quantization schemes have also been proposed [45,58,59] which do not necessarily force this approximation.

a. The fluxonium is not in the phase diagram

In the fluxonium circuit, the impedance seen by the junction has $\mathrm{Re}Z(\omega = 0) = 0$, which would naively locate it on the right axis of the SB phase diagram. However, in that limit, the system considered in the main text is ill-defined as neither the loop inductance L (which defines a new energy scale $E_L = \hbar^2/8e^2L$ in the problem) nor the external flux Φ_{ext} threading the loop are specified. Thus, the phase diagram would need to be refined with extra parameters close to the right axis.

Nevertheless, depending on its parameters, we expect the fluxonium's junction phase will evolve between fully decompactified (in a single well of the cosine) when $E_L \gg E_J$ and $\Phi_{\text{ext}} \bmod \Phi_0 \neq \frac{1}{2}$, partially decompactified (in several wells) when $E_L \sim E_J$, and essentially compact (populating many wells nearly equally) [25] when $E_L \to 0$.

5. Phase in current-biased junctions

When considering the case of a current-biased junction, where the current source "tilts the washboard potential," the different wells of the cosine appear as nonequivalent. Here again, the obligation to use an extended phase is only apparent.

First, the current source can be modeled by considering a very large inductor loaded with an initial flux. So we are back to considering the fluxonium case for which we argue above that there is no obligation to use an extended phase.

One can arrive at a similar conclusion by performing a time-dependent unitary transformation [34] that removes the tilt of the washboard, restoring the periodicity of the cosine potential. In this case, however, the states of the system will be time dependent.

In such a current-biased junction, the final degree of phase decompactification will depend on the dissipation in the system and on the ratio E_J/E_C (as in the unbiased case) but certainly also on the current bias I_b which sets an extra energy scale $I_b\Phi_0$ in the system, with an associated dynamics.

APPENDIX I: VALIDITY OF THE EFFECTIVE JOSEPHSON HAMILTONIAN AND CONSISTENCY OF THE CALDEIRA-LEGGETT MODEL

In the CL model, the junction is modeled using the effective Josephson Hamiltonian (i.e., the celebrated washboard potential for the junction phase) which describes only Cooper pair tunneling, and one couples this effective Hamiltonian to the linear environment.

This effective Josephson Hamiltonian emerges from the tunneling of quasiparticles at second order in perturbation theory in the absence of an environment [60,61], and it is commonly admitted it describes well a junction at energies much lower than the superconducting gap Δ and in the absence of quasiparticles (which is expected at $k_BT \ll 2\Delta$). Even when these conditions are fulfilled, one may wonder whether considering the effect of the environment on this effective Hamiltonian—as done in the CL model—is fully consistent.

A more rigorous and consistent way of considering the effect of the environment on the junction consists of going back to the tunneling of quasiparticles [23,62,63]. Doing so, one however finds that at second order in tunneling (corresponding to the effective Josephson Hamiltonian used in H or H'), the junction sees the bare zero-point fluctuations of the RC circuit. However, at that lowest order in perturbation, phase fluctuations are divergent for any Ohmic environment, and this divergence predicts a complete suppression of the supercurrent at all temperatures [23], even for $R < R_Q$, in the phase where a classical compact phase is predicted. This shows that the CL description of the system (using H or H') is inconsistent when considering an Ohmic environment. These inconsistencies resolve at higher orders in the tunneling Hamiltonian (or using a self-consistent approximation [23]), when the inductive backaction of the junction on the environment is taken into account: The junction and

environment become entangled, voltage and phase fluctuations are reduced, and they acquire an effective super-Ohmic spectral density for which no DQPT is expected, the junction preserving a finite supercurrent at $T = 0$ for all environmental impedances.

Our present work shows that even within the CL model (although it is not fully consistent), the predicted phase transition similarly disappears when considering the back-action of the junction on the environment.

APPENDIX J: RELATIONSHIP WITH PHASE TRANSITIONS IN OTHER SYSTEMS

The phase transition predicted by SB is closely related to a number of other phase transitions predicted in different systems (see Ref. [64]).

In particular, it is related to the impurity-induced transition in a 1D conducting channel of interacting spinless fermions (i.e., a Tomonaga-Luttinger liquid, TLL) predicted by Kane and Fisher [65] (KF), according to which, at $T = 0$, for any nonzero strength of the impurity potential, the channel conductance should vanish for repulsive interactions $g < 1$, while it should reach the perfect TLL conductance ge^2/h for attractive interaction $g > 1$. This behavior is akin to the SB prediction of a superconducting-to-insulating transition. Kane and Fisher showed that these systems are indeed described by the same effective action, and, according to the principle "the same equations have the same solutions" made famous by Feynman, no one questioned they would have the same phase transition physics until now, even when it became evident that the SB prediction conflicted with known results on Josephson junctions.

1. Confirmations of the KF phase transition

Repulsive Luttinger liquids with rational values of $g < 1$ have been extensively studied theoretically since they notably describe the low-energy physics of fractional quantum Hall edge states [66]. Thanks to the methods of integrable systems, exact results have been obtained for the specific values of $g = 1/2$ [67], $g = 1/3$ [68], and $g = 2/3$ [69]. All these results corroborate the perturbative RG analysis [65] predicting universal scaling laws for the dc conductance which drive the system to an insulating state as the temperature is lowered for all impurity back-scattering strength.

The KF phase transition physics was confirmed experimentally by taking advantage of a second mapping put forward by Safi and Saleur [70], who noticed the action of an impurity in a TLL is also equivalent to that of a single-channel quantum point contact in series with a resistor (QPC+R). In this mapping, the TLL interaction parameter g is controlled by the resistance $g = 1/(1 + R/4R_Q)$, and thus covers only the dynamics of repulsive TLLs. Since the physical implementation of QPC + R is much better controlled than that of fractional quantum Hall physics, this mapping enabled precise experimental investigations of the dc-conductance scaling laws. The experiments reported in Refs. [69,71,72] provide stringent tests of the predicted universal critical behavior at low energies (temperature and dc voltage), even though the system is not strictly in the scaling limit because of the finite charging energy.

2. Same equations but different solutions?

At first sight, it is quite shocking that we invalidate the SB phase transition after the KF one was accurately confirmed; it obviously violates "the same equations have the same solutions" principle.

The key of this paradox is that the principle makes implicit assumptions on the equations' *context*. Everyone knows a given real-coefficient polynomial $p(x)$ may have roots or not depending whether the context is $x \in \mathbb{C}$ or $x \in \mathbb{R}$. The SB and KF systems can be described by the same effective action, but when one goes back to the underlying microscopic descriptions, different phenomenologies arise, providing different contexts for searching the solutions to the equations.

For a Josephson junction, there is a gap in the excitation spectrum of its electrodes. Consequently, after a slow enough 2π phase slip, the junction is still in its ground state, and since the initial and final states of the junction are indiscernible, the junction's phase is compact. Superconductivity also yields a static phase coherence $\langle \cos\varphi \rangle \neq 0$, and an inductive response. Our work shows that this "superconducting context" is robust to connecting a resistor to the junction: The junction and the bath entangle, preserving finite coherences which forbids the phase transition. To put it more simply, in circuit engineering terms, the superconducting (ground-state) inductive response shunts the low-frequency phase fluctuations arising from the series resistance; this makes the global system super-Ohmic, allowing the junction to preserve its superconducting character.

No such mechanism can take place in KF or QPC + R systems. In the case of an open 1D electonic channel with a barrier connected at both ends to reservoirs, a 2π phase slip at the barrier (however slow) corresponds to a voltage pulse which, at $T = 0$, can excite electrons and/or holes at arbitrarily low energy and which will be dissipated in the reservoirs. Thus, a phase slip takes this system to an orthogonal (distinguishable) state, such that the phase needs to be regarded as an extended phase. The Fermionic baths hence provide a subtle mechanism that is not contained in the equations of the effective model (where the Fermions no longer appear) and that allows breaking the discrete translational invariance of the phase in a way that totally differs from the partial decompatification mechanism we identify in JJs. Furthermore, in this system there is no possibility of a supercurrent in the ground state, and thus no static coherence ($\langle \cos\varphi \rangle = 0$). Connecting a resistor to the channel brings the system in the critical regime of the DQPT, with the expected localization effect described by Schmid and Bulgadaev.

The above discussion in the main text suggests that the compactness of the phase—which we justify in the main text from the symmetry of the effective Josephson Hamiltonian—cannot be detached from the superconducting character of the Josephson junction and the existence of the inductive response.

3. Superconducting-to-insulating transition in 1D JJ arrays

Another superconducting-to-insulating phase transition is predicted in 1D JJ arrays [73]. This latter transition was related to the disordered-induced transition (i.e., Anderson localization) predicted in fermionic 1D systems [74]. Recently, Kuzmin *et al.* investigated experimentally 1D JJ arrays and observed they remained good superconducting transmission lines well beyond the threshold line impedance predicted for their transition to the insulating state [75]. Given the similarities between that system and the one we consider, we believe it could be worth revisiting the predicted transition in 1D JJ arrays taking into account what we understood on the sensitivity of the SB transition to the superconducting character of the underlying system.

[1] A. Schmid, *Diffusion and Localization in a Dissipative Quantum System*, Phys. Rev. Lett. **51**, 1506 (1983).

[2] S. A. Bulgadaev, *Phase Diagram of a Dissipative Quantum System*, JETP Lett. **39**, 315 (1984).

[3] F. Guinea, V. Hakim, and A. Muramatsu, *Diffusion and Localization of a Particle in a Periodic Potential Coupled to a Dissipative Environment*, Phys. Rev. Lett. **54**, 263 (1985).

[4] C. Aslangul, N. Pottier, and D. Saint-James, *Quantum Ohmic Dissipation: Particle on a One-Dimensional Periodic Lattice*, Phys. Lett. **111A**, 175 (1985).

[5] A. D. Zaikin and S. V. Panyukov, *Dynamics of a Quantum Dissipative System: Duality between Coordinate and Quasimomentum Spaces*, Phys. Lett. A **120**, 306 (1987).

[6] G. Schön and A. D. Zaikin, *Quantum Coherent Effects, Phase Transitions, and the Dissipative Dynamics of Ultra Small Tunnel Junctions*, Phys. Rep. **198**, 237 (1990).

[7] G.-L. Ingold and H. Grabert, *Effect of Zero Point Phase Fluctuations on Josephson Tunneling*, Phys. Rev. Lett. **83**, 3721 (1999).

[8] C. P. Herrero and A. D. Zaikin, *Superconductor-Insulator Quantum Phase Transition in a Single Josephson Junction*, Phys. Rev. B **65**, 104516 (2002).

[9] N. Kimura and T. Kato, *Temperature Dependence of Zero-Bias Resistances of a Single Resistance-Shunted Josephson Junction*, Phys. Rev. B **69**, 012504 (2004).

[10] H. Kohler, F. Guinea, and F. Sols, *Quantum Electrodynamic Fluctuations of the Macroscopic Josephson Phase*, Ann. Phys. (Amsterdam) **310**, 127 (2004).

[11] P. Werner and M. Troyer, *Efficient Simulation of Resistively Shunted Josephson Junctions*, Phys. Rev. Lett. **95**, 060201 (2005).

[12] S. L. Lukyanov and P. Werner, *Resistively Shunted Josephson Junctions: Quantum Field Theory Predictions versus Monte Carlo Results*, J. Stat. Mech. (2007) P06002.

[13] R. Yagi, S.-i. Kobayashi, and Y. Ootuka, *Phase Diagram for Superconductor-Insulator Transition in Single Small Josephson Junctions with Shunt Resistor*, J. Phys. Soc. Jpn. **66**, 3722 (1997).

[14] J. S. Penttilä, Ü. Parts, P. J. Hakonen, M. A. Paalanen, and E. B. Sonin, *Superconductor-Insulator Transition in a Single Josephson Junction*, Phys. Rev. Lett. **82**, 1004 (1999).

[15] L. S. Kuzmin, Yu. V. Nazarov, D. B. Haviland, P. Delsing, and T. Claeson, *Coulomb Blockade and Incoherent Tunneling of Cooper Pairs in Ultrasmall Junctions Affected by Strong Quantum Fluctuations*, Phys. Rev. Lett. **67**, 1161 (1991).

[16] V. Bouchiat, D. Vion, P. Joyez, D. Esteve, and M. H. Devoret, *Quantum Coherence with a Single Cooper Pair*, Phys. Scr. **T76**, 165 (1998).

[17] Y. Nakamura, Yu. A. Pashkin, and J. S. Tsai, *Coherent Control of Macroscopic Quantum States in a Single-Cooper-Pair Box*, Nature (London) **398**, 786 (1999).

[18] J. Koch, T. M. Yu, J. Gambetta, A. A. Houck, D. I. Schuster, J. Majer, A. Blais, M. H. Devoret, S. M. Girvin, and R. J. Schoelkopf, *Charge-Insensitive Qubit Design Derived from the Cooper Pair Box*, Phys. Rev. A **76**, 042319 (2007).

[19] J. A. Schreier, A. A. Houck, J. Koch, D. I. Schuster, B. R. Johnson, J. M. Chow, J. M. Gambetta, J. Majer, L. Frunzio, M. H. Devoret, S. M. Girvin, and R. J. Schoelkopf, *Suppressing Charge Noise Decoherence in Superconducting Charge Qubits*, Phys. Rev. B **77**, 180502 (2008).

[20] F. Nguyen, N. Boulant, G. Ithier, P. Bertet, H. Pothier, D. Vion, and D. Esteve, *Current to Frequency Conversion in a Josephson Circuit*, Phys. Rev. Lett. **99**, 187005 (2007).

[21] H. Grabert, U. Weiss, and P. Talkner, *Quantum Theory of the Damped Harmonic Oscillator*, Z. Phys. B **55**, 87 (1984).

[22] U. Vool and M. Devoret, *Introduction to Quantum Electromagnetic Circuits*, Int. J. Circuit Theory Appl. **45**, 897 (2017).

[23] P. Joyez, *Self-Consistent Dynamics of a Josephson Junction in the Presence of an Arbitrary Environment*, Phys. Rev. Lett. **110**, 217003 (2013).

[24] S. E. Nigg, H. Paik, B. Vlastakis, G. Kirchmair, S. Shankar, L. Frunzio, M. H. Devoret, R. J. Schoelkopf, and S. M. Girvin, *Black-Box Superconducting Circuit Quantization*, Phys. Rev. Lett. **108**, 240502 (2012).

[25] J. Koch, V. Manucharyan, M. H. Devoret, and L. I. Glazman, *Charging Effects in the Inductively Shunted Josephson Junction*, Phys. Rev. Lett. **103**, 217004 (2009).

[26] For devices made out of a BCS superconductor (with a gap Δ) and which conduct in the normal state, at frequencies $f \ll \Delta/h$ and temperatures $T \ll \Delta/k_B$, the linear response is dominated by an inductive behavior. For a Josephson junction, the effective inductance L_J^{eff} is at least $\hbar^2/4e^2E_J$ and can be enlarged due to environment-induced phase fluctuations [23]. An insulating behavior would correspond to a divergence of this inductance. See also Appendix F.

[27] B. Huard, H. Pothier, D. Esteve, and K. E. Nagaev, *Electron Heating in Metallic Resistors at Sub-Kelvin Temperature*, Phys. Rev. B **76**, 165426 (2007).

[28] M. Vojta, *Quantum Phase Transitions*, Rep. Prog. Phys. **66**, 2069 (2003).

[29] A. Grimm, F. Blanchet, R. Albert, J. Leppäkangas, S. Jebari, D. Hazra, F. Gustavo, J.-L. Thomassin, E. Dupont-Ferrier, F. Portier, and M. Hofheinz, *Bright On-Demand Source of Antibunched Microwave Photons Based on Inelastic Cooper Pair Tunneling*, Phys. Rev. X **9**, 021016 (2019).

[30] J. S. Penttilä, P. J. Hakonen, E. B. Sonin, and M. A. Paalanen, *Experiments on Dissipative Dynamics of Single Josephson Junctions*, J. Low Temp. Phys. **125**, 89 (2001).

[31] A. O. Caldeira and A. J. Leggett, *Quantum Tunnelling in a Dissipative System*, Ann. Phys. (N.Y.) **149**, 374 (1983).

[32] Note that in standard CPB circuits where the junction is isolated from the dissipative environment by a gate capacitor not allowing a dc charge flow, this translational invariance of the charge is suppressed, and the quasicharge is a relevant parameter.

[33] K. Mullen, D. Loss, and H. T. C. Stoof, *Resonant Phenomena in Compact and Extended Systems*, Phys. Rev. B **47**, 2689 (1993).

[34] D. Loss and K. Mullen, *Effect of Dissipation on Phase Periodicity and the Quantum Dynamics of Josephson Junctions*, Phys. Rev. A **43**, 2129 (1991).

[35] S. M. Apenko, *Environment-Induced Decompactification of Phase in Josephson Junctions*, Phys. Lett. A **142**, 277 (1989).

[36] M. P. A. Fisher and W. Zwerger, *Quantum Brownian Motion in a Periodic Potential*, Phys. Rev. B **32**, 6190 (1985).

[37] H. Spohn, *Ground State(s) of the Spin-Boson Hamiltonian*, Commun. Math. Phys. **123**, 277 (1989).

[38] K. Le Hur, *Entanglement Entropy, Decoherence, and Quantum Phase Transitions of a Dissipative Two-Level System*, Ann. Phys. (Amsterdam) **323**, 2208 (2008).

[39] S. Bera, S. Florens, H. U. Baranger, N. Roch, A. Nazir, and A. W. Chin, *Stabilizing Spin Coherence through Environmental Entanglement in Strongly Dissipative Quantum Systems*, Phys. Rev. B **89**, 121108 (2014).

[40] S. Bera, A. Nazir, A. W. Chin, H. U. Baranger, and S. Florens, *Generalized Multipolaron Expansion for the Spin-Boson Model: Environmental Entanglement and the Biased Two-State System*, Phys. Rev. B **90**, 075110 (2014).

[41] H. Grabert unpublished.

[42] U. Weiss, *Quantum Dissipative Systems*, 4th ed. (World Scientific, Singapore, 2012), https://doi.org/10.1142/8334.

[43] A. J. Kerman, *Flux-Charge Duality and Topological Quantum Phase Fluctuations in Quasi-One-Dimensional Superconductors*, New J. Phys. **15**, 105017 (2013).

[44] J. E. Mooij and Yu. V. Nazarov, *Superconducting Nanowires as Quantum Phase-Slip Junctions*, Nat. Phys. **2**, 169 (2006).

[45] J. Ulrich and F. Hassler, *Dual Approach to Circuit Quantization Using Loop Charges*, Phys. Rev. B **94**, 094505 (2016).

[46] P. Joyez, D. Vion, M. Götz, M. H. Devoret, and D. Esteve, *The Josephson Effect in Nanoscale Tunnel Junctions*, J. Supercond. **12**, 757 (1999).

[47] A. Steinbach, P. Joyez, A. Cottet, D. Esteve, M. H. Devoret, M. E. Huber, and J. M. Martinis, *Direct Measurement of the Josephson Supercurrent in an Ultrasmall Josephson Junction*, Phys. Rev. Lett. **87**, 137003 (2001).

[48] D. Vion, M. Götz, P. Joyez, D. Esteve, and M. H. Devoret, *Thermal Activation above a Dissipation Barrier: Switching of a Small Josephson Junction*, Phys. Rev. Lett. **77**, 3435 (1996).

[49] D. M. Pozar, *Microwave Engineering*, 4th ed. (John Wiley & Sons, Hoboken, NJ, 2011).

[50] C. Rolland, A. Peugeot, S. Dambach, M. Westig, B. Kubala, Y. Mukharsky, C. Altimiras, H. le Sueur, P. Joyez, D. Vion, P. Roche, D. Esteve, J. Ankerhold, and F. Portier, *Antibunched Photons Emitted by a dc-Biased Josephson Junction*, Phys. Rev. Lett. **122**, 186804 (2019).

[51] S. Léger, J. Puertas-Martínez, K. Bharadwaj, R. Dassonneville, J. Delaforce, F. Foroughi, V. Milchakov, L. Planat, O. Buisson, C. Naud, W. Hasch-Guichard, S. Florens, I. Snyman, and N. Roch, *Observation of Quantum Many-Body Effects due to Zero Point Fluctuations in Superconducting Circuits*, Nat. Commun. **10**, 5259 (2019).

[52] I. Safi and P. Joyez, *Time-Dependent Theory of Nonlinear Response and Current Fluctuations*, Phys. Rev. B **84**, 205129 (2011).

[53] G.-L. Ingold and Yu. V. Nazarov, in *Single Charge Tunneling*, edited by H. Grabert and M. H. Devoret, NATO ASI Series B Vol. 294 (Plenum Press, New York, 1992), pp. 21–107.

[54] M. Hofheinz, F. Portier, Q. Baudouin, P. Joyez, D. Vion, P. Bertet, P. Roche, and D. Esteve, *Bright Side of the Coulomb Blockade*, Phys. Rev. Lett. **106**, 217005 (2011).

[55] D. V. Averin, A. B. Zorin, and K. K. Likharev, *Bloch Oscillations in Small Josephson Junctions*, Sov. Phys. JETP **61**, 407 (1985).

[56] W. Zwerger, A. T. Dorsey, and M. P. A. Fisher, *Effects of the Phase Periodicity on the Quantum Dynamics of a Resistively Shunted Josephson Junction*, Phys. Rev. B **34**, 6518 (1986).

[57] V. E. Manucharyan, J. Koch, L. I. Glazman, and M. H. Devoret, *Fluxonium: Single Cooper-Pair Circuit Free of Charge Offsets*, Science **326**, 113 (2009).

[58] G. Burkard, R. H. Koch, and D. P. DiVincenzo, *Multilevel Quantum Description of Decoherence in Superconducting Qubits*, Phys. Rev. B **69**, 064503 (2004).

[59] G. Burkard, *Circuit Theory for Decoherence in Superconducting Charge Qubits*, Phys. Rev. B **71**, 144511 (2005).

[60] V. Ambegaokar and A. Baratof, *Tunneling between Superconductors*, Phys. Rev. Lett. **10**, 486 (1963).

[61] V. Ambegaokar, U. Eckern, and G. Schön, *Quantum Dynamics of Tunneling between Superconductors*, Phys. Rev. Lett. **48**, 1745 (1982).

[62] J. M. Martinis, M. Ansmann, and J. Aumentado, *Energy Decay in Superconducting Josephson-Junction Qubits from Nonequilibrium Quasiparticle Excitations*, Phys. Rev. Lett. **103**, 097002 (2009).

[63] M. H. Ansari, F. K. Wilhelm, U. Sinha, and A. Sinha, *The Effect of Environmental Coupling on Tunneling of Quasiparticles in Josephson Junctions*, Supercond. Sci. Technol. **26**, 125013 (2013).

[64] E. Dalla Torre and E. Sela, *Viewpoint: Circuit Simulates One-Dimensional Quantum System*, Physics **11**, 94 (2018).

[65] C. L. Kane and M. P. A. Fisher, *Transport in a One-Channel Luttinger Liquid*, Phys. Rev. Lett. **68**, 1220 (1992).

[66] X. G. Wen, *Electrodynamical Properties of Gapless Edge Excitations in the Fractional Quantum Hall States*, Phys. Rev. Lett. **64**, 2206 (1990).

[67] C. L. Kane and M. P. A. Fisher, *Transmission through Barriers and Resonant Tunneling in an Interacting One-Dimensional Electron Gas*, Phys. Rev. B **46**, 15233 (1992).

[68] P. Fendley, A. W. W. Ludwig, and H. Saleur, *Exact Conductance through Point Contacts in the $\nu = 1/3$ Fractional Quantum Hall Effect*, Phys. Rev. Lett. **74**, 3005 (1995).

[69] A. Anthore, Z. Iftikhar, E. Boulat, F. D. Parmentier, A. Cavanna, A. Ouerghi, U. Gennser, and F. Pierre, *Circuit Quantum Simulation of a Tomonaga-Luttinger Liquid with an Impurity*, Phys. Rev. X **8**, 031075 (2018).

[70] I. Safi and H. Saleur, *One-Channel Conductor in an Ohmic Environment: Mapping to a Tomonaga-Luttinger Liquid and Full Counting Statistics*, Phys. Rev. Lett. **93**, 126602 (2004).

[71] S. Jezouin, M. Albert, F. D. Parmentier, A. Anthore, U. Gennser, A. Cavanna, I. Safi, and F. Pierre, *Tomonaga-Luttinger Physics in Electronic Quantum Circuits*, Nat. Commun. **4**, 1802 (2013).

[72] F. D. Parmentier, A. Anthore, S. Jezouin, H. le Sueur, U. Gennser, A. Cavanna, D. Mailly, and F. Pierre, *Strong Back-Action of a Linear Circuit on a Single Electronic Quantum Channel*, Nat. Phys. **7**, 935 (2011).

[73] R. M. Bradley and S. Doniach, *Quantum Fluctuations in Chains of Josephson Junctions*, Phys. Rev. B **30**, 1138 (1984).

[74] T. Giamarchi and H. J. Schulz, *Anderson Localization and Interactions in One-Dimensional Metals*, Phys. Rev. B **37**, 325 (1988).

[75] R. Kuzmin, R. Mencia, N. Grabon, N. Mehta, Y.-H. Lin, and V. E. Manucharyan, *Quantum Electrodynamics of a Superconductor–Insulator Phase Transition*, Nat. Phys. **15**, 930 (2019).

Part III

The quantum phase slip box

In this second part, we explore the behaviour of nanowires made of highly disordered superconductor, supposedly implementing the dual of the Josephson junctions. Indeed, fluctuations of the superconducting order parameter Δ in those nanowires can induce quantum tunneling of the superconducting phase. This results in phase slips of $\pm 2\pi$, and it was predicted by Mooij et al. [12] that such nanowire would display the dual properties of a Josephson junction. More precisely, it was predicted [34] that a microwave resonator based on a highly inductive nanowire would realise the dual of the Cooper-pair box. Such device would then show a periodic modulation of its resonance frequency with the voltage applied on a local gate. Our goal here is to realise this device and measure its properties and, hopefully, this modulation.

To realise this goal, we first need to obtain a suitable disordered superconductor which presents, at the same time, a high kinetic inductance and low microwave losses. We explore two different materials, boron doped diamond and titanium nitride. Using titanium nitride, we proceed to fabricate superconducting resonators based on highly inductive nanowires, and measure their behaviour. But before those results, we first introduce highly disordered superconductors and their peculiarities, quantum phase slips being one of them.

Chapter 1
Introduction

1.1 High kinetic inductance superconductors

Passing current through a superconductor requests the superconducting phase to have a gradient, which results in an energy linked to an inductive response, i.e. the kinetic inductance (see section 2.2 in part I). The kinetic inductance L_K of a superconducting structure is linked to its normal state resistance R_N:

$$L_K = \hbar R_N / \pi \Delta \tag{1.1}$$

with Δ the modulus of the superconducting gap. This inductance adds up with the geometrical inductance of the structure. Large kinetic inductance materials are now used in a variety of devices. Their main application is for microwave kinetic inductance detectors, pioneered in 2003 for astronomical observations by J. Zmuidzinas [35]. They have also applications in quantum devices, such as in phase slip devices [36, 37]. More generally speaking, they can be used to miniaturise any inductances in a microwave circuit.

In large superconducting structures, the kinetic inductance is small due to their small normal state resistance R_N, and hence negligible compared to their geometrical inductance. However, if we consider superconducting thin films, the normal state resistance increases. One usually uses the sheet resistance $R_N^\square$ and the sheet inductance $L_K^\square$ to describe the properties of such thin film. They are defined by:

$$R_N^\square = \frac{w}{L} R_N = \frac{\rho}{t}$$

$$L_K^\square = \frac{w}{L} L_K$$

where R_N and L_K are the resistance and kinetic inductance of a rectangle of width w and length L patterned in a superconducting thin film of thickness t and resistivity ρ. The bulk parameters can be freely replaced by their sheet counterparts in equation (1.1):

$$L_K^\square = \hbar R_N^\square / \Delta \tag{1.2}$$

The sheet resistance $R_N^\square$ naturally increases when t is decreased for a constant material. However, due to the production processes of those thin films, there is a lower limit for the thickness of the films one can make before they become discontinuous.

To further increase $L_K^\square$ at a constant t, one usually switches to disordered superconductors such as alloys which have a higher ρ than usual pure superconductors like niobium. Other means to obtain high kinetic inductance are also under investigations, like using graphene sheets to realise small footprint room temperature inductors [38].

Using the relation (1.2), one expects to increase $L_K^\square$ of a disordered superconductor thin film linearly with $R_N^\square$. However, a large disorder may also affects Δ, and can even suppress it.

1.2 Disorder driven superconducting insulator transition

In highly disordered 2D superconductor thin films, fluctuations becomes significant and several effects affect superconductivity [39, 40]. A quantum phase transition is observed at a certain level of disorder at which superconducting thin films become insulating, i.e. the Superconducting-Insulator Transition (SIT). This $T = 0$ quantum phase transition has observable effects at finite temperature. For example, in figure 1.1a is shown the temperature dependance of a homogeneous lead thin film of different thickness, deposited and measured without breaking the vacuum at cryogenic temperature.

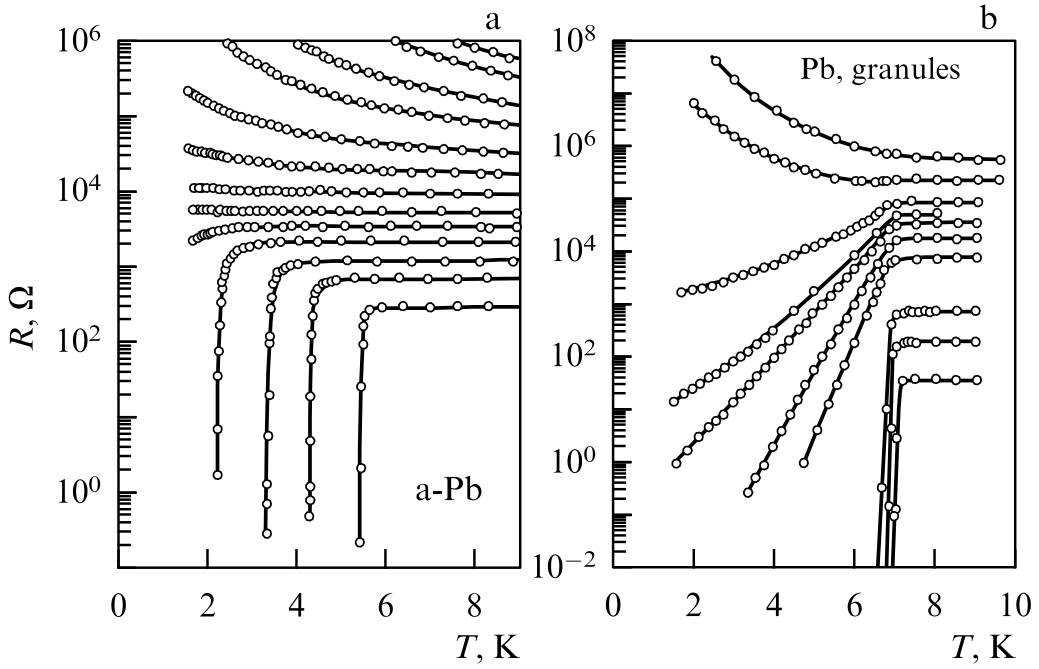

Figure 1.1. Temperature dependence of the sheet resistance of thin films during their cryogenic deposition, with increasing thickness (top to bottom). **a:** A thin Ge film of several atomic layers is deposited prior to Pb deposition, resulting in an homogeneous layer. **b:** Pb is deposited on a SiO bare substrate with no intermediate layer, resulting in the formation of a granular thin film. Reproduced from [41].

When the disorder is increased in those thin films (i.e. when the thickness is decreased, bottom to top curves), T_C first decreases. When the disorder reaches a point where the sheet resistance of the thin film $R_N^{\square}$ approaches $R_Q = h/4e^2 \approx 6.45\,k\Omega$, the superconducting state disappears and is replaced by an insulating state with diverging resistance as $T \to 0$. This insulating state has peculiar properties, with some experimental evidences of the persistence of local superconducting coherence in the insulating regime [42, 43]. This transition has different origins, depending on the specific material under consideration.

Two main scenarios are used to describe this SIT, either fermionic or bosonic [39, 40]. In the fermionic scenario, the disorder gradually reduces the effective electron-electron interaction until no Cooper pairs can be formed. Localisation effects then take the place of the superconducting interactions in the resulting fermionic system. In the bosonic scenario, similar to the superconducting BKT transition [44], phase fluctuations destroy the global superconducting coherence, but Cooper pairs can still exist in the material. This view explains the residual superconducting coherence observed in some of those systems.

The second scenario yields a different temperature dependence than the first one, and is favored in strongly granular films (see figure 1.1b). Indeed, in those thin films, the superconductivity can be described as an ensemble of superconducting grains in a normal metal lattice. When the disorder is increased, the global coherence between those grains is lost before the internal Cooper pairs are destroyed.

Below the SIT, the presence of strong fluctuations in those materials also induces large effects at $T \neq 0$. For example, in some TiN thin films, the sheet resistance can increase just before T_C by a large amount [45]. The so called Quantum Corrections to Conductance (QCC) are used to described those effects at $T \gtrsim T_C$. Those effects include weak localisation and superconductivity fluctuations, like the out of equilibrium flickering of Cooper pairs above T_C, resulting in the non monotonic features of some of those films.

1.3 Quantum phase slips

In low dimensionality conductors, transport properties strongly depend on geometry, and are affected by thermal and quantum fluctuations. In 1D superconducting nanowires, i.e. wires with transverse dimensions smaller than the superconducting coherence length ξ, the DC resistance does not vanish below T_C due to phase slips events [46]. During those events, fluctuations of the superconducting order parameter $\Delta(x) = |\Delta(x)|e^{i\Phi(x)}$ bring the modulus $|\Delta(x_{\text{qps}})|$ to zero at some point in the wire (see Figure 1.2), effectively suppressing the superconductivity locally. The constraints on the phase $\Phi(x_{\text{qps}})$ thus vanishes, and the phase can jump by $\pm 2\pi n$, where n is an integer. As soon as the modulus recover its non-zero value, the phase can no longer vary discontinuously. When a current is passed through the wire, phase jumps mostly occur with the same sign, resulting in a phase difference across the wire increasing over time, corresponding to a mean voltage difference across the wire. Assuming that those events are rare, we consider only individual phase slips events with $n = 1$. The length scale of those phase slips is of the order of the superconducting coherence length ξ.

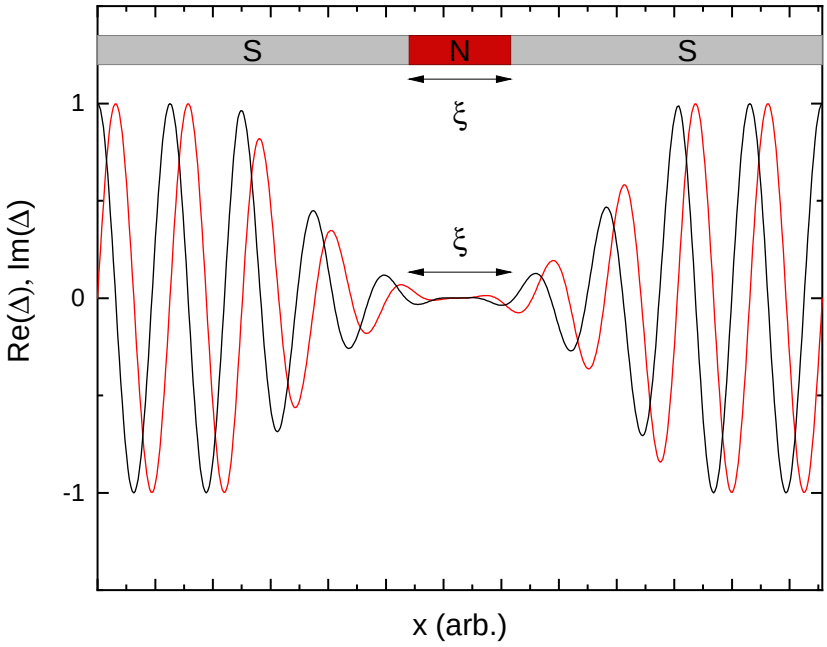

Figure 1.2. Variation of the superconducting order parameter $\Delta(x) = |\Delta(x)|e^{i\varphi(x)}$ around a phase slip event in a nanowire. The superconductivity is suppressed on a length scale of the order of ξ and $|\Delta(x)|$ vanishes at this point, allowing a shift of $\pm 2\pi$ of $\Phi(x)$.

Just below T_C, thermal fluctuations are driving the phase slip events and explain the phase slip rate related to the non-zero resistance [47, 48] that generally vanishes exponentially at lower temperature [48]. However, in some experiments with ultra-thin superconducting wires [49, 50, 51],

the resistance did not follow this thermal dependence, and the non-zero resistance did not vanish at lower temperature. In those experiments, quantum fluctuations of the order parameter were proposed as the origin of the phase slips, hence the name Quantum Phase Slips (QPS). During a QPS, the order parameter is virtually suppressed due to quantum tunneling of the order parameter through a barrier [46] and the phase winds up around the suppressed zone by $\pm 2\pi$. This quantum description for the phase slips enabled physicists to explain the persistance of a finite resistance observed in superconducting nanowires down to the lowest temperature.

Following the theoretical treatment [52] and the first experimental results [53] on QPS in nanowires, several propositions emerged concerning the use of QPS in coherent quantum devices. It was proposed by Mooij and Harmans [54] to use the QPS tunneling to coherently couple states in a superconducting loop and thus create a Quantum-bit (Qubit). Soon after, Mooij and Nazarov proposed that coherent QPS in a nanowire could realise a exact quantum dual to the Josephson Junction (JJ), the QPS junction [12].

1.3.1 The QPS junction

To illustrate the duality of the QPS junction with the JJ, we will follow the discussion presented in [12] and use the circuits presented in figure 1.3. The first one is a Cooper pair box [28] in which a JJ is voltage-biased through a capacitor C. In the second, a QPS junction is introduced in a closed superconducting loop with an inductor L.

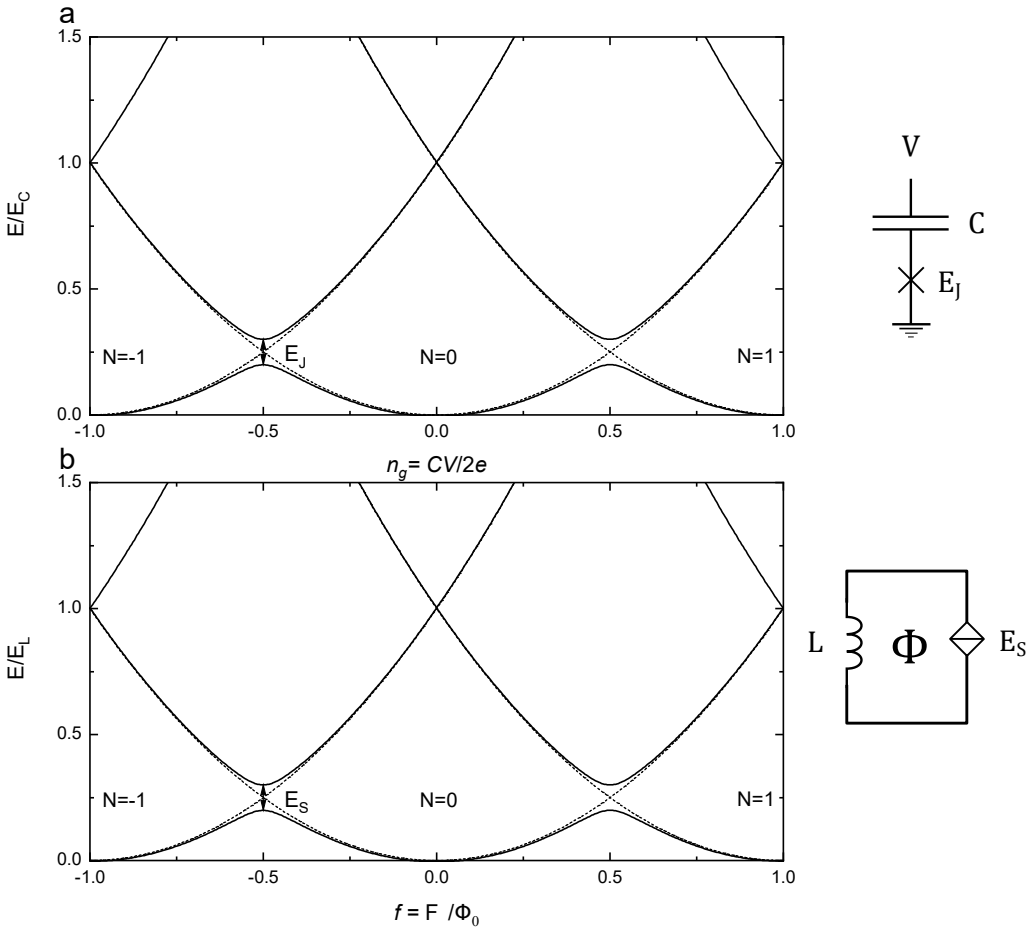

Figure 1.3. Circuit and energy levels of a Cooper pair box (**a**) and a QPS Qubit [12] (**b**), in the limits $E_J \ll E_C$ and $E_S \ll E_L$, respectively. The diamond shape with the energy E_S represents the QPS junction. The dashed lines represents the unmixed charging and inductive energy for each N. From

In the limit $E_J \ll E_C$, with $E_C = \frac{(2e)^2}{2C}$ and $n_g = \frac{CV}{2e}$, we can write the following Hamiltonian for the Cooper-pair box [55]:

$$H_{JJ} = E_C(N - n_g)^2 - \left(\frac{E_J}{2} \sum_n |N+1\rangle\langle N| + h.c. \right) \tag{1.3}$$

where $h.c.$ represents the hermitian conjugate. In the case of the QPS Qbit (figure 1.3b), this is now the inductive energy that depends parabolically on the applied flux $f = \Phi / \Phi_0$, with N now defining the number of fluxoid in the loop. The QPS junction mixes the states of neighbouring values of the fluxoid number N, lifting the degeneracy at half integer values of f. In the limit $E_S \ll E_L$, where E_S is the energy associated with the phase slip junction and $E_L = \frac{\Phi_0^2}{2L}$ is the inductive energy scale, Mooij and Nazarov [12] have proposed the following Hamiltonian for the QPS Qbit:

$$H_{\mathrm{QPS}} = E_L(N - f)^2 - \left(\frac{E_S}{2} \sum_n |N+1\rangle\langle N| + h.c. \right) \tag{1.4}$$

As is evident by the comparison of (1.3) and (1.4), both the Cooper-pair box and the QPS Qbit presented in figure 1.3b are equivalent, given we exchange E_C for E_L, E_J for E_S and n_g for f.

The duality of the JJ with the QPS junction can be derived from the canonically conjugated quantum variables of phase and charge. Indeed, the operator of charge $\hat{q}$ and phase $\hat{\Phi}$ obey the commutation relation $[\hat{q}, \hat{\Phi}] = -i\hbar$. We can write the Hamiltonian of any circuit containing a JJ with either a voltage or current bias as [56]:

$$\hat{H}_{JJ} = E_C \left(\frac{\hat{q}}{2e} \right)^2 - E_J \cos(\hat{\Phi}) + \hat{H}_{\mathrm{env}} + \hat{H}_{\mathrm{coupl}} \tag{1.5}$$

where $\hat{H}_{\mathrm{env}}$ describe the bosonic environment and $\hat{H}_{\mathrm{coupl}}$ represent the coupling terms, which depends on the coupling scheme used. Similarly, for the Hamiltonian of a QPS junction in a circuit we have [12]:

$$\hat{H}_{\mathrm{QPS}} = \frac{E_L}{(2\pi)^2} \hat{\Phi}^2 - E_S \cos\left(2\pi \frac{\hat{q}}{2e} \right) + \hat{H}_{\mathrm{env}} + \hat{H}_{\mathrm{coupl}} \tag{1.6}$$

Considering the canonical transformation, $[\hat{q}, \hat{\Phi}] \leftrightarrow \left[-\frac{\hat{\Phi}}{2\pi}, 2\pi\hat{q} \right]$, which conserve the commutation relations, we can transform the Hamiltonian of a JJ into the one of a QPS junction, and vice-versa. The transformation also comes with the exchange between the current and voltage bias scheme and changes in the characteristic energies: $E_C \leftrightarrow E_L$ and $E_J \leftrightarrow E_S$.

This duality relation allows one to map the known result of JJ circuits (see section 1 in part II) to the new dual circuits containing QPS junctions. Those circuits include the JJ circuit used as a voltage standard, i.e. the current biased Josephson junction. The dual of this standard, the voltage biased QPS junction, would then realise a current standard with possible metrological accuracy.

Some devices containing a QPS junction can, like the ones using JJ, be considered as two level systems and used to realise Qubits. The duality relation allows one to map results concerning JJ based Qubits on the dual QPS based Qubits.

1.3.2 Phase slip energy E_S

The characteristic energy E_S in (1.4) and (1.6) was obtained from the quantum phase slip rate γ_{qps} derived by Zaikin et al. [52] to explain the low temperature saturation of the resistance of

superconducting nanowires. The energy E_S is linked to the rate γ_{qps} by:

$$E_S = h\gamma_{\text{qps}}$$

The rate γ_{qps} was obtained using path integral formalism and the results are summed up here. The QPS rate in a superconducting nanowire can be expressed as:

$$\gamma_{\text{qps}} = b\frac{S_{\text{qps}}L}{\tau_0 x_0}\exp(-S_{\text{qps}})$$

where τ_0, x_0 and S_{qps} are the timescale, the spatial scale and the action associated with the QPS event, respectively, and L is the nanowire length. The coefficient b is of order one. To maximise γ_{qps}, one needs to obtain $S_{\text{qps}} \approx 1$. The QPS action is composed of two parts:

$$S_{\text{qps}} = S_{\text{core}} + S_{\text{out}}$$

where S_{core} is the action associated with the phase slip core, where the superconductivity is suppressed, and S_{out} is the action associated with the long range electromagnetic part outside the core. Using parameters relevant for superconducting nanowires, we usually are in the limit $S_{\text{out}} \ll S_{\text{core}}$, which allows us to neglect S_{out}. The core action S_{core} takes a different expression in the short or long wire limit, i.e. depending if one can neglect the capacitive effect of the nanowire or not. If $L \ll \xi\frac{e^2 N_0 s}{C}$, with s the nanowire section, C its linear capacitance and N_0 the density of states at the Fermi energy, one has [46]:

$$S_{\text{core}} = A\frac{R_Q}{R_N}\frac{L}{\xi} = A\frac{R_Q}{R_\xi}$$

with A a coefficient of order 1, $R_Q = h/4e^2$, R_N the nanowire normal state resistance, L its length and $R_\xi = \frac{R_N \xi}{L}$ the normal state resistance of a length ξ of the nanowire. In the opposite limit $L \gg \xi\frac{e^2 N_0 s}{C}$, we have to take the capacitive effects of the wire into account and the core action is more complex:

$$S_{\text{core}} = A'\frac{R_Q}{R_N}\left(\frac{L}{\xi}\right)^{3/2}\sqrt{\frac{C}{e^2 N_0 s}} = A'\frac{R_Q}{R_\xi}\left(\frac{L}{\xi}\right)^{1/2}\sqrt{\frac{C}{e^2 N_0 s}}$$

with A' a coefficient of order 1. Both of those S_{core} expressions illustrate the variation of γ_{qps} with the resistance of the nanowire. Indeed, in both limit $S_{\text{core}} \propto \frac{R_Q}{R_\xi}$ and to obtain $S_{\text{core}} \approx 1$, one needs to increase R_ξ close to R_Q. In the short wire limit, using $\tau_0 \approx h/\Delta_0$ and $x_0 \approx \xi$ we obtain:

$$E_S = h\gamma_{\text{qps}} \approx h\Delta_0\frac{R_Q}{R_\xi}\frac{L}{\xi}\exp\left(-A\frac{R_Q}{R_\xi}\right) \tag{1.7}$$

where Δ_0 is the superconducting energy gap of the material. Given the exponential dependence of E_S on A, precisely estimating E_S for a given device is difficult. However, we can consider equation (1.7) as an upper bound on E_S. To derive this formula, it is assumed that the nanowire presents a constant width and homogeneous parameters such as QPS events would occur all along its length. This idela regime is not achievable in experiments, where fluctuations of the width or the conductance of the nanowire have to be taken into account. Typically, if the nanowire presents width variations, one expects most of the QPS events to take place in the thinner parts due to the exponential dependence of γ_{qps}. This results in a different expression [57]:

$$E_S \approx 0.3h\Delta_0\sqrt{\frac{R_Q}{R_\xi}}\frac{L}{\xi}\exp\left(-0.36\frac{R_Q}{R_\xi}\right) \tag{1.8}$$

which holds for a long diffusive wire with weak inhomogeneities. This last expression results in lower values for E_S, and we will use it for our estimations in our devices.

1.3.3 QPS experiments

Several implementations of the circuit presented in figure 1.3b have already been realised [37, 58, 59], and we present some of their results here. In those experiments, an inductive loop containing a QPS junction is coupled to a readout CPW resonator (see figure 1.4). Coherent QPS occur in a 40nm wide constriction of the inductive loop. Using two-tone spectroscopy measurements of the readout resonator, the presence of QPS Qubits was revealed and their frequency measured (figure 1.4a).

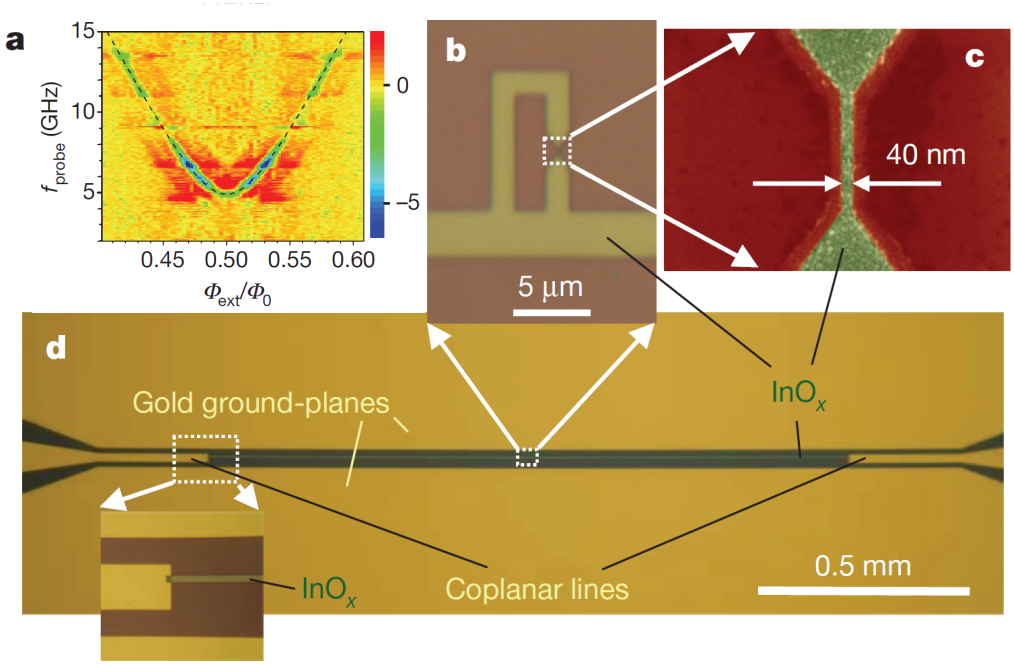

Figure 1.4. **a:** Two tones spectroscopy of the QPS Qubit made in Ref. [37] (**b**) realised with an inductive loop made of InO_X and (**c**) a nanowire implementing the QPS junction. **d:** The readout resonator made of InO_X connected to gold coplanar microwaves transmission lines. Reproduced from Ref. [37].

Several materials have been used to realise those experiments (InO_X, NbN, TiN), and the results were quite similar, demonstrating the presence of a two level system attributed to the QPS junction inside the inductive loop (see figure 1.4b). The transition linewidth of those Qubits varied from 20 MHz to 250 MHz, which is large compared to the typical values presently obtained in JJ Qubits [60].

Recent experiments by the same authors [36] have measured charge control of Cooper-pairs blockade in highly inductive nanowires compatible with the presence of QPS. The dual of the well known SQUID (see section 1.5.2 in part II), the Charge Quantum Interference Device, has been investigated and a behaviour similar to the SQUID was observed [61, 62]. Tentative implementations of a quantum standard for current using QPS junctions have also been reported [62]. However, most of those applications have encountered significant challenges, like spurious heating or quasiparticle poisoning, which reduced the overall coherence of the devices.

1.3.4 QPS box proposition

The proposition by Hriscu et al. [18, 34] is the basis for our circuit design: the so-called QPS box, which is a Cooper-Pair box where the JJ is replaced by a QPS junction made of a thin superconducting wire. In this circuit, represented in figure 1.5b, a QPS junction made of a thin superconducting wire is coupled through a capacitor to a voltage source. We neglect the self capacitance of the wire in our description. The voltage source provides DC and AC excitation to the circuit.

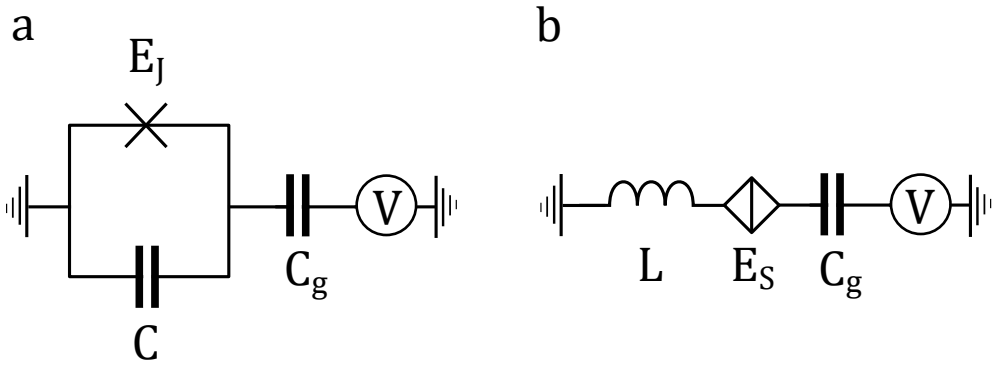

Figure 1.5. a: Cooper-pair box with a JJ associated with the energy E_J and a capacitance C, **b:** Quantum Phase Slip box (QPS box) with a QPS junction associated with the energy E_S and inductance L.

In absence of QPS (i.e. $E_S = 0$), the resulting circuit is a simple LC resonator with frequency $\omega_0 = \frac{1}{\sqrt{LC_g}}$ and characteristic impedance $Z_c = \sqrt{\frac{L}{C_g}}$, with energy levels $E_n = \hbar\omega_0\left(n + \frac{1}{2}\right)$. If $E_S \neq 0$ and $E_S \ll \hbar\omega_0$, the effect of the QPS junction on the resonator can be treated pertubatively. If $E_S \gg \hbar\omega_0$, the system develops strong coulomb blockade. In the perturbative case, the presence of a QPS junction in the device induces a shifts δE_n in the energy levels, and the first order correction was calculated in [18]:

$$\delta E_n = 2E_S \cos\left(\frac{\pi q}{e}\right) \exp(-\gamma^2/2)\, {}_1F_1[-n, 1, \gamma^2] \tag{1.9}$$

where $\gamma = \sqrt{\frac{\pi R_{2q}}{Z_c}}$, and ${}_1F_1$ the hypergeometric function. If $\gamma \in [0.3, 3]$ and $n \neq 0$, this shift can be approximated by:

$$\delta E_n \approx 2E_S \cos\left(\frac{\pi q}{e}\right) \frac{\cos\left(2\gamma\sqrt{n} - \frac{\pi}{4}\right)}{\sqrt{\pi\gamma}\, n^{1/4}} \tag{1.10}$$

It depends periodically on the induced charge q and is proportional to E_S. The QPS junction introduces strong non-linearities in the resonator, with δE_n oscillating with $\sqrt{n}$. The shift is also suppressed when $n \gg 1$ or $\gamma \gg 1$. This energy shift produces a frequency correction in the $n: 0 \to 1$ transition frequency which, in the limits $k_B T \ll \hbar\omega_0$ and $\gamma \approx 1$, writes [18]:

$$\delta\omega_{0\to1} = (\delta E_1 - \delta E_0)/\hbar = -\frac{2E_S\gamma^2}{\hbar} \cos(\pi q/e) \exp\left(-\frac{\gamma^2}{2} \operatorname{cotanh} \frac{\omega_0}{2\Gamma}\right) \tag{1.11}$$

Like δE_n, $\delta\omega_{0\to1}$ is modulated periodically with the induced charge q on the capacitor and proportional to E_S. However, in most experiments, $n \gg 1$, and as described by formula (1.10) the amplitude of the modulation in q is reduced as n increases. The resulting transition frequency correction $\delta\omega(n) = (\delta E_{n+1} - \delta E_n)/\hbar$ is presented in figure 1.6, normalised by $2E_S \cos\left(\frac{\pi q}{e}\right)/\hbar$.

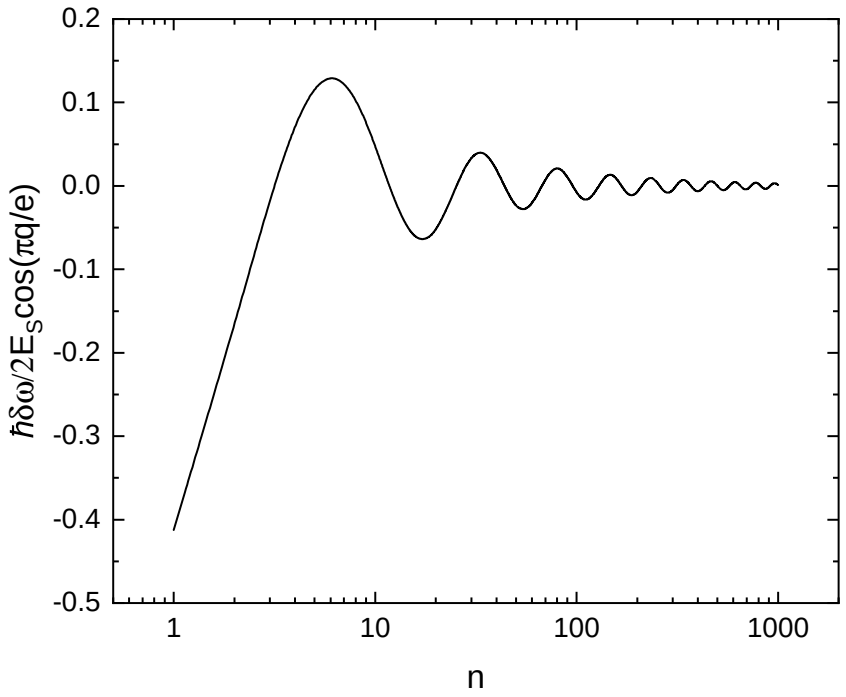

Figure 1.6. Transition frequency shift $\delta\omega(n)$ of the QPS box proposition obtained using (1.10), normalised by $2E_S\cos(\pi q/e)$, where $\gamma = 1$.

It is argued in Ref. [18] that to obtain a measurable value of $\delta\omega(n)$ with $n \gg 1$, one needs to have $E_S \geqslant \hbar\Gamma n^{\frac{3}{4}}$ where Γ is the resonator linewidth resulting from spurious losses.

Experiment design considerations

Our goal here is to implement the QPS box and observe those modulation of its frequency with q. To realise this goal, we need a material suitable with this device. As we have seen, the modulation $\delta\omega$ is linked to several characteristics of the device and the material used for its realisation. We need $\hbar\Gamma \ll E_S < \hbar\omega_0$ and $\gamma \leqslant 1$. Both those values are related to the superconducting material used to realise the inductive wire, and in particular, to its kinetic inductance L_K. Indeed, $\gamma \propto \frac{1}{\sqrt{L_K + L_G}}$, where L_G is the geometrical inductance of the wire, and $E_S \propto e^{-\frac{1}{L_K}}$. We thus need to have an inductive superconducting wire with high linear inductance. At the same time, we need the microwave losses in the devices to stay small, in order to obtain a Γ as low as possible. To achieve such wire, we will look into disordered superconductors thin films, which present high sheet inductance. However, as we saw before, those materials present a disorder driven SIT. While we will aim for a disordered superconducting thin film laying on the superconducting side of this transition, several other effects could pose some problems in their use: the self-Kerr non linearity and the coupling of the device to spurious defects.

1.4 Self-Kerr effect in superconducting resonators

An important nonlinear effect known in superconducting resonators is the self-Kerr effect, due to the supercurrent circulating in the resonator. When a supercurrent is passed through a superconductor, its superconducting gap Δ is reduced through depairing [63]. In 2D superconducting

resonators, this effect translates into a non linear behaviour caused by the increase of the sheet kinetic inductance of the material $L_K^{\square} = \hbar R_N^{\square} / \Delta$. The frequency f_m of the resonant mode m decreases with the average number of photons $\bar{n}$ stored in the resonator as:

$$f_m = f_m^0 - K_m \bar{n} \tag{1.12}$$

where K_m is the self-Kerr coefficient of the mode m. To estimate the value of K_m for a $\lambda/2$ CPW resonator, one needs to integrate the depairing effect caused by the oscillating supercurrents in the superconductor [64]. The resulting Kerr coefficient for mode m is:

$$K_m \approx \alpha m^2 \frac{9\pi^2}{8} \frac{Z_C}{R_Q} \left(\frac{\xi}{l} \right)^2 \hbar\omega_0 \tag{1.13}$$

where $\alpha = \frac{L_K}{L_K + L_{\text{geom}}}$ is the kinetic inductance ratio, Z_C is the characteristic impedance of the resonator, l the resonator length and ω_0 the first mode resonance frequency. In the case of a $\lambda/4$ CPW resonator of length l', one needs to replace l by $2\,l'$ in formula (1.13). Similar derivation can be done for a lumped resonator, which host only one resonating mode:

$$K \approx \alpha \frac{3\pi}{4} \frac{Z_C}{R_Q} \left(\frac{\xi}{l} \right)^2 \hbar\omega_0 \tag{1.14}$$

As we consider highly inductive wires for the inductance in our devices, their length l will be small compared to regular low inductance wires. We thus expect the Kerr coefficients to be large in our devices made of highly inductive superconductor.

1.5 Two Level Systems in solids

Amorphous solids host a variety of defects that can interact with microwave devices. The low temperatures properties of these defects follow an universal behaviour well described by the so-called Standard Tunneling Model (STM) [65, 66, 67], which describes the existence of Two Level Systems (TLSs). Those TLSs are noticeably known to occur in amorphous oxide layers and at interfaces between thin films [68]. Their presence in superconducting quantum devices, such as in the oxide layer of Josephson junctions, is a major source of noise and decoherence [69]. In this section, we will give a quick description of the STM and its implications for our high impedance devices, mainly following the ideas presented in [67].

Two level systems can fall in two different regimes, coherent or incoherent TLS, differentiated by their level of interaction with their environment. A coherent TLS has sufficiently low coupling to its environment to exhibit coherent dynamics between its two states. It can resonantly absorbs energy from any coupled system. On the other hand, an incoherent TLS, or fluctuator, is in strong interaction with its environment, leading to incoherent dynamics. It presents random flips between its two states, which prohibits any resonant interaction. A fluctuator can still couple to the host circuit and produces random fluctuation in the circuit, resulting in low frequency noise [70].

1.5.1 Standard Tunneling Model

While the exact nature of those TLSs is usually unknown, the STM makes the following assumptions for their description:

- They exist in two energetically similar configurations.
- They can be modeled as the two minima in a double-well potential separated by a barrier.
- Their dynamics is supposed to be governed by quantum tunneling through this barrier and transitions can be induced between the states by coupling to an appropriate field.
- Due to the random origin of the defects, a TLS ensemble is spanning large range of characteristic energy and switching rates.

1.5.1.1 Tunneling two level system

The double-well potential of a TLS is presented in figure 1.7, with an asymmetry energy δ and an energy associated with the tunneling through the barrier ε_0. The Hamiltonian of the system is the following:

$$H_{\mathrm{TLS}} = \frac{1}{2}\begin{pmatrix} \delta & \varepsilon_0 \\ \varepsilon_0 & -\delta \end{pmatrix} \tag{1.15}$$

The tunneling between the two wells hybridise the two lowest eigenstates of the left ($|L\rangle$) and right ($|R\rangle$) well to form the eigenstates:

$$|\psi_+\rangle = \sin\left(\frac{\theta}{2}\right)|L\rangle + \cos\left(\frac{\theta}{2}\right)|R\rangle \tag{1.16}$$

$$|\psi_-\rangle = \cos\left(\frac{\theta}{2}\right)|L\rangle - \sin\left(\frac{\theta}{2}\right)|R\rangle \tag{1.17}$$

with the mixing angle θ defined by $\tan\theta = \varepsilon_0/\delta$. The Hamiltonian can be expressed as:

$$H_{\mathrm{TLS}} = \frac{1}{2}\varepsilon_{\mathrm{tls}}\sigma_z \tag{1.18}$$

with $\varepsilon_{\mathrm{tls}} = \hbar\omega_{\mathrm{tls}} = E_+ - E_- = \sqrt{\varepsilon_0^2 + \delta^2}$ is the difference between those two eigenstates.

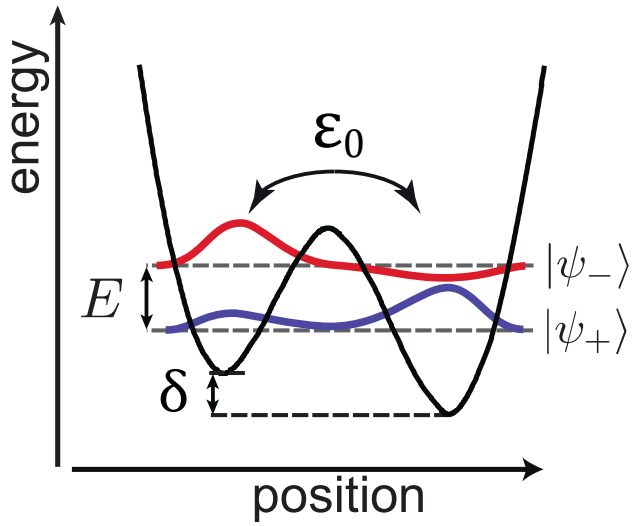

Figure 1.7. Two wells potential of a TLS with the tunneling energy ε_0 and the asymmetry δ. From [67].

If the TLS has a dipole moment $\vec{p}$, the asymmetry can be tuned by an external electric field $\vec{E}$: $\delta = \delta_0 + 2\vec{p}.\vec{E}$, where δ_0 is the asymmetry imposed to the TLS by its local environment. We can write the asymmetry as:

$$\delta = \vec{\gamma}.(\vec{E} - \vec{E_0})$$

with $\vec{\gamma} = 2\vec{p}$ and $\vec{E_0} = -\frac{\delta_0\,\vec{p}}{2\|\vec{p}\|^2}$. The resulting TLS energy then writes:

$$\varepsilon_{\mathrm{tls}} = \sqrt{\varepsilon_0^2 + (\vec{\gamma}.(\vec{E} - \vec{E_0}))^2} \tag{1.19}$$

which, for $\vec{E} = \vec{E_0}$, is minimal at $\varepsilon_{\mathrm{tls}} = \varepsilon_0$. Experimentally, the electric field is often applied via a local gate on the device, and we can consider an external field applied only in one direction, $\vec{E} = E\vec{x}$. We can thus reduce (1.19) to:

$$\varepsilon_{\mathrm{tls}} = \sqrt{\tilde{\varepsilon_0}^2 + \tilde{\gamma}^2(E - \tilde{E_0})^2} \tag{1.20}$$

where $\tilde{\gamma} = 2\vec{p}.\vec{x}$, $\widetilde{E}_0 = \vec{E_0}.\vec{x}$ and $\tilde{\varepsilon_0}^2$ now contains the terms of $\vec{\gamma}.\vec{E_0}$ orthogonal to $\vec{x}$.

1.5.1.2 TLS dissipation and TLS-TLS interactions

Nearly every TLS is strongly impacted by its close environment, which causes dissipation in its dynamics. Depending on the intensity of this dissipation, a TLS follows a coherent dynamics or is subject to incoherent jumps between state. This can be described using the TLS decoherence rate $\Gamma_{\text{tls}} = \frac{1}{2}\Gamma_1 + \Gamma_\varphi$, where Γ_1 is the inverse TLS lifetime and Γ_φ is the pure dephasing rate. This dephasing rate originates mainly from coupling to the phonon modes, which induce variations in the TLS wells groundstate energy and results in fluctuations of the asymmetry energy δ. Additionally, low energy TLS can be thermally excited, which results in a bath of low frequency incoherent fluctuators.

Interactions between TLSs were originally neglected in the STM, but further observations revealed the importance of TLS-TLS interactions [71, 72]. Indeed, if their separation is of the order of several nanometers, TLS can interact between each other via elastic or electric dipole coupling. Two coherent TLS can even display a strong interaction which dominates their dynamics [73]. Furthermore, the interaction of a coherent TLS with incoherent fluctuators, which is considered in an extension of the STM [74], gives rise to fluctuations in the coherent TLS energy. Each fluctuator coupled to a coherent TLS induces random telegraphic noise in its excitation frequency. A large number of fluctuators yields temporal drifts, or spectral diffusion [71] of this frequency.

1.5.1.3 TLS origin

While those TLSs have been studied intensively in amorphous materials [75, 76], their origin still remains unclear. We will quickly describe in this section several microscopic models for the TLS, but because of the complexity of the amorphous oxide layers in superconducting devices, one does not expect all the TLSs in a device to fall in a single category.

A first category involves the motion of atoms in the solid: collective motions of a small group of atoms between two energy minima, individual motion of an atom tunneling between two positions, dangling electronic bonds and other effects leading to change in the local lattice of the solid. A similar description can be done using the electrons instead of the atoms, which results in higher TLS energy, usually far above microwave frequencies. However, non trivial descriptions involving collective phononic states or metal-induced gap states find lower energy for those electronic TLS [77, 78].

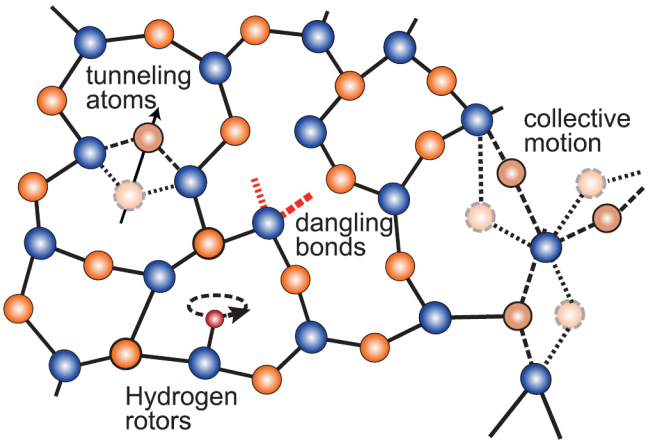

Figure 1.8. Types of possible movements in an atom lattice. Reproduced from [67].

Another category of TLSs involves the spin of electrons or atoms in the device. Those spins may fluctuate between two or more states and result in the formation of magnetic TLS. More exotic models have been proposed, and the list presented here is far from complete. However, this large amount of models illustrates the overwhelming presence of TLS in condensed matter and the many efforts deployed to understand their origin. Most of those models have similar implications, and we can safely use the STM framework without knowing the exact origin of the TLS involved.

1.5.2 Types of interaction with quantum devices

We now discuss the effects of TLSs on quantum devices. Indeed, beside interacting between each other in the host material, TLS can also couple to any electronic devices.

The most widespread model for TLS-device interaction is the electrostatic interaction. In this model, the TLS hosts an electric dipole of moment $\vec{p}$ which couples to the electric field $\vec{E}$ in the capacitive parts of the device. This model successfully describes most of the results obtained in superconducting devices.

A second model describes the TLS as magnetic impurity creating a stray magnetic field. This magnetic field depends on the TLS state and can couple to devices like SQUID loops, which produces flux noise. The magnetic and electrostatic interaction models are closely related, as illustrated in [79].

Finally, in a less common model that applies to Josephson junctions, a TLS in the junction dielectric barrier induces critical current fluctuations. The two states of the TLS are associated with two configurations of a close-by conduction channel, modifying its transparency. If the junction has a small number of conduction channels, this interaction can have a large impact on its critical current, and thus its Josephson energy E_J. This results in an additional fluctuating term in the Hamiltonian of the circuit.

1.5.3 Effects of TLS on superconducting resonators

The coupling of TLS to superconducting resonators is one of the main limits to the realisation of low loss devices. It has been shown that TLS mainly reside in oxide layers at the resonator interfaces [80]. The main coupling scheme used to describe those experiments is the interaction of the TLS dipoles with the electric field in the capacitance of the resonators. Using this approach, we describe some of the effects of a single TLS and an ensemble of TLS on a superconducting resonator.

1.5.3.1 Coupling of a single TLS to a resonator

In the case of the coupling of a coherent TLS to a superconducting resonator, and neglecting dissipation, we can describe the system using the Jaynes-Cumming Hamiltonian [81] under the rotating wave approximation [82]:

$$\hat{H} = \hbar\omega_0\left(\hat{a}^\dagger\hat{a} + \frac{1}{2}\right) + \hbar\omega_{\text{tls}}\,\hat{\sigma}_z + \hbar g\left(\hat{\sigma}_+\hat{\text{a}} + \hat{\sigma}_-\hat{\text{a}}^\dagger\right) \tag{1.21}$$

where $\hat{a}^\dagger$ and $\hat{a}$ are the photon creation and annihilation operators of the resonator, $\hat{\sigma}_+ = |\uparrow\rangle\langle\downarrow|$ and $\hat{\sigma}_- = |\downarrow\rangle\langle\uparrow|$ are the raising and lowering operators acting on the ground $|\downarrow\rangle$ and excited $|\uparrow\rangle$ states of the TLS and g the coupling strength between the TLS and the vacuum field of the resonator. The resulting hybridised eigenstates and eigenenergies of the Jaynes-Cummings ladder are [83]:

$$\begin{aligned}
|n,+\rangle &= \cos\left(\frac{\theta_n}{2}\right)|\uparrow,n\rangle + i\sin\left(\frac{\theta_n}{2}\right)|\downarrow,n+1\rangle \\
|n,-\rangle &= \sin\left(\frac{\theta_n}{2}\right)|\uparrow,n\rangle - i\cos\left(\frac{\theta_n}{2}\right)|\downarrow,n+1\rangle \\
|g\rangle &= |\downarrow,0\rangle \\
E_{n,\pm} &= (n+1/2)\,\hbar\omega_0 \pm \hbar\sqrt{\left(\frac{\Delta\omega}{2}\right)^2 + (n+1)g^2} \\
E_g &= -\hbar\omega_{\text{tls}}/2
\end{aligned} \tag{1.22}$$

where $\Delta\omega = \omega_{\text{tls}} - \omega_0$, $\tan(\theta_n) = \frac{g\sqrt{n+1}}{\Delta\omega}$, and $|n,\pm\rangle$ the states of the hybrid system with n photons stored. The resonance frequency of the resonator writes:

$$f_n^\pm = (E_{n+1}^\pm - E_n^\pm)/h = \frac{\omega_0}{2\pi} \pm \frac{1}{2\pi}\left(\sqrt{\left(\frac{\Delta\omega}{2}\right)^2 + (n+2)g^2} - \sqrt{\left(\frac{\Delta\omega}{2}\right)^2 + (n+1)g^2}\right) \tag{1.23}$$

In the dispersive limit, i.e. $|\Delta\omega| \gg \sqrt{n+1}\,g$ or in the case of the $|g\rangle \to |0,\pm\rangle$ transition, the excitation frequency of the resonator writes:

$$f^{\pm} = (E_0^{\pm} - E_g)/h = (E_{n+1}^{\pm} - E_n^{\pm})/h \approx \frac{f_0 + f_{\text{tls}}}{2} \pm \sqrt{\left(\frac{\Delta\omega}{4\pi}\right)^2 + \left(\frac{g}{2\pi}\right)^2} \tag{1.24}$$

Those frequencies are presented in figure 1.9a for a linear variation of f_{tls} and in figure 1.9b when f_{tls} is tuned by the electric field to cross the resonator, as described in section 1.5.1.1. Note that we plot the values of $f^{\pm}$ even at $\Delta\omega \simeq 0$ although the dispersive limit does not hold in that range. Indeed, when f_{tls} approaches f_{res}, one should use the exact formula (1.23). However, $f_n^{\pm}$ depend on the value of n: their variations with f_{tls} are reduced when n is increased (see inset of figure 1.9a).

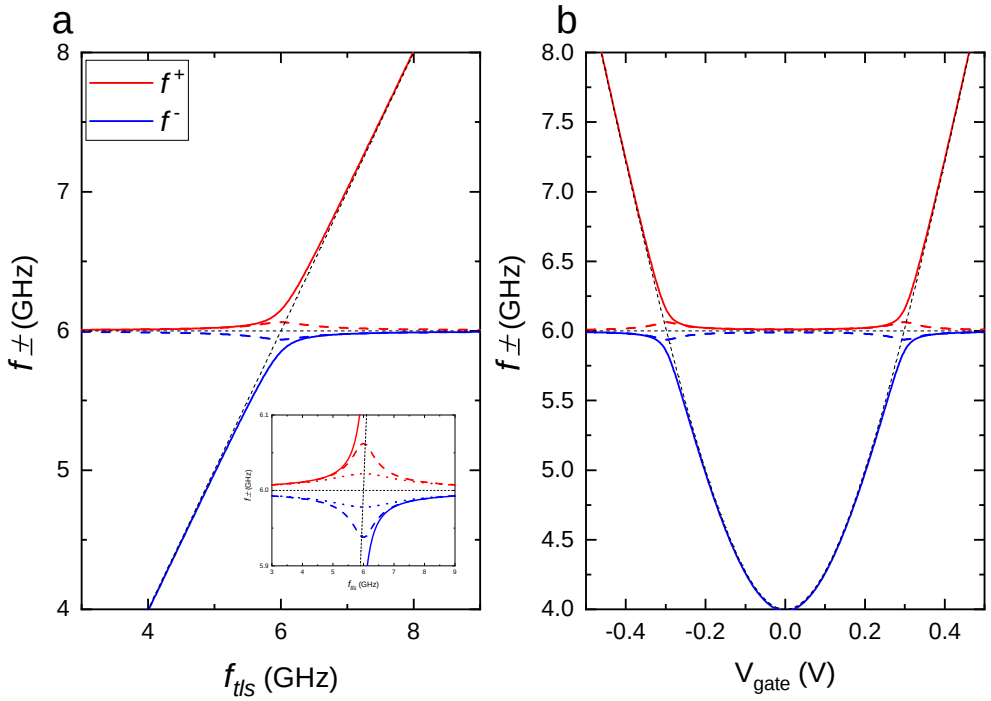

Figure 1.9. Excitation frequencies $f^{\pm}$ (lines), $f_0^{\pm}$ (dash) and $f_{10}^{\pm}$ (dots, inset). The black dashed lines correspond to the resonator and TLS bare frequencies. **a:** Anticrossing of a resonator of frequency $f_0 = 6\,\text{GHz}$ with a TLS of varying f_{tls}, with $g = 150\,\text{MHz}$. **b:** Anticrossing of a resonator of frequency $f_0 = 3\,\text{GHz}$ with a TLS whose energy follows equation (1.20) with $\widetilde{E}_0 = 0\,V.m^{-1}$, $f_{\text{tls}}^0 = \tilde{\varepsilon_0}/h = 4\,\text{GHz}$, $\tilde{\gamma} = 15.10^9 J.V^{-1}$ and $g = 150\,\text{MHz}$.

When using the approximation (1.24) instead the exact values in (1.23) to describe our system, we neglect a reduction of the frequency shift which depends on n. With this in mind, we can view f^+ (f^-) as an upper (lower) bound for the measured frequency. Hence, given experiments are carried out with a finite photon number, when using $f^{\pm}$ to fit experimental data, we obtain a lower bound for the coupling g.

If the TLS frequency does not cross f_{res} and $|\Delta\omega| \gg \sqrt{n+1}\,g$, the TLS is always weakly coupled and induces a small dispersive shift $\delta f \approx \pm\frac{g^2}{2\pi\Delta\omega}$, depending on the TLS state.

1.5.3.2 Coupled ensemble of TLS

The effects of any individual TLS coupling are usually smeared out by the large number of uniformly distributed TLS. In the case of dipole TLSs electrostatically coupled to a resonator, the net effect of the ensemble is to induce dielectric losses, a resonance frequency shift and low frequency $1/f$ noise. Each TLS has its own relaxation rate Γ_1 and dephasing rate Γ_φ. A TLS is considered coherent if $f_{\text{tls}} > \Gamma_1, \Gamma_\varphi$ and incoherent if $f_{\text{tls}} \ll \Gamma_1, \Gamma_\varphi$. Coherent TLSs can be resonantly or thermally

(if $f_{\text{tls}} < \frac{k_b T}{h}$) excited. If a TLS is excited at an effective Rabi-frequency $\Omega_R > \sqrt{\Gamma_1 \Gamma_\varphi}$, with $\Omega_R = 2\vec{p}.\vec{E}\frac{\varepsilon_0}{\hbar\varepsilon_{\text{tls}}}$ where $\vec{p}$ is the TLS dipole and $\vec{E}$ is the resonant electric field, then it saturates with a stationary excitation probability of $1/2$. This saturation effect removes most of the impact of the TLS on the resonator, the only remaining impact would be high frequency noise at Ω_R. Figure 1.10 gives an overview of the effects of a TLS bath on a resonator.

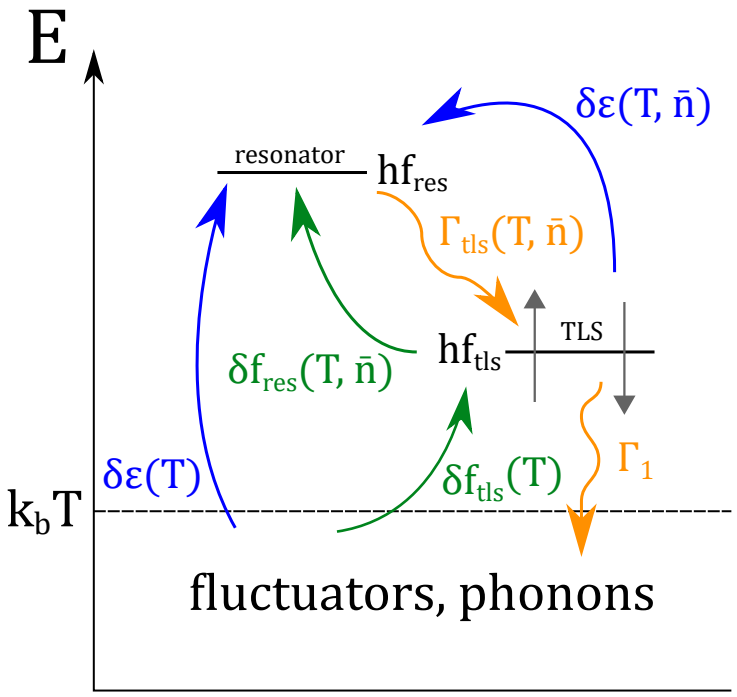

Figure 1.10. Overview of the effects described by the STM of a bath of coherent and incoherent (thermal fluctuators) TLS on a superconducting resonator. The orange paths represent energy transfers from the resonator to a coherent TLS of dissipation rate Γ_1 and then to the environment (fluctuators, phonons). The blue arrows depict the mean contribution of the TLSs increasing the dielectric constant. The green arrows stand for the time dependent fluctuations of the coherent TLS frequency which in turn induce fluctuations in the resonance frequency of the resonator.

Dielectric losses

The coupling of coherent TLSs to the resonator introduces new relaxation paths for the energy (see orange path in figure 1.10), resulting in an increase of the dielectric losses. These losses are reduced when the average number of photons in the resonator $\bar{n}$ increases above a certain critical value n_c, which results in saturation of the coherent TLS coupled to the resonator. This reduction can also arise from thermal saturation of the TLS ensemble. Experimentally, when TLS losses dominate in the low power regime, it is expected that the internal quality factor Q_{int} of the resonator scales as [84, 85]:

$$\frac{1}{Q_{\text{int}}} \propto \sum_i p_i \tan\delta_i \frac{\tanh\left(\frac{\hbar\omega_r}{2k_bT}\right)}{\sqrt{1+\left(\frac{\bar{n}}{n_c}\right)^\beta}} + \tan\delta_0 \tag{1.25}$$

where the sum runs over each volume i with a TLS dielectric loss rate $\tan\delta_i$ and participation ratio p_i (ratio of the electric field energy of the volume i over the total electric field energy of the resonator), ω_r is the resonant frequency of the resonator and $\tan\delta_0$ is the residual loss rate due to other mechanisms. The exponent β is of the order of unity. This loss mechanism results in a non monotonic variation of Q_{int} with the measurement power. When $\bar{n}$ is increased from zero, Q_{int} initially increases up to a maximum, and then decreases due to other processes at high value of $\bar{n}$ (e.g. depairing or non-linear losses).

Frequency shift

Coherent and incoherent TLS, as dipoles, contribute to the dielectric constant of their host material (blue arrows in figure 1.10), and thus reduce the resonance frequency f_{res}. Similarly to the dielectric losses described above, the dielectric contribution of coherent TLSs reduces when they saturate. However, the bath of incoherent TLSs also contribute to the dielectric constant, and those TLSs do not saturate with increasing power. In fact, their number grows when the temperature is increased. As observed for the dielectric losses, this results in a non-monotonic variation of f_{res} at constant temperature, with a maximum obtained at intermediate probing power.

Low frequency noise

While the impact of strongly coupled coherent TLS is large, their number is usually small, and the main contribution to the frequency comes from the numerous weakly-coupled coherent TLSs. On top of the frequency shift discussed above, the individual weak coupling of coherent TLS induces fluctuations in f_{res} (green arrows in figure 1.10). Indeed, each weakly coupled coherent TLS shifts f_{res} by $\pm\frac{g^2}{2\pi\Delta\omega}$. Those coherent TLSs are also coupled to fluctuators in their environment, which introduces random jumps between their states or even spectral diffusion. When considering a large TLS ensemble, this results in low frequency fluctuations of f_{res}.

Following the derivations in Ref. [86, 87, 88], we describe the fluctuators as Random Telegraph Signals (RTS) of switching rates γ with distribution $P(\gamma)=P_\gamma/\gamma$ where $P_\gamma=1/\ln(\gamma_{\max}/\gamma_{\min})$. Their effect is to induce spectral diffusion of the coherent TLSs coupled to the resonator, which in turn produce fluctuations of $f_{\text{res}}(t)$. This is measured as low frequency noise in the fractional frequency fluctuations of the resonator $y(t)=\frac{f_{\text{res}}(t)-f^0_{\text{res}}}{f^0_{\text{res}}}$, which can be written as:

$$S_y(f)=\frac{1}{f}\frac{F^2P_\gamma}{\sqrt{1+\frac{\bar{n}}{n_c}}}\frac{\chi}{N_{\text{tls}}(T)}\left(\frac{f_{\text{res}}}{T}\right)^{\mu} \tag{1.26}$$

where $F=\frac{\int_{V_h}\varepsilon_h|\vec{E}|^2\text{dV}}{2\varepsilon\int_V|\vec{E}|^2\text{dV}}$ is a filling factor, $\chi=P_0U_0$ with P_0 the TLS density and $U_0=d_0^2/\varepsilon_h$ the TLS-TLS interaction energy scale and $N_{\text{tls}}(T)\approx P_0V_hT$ the number of fluctuators (thermal TLS). This expression holds for $k_bT\ll\hbar\omega_{\text{res}}$ and $|\vec{E}|\ll E_c$, and one finds:

$$\begin{aligned} S_y(f) &\propto f^{-1} \\ S_y(f) &\propto T^{-(1+\mu)} \\ S_y(f) &\propto \left(1+\frac{\bar{n}}{n_c}\right)^{-1/2} \end{aligned}$$

Experiments have confirmed the frequency, temperature and power dependence of the TLS induced noise in superconducting resonators [89, 90, 91, 92] with $\mu\approx 0.2\,\text{to}\,0.7$ [67].

1.5.4 TLS coupled to highly inductive nanowires devices

In the highly inductive nanowires we consider (see section 1.3.4), the number of conduction channels should be small ($\approx 100-1000$), and the characteristic impedance of the resulting resonators ($Z_C=\sqrt{L/C}$) should be of a magnitude comparable to $R_Q=\frac{h}{4e^2}$.

1.5.4.1 Capacitive coupling of TLS to high impedance resonators

If we consider the capacitive coupling of a dipole TLS $\vec{p}$ to a resonator, the coupling energy writes $\hbar g=\vec{p}.\vec{E}_{\text{zpf}}$, with $\vec{E}_{\text{zpf}}$ the zero point fluctuation electric field in the capacitor of the resonator. If L is the distance between the capacitor pads, we have $\vec{E}_{\text{zpf}}=\frac{h\,f_0}{e\,L}\sqrt{\frac{\pi Z_C}{4R_Q}}\,\vec{l}$ where $\vec{l}$ is the unitary vector of the capacitor. The resulting coupling strength g for a dipole $\vec{p}=e\,\vec{a_0}$, i.e. a dipole of 1 Debye, writes:

$$g\approx\frac{a_0h\,f_0}{\hbar L}\sqrt{\frac{\pi Z_C}{4R_Q}} \tag{1.27}$$

In the case of a coplanar waveguide superconducting resonator with the common value $Z_C\approx 50\,\Omega$ and $L\approx 10\,\mu m$, this results in $g/2\pi\approx 2.10^3$ Hz. However, in our case, we aim to realise high impedance lumped resonator with $Z_C\approx R_Q$, which increases g ten folds over the usual $50\,\Omega$ resonator. We thus expect the electic dipole TLS ensemble in our devices to have a significant impact on their properties.

1.5.4.2 Critical current fluctuations of nanowires

Similarly to the critical current fluctuations described for Josephson junctions (see section 1.5.2), we can also expect TLSs to affect the critical current of our nanowires. If a TLS is close to a nanowire, its dipole electric field can interact with the conduction channels of the nanowire, changing their transparencies T_i, and thus the nanowire conductance $G_N = G_0 \sum_i T_i$. In the normal state, this results in fluctuations of G_N, which, in the superconducting state, translates into fluctuations of the nanowire kinetic inductance L_K.

The qualitative derivation of this model, as well as its implications, are laid out in one of our previous work [93]. While this work is incomplete, we nonetheless reproduce it here. Its main point is the description of the so-called TLS Induced Dephasing Mechanism (TLSIDM) which would result in a stronger impact of the TLS ensemble on high impedance devices, such as higly disordered superconducting nanowires.

1.5.4.3 "Microscopic charge fluctuators as a limit to the coherence of disordered superconductor devices"

Microscopic charged fluctuators as a limit to the coherence of disordered superconductor devices

Hélène le Sueur,[1,*] Artis Svilans,[2,†] Nicolas Bourlet,[2] Anil Murani,[2] Laurent Bergé,[1] Louis Dumoulin,[1] and Philippe Joyez[2,‡]

[1] *CSNSM, Univ. Paris-Sud, CNRS/IN2P3, Université Paris-Saclay, 91405 Orsay, France*

[2] *Quantronics group, SPEC, CEA, CNRS (UMR 3680), Université Paris-Saclay, CEA Saclay 91191 Gif-sur-Yvette Cedex, France*

By performing experiments with thin-film resonators of NbSi, we elucidate a decoherence mechanism at work in disordered superconductors. This decoherence is caused by charged Two Level Systems (TLS) which couple to the conduction electrons in the BCS ground state; it does not involve any out-of-equilibrium quasiparticles, vortices, etc. Standard theories of mesoscopic disordered conductors enable making predictions regarding this mechanism, notably that decoherence should increase as the superconductor cross section decreases. Given the omnipresence of charged TLS in solid-state systems, this decoherence mechanism affects, to some degree, all experiments involving disordered superconductors. In particular, we show it easily explains the poor coherence observed in quantum phase slip experiments and may contribute to lowering the quality factors in some disordered superconductor resonators.

* now at Quantronics group, SPEC, CEA, CNRS (UMR 3680), Université Paris-Saclay, CEA Saclay 91191 Gif-sur-Yvette Cedex, France

† now at Division of Solid State Physics and NanoLund, Lund University, Box 118,S-221 00 Lund, Sweden

‡ Corresponding author, Email: philippe.joyez@cea.fr

Introduction. In highly disordered superconductor films, the kinetic inductance of carriers can exceed the geometrical inductance by orders of magnitude. These materials have been proposed for fabricating new, purely dispersive, high-impedance electronic devices such as tunable (super)inductors [1, 2], slow-wave transmission lines [3], photon detectors [4, 5] and coherent Quantum Phase Slip Junctions (QPSJ)[6], the latter being the dual component of the celebrated Josephson Junction (JJ). The QPSJ proposal has drawn particular interest, as it enables designing new superconducting quantum circuits [7–10] that operate in the previously inaccessible high impedance domain, and which could find applications in quantum technologies. In the recent years, circuits embedding QPSJ of different materials have been tested [11–16], but they all displayed low coherence times compared to those routinely achieved in JJ-based circuits. In the present work, we bring to light a new decoherence mechanism in highly disordered superconductor, due to the charged TLS omnipresent at interfaces and in insulators in solid state systems. This mechanism easily explains the poor coherence observed in QPSJ devices. It also likely contributes to lower-than-expected quality factors reported in resonators made with disordered superconductors [12, 15, 17–19], even though this mechanism is non-dissipative. This mechanism should affect all the proposals mentioned above, but also experiments probing the Superconductor to Insulator quantum phase Transition (SIT) [20, 21], or the Berezinskii–Kosterlitz–Thouless (BKT)[22–24] phase transition.

Thin-films of various disordered superconductors have been used to implement high kinetic inductance circuits. Provided they are not too close to the SIT (occurring at a normal state sheet resistance $R_{N\square}$ of order $h/4e^2 \simeq 6.5$ kΩ), these materials can still be qualitatively described by the BCS theory. In this framework, well below the critical temperature, the low-frequency linear response of a diffusive superconductor is described by a kinetic inductance L_K proportional to its normal state resistance R_N [25],

$$L_K = \frac{R_N}{\pi \omega_{\rm gap}}, \tag{1}$$

where $\omega_{\rm gap} = \Delta/\hbar$, with Δ the superconducting gap. With thin films having $R_{N\square} \sim 1$kΩ, and given the common superconducting gaps are in the range 0.2-2.0 meV, one can then achieve sheet kinetic inductance $L_{K\square}$ of the order of 1 nH. Thus, these materials should enable highly inductive components that operate up to frequencies of the order of $\omega_{\rm gap}$ (*i.e.* tens to hundreds of GHz) which are otherwise unfeasible.

Experiments. In this work we have used $\mathrm{Nb}_x\,\mathrm{Si}_{1-x}$ alloy, with $x = 0.18$, and a film thickness $t = 15$ nm, deposited on an intrinsic Si substrate. The alloy was co-evaporated as described in Ref. [26]. In the normal state, this film has a sheet resistance $R_{N\square}$ of about 600 Ω, weakly dependent on temperature. The RF properties of the Nb Si layer were first characterized by fabricating a half-wavelength coplanar waveguide resonator with a 10 µm-wide, 700 µm-long central conductor and measuring it at 17 mK, well below the critical temperature of 0.85 K. From the fundamental resonance (at 6.687 GHz), we extracted the sheet inductance $L_{K\square} = 0.83$ nH. The measured quality factor $Q_{\rm meas} = 1.6 \times 10^4$ of the resonance was much lower than the designed external quality factor $Q_{\rm ext} = 1.6 \times 10^5$, set by the capacitive coupling to the input and output 50Ω lines. Lower-than-expected quality factors have been reported in several resonators made of disordered superconductors [12, 15, 17, 18]; they are usually attributed to unspecified "internal losses", although dissipative mechanisms are unexpected at these temperatures in BCS superconductors. Finally, the non-linear response to the amplitude of the probe signal gave access to the superconducting coherence length $\xi \simeq 40$ nm of the material (see Ref. [27] for details).

Using the above value for $L_{K\square}$, we designed lumped-element LC resonators in which the inductors were narrow wires 100-180 nm in width, and the capacitors were rectangular pads at both ends of the inductor (see Fig. 1a). The dimensions were chosen with the aid of numerical simulations in

order to produce well-separated resonance frequencies between 6 and 8 GHz (see Table 1). The resonators were all capacitively coupled to the same input and output 50 Ω transmission lines, weakly enough to all have quality factors larger than 10^4 in absence of internal losses. The design was transferred into the NbSi layer using e-beam lithography and dry etching in a $CF_4 - Ar$ mixture with the negative ma-N resist acting as a mask. After removal of the mask, the sample was wire-bonded on a printed-circuit board and cooled down in a dilution refrigerator. As shown in Fig. 1a, the wiring of the sample incorporated a bias tee and a DC voltage source letting us apply an electric field on the resonators.

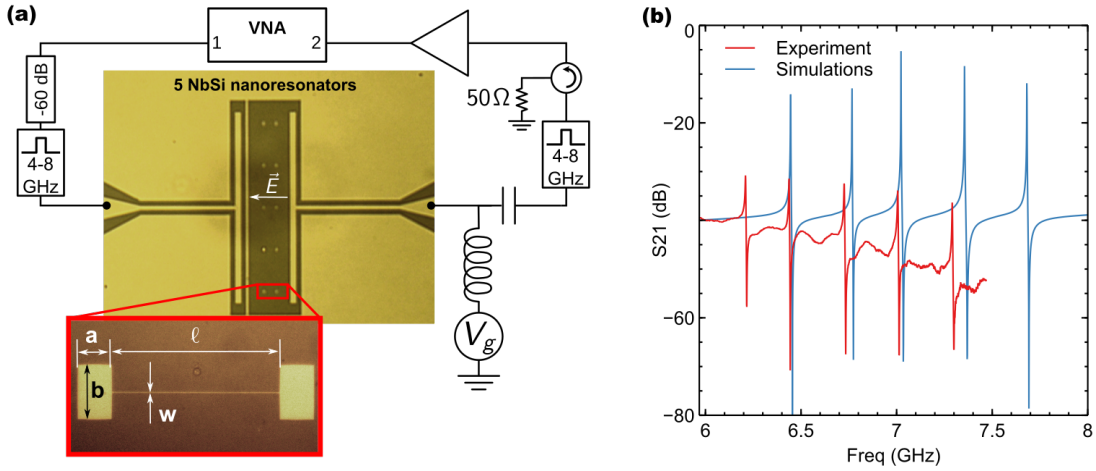

Figure 1. **(a)** Simplified schematic of the setup. Five different NbSi nanoresonators are measured in transmission, using a Vector Network Analyzer. A bias tee and a voltage source V_g enable applying an electric field along the resonators. **(b)** Simulated (assuming zero internal losses) and measured transmission S_{21} of the sample. The resonance peaks have a Fano resonance shape due to the stray direct coupling of the input and output transmission lines in addition to the coupling through the resonator. The experimental curve is offset vertically to account for the total attenuation and amplification of the setup at 6 GHz. Experimental resonances reach much lower peak transmissions than the simulations, usually indicating that internal losses dominate.

Resonator	w(nm)	ℓ (µm)	$a(m)$	$b(m)$	f_{des} (GHz)	f_{meas} (GHz)	Q_{ext}	Q_{meas}
1	100	50	10	10	6.44	6.21	17100	1890
2	120	50	12	10	6.76	6.44	20900	2280
3	140	50	14	10	7.02	6.73	14000	2020
4	160	50	15	10	7.35	7.00	12900	2140
5	180	50	16	10	7.68	7.29	16000	2650

Table I. Design parameters of the five resonators and results of their experimental characterization (see Fig. 1a for resonator dimensions). f_{des} is the designed resonance frequency and Q_{ext} is the designed external quality factor (i.e. simulated total quality factor, with no internal losses). f_{meas} and Q_{meas} are the measured resonance frequency and total quality factor, obtained by fitting S_{21}.

In Fig. 1b we show the simulated and measured transmission S_{21} through the five resonators.

The measurements were done at 30 mK, with sufficiently low power for the resonators to be well within their linear response regime. We observe that the resonance frequencies are well-spaced, as designed, with, however, a systematic shift towards lower frequencies which we attribute to a slightly non-nominal fabrication process. We also observe that the measured resonance peaks are markedly lower than the simulated values. Correspondingly, the measured quality factors $Q_{\rm meas}$, obtained by fitting the S_{21} data as a function of frequency, are much lower than the external quality factors $Q_{\rm ext}$ predicted by simulations (see Table 1). We further observe that $Q_{\rm meas}$ is about an order of magnitude lower than what had been determined in the large half-wavelength resonator. Since the small and large resonators were made out of the same NbSi layer and following nominally the same process, the large decrease in $Q_{\rm meas}$ suggests the quality factor in NbSi resonators depends on the lateral dimension, and is higher in wider structures.

In Fig. 2a we show the variations of the phase of S_{21} at a fixed frequency $f = 6.2086\,\mathrm{GHz}$, close to the maximum transmission of resonator #1, while the gate voltage is repeatedly swept from 0 to 110 mV over 3.5 s. In each sweep, we observe several abrupt changes in the phase. The gate voltage at which these jumps occur varies from one sweep to another, showing slow drifts and telegraphic signal-like jumps. Furthermore, such measurements repeated at different times displayed long-term variability typical of $1/f$-like noise. Figure 2b shows that the observed flicker noise corresponds to fluctuations in the *resonance frequency*. Similar features were observed in the other 4 nanoresonators. Due to the frequency fluctuations, the phase of the (electromagnetic) quantum state of the resonator becomes unknown after some time (the *dephasing* time) and the state can no longer be manipulated deterministically –a phenomenon known as *dephasing* or *decoherence*.

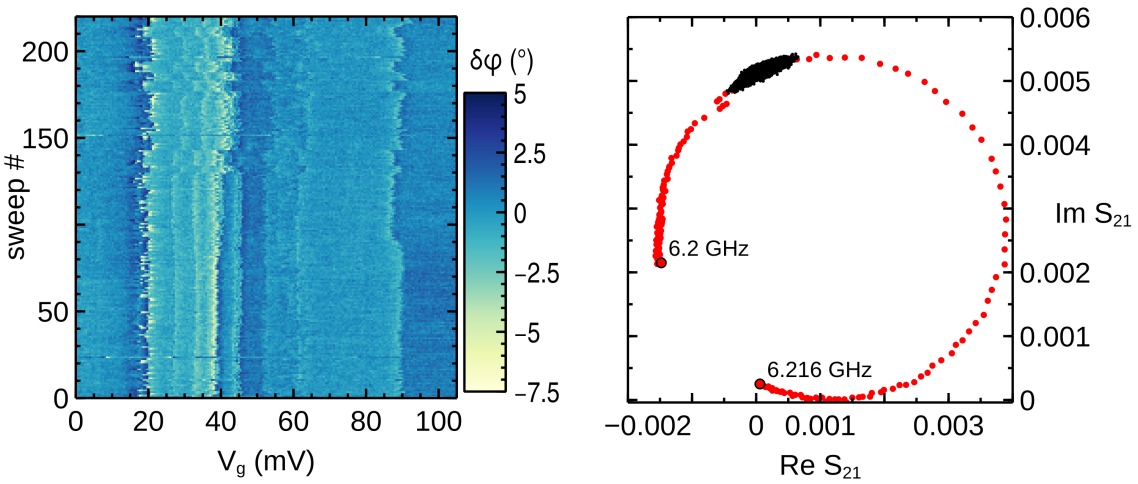

Figure 2. **(a)** Variations of the phase of S_{21} at a fixed frequency $f = 6.2086\,\mathrm{GHz}$, close to the maximum transmission of resonator #1, while the gate voltage is repeatedly swept from 0 to 110 mV over 3.5 s **(b)** S_{21} in the complex plane for resonator #1. Red dots were obtained by varying the frequency across the resonance. The cloud of black dots corresponds to all the data points in **(a)**. It is aligned along the resonance circle, showing that the jumps observed are really resonance frequency jitter.

Interpretation. It is tempting to attribute the fluctuations in the resonance frequency of our nanoresonators to the mechanisms already known to occur in superconducting resonators. Indeed, it was understood in the recent years that microscopic charge systems present in the dielectric material

surrounding superconducting resonators cause frequency jitter and losses in these resonators [28–31], on the grounds of the so-called Generalized Tunneling Model (GTM) [32]. In this model, the losses are due to TLSs resonantly coupled to the resonator via the AC electric field, each of these TLSs also interacting strongly with other, non-resonant, thermally activated TLSs. Overall, these couplings result in fluctuations of the dielectric constant at the resonant frequency, i.e. fluctuations in the effective capacitance of the resonator. While this TLS-induced dielectric loss mechanism is certainly present in our experiments, one does not expect it to yield observable individual TLS switching events. This is because in our geometry, any TLS occupies an extremely small volume fraction of the resonator mode, and it can only modify the capacitance accordingly. Coupling to spin impurities (magnetic TLSs) may also be a source of fluctuations in superconducting resonators [17, 33], but strong resonant magnetic coupling with individual localized spin impurities is similarly ruled out.

A new dephasing mechanism. Here, we propose an alternative explanation for the observed fluctuations. We argue it is the direct interaction of the TLSs with the conduction electrons which causes flicker noise of the kinetic inductance. In the GTM [32], the corresponding interaction Hamiltonian for a single TLS reads

$$H_{\text{TLS-el}} = \sigma_z \sum_{kk'\eta} V_{kk'} c^\dagger_{k\eta} c_{k'\eta} \tag{2}$$

where $V_{kk'}$ describes the scattering potential, $c^\dagger_{k\eta}(c_{k\eta})$ creates (annihilates) a fermion of wave vector k and spin η, and σ_z is the Pauli matrix describing the TLS. However, in Ref. [32] this term is only considered for its relaxation effect on the TLS, neglecting the corresponding back-action on the conduction electrons. We show below this is legitimate in conventional superconducting resonators in which the kinetic inductance is a negligible part of the total inductance (it happens to be the case for all experiments where TLS losses were carefully analyzed [28–31]), but not in highly disordered superconductors.

For simplicity, we first consider the case where the length ℓ of the inductor wire in our resonators is shorter than the electronic coherence length L_φ in NbSi and use the Landauer-Büttiker framework [34] to describe transport. The normal-state conductance of the wire is given by the Landauer formula,

$$G_N = 2G_0 \sum_n T_n$$

where $G_0 = e^2/h$, and the T_n are the transmission probabilities of the channels, i.e. the square modulus of the transmission eigenvalues. For disordered materials like our wires, the transmission results from multiple-path interferences though the wire, analogous to a speckle pattern in optics. In other words, the T_n depend in an intricate manner on the specific disorder realization which is unknown. Theory [34] nevertheless provides statistical predictions regarding G_N, namely that it has

- an expectation value related to the macroscopic sheet resistance of the material and wire dimensions

$$\langle G_N \rangle = \frac{w}{\ell R_{N\square}} \tag{3}$$

- a standard deviation σ_G according to Universal Conductance Fluctuations (UCF), *i.e.* $\sigma_G \sim G_0$ in the "metallic case" ($G_N > G_0$), and slowly decreasing approximately as $\sigma_G \sim G_0 \times$

$\sqrt{G_N/G_0}$ in the crossover to the Anderson insulator regime ($G_N < G_0$) [35], independently of the wire material or dimensions.

When a TLS changes state, it locally modifies the electronic scattering potential in its vicinity, imparting new phaseshifts to the electronic trajectories. For the whole wire, this results in a change of the global electronic speckle pattern, i.e. a modification of the channels, with a change of the conductance $G_N \to G_N + \delta G$. If the TLS is located far away from the wire, the change in the potential is vanishingly small and $\delta G = 0$. In the opposite limit of "strong interaction" where the switching of the TLS radically changes the speckle pattern, δG has a random value with a standard deviation constrained by the UCF. Hence, for any given TLS one expects $0 \leqslant |\delta G| \lesssim G_0$ depending on the type of TLS and its distance to the wire. In other words, the random conductance jumps of the individual TLSs follow a distribution, itself derived from the distribution of the coupling strengths (hereafter denoted $\mathcal{D}_{\rm cs}$). Another important characteristic of a TLS is its switching time; for the TLS ensemble, switching times are random, following a distribution $\mathcal{D}_{\rm st}$.

In the superconducting state, δG causes a change of the kinetic inductance of the wire (Eq. (1) with $R_N = G_N^{-1}$). This has an effect on the resonance frequency $f = 1/2\pi\sqrt{(L_K + L_{\rm geom})C}$ with C the capacitance of the resonator and $L_{\rm geom}$ the geometrical inductance. To first order, a TLS Switching Event (SE) induces a relative change in the resonance frequency

$$\frac{\delta f}{f} = -\frac{\alpha}{2}\frac{\delta L_K}{L_K} = \frac{\alpha}{2}\frac{\delta G}{G_N}, \tag{4}$$

where $\alpha = L_K/(L_K + L_{\rm geom})$ is the participation ratio of L_K in the total inductance. While $\alpha \simeq 1$ in our disordered resonator, it is vanishingly small in "conventional" superconducting resonators which are then not dephased by TLS through this mechanism (the dielectric losses of the GTM then being dominant).

Successive single TLS SEs produce a random-walk-like evolution for the conductance (bounded by UCF) and of the resonance frequency. Measured over many SEs, this leads to an increased resonance width $\Delta f_{\rm FWHM}$ accompanied with a reduction of the peak transmitted power because the resonator never stays long in optimum transmission condition. Assuming the TLS fluctuations are the main cause of the resonance width $\Delta f_{\rm FWHM}$, the corresponding quality factor $Q_{\rm TLS} = f/\Delta f_{\rm FWHM}$ is given by

$$Q_{\rm TLS}^{-1} \sim \frac{2\langle \delta f \rangle_{\rm rms}}{f} = \alpha \frac{\langle \delta G \rangle_{\rm rms}}{G_N} \tag{5}$$

where $\langle \ldots \rangle_{\rm rms}$ denotes the rms-averaged quantity over all single TLS jumps during the measurement. $\langle \delta G \rangle_{\rm rms}$ can be obtained from the distributions $\mathcal{D}_{\rm cs}$ and $\mathcal{D}_{\rm st}$. The UCF upper bound $\langle \delta G \rangle_{\rm rms} = \sigma_G \sim G_0$ is reached when the speckle pattern is sufficiently reorganized during the measurement, requiring sufficiently strongly coupled and fast TLSs. From Eqs. (4) and (5), one expects a larger effect of TLSs in systems with a smaller conductance, *i.e.* a smaller number N of conduction channels, as $N \propto G_N \propto w \times t$.

Microscopic and macroscopic dephasing. The above discussion brings to light a TLS-Induced Dephasing Mechanism (TLSIDM) in disordered superconductor resonators, i.e. the dephasing of collective, macroscopic, electromagnetic degrees of freedom in the circuit. These results were obtained considering that electrons in the inductors are fully phase-coherent. However, this assumption is unrealistic because our inductors are longer ($\ell = 50\mu$m) than the largest published values for L_φ in metals. Moreover, TLS SEs themselves introduce random electronic phase shifts, contributing to shortening L_φ. In the following we take into account such (microscopic) dephasing of individual electrons in our analysis, and work out how it modifies the (macroscopic) TLSIDM.

To this effect, we first examine electronic dephasing only. On average, SEs dephase the electrons after a time $\tau_{\rm TLS}$ stemming from $\mathcal{D}_{\rm cs}$ and $\mathcal{D}_{\rm st}$ (which already determine $\langle\delta G\rangle_{\rm rms}$). Assuming TLSs are the main source of electron dephasing, one then has $L_\varphi = \sqrt{D\tau_{\rm TLS}}$ where D is the diffusion constant. Yet, the value of L_φ in the experiment is not known, partly because the standard weak localization determination cannot be performed in the superconducting state. How does this dephasing of individual electronic states affect the collective superconducting state (i.e. the BCS state)? As long as $\tau_{\rm TLS}$ is large compared to the timescale of the pairing interaction $\hbar/\Delta$ (i.e. $L_\varphi \gg \xi$), the superconducting order adapts to such fluctuations and $|\Delta|$ remains essentially unchanged, just as if the disorder were static (Anderson's theorem). The phase of the order parameter, however, is a macroscopic electromagnetic degree of freedom which is affected by TLS-induced dephasing proportionally to α, as in Eq. (4). In the opposite limit $\tau_{\rm TLS} < \hbar/\Delta$, fast electron dephasing simply inhibits the formation of the superconducting state. In the crossover, one expects $|\Delta|$ to be reduced and the density of states to be modified, which could be related to anomalous properties reported in some disordered superconductor resonators [36]. In the following, for simplicity, we assume $L_\varphi \gg \xi$.

How does the finite coherence length of electrons modify the TLSIDM? In a quasi-1D incoherent inductor wire (*i.e.* with $w, t \ll L_\varphi < \ell$), an individual TLS SE modifies the normal state conductance of the wire only over an L_φ-long segment, yielding a δG typically smaller by a factor $(L_\varphi/\ell)^2$ than in the coherent case (*i.e.* $0 \leqslant |\delta G| \lesssim (L_\varphi/\ell)^2 G_0$). The resistance changes corresponding to SEs in different segments add in a random walk fashion, so that, averaged over many TLS configurations, $\langle\delta G\rangle_{\rm rms}$ is smaller than in a coherent wire by a factor $(L_\varphi/\ell)^{3/2}$, just like σ_G is reduced in incoherent mesoscopic conductors [34]. Assuming strongly coupled TLSs, one then gets the upper limit for $\langle\delta G\rangle_{\rm rms}$

$$\langle\delta G\rangle_{\rm rms} \sim \left(\frac{L_\varphi}{\ell}\right)^{3/2} G_0 \tag{6}$$

(recalling however that L_φ and $\langle\delta G\rangle_{\rm rms}$ are not fully independent). Then, using Eqs. (5) and (3), this yields the strong-coupling prediction

$$Q_{\rm TLS}^{-1} \simeq \alpha \left(\frac{L_\varphi}{\ell}\right)^{3/2} \frac{\ell}{w} G_0 R_\square, \tag{7}$$

setting an absolute lower bound for the quality factor due to TLSIDM.

Comparison with our experiments. The above analysis is in qualitative agreement with our observations. In the first place, the mechanism we propose can explain the observed telegraphic-like frequency jitter, the resulting dephasing and the lower-than-expected quality factors. In the second place, the prediction of larger relative frequency fluctuations in systems with fewer conduction channels explains why the nanoscale resonators appear more lossy than the larger resonator, although they are made of the same material, with (nominally) the same density of volume and surface defects. The data from our 5 nanoresonators is also qualitatively compatible with the proportionality between the quality factor and the nanowire width (Eqs. (5) & (3)), but there are too few samples and a too narrow range of widths to regard this as a solid demonstration.

Let us now try to be more quantitative. The largest jumps in Fig. 2 are of the order of 10°, which, given the S_{21} resonance circle, corresponds to $\delta f \simeq 0.6$ MHz, and, according to Eq. (4), a change in the normal state conductance $|\delta G| \simeq 1.4 \times 10^{-5} G_0$. Since we have selected the largest jump observed, we boldly assume it corresponds to a strongly coupled TLS inducing a change of conductance of the order of the disorder-averaged rms value $\sim (L_\varphi/\ell)^2 G_0$, which then yields an estimate of $L_\varphi \sim 0.2$µm. Similarly, if we assume a strongly coupled TLS ensemble, then, matching

the measured quality factor $Q_{\rm meas} \sim 2 \times 10^3$ with $Q_{\rm TLS}$ in Eq. (7) yields $L_\varphi \sim 0.6$µm, which is of the same order than the above crude estimate. This assumption of strongly coupled TLSs yields a lower bound for L_φ. It could be that there are no strongly coupled TLS in our resonators ($|\delta G| \ll (L_\varphi/\ell)^2 G_0$ for all individual TLSs), in which case the observations would be consistent with a larger L_φ.

TLS types. We now discuss the type of TLS that cause such decoherence. As NbSi is an amorphous material, TLSs may be atoms jumping between metastable positions in the bulk of the material. However, the observed effect of a DC electric field proves that charged traps or dipolar defects in the vicinity of the wire are at work. It is indeed well known that such charged TLSs are omnipresent in insulators or at interfaces in solid-state electronic devices where, besides the GTM dielectric noise already mentioned [32], they cause charge noise by coupling to surface electronic states (within a Thomas-Fermi screening length $\lambda_{\rm TF}$). This charge noise is well documented in mesoscopic circuits such as single electron transistors [37, 38], charge qubits [39, 40] or quantum point contacts [41], but also in MOS transistors [42]. The microelectronics industry has shown that a careful choice of materials and process engineering can much reduce the number of charged TLSs, but never completely suppress them. Note that besides the TLSIDM dependence on the number of channels $N \propto w \times t$, for charged TLSs one further expects the TLSIDM to become stronger when the thickness t is reduced to become comparable to $\lambda_{\rm TF}$, as charged TLSs then interact with a larger fraction of conduction electrons.

Comparison with other experiments. The TLSIDM we point out also directly affects QPS experiments in disordered superconductors. The phase slip energy of a uniform quasi-1D nanowire is predicted [6, 43] to scale as

$$E_S = \Delta \frac{G_N}{G_0} \left(\frac{\ell}{\xi}\right)^2 \exp\left(-A \frac{G_N}{G_0} \frac{\ell}{\xi}\right) \tag{8}$$

where Δ is the superconducting gap energy, ξ the superconducting coherence length, ℓ the nanowire length, and A a numerical factor of order 1. In order to have non vanishing E_S, one needs nanowires with a small number of conduction channels. In Ref. [14], it was already noticed that the randomness in disorder realizations induces a relatively large (static) dispersion in values of G_N of order G_0, resulting in an irreproducibility of E_S among nominally identical samples. It was also pointed that random offset charges (i.e. essentially frozen charged TLS) were likely contributing to this disorder. Here, we simply extend this reasoning, arguing that charged TLS in the vicinity of the wire also induce *dynamical* fluctuations in E_S. These fluctuations of E_S are dual to fluctuations in the Josephson energy of JJs due to TLS in the tunnel barrier [44], both resulting in decoherence.

We now examine whether the TLSIDM we propose could explain a few published experimental results. In Ref. [18], using the values given for the granular Aluminum resonator shown in Fig. 3a, the measured quality factor would be consistent with $Q_{\rm TLS}$ of strongly coupled TLSs (Eq. (7)) provided $L_\varphi \sim 0.5$µm. In Ref. [15], using the values given for the InO_x QPSJs and Eq. (8), one predicts that a conductance noise $\langle \delta G \rangle_{\rm rms} \sim 1.4 \times 10^{-2} G_0$ due to charge fluctuators would yield a $\langle \delta E_S \rangle_{\rm rms}/E_S \sim$5% fully explaining the observed Gaussian spectroscopic linewidth. Strongly coupled TLSs (Eq. (6)) would yield such $\langle \delta G \rangle_{\rm rms}$ figure provided $L_\varphi \simeq$15 nm, however, this seems exaggeratedly low for the quoted $\xi = 30$ nm. Similar analysis carried out for the NbN QPSJs in Ref. [14], the NbTiN resonators in Ref. [17], or the granular Aluminum resonator #4 in Ref. [19] all lead to similarly low estimates of $L_\varphi \sim \xi$. As discussed in the case of our resonator, all these experiments could also (more realistically) correspond to weakly coupled TLS and larger L_φ. Thus, given a suitable ensemble of charged TLS, the mechanism we propose could entirely explain the observed decoherence in all these devices. On the other hand, in some of these devices other mechanisms are clearly contributing to the overall decoherence (in which case the TLSIDM must be

weaker than we have just estimated). For instance, in Ref. [17] spin impurities are shown to play an important role; for the granular Al resonator of Ref. [18], out-of-equilibrium quasiparticles have been identified as a limiting factor [45], and in Ref. [19] the power dependence of the quality factor suggests that TLS dielectric losses of the GTM contribute to the resonance width. Note however that, in the latter Ref. [19], telegraphic fluctuations in the resonance frequency are reported. This is similar to what we observe in our resonators and, for the same reasons, we believe this is a manifestation of the TLSIDM.

Discussion. Let us address or clarify a few points regarding the TLSIDM presented above.

– In resonators, internal energy losses (with an energy decay rate $\kappa_{\rm int} > 0$) imply a lowering of the quality factor. The reciprocal connection is generally assumed to exist (*i.e.* lower-than-expected $Q \Rightarrow \kappa_{\rm int} > 0$), but the TLSIDM is a counter-example disproving it. Indeed, this mechanism operates within the BCS ground state and it is thus strictly non-dissipative ($\kappa_{\rm int} = 0$). If it were possible to measure fast enough between TLS switching events, one would observe at all times the narrow resonance limited by $Q_{\rm ext}$, with the peak frequency jumping randomly. It is only after averaging over many TLS configurations (*e.g.* due to the measurement bandwidth) that one gets the reduced quality factor (Eq. (5)), mimicking what internal losses would yield. As well, in Fig. 1b, the fact that the measured peak transmission is much lower than in the lossless simulations does not indicate energy being dissipated in the resonator, but power reflected to the input line when the TLSs shift the resonator out of resonance with the probe frequency. Given the jump dynamics involved in the disguise of the dissipationless mechanism as a lossy mechanism, in dubious cases, the relevant mechanism could be diagnosed by measuring with sufficient bandwidth the time-resolved transmitted power at a fixed frequency.

– The TLSIDM does not require any out-of-equilibrium quasiparticles, vortices, etc. which are usually invoked to explain decoherence in superconducting systems. The presence of such features would of course open additional decoherence channels.

– Although the TLSIDM we discuss is lossless, the GTM [32] shows that the TLS ensemble provides a dissipative bath able to absorb the resonator's microwave photons. This *different* GTM mechanism does yield internal energy losses (and decoherence) which are not taken into account in the present work, but which may contribute in some experiments. A distinctinctive feature in the GTM predictions is the non-monotonic dependence of losses on microwave power and temperature, due to the saturation of the resonant TLS. For the TLSIDM, TLSs couple to the wire independently of their energy splitting. Thus, for an ensemble of weakly coupled TLSs ($|\delta G| \ll (L_\varphi/\ell)^2 G_0$), we rather expect that the frequency fluctuations (respectively, the quality factor) due to this mechanism should decrease (resp., increase) monotonically when lowering the temperature, because less and less TLSs get thermally excited.

– It is well known that disordered superconductors develop spatial inhomogeneities in $|\Delta|$ [46] that eventually dominate the properties of the material close to the SIT [47]. Since we only consider superconductors sufficiently far away from the SIT, we assume these inhomogeneities remain small and we have not taken them into account (e.g. in Eq. (1)), but accounting for them would not qualitatively modify the TLSIDM we describe.

– Could the effect of charge noise be engineered-out for achieving highly coherent disordered superconductor circuits? After all, in JJ-based qubits this was achieved by operating the Cooper pair box at a "sweet spot" [39, 40], or by using the Transmon design [48, 49] in which

charge sensitivity is suppressed exponentially. However, in these qubits, charge noise affects the charge degree of freedom in the system Hamiltonian, while in disordered superconductors charge noise modulates a parameter (L_K) of the Hamiltonian and, therefore, it cannot be mitigated in a similar way. Short of reducing TLS charge noise itself to an acceptable level, the only way to reduce the effect of TLSIDM is to reduce accordingly the kinetic inductance participation ratio α, giving up at the same time the desired high kinetic inductance properties of the circuit. As an alternative, one may wonder if 1D topological superconducting channels, which are impervious to fluctuations in scattering, could form a basis for decoherence-free QPSJs or other high kinetic inductance devices.

Conclusions. Because of the omnipresence of charged TLS, the TLSIDM we describe is certainly at work in disordered superconductors devices. We show it can easily explain the disappointing coherence of QPSJ, and that it is likely contributing to the lower-than-expected quality factors of some disordered superconductor resonators. Our results call for more in-depth theoretical and experimental explorations of this TLSIDM, in order to determine the expected distributions $\mathcal{D}_{\rm cs}$ and $\mathcal{D}_{\rm st}$ for known TLSs, and obtain quantitative predictions for the various noise spectra, coherence times, temperature dependence, etc.

Finally, beyond disordered superconductors devices, we also ponder that fluctuators could have some impact on experiments investigating the SIT [20, 21] or BKT [22–24] phase transitions in these materials. For instance, it is plausible that the recently reported [50] telegraphic-like reconfigurations in a disordered superconductor are due to the coupling to charged TLS described above. As far as we know, all the theories for these phase transitions assume a static disorder, and one may thus ask if and how the TLS-induced dynamics would modify the characteristics of these transitions. Then, the different densities and types of TLS in various experiments could perhaps explain departures from the expected universality of the SIT [21].

Acknowledgments. The authors are grateful to Genevieve Fleury, Marc Westig and SPEC's Quantronics Group and Nanoelectronics Group members for discussions, comments and support. This work was supported in part by ANR grant ANR-15-CE30-0021-01, and by PALM and P2IO interLabex project NDS-NbSi.

[1] A. A. Adamyan, S. E. Kubatkin, and A. V. Danilov. Tunable superconducting microstrip resonators. *Applied Physics Letters*, 108(17):172601, apr 2016.

[2] Anthony J. Annunziata, Daniel F. Santavicca, Luigi Frunzio, Gianluigi Catelani, Michael J. Rooks, Aviad Frydman, and Daniel E. Prober. Tunable superconducting nanoinductors. *Nanotechnology*, 21(44):445202, 2010.

[3] A. A. Adamyan, S. E. de Graaf, S. E. Kubatkin, and A. V. Danilov. Kinetic inductance as a microwave circuit design variable by multilayer fabrication. *Superconductor Science and Technology*, 28(8):85007, 2015.

[4] P. Diener, H. G. Leduc, S. J. C. Yates, Y. J. Y. Lankwarden, and J. J. A. Baselmans. Design and Testing of Kinetic Inductance Detectors Made of Titanium Nitride. *Journal of Low Temperature Physics*, 167(3-4):305–310, may 2012.

[5] Henry G. Leduc, Bruce Bumble, Peter K. Day, Byeong Ho Eom, Jiansong Gao, Sunil Golwala, Benjamin A. Mazin, Sean McHugh, Andrew Merrill, David C. Moore, Omid Noroozian, Anthony D. Turner, and Jonas Zmuidzinas. Titanium nitride films for ultrasensitive microresonator detectors. *Applied Physics Letters*, 97(10):102509, sep 2010.

[6] J. E. Mooij and Yu V. Nazarov. Superconducting nanowires as quantum phase-slip junctions. *Nature Physics*, 2(3):169–172, mar 2006.

[7] A. M. Hriscu and Yu. V. Nazarov. Model of a Proposed Superconducting Phase Slip Oscillator: A Method for Obtaining Few-Photon Nonlinearities. *Physical Review Letters*, 106(7):77004, feb 2011.

[8] A. M. Hriscu and Yu. V. Nazarov. Coulomb blockade due to quantum phase slips illustrated with devices. *Physical Review B*, 83(17):174511, may 2011.

[9] Andrew J. Kerman. Metastable Superconducting Qubit. *Physical Review Letters*, 104(2):27002, jan 2010.

[10] A. M. Hriscu and Yu. V. Nazarov. Quantum Synchronization of Conjugated Variables in a Superconducting Device Leads to the Fundamental Resistance Quantization. *Physical Review Letters*, 110(9):97002, feb 2013.

[11] J. T. Peltonen, P. C. J. J. Coumou, Z. H. Peng, T. M. Klapwijk, J. S. Tsai, and O. V. Astafiev. Hybrid rf SQUID qubit based on high kinetic inductance. *Scientific Reports*, 8(1):10033, jul 2018.

[12] J. T. Peltonen, Z. H. Peng, Yu. P. Korneeva, B. M. Voronov, A. A. Korneev, A. V. Semenov, G. N. Gol'tsman, J. S. Tsai, and O. V. Astafiev. Coherent dynamics and decoherence in a superconducting weak link. *Physical Review B*, 94(18):180508, nov 2016.

[13] K. Yu. Arutyunov and J. S. Lehtinen. Junctionless Cooper pair transistor. *Physica C: Superconductivity and its Applications*, 533:158–160, feb 2017.

[14] J. T. Peltonen, O. V. Astafiev, Yu. P. Korneeva, B. M. Voronov, A. A. Korneev, I. M. Charaev, A. V. Semenov, G. N. Golt'sman, L. B. Ioffe, T. M. Klapwijk, and J. S. Tsai. Coherent flux tunneling through NbN nanowires. *Physical Review B*, 88(22):220506, dec 2013.

[15] O. V. Astafiev, L. B. Ioffe, S. Kafanov, Yu A. Pashkin, K. Yu Arutyunov, D. Shahar, O. Cohen, and J. S. Tsai. Coherent quantum phase slip. *Nature*, 484(7394):355–358, apr 2012.

[16] S. E. de Graaf, S. T. Skacel, T. Hönigl-Decrinis, R. Shaikhaidarov, H. Rotzinger, S. Linzen, M. Ziegler, U. Hübner, H.-G. Meyer, V. Antonov, E. Il'ichev, A. V. Ustinov, A. Ya Tzalenchuk, and O. V. Astafiev. Charge quantum interference device. *Nature Physics*, 14(6):590–594, jun 2018.

[17] N. Samkharadze, A. Bruno, P. Scarlino, G. Zheng, D. P. DiVincenzo, L. DiCarlo, and L. M. K. Vandersypen. High-Kinetic-Inductance Superconducting Nanowire Resonators for Circuit QED in a Magnetic Field. *Physical Review Applied*, 5(4):44004, apr 2016.

[18] N. Maleeva, L. Grünhaupt, T. Klein, F. Levy-Bertrand, O. Dupre, M. Calvo, F. Valenti, P. Winkel, F. Friedrich, W. Wernsdorfer, A. V. Ustinov, H. Rotzinger, A. Monfardini, M. V. Fistul, and I. M. Pop. Circuit quantum electrodynamics of granular aluminum resonators. *Nature Communications*, 9(1):3889, sep 2018.

[19] Wenyuan Zhang, K. Kalashnikov, Wen-Sen Lu, P. Kamenov, T. DiNapoli, and M. E. Gershenson. Microresonators fabricated from high-kinetic-inductance Aluminum films. *ArXiv:1807.00210 [cond-mat, physics:physics]*, jun 2018.

[20] Vsevolod F. Gantmakher and Valery T. Dolgopolov. Superconductor–insulator quantum phase transition. *Physics-Uspekhi*, 53(1):1, 2010.

[21] Yen-Hsiang Lin, J. Nelson, and A. M. Goldman. Superconductivity of very thin films: The superconductor–insulator transition. *Physica C: Superconductivity and its Applications*, 514:130–141, jul 2015.

[22] E. J. König, A. Levchenko, I. V. Protopopov, I. V. Gornyi, I. S. Burmistrov, and A. D. Mirlin. Berezinskii-Kosterlitz-Thouless transition in homogeneously disordered superconducting films. *Physical Review B*, 92(21):214503, dec 2015.

[23] R. Schneider, A. G. Zaitsev, D. Fuchs, and H. von Löhneysen. Excess conductivity and Berezinskii–Kosterlitz–Thouless transition in superconducting FeSe thin films. *Journal of Physics: Condensed Matter*, 26(45):455701, 2014.

[24] Weiwei Zhao, Qingyan Wang, Minhao Liu, Wenhao Zhang, Yilin Wang, Mu Chen, Yang Guo, Ke He, Xi Chen, Yayu Wang, Jian Wang, Xincheng Xie, Qian Niu, Lili Wang, Xucun Ma, Jainendra K. Jain, M. H. W. Chan, and Qi-Kun Xue. Evidence for Berezinskii–Kosterlitz–Thouless transition in atomically flat two-dimensional Pb superconducting films. *Solid State Communications*, 165:59–63, jul 2013.

[25] Ya. V. Fominov, M. Houzet, and L. I. Glazman. Surface impedance of superconductors with weak magnetic impurities. *Physical Review B*, 84(22):224517, dec 2011.

[26] Olivier Crauste, Claire A. Marrache-Kikuchi, Laurent Bergé, Sophie Collin, Youri Dolgorouky, Stefanos Marnieros, Claudia Nones, and Louis Dumoulin. Tunable Superconducting Properties of a-NbSi Thin Films and Application to Detection in Astrophysics. *Journal of Low Temperature Physics*, 163(1):60–66, apr 2011.

[27] Nicolas Bourlet et al. In preparation. 2018.

[28] Jiansong Gao. *The Physics of Superconducting Microwave Resonators*. Phd, California Institute of Technology, 2008.

[29] D. P. Pappas, M. R. Vissers, D. S. Wisbey, J. S. Kline, and J. Gao. Two Level System Loss in Superconducting Microwave Resonators. *IEEE Transactions on Applied Superconductivity*, 21(3):871–874, jun 2011.

[30] S. E. de Graaf, L. Faoro, J. Burnett, A. A. Adamyan, A. Ya Tzalenchuk, S. E. Kubatkin, T. Lindström, and A. V. Danilov. Suppression of low-frequency charge noise in superconducting resonators by surface spin desorption. *Nature Communications*, 9(1):1143, mar 2018.

[31] C. M. Quintana, Yu Chen, D. Sank, A. G. Petukhov, T. C. White, Dvir Kafri, B. Chiaro, A. Megrant, R. Barends, B. Campbell, Z. Chen, A. Dunsworth, A. G. Fowler, R. Graff, E. Jeffrey, J. Kelly, E. Lucero, J. Y. Mutus, M. Neeley, C. Neill, P. J. J. O'Malley, P. Roushan, A. Shabani, V. N. Smelyanskiy, A. Vainsencher, J. Wenner, H. Neven, and John M. Martinis. Observation of Classical-Quantum Crossover of $1/f$ Flux Noise and Its Paramagnetic Temperature Dependence. *Physical Review Letters*, 118(5):57702, jan 2017.

[32] Lara Faoro and Lev B. Ioffe. Interacting tunneling model for two-level systems in amorphous materials and its predictions for their dephasing and noise in superconducting microresonators. *Physical Review B*, 91(1):14201, jan 2015.

[33] S. E. de Graaf, A. A. Adamyan, T. Lindström, D. Erts, S. E. Kubatkin, A. Ya. Tzalenchuk, and A. V. Danilov. Direct Identification of Dilute Surface Spins on Al_2O_3: Origin of Flux Noise in Quantum Circuits. *Physical Review Letters*, 118(5):57703, jan 2017.

[34] Tero T. Heikkilä. *The Physics of Nanoelectronics: Transport and Fluctuation Phenomena at Low Temperatures*. Oxford Master Series in Physics. Oxford University Press, Oxford, 2013.

[35] Zhenhua Qiao, Yanxia Xing, and Jian Wang. Universal conductance fluctuation of mesoscopic systems in the metal-insulator crossover regime. *Physical Review B*, 81(8):85114, feb 2010.

[36] E. F. C. Driessen, P. C. J. J. Coumou, R. R. Tromp, P. J. de Visser, and T. M. Klapwijk. Strongly Disordered TiN and NbTiN *s*-Wave Superconductors Probed by Microwave Electrodynamics. *Physical Review Letters*, 109(10):107003, sep 2012.

[37] Martin V. Gustafsson, Arsalan Pourkabirian, Göran Johansson, John Clarke, and Per Delsing. Thermal properties of charge noise sources. *Physical Review B*, 88(24):245410, dec 2013.

[38] A. B. Zorin, F.-J. Ahlers, J. Niemeyer, T. Weimann, H. Wolf, V. A. Krupenin, and S. V. Lotkhov. Background charge noise in metallic single-electron tunneling devices. *Physical Review B*, 53(20):13682–13687, may 1996.

[39] D Vion, A Aassime, A Cottet, P Joyez, H Pothier, C Urbina, D Esteve, and MH Devoret. Manipulating the quantum state of an electrical circuit. *SCIENCE*, 296(5569):886–889, may 2002.

[40] G. Ithier, E. Collin, P. Joyez, P. J. Meeson, D. Vion, D. Esteve, F. Chiarello, A. Shnirman, Y. Makhlin, J. Schriefl, and G. Schön. Decoherence in a superconducting quantum bit circuit. *Physical Review B*, 72(13):134519, oct 2005.

[41] A. Halbritter, L. Borda, and A. Zawadowski. Slow two-level systems in point contacts. *Advances in Physics*, 53(8):939–1010, dec 2004.

[42] Ming-Long Fan, Shao-Yu Yang, Vita Pi-Ho Hu, Yin-Nien Chen, Pin Su, and Ching-Te Chuang. Single-trap-induced random telegraph noise for FinFET, Si/Ge Nanowire FET, Tunnel FET, SRAM and logic circuits. *Microelectronics Reliability*, 54(4):698–711, apr 2014.

[43] Andrei D. Zaikin, Dmitrii S. Golubev, Anne van Otterlo, and Gergely T. Zimányi. Quantum Phase Slips and Transport in Ultrathin Superconducting Wires. *Physical Review Letters*, 78(8):1552–1555, feb 1997.

[44] R. W. Simmonds, K. M. Lang, D. A. Hite, S. Nam, D. P. Pappas, and John M. Martinis. Decoherence in Josephson Phase Qubits from Junction Resonators. *Physical Review Letters*, 93(7):77003, aug 2004.

[45] Lukas Grünhaupt, Nataliya Maleeva, Sebastian T. Skacel, Martino Calvo, Florence Levy-Bertrand, Alexey V. Ustinov, Hannes Rotzinger, Alessandro Monfardini, Gianluigi Catelani, and Ioan M. Pop. Loss Mechanisms and Quasiparticle Dynamics in Superconducting Microwave Resonators Made of Thin-Film Granular Aluminum. *Physical Review Letters*, 121(11):117001, sep 2018.

[46] B. Sacépé, C. Chapelier, T. I. Baturina, V. M. Vinokur, M. R. Baklanov, and M. Sanquer. Disorder-Induced Inhomogeneities of the Superconducting State Close to the Superconductor-Insulator Transition. *Physical Review Letters*, 101(15):157006, oct 2008.

[47] M. V. Feigel'man and L. B. Ioffe. Microwave Properties of Superconductors Close to the Superconductor-Insulator Transition. *Physical Review Letters*, 120(3):37004, jan 2018.

[48] Jens Koch, Terri M. Yu, Jay Gambetta, A. A. Houck, D. I. Schuster, J. Majer, Alexandre Blais, M. H. Devoret, S. M. Girvin, and R. J. Schoelkopf. Charge-insensitive qubit design derived from the Cooper pair box. *Physical Review A*, 76(4):42319, oct 2007.

[49] J. A. Schreier, A. A. Houck, Jens Koch, D. I. Schuster, B. R. Johnson, J. M. Chow, J. M. Gambetta, J. Majer, L. Frunzio, M. H. Devoret, S. M. Girvin, and R. J. Schoelkopf. Suppressing charge noise decoherence in superconducting charge qubits. *Physical Review B*, 77(18):180502, may 2008.

[50] A. Kremen, H. Khan, Y. L. Loh, T. I. Baturina, N. Trivedi, A. Frydman, and B. Kalisky. Imaging quantum fluctuations near criticality. *Nature Physics*, page 1, aug 2018.

Chapter 2

Material characterisation

To implement the QPS box presented in section 1.3.4, we need need a disordered superconducting thin film with a large sheet kinetic inductance and low microwave losses. We consider two different superconductors: Boron-Doped Diamond (BDD) and Titanium Nitride (TiN). We investigated their characteristics using DC and microwave measurements.

We first looked into superconducting thin films made of BDD. We found that the microwave losses in those thin films where so large that they render these films not suitable for our experiments.

We then switched to Titanium Nitride (TiN) thin films for which high quality factor microwave resonators had already been reported [94, 95]. We developed in-house deposition of TiN thin films, and the results obtained on those films are compatible with our requirements.

The characterisation of BDD and TiN thin films is presented in this chapter.

2.1 Boron Doped Diamond

2.1.1 Introduction

Diamond has been the focus of many interests throughout the years because of its remarkable characteristics. It possesses exceptional hardness due to its diamond cubic structure with each carbon atom forming 4 covalent bonds, it is a high breakdown field insulator with a wide 5.47 eV band gap, it is chemically inert under normal condition making it biocompatible and it is of course highly valued in jewelry. However, natural diamond price is high, and variations of characteristics (linked to the variation of natural dopants concentration) render its systematic use quite challenging. Artificial synthesis of diamond by High Pressure High Temperature (HPHT) techniques in the 50s led to a broadening of its use in both research and industry [96]. This technique reproduces the high pressure (P>7 GPa) and the high temperature (T>1400 °C) found in the birth place of natural diamond, deep within the earth crust. While this method transforms graphite into diamonds, their characteristics are poorly controlled, especially concerning impurity concentrations [97]. Furthermore, HPHT growth of diamond is incompatible with thin films production.

The development of Chemical Vapor Deposition (CVD) diamond in the 80s enabled the production of controlled purity diamond thin films. The CVD growth of diamond is performed at high temperature (≈850 °C) in a hydrocarbon-hydrogen (usually methane-hydrogen) low pressure (≈10 kPa) plasma. Nowadays, CVD growth of diamond with controlled doping is easily performed, and using a single-crystal diamond as the substrate leads to the growth of a single-crystal epitaxial diamond thin film. Several dopant can be added in the resulting material, and one dopant is of

particular interest here: boron.

Boron-doped diamond is a p-type semiconductor [98, 99] and was theoretically predicted in 2003 [100] to be a superconductor when doped at boron concentration above its Metal to Insulator Transition (MIT) value ($n_B^{\mathrm{MIT}} \approx 4.10^{20}\,\mathrm{cm}^{-3}$[101]). Experimental confirmation came in 2004 [102] in a boron doped polycrystalline HPHT diamond ($n_B \approx 10^{21}\,\mathrm{cm}^{-3}$). It was also confirmed that BDD prepared with different techniques, single-crystalline or polycrystalline, was also superconducting [103, 104, 105, 106, 107] above the MIT boron concentration. A maximum superconducting temperature T_C of around 10 K has been reached [108, 97], well below predictions of up to 60 K [109, 110]. This type II superconductor [107] is intrinsically disordered, as the boron atoms randomly replace the carbon atoms and randomly occupy the interstitial sites in the diamond lattice. At low boron concentration, the resistivity increases and the fluctuations of disorder are enhanced. Given that slightly doped BDD thin films (thickness ≈ 50nm, $n_B \approx 10^{21}\mathrm{cm}^{-3}$) exhibit a large sheet resistance in the normal state ($R_N^{\square} > 100\Omega$), their sheet kinetic inductance $L_K^{\square}$ should also be large in the superconducting state. This material could match our requirements, and the fact that it is crystalline and extremely stable in normal condition lead us to think that microscopic TLS could be fewer and less problematic in this material.

In this section, we investigate the microwave properties of CVD-grown single-crystal BDD thin films deposited at Institut Néel, in Grenoble [111, 97]. A 60 nm thick layer of CVD BDD with a boron concentration n_B of around $2.10^{21}\,\mathrm{cm}^{-3}$ was grown on top of several 4x4x0.5 mm HPHT diamond substrates. This boron concentration places our samples in the metallic phase, but close to the MIT of BDD, and yields an highly disordered conductor. While their DC characteristics have already been investigated [97, 111], their Radio-Frequency (RF) properties have not been fully characterised. In the aim to fill this gap, we performed several DC and RF measurements down to 300 mK on 4 BDD thin films, referred below as sample 1 to 4. Those samples were fabricated following the same process, with slightly different n_B. Only sample 3 and 4 were used for the measurements described in sections 2.1.3.2 and 2.1.3.3 (3D cavity and broadband impedance measurements), while only samples 1 and 2 were used for the CPW resonators experiments (section 2.1.3.3).

2.1.2 DC characteristics

2.1.2.1 Sheet resistance versus temperature

The standard theory of superconductivity –the BCS theory [112], see section 2.1 in part I– predicts that when the material is cooled below its transition temperature T_C, its resistivity drops sharply to zero, due to the opening of a gap in the density of states. Hence, we measured the temperature dependence of the sheet resistance of BDD thin-film samples down to 300 mK to find their superconducting transition temperature T_C. In all the samples, the sheet resistance falls down to zero under a temperature ranging between 1 K and 1.7 K. Four-probe measurements of the sheet resistance of samples 3 and 4 are presented in figure 2.1.

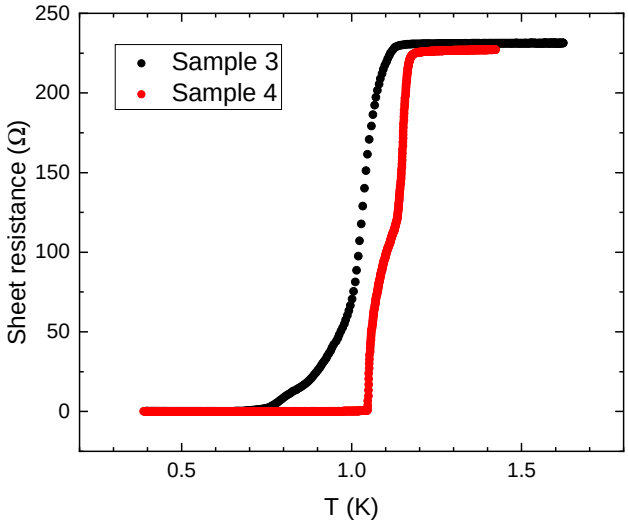

Figure 2.1. Variations of the sheet resistance of samples 3 and 4 with temperature. Four-probe measurements made using an SR830 lock-in amplifier at 78 Hz in the sample holder described in section 2.1.3.3.

The superconducting transition, which we define as the temperature where the sheet resistance equals half of its maximum value just above the transition, occurs around 1 K and 1.2 K for sample 3 and 4 respectively. The normal state sheet resistance $R_N^{\square}$ above the transition is equal to 231 and 227 Ω for films 3 and 4 respectively. While the transitions are significantly broadened, the sheet resistance does reach zero in both films, which is also true for the two other samples not presented here. Despite this non-ideal behavior, we still use the BCS theory to estimate the sheet kinetic inductance of those films from the measured values of T_C and $R_N^{\square}$:

$$L_K^{\square} = \frac{\hbar R_N^{\square}}{\pi \Delta_0} \tag{2.1}$$

where $\Delta_0 = 1.764 k_B T_C$. Using this formula, we predict $L_K^{\square}$ to be around 310 pH and 277 pH for samples 3 and 4 respectively.

Sample	T_C	$R_N^{\square}$ (Ω)	Thickness (nm)	ρ_N ($\mu\Omega$.cm)	$L_K^{\square}$ (pH)	l_e(nm)	n_B (cm^{-3})
3	1.03	231	60	1386	310	1.30	2.10^{21}
4	1.13	227	60	1362	277	1.32	2.10^{21}

Table 2.1. Summary of the electrical and superconducting characteristics of samples 3 and 4.

Those T_C will allow us to use the 300mK cryostat used for the DC measurement presented here for further investigation into the RF behaviour of those films. It might even allow the measurement of microwave devices made of those BDD films at 300mK. Furthermore, the high value for the estimated sheet kinetic inductance suits our needs.

2.1.2.2 Two step superconducting transition in sample 4

We will now discuss a bit further on the particular dependence of sample 4 sheet resistance with temperature. Broad superconducting transition0s have already been observed in other works concerning BDD [113, 114, 115] and have been explained by the non-homogeneous characteristics of this material. Indeed, we know that the superconducting gap can strongly fluctuate, even within single-crystal grains [114, 116, 117], and lead to non-homogeneous superconducting transition.

This non-homogeneity leads to the formation of isolated superconducting islands around T_C, that progressively coalesce at lower temperature to enable the percolation of the superconducting state throughout the sample. We believe this percolation picture, similar to the superconducting BKT transition [45, 44], can describe the broad transition of sample 3 as well as the two-step superconducting transition observed in sample 4:

- At T_C, superconducting islands start to form within the thin film, without any global superconducting phase coherence. The islands are linked through the non-superconducting metallic BDD. This initially decreases the sheet resistance of the sample.
- When the temperature is decreased, the islands grow and start to interact. Percolation is starting to take place and connected islands share the same superconducting phase.
- At low temperature, islands coalesce and a global superconducting state sets in the whole sample.

In a large ensemble of islands with different T_C, this percolation picture naturally results in a broadening of the superconducting transition, as observed in sample 3. Similarly, two sets of islands with different critical temperatures would yield a two-step superconducting transition, as observed in sample 4. We will see in section 2.1.3.3 that this percolating picture can also explain some of our other results.

2.1.3 RF measurements

To probe the RF behaviour of our samples at different frequencies, we use resonant and non-resonant measurements. In the resonant technique, we used either planar CPW or 3D cavity resonators. The BDD films were placed in the microwave field of the resonant cavity. In the non-resonant technique, the BDD samples were embedded in a section of a CPW transmission line. We measured the transmission of this line, and using proper calibration, we extracted the value of the sample impedance over a large range of frequencies.

2.1.3.1 CPW resonator measurements

We fabricated several $\lambda/2$ CPW resonators on sample 1 which is similar to sample 3 and 4 presented in the previous section. We used only sample 1 here in order to keep the other samples unprocessed. The resonance frequency of such CPW resonators gives direct access to the material's kinetic inductance and the quality factor provides information on the losses within the material. We patterned transmission lines and resonators on the BDD thin film using an aluminum mask and RIE techniques, and the resulting devices are presented in figure 2.2.

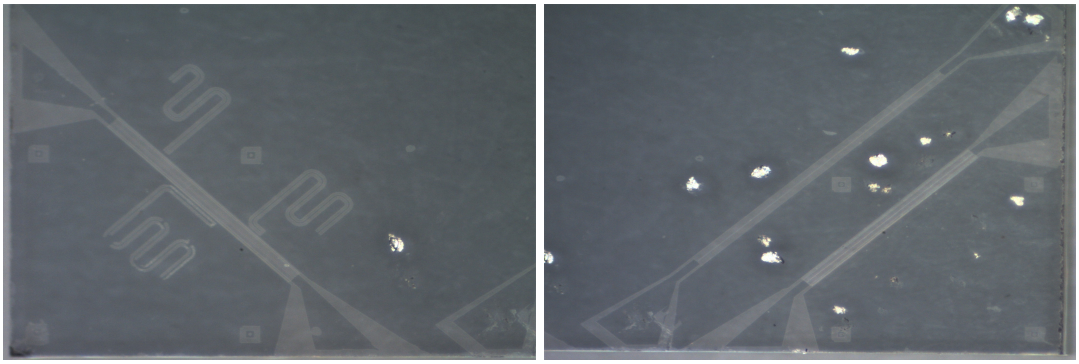

Figure 2.2. Devices realised on sample 1. **a:** Three CPW hanger resonators coupled to a 50Ω transmission line. **b:**Two impedance mismatch resonator each embedded in a 50Ω transmission line.

In the device of figure 2.2a, three CPW hanger resonators are coupled to a 50Ω transmission line

and short it to the ground at their resonance frequency. This should manifest as several dips in the measured S_{21} of the transmission line. The resonator coupling factors Q_c range between 16k and 500k. We measured the transmission of this device at 300 mK using a standard microwave setup (i.e. with a VNA). However, we did not observe any resonance for this device. This indicates that either the fabrication of the device failed or that the internal quality factors Q_{int} of the resonators were far smaller than the values of Q_c.

To clarify this issue, we realised two other devices, implementing resonators with lower Q_c. Those devices are presented in figure 2.2b, where we embedded $\lambda/2$ CPW impedance mismatch resonators within $50\,\Omega$ transmission lines. Such resonators achieve very low Q_c ($\approx$10) and are measured in transmission, i.e. they let the signal through only at their resonance frequencies. We measured those devices in the same conditions as before, and this time we found a resonance peak presented in figure 2.3.

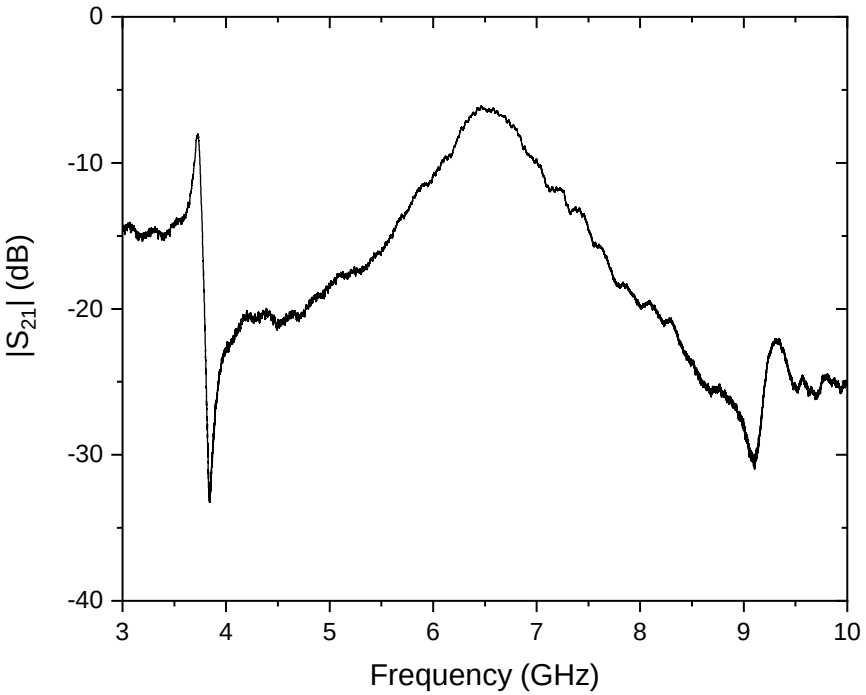

Figure 2.3. Transmission measurement at 300 mK of one of the devices presented in figure 2.2b. The resonance of interest here is the central peak around 6.5 GHz. The sharp resonances around 4 and 9 GHz were identified as spurious box modes.

By fitting the resonance shape, we extracted the value of the internal quality factor Q_{int} of this resonator, and we found it to be around 10. This value is extremely low, indicating the presence of huge microwave losses inside our BDD thin films. Although this clearly renders those BDD thin

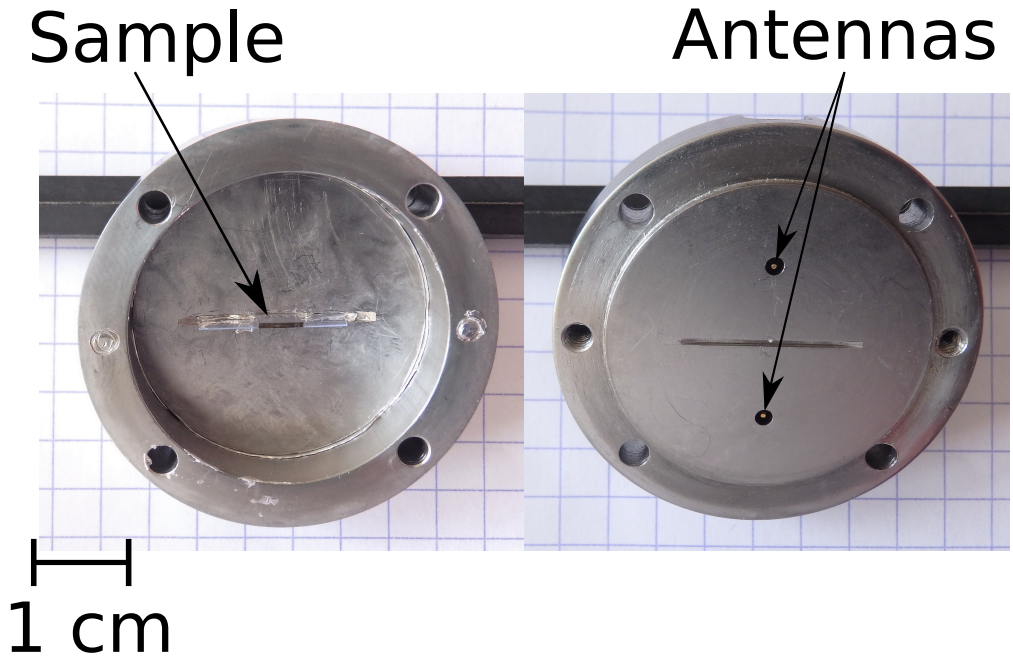

Figure 2.4. Niobium 3D cavity used in this experiment. The samples are glued with PMMA to a silicate slab standing in the RF field (left picture). The lid of the cavity (right) contains two RF antennas used to measure the transmission of the cavity. An indium seal is used when assembling both parts to ensure lossless contact and avoid radiation leakage.

films unsuitable for our experiments, we decided to further characterise those losses with two other techniques.

2.1.3.2 Niobium resonant cavity measurements

We used another resonant technique to measure the microwave losses in unprocessed BDD samples 3 and 4. This technique is based on a cylindrical 3D cavity resonator made of niobium, with the sample under test placed in the center of the cavity as shown in figure 2.4. By comparing the resonance overall quality factor Q with and without the sample inside, we get access to the losses induced by the sample. However this technique as two drawbacks:

- it relies on a indium seal to properly close the cavity lid, which has to be manually made anew each time the cavity is opened. The internal quality factor Q_{int} of the resonance is also highly dependent on this seal, and thus suffers from the variability of the seal's quality.

- The positions of the antennas used to measure the transmission S_{21} of the cavity (and thus its resonance shape) affect the cavity coupling, Q_c. While these antennas are not supposed to move when opening the cavity, they are not perfectly fixed (in fact, they are SMA connectors held by screws). Simulations show that even a small change in their position leads to a sizeable change in Q_c.

This measurement is thus subject to potentially large variations and is only qualitative for small changes in the total Q, i.e. samples with small losses. However, it is truly quantitative for samples with huge losses that dominate the cavity damping. Nevertheless, we took great care to avoid any displacement of the antennas and to achieve a reproducible indium seal.

As presented in figure 2.5, the introduction of a BDD sample inside the 3D cavity has a profound impact on its resonance properties at 300 mK. While the empty cavity has an overall quality factor of the order of 100k, the same cavity loaded with our samples drops to $Q \approx 100$. In some cases, we could not observe the cavity resonance at all.

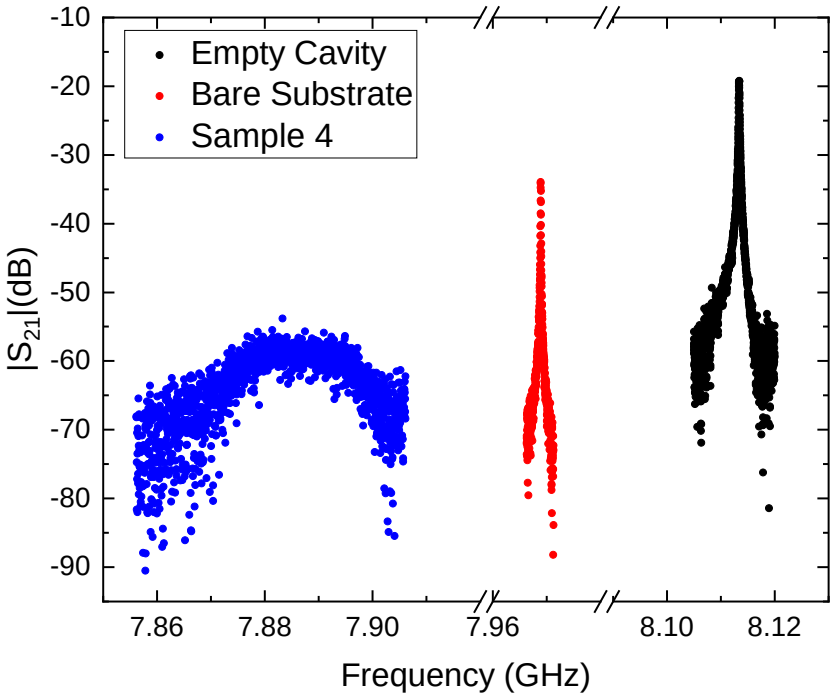

Figure 2.5. Transmission measurement of the Nb cavity at 300 mK in different conditions: empty (black), a bare 4x4x0.5 mm HPHT diamond substrate (red) and sample 4, ie. 60 nm of BDD on top of the HPHT diamond substrate (blue).

On the other hand, we measured the HPHT diamond substrate prior to BDD deposition, and we found that it only induces negligeable losses, contrary to BDD samples. Furthermore, we tested two pure CVD diamond films deposited on HPHT substrate without boron doping. Those films are 50 nm and 1 μm thick, and their results are presented in figure 2.6. While we can see the impact of the CVD diamond presence on the resonance frequency, the resonance itself is still clearly observable with a large quality factor. This confirms that the huge losses found are caused by the presence of the conductive BDD thin films themselves.

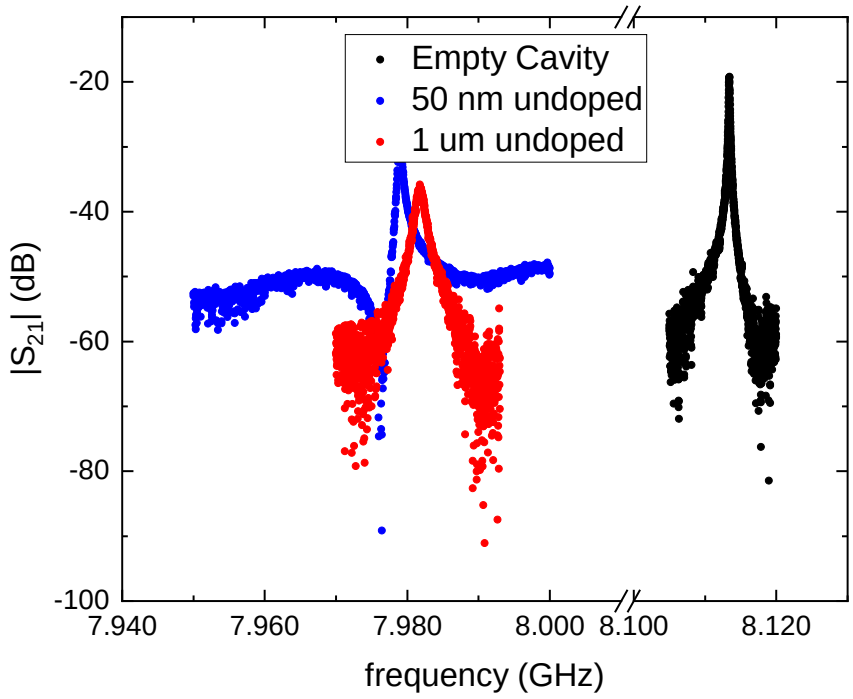

Figure 2.6. Transmission measurement of the Nb cavity at 300 mK in different conditions: empty (black), 50 nm of undoped CVD diamond (blue) and 1 μm of undoped CVD diamond (red). The CVD diamond is on top of 4x4x0.5 mm HTHP diamond substrate.

Together with the CPW resonator experiment previously discussed, this result clearly indicates that huge microwave losses occur in our BDD samples. That makes those BDD thin films not suitable for our project. However, those two experiments were restricted to a set of given frequencies. We found interesting to characterise these BDD samples over a large frequency range.

2.1.3.3 Broadband Impedance Measurement

We measured the impedance of our BDD samples over a large frequency range (100 Hz to 3 GHz) using an impedance mismatch measurement setup [118].

Impedance mismatch measurement concept

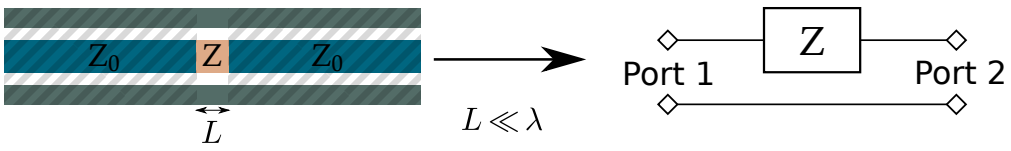

Figure 2.7. Adding a impedance Z in series in a CPW transmission line with characteristic impedance Z_0 can be, if the length of the impedance is lower than the wavelength λ, treated as a two-port network of an impedance Z.

A short sample of impedance Z is embedded in a RF transmission line of characteristic impedance Z_0 (commonly 50 Ω). The impedance mismatch between the sample and the transmission line leads to the reflection of the incident microwave, which reduces the transmitted power. If we use

network analysis, we can describe the sample as a two-port network (see figure 2.7) and write its scattering matrix S as [119]:

$$S = \begin{pmatrix} \frac{Z}{2Z_0+Z} & \frac{2Z_0}{2Z_0+Z} \\ \frac{2Z_0}{2Z_0+Z} & \frac{Z}{2Z_0+Z} \end{pmatrix} \tag{2.2}$$

By measuring the sample's scattering parameters, we can deduce its impedance. For example, from S_{21} we obtain:

$$Z = 2Z_0 \frac{1-S_{21}}{S_{21}} \tag{2.3}$$

One difficulty that arises with this kind of measurements is the impossibility to directly measure the sample's scattering parameters, especially when using complex RF setup like those present in our cryostats. Indeed, each and every single RF element in the setup (RF cables, connectors, attenuators, amplifiers, ...) adds its own imperfections to the final measurement, such as spurious reflection, attenuation or even cross-talk between cables.

Setup calibration

A proper calibration of the setup allows us to remove those spurious effects and obtain the sample's S parameters [119, 118]. To do so, we need to obtain the scattering matrix of our setup with the sample replaced by proper calibration standards. This will enable us to quantify its deviation from the scattering matrix of a perfect RF transmission line, i.e. the Pauli matrix σ_x. This procedure is similar to the standard procedure used for a VNA calibration, albeit with far from perfect cables and standard devices.

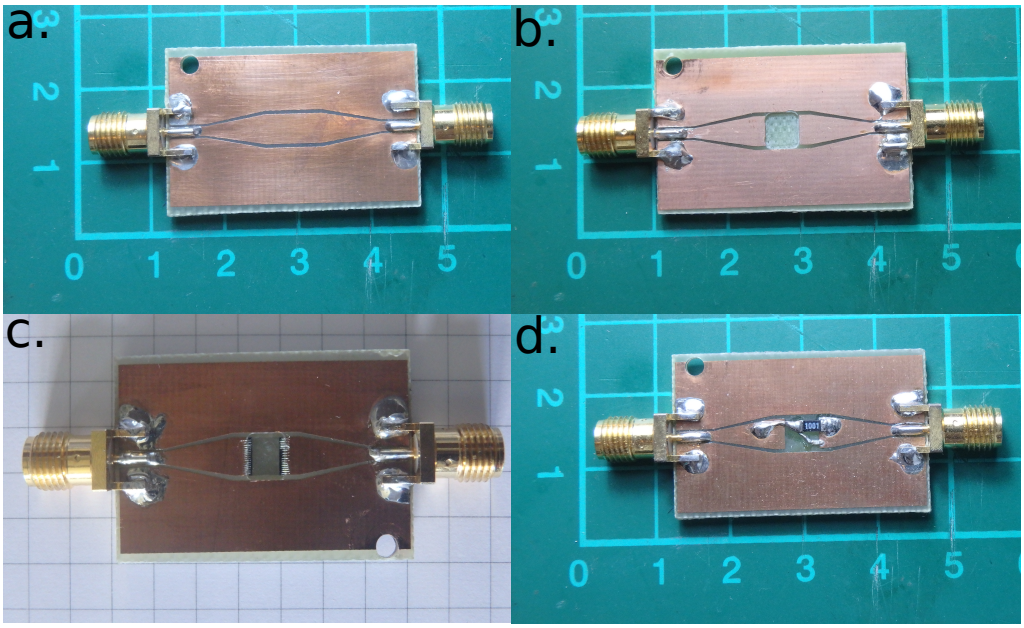

Figure 2.8. The different calibration devices and the sample holder used in our setup. **a**: 50Ω transmission line on copper PCB, acting as a THROUGH standard. **b:** the same transmission line as the one in a. but with the transmission line cut by a 4x4 mm recess, made to fit our 4x4 mm samples. Without any sample, it acts as a REFLECT standard. **c:** the actual sample holder, same as c., with a BDD sample in its recess. The sample is glued to the PCB and bonded to the copper transmission line with aluminium wire. **d:** Same PCB as the sample holder, but with an inductance and a resistance in parallel soldered instead of a sample. This device was used to confirm the model presented in (2.7).

Our devices presented in figure 2.8a and b implement the THROUGH (perfect transmission) and REFLECT (perfect reflection) standards, respectively. The impedance of these standards is:

$$Z_{\text{through}} = 0 \quad Z_{\text{reflect}} = \infty$$

Those devices, as well as the sample holder (figure 2.8c), where sandwiched between two machined RF absorbing urethane pads, in order to eliminate spurious resonances inside the cryostat. Because our setup (see figure 2.9) includes RF amplifiers, we don't have access to the S_{22} and S_{12} parameters, we thus measured only the S_{11} and S_{21} parameters of our setup with each standard at 300 mK. The calibrated S_{11} and S_{21} parameters of a sample write as:

$$S_{11}^{\text{cal}} = \frac{S_{11}^{\text{meas}} - S_{11}^{\text{through}}}{S_{11}^{\text{reflect}} - S_{11}^{\text{through}}} \quad S_{21}^{\text{cal}} = \frac{S_{21}^{\text{meas}} - S_{21}^{\text{reflect}}}{S_{21}^{\text{through}} - S_{21}^{\text{reflect}}} \tag{2.4}$$

The measured value for S_{11}^{through} and S_{21}^{reflect} were negligible with respect to the other calibration measurements as well as the samples measurements S^{meas}. The value for the calibrated S parameters then simplify to:

$$S_{11}^{\text{cal}} = \frac{S_{11}^{\text{meas}}}{S_{11}^{\text{reflect}}} \quad S_{21}^{\text{cal}} = \frac{S_{21}^{\text{meas}}}{S_{21}^{\text{through}}} \tag{2.5}$$

Measurement setup

In our experiment, we used a VNA and a UHF lock-in amplifier (100 Hz to 600 MHz) from Zurich Instrument to measure the transmission parameter S_{21} of our BDD thin films from 100 Hz to several GHz. Prior to each run, we measured the THROUGH standard device at 300 mK to calibrate the measurement as presented above. Despite the fact that no cables were disconnected between the cooldown of the standard and the sample, the calibration still suffers from slight imperfections. The RF setup used is presented in figure 2.9.

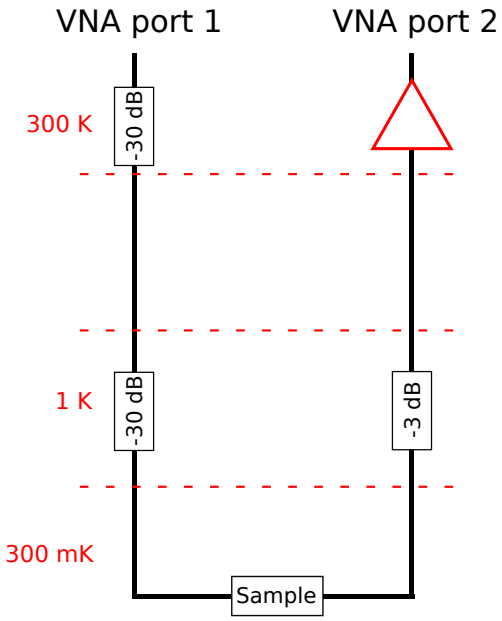

Figure 2.9. Cryogenic RF setup used for broadband impedance measurements. The sample was placed in a 300 mK cryostat with two RF coaxial lines. The signal input line (Port 1) was strongly attenuated with a 30 dB attenuator both at room temperature and at 1K. The signal output line (Port 2) is amplified by room temperature amplifiers, and a 3dB attenuator was placed just after the sample at 1K to attenuate the thermal noise coming from the input stage of the first amplifier.

Samples were placed in the recess of a PCB similar to the REFLECT calibration device (see figure 2.8c), and connected to the 50Ω copper transmission line with aluminium bonding wires. To facilitate the bonding procedure, and to provide a clear delimitation of the probed area of the sample, Ti-Al pads (4 and 96 nm resp.) were deposited on opposite sides of samples 3 and 4. This reduced the effectively probed BDD samples to 3x4 mm (i.e. 3/4 of a square). The copper transmission lines are connected to the rest of the circuit through SMA launchers.

Results below the superconducting transition temperature

We measured the transmission of our setup at different temperatures from 300 mK to 1.2 K using the lock-in amplifier from 100 Hz to 600 MHz and the VNA from 600 MHz to 3 GHz. The measurements were then concatenated to provide data from 100 Hz to 3 GHz.

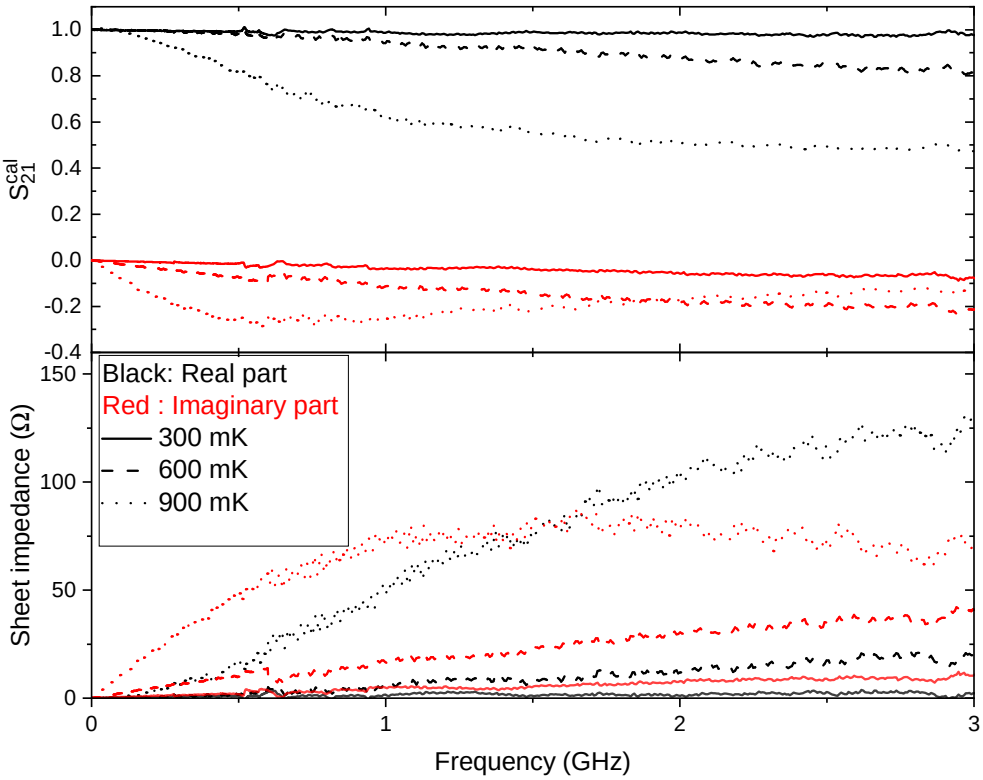

Figure 2.10. Sample 4 RF measurements at different temperatures. **top:** Calibrated transmission measurement of the sample as function of the frequency. **bottom:** Sheet impedances extracted from the transmissions using formula (2.3).

We plot the transmission of sample 4 at different temperatures in figure 2.10, along with the sheet impedance extracted using formula (2.3). Similar results were obtained for sample 3, and are not presented here. The real part of the sheet impedance significantly differs from zero above 500 MHz, down to the lowest temperature probed of 300 mK. This points to the presence of a dissipation in those samples, even at 300 mK, in agreement with the low quality factors measured in section 2.1.3.1 and 2.1.3.2.

The conductivity of a superconducting thin film is as the sum of a real and an imaginary part:

$$\sigma = \sigma_1 + i\sigma_2 \tag{2.6}$$

where σ_1 describes dissipation and σ_2 describes the reactive behaviour of the superconductor (i.e. its kinetic inductance). We model σ as the conductance of a perfect resistor in parallel with a perfect inductor [120]. The corresponding impedance writes:

$$Z_{L/\!/R} = \frac{iL\omega R}{iL\omega + R} = \frac{(L\omega)^2 R}{(L\omega)^2 + R^2} + i\frac{L\omega R^2}{(L\omega)^2 + R^2} \tag{2.7}$$

For a perfectly BCS superconductor thin film (such as aluminium), one would expect:

$$L = \infty \text{ and } R = R_N^{\square} \text{ for } T \geqslant T_C \tag{2.8}$$

$$L = L_K^{\square} \text{ and } R = \infty \text{ for } T = 0 \tag{2.9}$$

Applying this model to the sheet impedance of a sample, R and L are respectively the sheet resistance and the sheet inductance. The fit of this model to sample 4 measurements are presented in figure 2.11 for three temperatures, along with the fit values for R and L at all temperatures.

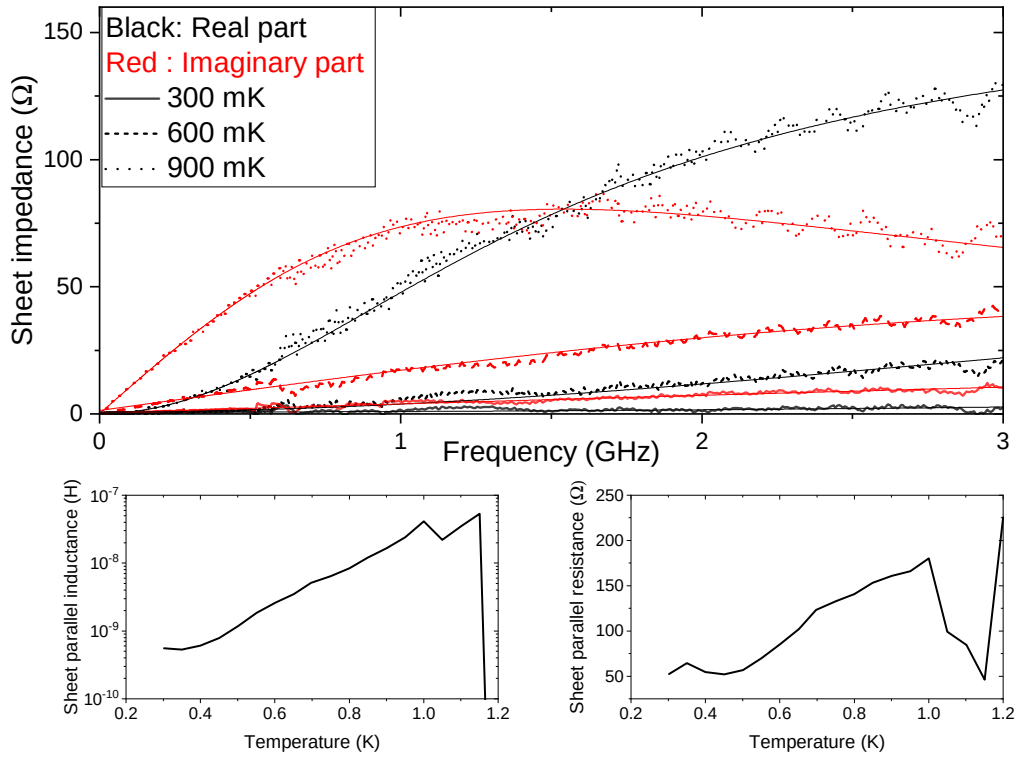

Figure 2.11. Fit of the sheet impedance of sample 4 at different temperature with the model in (2.7) **top:** Same data as in Fig. 9, and plain lines represent the model fit. **bottom:** Extracted values for the fitting parameters R and L between 300 mK and 1.2 K. Above 1K, our model (2.7) is not sufficient to fit the data and additional parameters, discussed in the next paragraph, are needed.

We observe that for the different temperatures shown, the fits reproduce the main variations of the sheet impedance between 100 Hz and 3 GHz. Repeating those fits, we can extract the value of the sheet parallel inductance and the sheet parallel resistance at all temperatures. The sheet parallel inductance decreases when temperature is lowered, with a plateau at about 540 pH at low temperature. This value is 1.95 times the BCS estimate of section 2.1.2. The extracted parallel resistance is not the one expected for a perfectly BCS superconductor. Indeed, whereas we would expect R to diverge toward infinity below T_C, we find it decreases instead, from 200 Ω at 1 K down to about 50 Ω at 300 mK. This value at 300 mK is in agreement with the observation of huge losses in our two previous resonant measurements.

Results close to T_C

Close to the transition temperature ($T \geqslant 1\,K$), our model (2.7) can no longer suitably fit the data and we need to introduce an extra series impedance $Z_{\text{fit}} = Z_{L//R} + Z_{\text{off}}$. This extra impedance can be interpreted as the loss of percolation of the superconducting state in the sample (see section 2.1.2.2). This introduction of Z_{off} has an impact on the expected value for our model at $T \geqslant T_C$ initially presented in (2.8). Indeed, Z_{off} acts as a new fit parameter, and we now have several possibilities, depending on the initial values used for the fits:

$$L = \begin{cases} \infty \Rightarrow R + \text{Re}(Z_{\text{off}}) = R_N^{\square} \\ 0 \Rightarrow \text{Re}(Z_{\text{off}}) = R_N^{\square} \end{cases} \text{for } T \geqslant T_C \tag{2.10}$$

If $L = 0$, R is irrelevant, and thus can take any possible value. This is what we observed for our fits (see figure 2.11) at 1.2K, where L goes to zero and R to a large value. We chose the initial parameters for our fits in order to be in this case for both sample 3 and 4. We have shown above that in the low temperature range this Z_{off} was not needed to fit the measurements and it is indeed found to become very small (see figure 2.12); its residual values can perhaps be attributed to imperfect calibrations. If we look at the value of Z_{off} near T_C, we can observe a noticeable similarity between Re(Z_{off}) (the offset resistance) and the R(T) curve presented in figure 2.1.

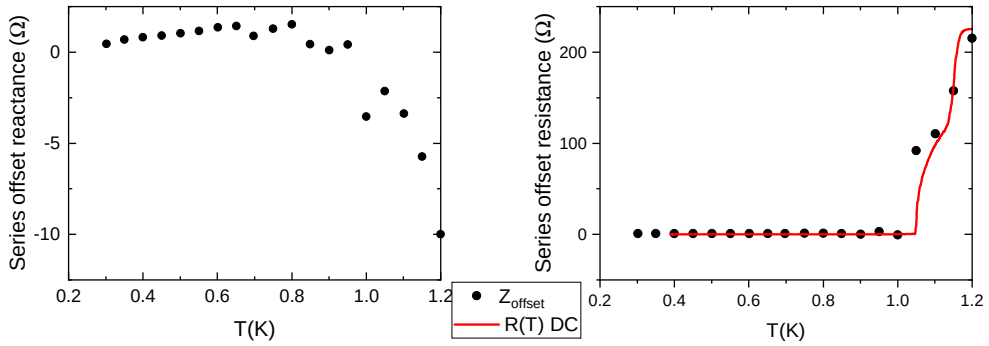

Figure 2.12. Fit offset as a function of temperature for sample 4. The straight red line is the sheet resistance versus temperature measured in section 2.1.2 for the same sample.

The value of Re(Z_{off}) is following quite well the variations with temperature dependence of the measured sheet resistance. The fact that those measurements, one in RF and the other in DC, agree with one another further support the picture presented in section 2.1.2.2:

- At T=300 mK, the superconducting state percolates through the sample. $Z_{\text{off}} = 0$ and we measure an inductive response of the sample through a non zero value of L. The presence of a finite value of R can be interpreted as the fact that some parts of the sample have not undergone the superconducting transition, i.e. that the sample has not coalesced completely.
- At the foot of the transition (around 1.05 K) the percolation path breaks down, thus introducing a resistive part in series to what remains of the superconducting percolating state. This translate in a non-zero value for Z_{off} and a drop in the value of L, because the superconducting path is shorter. We also measure a smaller R parallel to L because of this shorter path.
- When T reaches 1.2 K, every remaining superconducting islands in the samples are gone, and Z_{off} value goes to R_N, the normal sheet resistance measured in section 2.1. The value of L goes to zero, and R becomes meaningless, as explained earlier.

While we focused on sample 4 in this section, the same conclusions were drawn for sample 3. Indeed, we also fitted its impedance with the same model, and the results were qualitatively the same: there is a parallel resistance with non infinite value at 300 mK. The series offset resistance is also similar to the R(T) measured in section 2.1.2 for this sample.

2.1.4 Conclusions on BDD

We have shown that, despite the fact that our BDD thin films are superconducting with a T_C around 1.1 K, they present high losses at microwave frequencies, down to the lowest temperature probed here of 300 mK. Those losses can be modeled by a low resistance parallel to the superconducting kinetic inductance, with finite value even at 300 mK. We hypothetically attribute this resistance to a inhomogeneous coalescence of superconductivity in our sample, suggesting that some parts of the BDD thin films remain in a normal state at 300 mK.

As a final note on BDD, we point out that recent works [121, 122] report the presence of dissipative state within superconducting gap of polycrystalline BDD on Si substrate. Although our single-crystal BDD samples on diamond substrate differ, the presence of such states in our samples could also explain the losses we observed.

Our conclusion here is that our BDD samples are of no use for our project. We must then explore different options regarding high kinetic inductance material. Our interest was drawn to titanium alloys, and more precisely to titanium nitride.

2.2 Titanium nitride thin films

2.2.1 Introduction

Titanium nitride (TiN) is an extremely hard ceramic with a metallic behaviour commonly used as a protective coating for metallic tools such as drill bits, for a decorative purpose or even as a non toxic passivation layer for medical implants. TiN is also known to be a superconductor since 1930 [123] with transition temperature up to 6 K [124] for single crystals. In TiN thin films, the properties (resistivity, T_C,..) are known to be extremely dependent on sample preparation [125, 126, 127, 128]. Those thin films undergo a disorder-driven Superconducting to Insulator Transition (SIT) at sufficiently high disorder [45, 129], effectively creating an insulator, which presents an infinite resistivity at zero temperature, as discussed in section 1.2.

Titanium nitride thin films have been used to realise superconducting devices [94, 130, 131, 132], including CPW resonators with quality factors as high as 10^6 [94]. Closer to the SIT, this material presents a large kinetic inductance, while still maintaining decent quality factors [133].

For our project, those low loss and large kinetic inductance TiN thin films provide an appealing choice worth being investigated. The tunability of their properties (normal state resistivity and T_C) is furthermore quite attractive. Indeed, a wide range of disorder is attainable when changing the deposition parameters (from low resistivity/high T_C to high resistivity/low T_C). We can even increase this disorder by reducing the film thickness, as we will see further in this section.

2.2.1.1 The TiN_x system

The properties of the TiN_x system highly depend on the nitrogen to titanium ratio x. A the nitrogen content in the titanium lattice is increased, TiN_x can be present in different phases [134]:

- an hexagonal close-packed (hcp) Ti phase with inclusion of nitrogen in interstitial sites for $x < 0.5$,
- a body-centered cubic (bcc) Ti_2N phase in a small range around $x = 0.5$
- and a face-centered cubic (fcc) TiN phase for $x > 0.5$.

Each phase has different mechanical, electrical and structural properties. Only the Ti ($T_C \approx 400\,\mathrm{mK}$[135]) and the TiN ($T_C^{\mathrm{bulk}} \approx 6\,\mathrm{K}$ [124]) phases have been found to be superconducting, Ti_2N remaining in a normal state down to 50 mK [135, 136] (see figure 2.13). We have only investigated the TiN phase, i.e. TiN_x material with $x > 0.5$, which we simply write TiN for simplicity.

Within this phase, the superconducting properties are highly related to the nitrogen content, which is controlled by the deposition parameters, as depicted in figure 2.13.

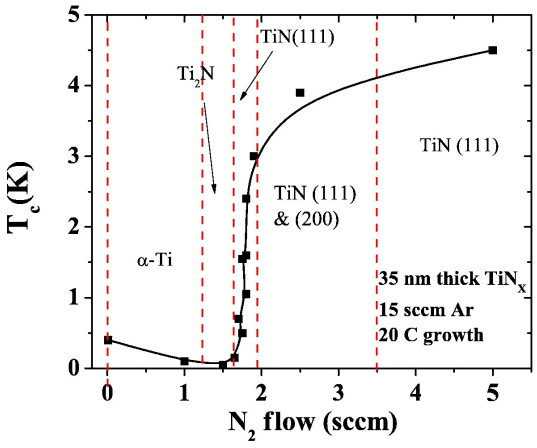

Figure 2.13. Superconducting transition of 35 nm thick TiN_x thin films sputtered at different nitrogen flow, which directly relates to the nitrogen content in the films. The argon is kept at 15 sccm. The dashed red lines represent the phase changes in the TiN_x system. From [136].

We investigated the properties of TiN thin films that we can produce in-house, their reproducibility and their suitability for making low-loss highly inductive circuits.

2.2.1.2 In-house deposition of TiN

Titanium nitride is commonly produced by reactive sputtering of titanium in a nitrogen/argon plasma. The nitrogen present in the plasma is reacting with the sputtered titanium to form TiN, which deposits a TiN thin film on the substrate. We developed titanium nitride deposition in our nanofabrication facility using two different sputtering machines: one with a DC voltage and the other with an RF voltage driven plasma. Whereas the RF machine provides a precise control over the gas mass flow and the total pressure in the chamber, the DC machine only has a precise control over the total pressure. Besides these differences, they also present other differences concerning: the substrate temperature during sputtering, target size, chamber size, etc., but the role of those variables was not investigated.

The DC sputtering machine was initially used to realise our TiN thin films and for the first investigations. Those first films did not fully reached our expectations (e.g. $T_C < 4\,K$), and were poorly reproducible. The RF sputtering machine yielded higher quality (higher T_C) and better reproducible TiN thin films. In this manuscript, all thin films were thus realised using the RF sputtering machine.

2.2.2 DC characteristics of TiN thin films

2.2.2.1 Optimisation of the RF sputtering process

Description

We made about 50 samples, each using different deposition parameters, in order to find a suitable recipe for TiN deposition in our sputtering machine. We measured their room temperature properties (thickness, surface texture, resistivity), as well as their electronic properties (T_C, $R_N^{\square}$)

using a ^{3}He 300mK cryostat. The main independent parameters of this optimisation are:

- the total pressure inside the sputtering chamber during deposition (P_{tot}),
- the nitrogen flow and
- the RF power injected into the plasma.

We used three different values of P_{tot}, 5, 10 and 20 μbar, which is regulated independently of either the nitrogen or argon flow. The argon flow was kept at a constant value of 15 sccm, and the distance between the target and the substrate held at 8 cm. The substrate was not heated during this optimisation, and its temperature during deposition did not increase significantly ($\Delta T < 20$ °C) from ambient temperature (≈20 °C). For these tests, we used 7x7 mm 300 μm thick oxidised silicon substrates. Finally, due to the lack of film thickness monitoring during the sputtering, the deposition time was kept constant at 180 seconds for most of the samples. The thickness of the deposited films was measured using a KLA Tencor Alpha-step IQ profilometer, and the deposition rates were deduced from this measurement. The resulting film thicknesses ranged between 3 and 220 nm. For samples deposited at low power (100 W), and thus at very low deposition rates, we increased the deposition time to obtain thicknesses from 23 to 220 nm.

In each sample, we cut a rectangle of 1.5x7mm and placed it into a DC sample holder in order to measure its sheet resistance temperature dependance down to 300mK. A typical measurement is shown in figure 2.14, which yields $R_N^{\square} = 523\,\Omega$ and $T_C = 2.25\,\mathrm{K}$ for this sample.

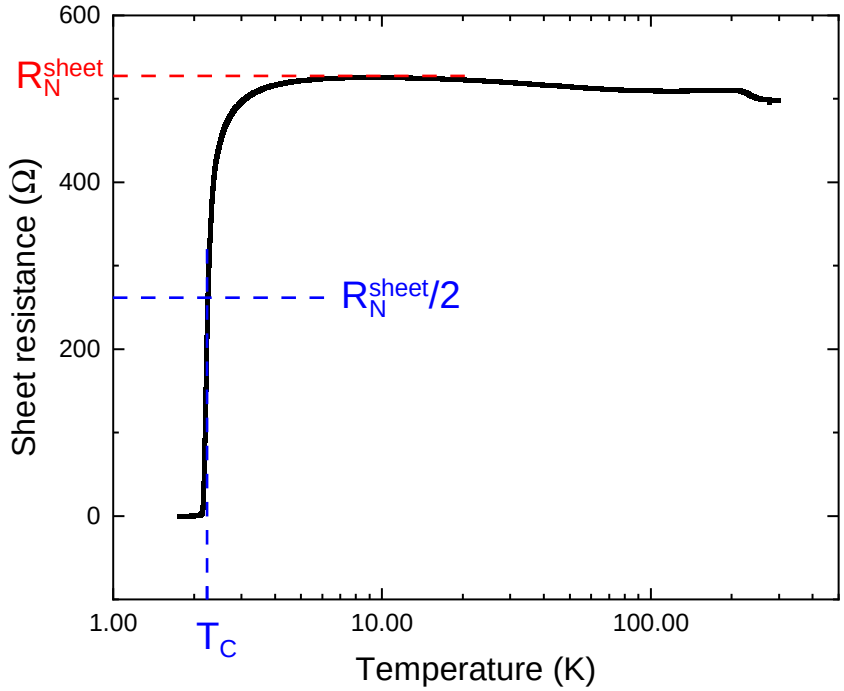

Figure 2.14. Typical sheet resistance versus temperature measurement for a TiN thin film on silicon, starting from room temperature. The initial increase just below RT is due to the substrate loss of conduction. On this sample, $R_N^{\square} = 523\Omega$ and $T_C = 2.25\mathrm{K}$.

Nitrogen flow and P_{tot} dependence

The nitrogen flow, and thus the nitrogen-to-argon ratio in the deposition plasma, controls the amount of nitrogen included in the deposited TiN thin film. As explained in section 2.2.1.1, the nitrogen content of those films affects their properties. We first use nitrogen flow from 1 to 4 sccm, at three different P_{tot} (5, 10 and 20 μbar), while keeping the RF power injected into the plasma set at 500 W. The obtained T_C, normal state sheet resistivity and deposition rates are presented in figure 2.15.

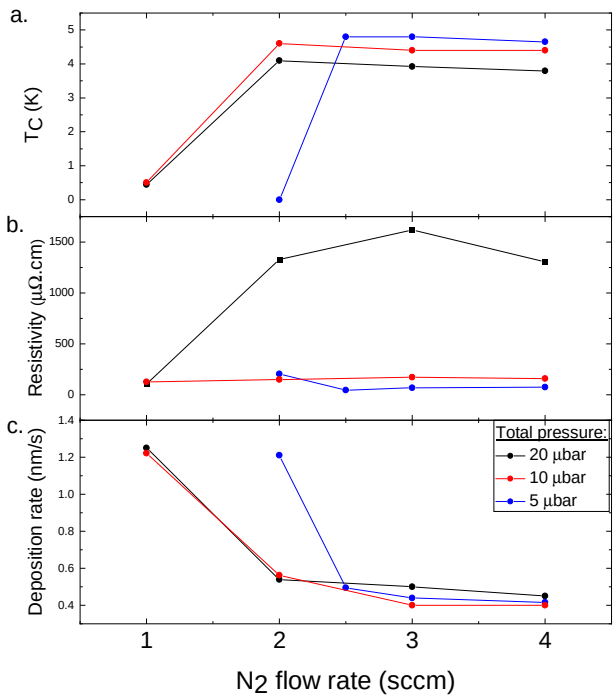

Figure 2.15. Characteristics of deposited TiN thin films under different total pressure versus nitrogen flow. **a:** Superconducting transition temperature; **b:** Resistivity; **c:** Deposition rate.

We find that T_C sharply increases with the nitrogen flow rate up to a threshold value of 2 sccm for $P_{\mathrm{tot}} = 10$ and $20\,\mu$bar (2.5 sccm for $P_{\mathrm{tot}} = 5\,\mu$bar, see figure 2.15). Below this threshold, T_C is around 500 mK (under 300 mK for $P_{\mathrm{tot}} = 5\,\mu$bar at 2 sccm, so out of reach of our 300 mK cryostat;

it is shown here at 0 K). Above the threshold, T_C is roughly stable around 4 K. This variation of the superconducting temperature of our film is compatible with published works [136]. This is the sign that the deposited material phase changes from TiN at large N_2 flow to Ti_2N and/or titanium below the threshold value.

We also find a sharp decrease of the deposition rate of our films up to this threshold (figure 2.15c), and a slower decrease above. This can be explained by the poisoning of the Ti target, i.e. the formation of a nitrided layer on the surface of the target. This layer has a lower sputtering yield than pure metallic titanium, thus reducing the effective deposition rate [134]. These low rates allow us to achieve a fine control over the thickness of the films, and thus of the effective disorder. Deposition rates of around 0.5 nm/s as is obtained here is suitable to deposit down to 10 nm thick thin films in a reproducible way. We will see later that this rate can even be lowered further.

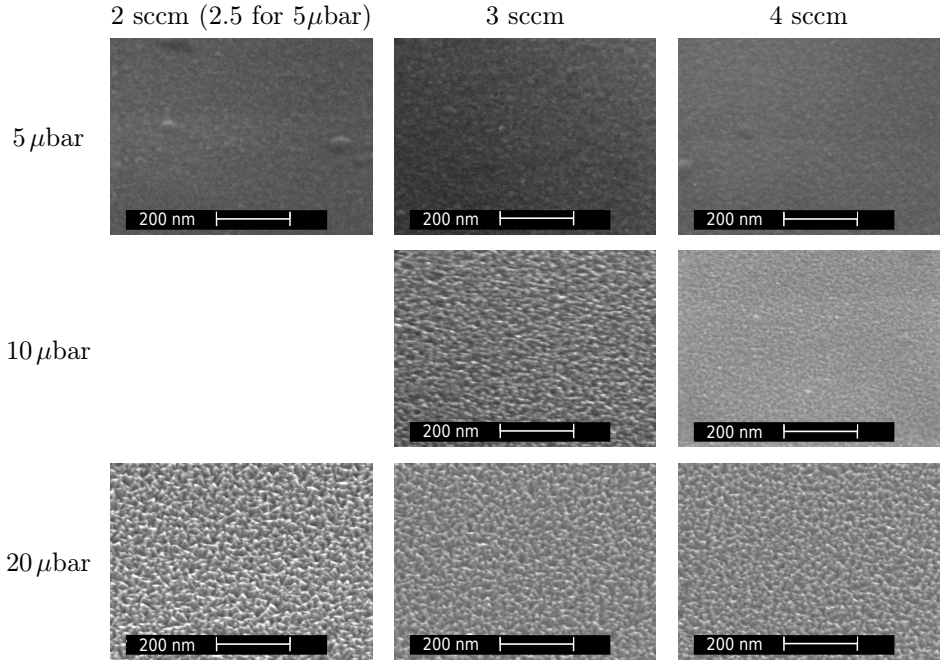

Figure 2.16. SEM images of the TiN film surfaces under a 30° angle for different N_2 flow and P_{tot}. The deposition power was fixed at 500 W.

Most samples made using an N_2 flow rate above 2 sccm (2.5 sccm for $P_{tot} = 5\,\mu$bar) have a T_C above 4K, and some samples made using $P_{tot} = 5\,\mu$bar even have a T_C close to 5K. While those samples have a T_C approaching the bulk value of 6K, they also illustrate the impact of P_{tot} on T_C and the resistivity. As P_{tot} is increased, the superconducting critical temperature decreases and the resistivity increases (at larger N_2 flow). These variations can be linked to the morphology of the film surface (see figure 2.16), which present different degrees of roughness. The higher P_{tot} samples have a more irregular surface and more visible TiN grains than the lower P_{tot} ones. This increased surface roughness leads to an increased resistivity and a decreased T_C at higher P_{tot}.

Sputtering at a nitrogen flow rate of 4 sccm ensures that the deposited material is stoechiometric or slightly over-nitrided TiN, with a regular surface. For the remaining part of this optimisation, we only use a nitrogen flow rate of 4 sccm.

Sputtering power dependence

The last main parameter to vary is the RF power fed to the plasma. We realised a set of samples to probe the RF power dependency of the thin films characteristics, while keeping the nitrogen flow rate at 4 sccm. Due to the excessive roughness obtained at $P_{tot} = 20\,\mu$bar, this value is omitted in

this section.

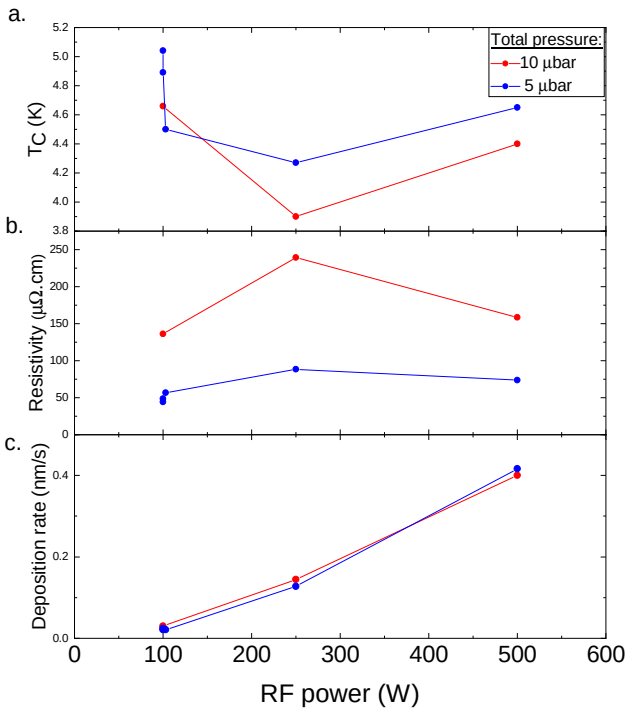

Figure 2.17. Characteristics of deposited TiN thin films under different total pressure versus RF power used during the deposition. **a:** Superconducting temperature; **b:** Resistivity; **c:** Deposition rate.

While having a low impact on resistivity and T_C, the RF plasma power greatly modifies the deposition rates. Indeed, those rates go from around 0.4 nm/s at 500 W to approximately 0.025

nm/s at 100 W, allowing us to deposit extremely thin TiN films. The increase of resistivity (and the decrease in T_C) at the intermediate power of 250 W is explained by the thickness difference of these films. Indeed, whereas the thickness for all the other samples is around 80 nm, the two samples made at 250 W have a thickness of the order of 20 nm (26 nm at 10 μbar and 23 nm at 5 μbar). Those values are of the order of the ≈15 nm elastic mean free path of the electrons in those layers, which explains this resistivity increase.

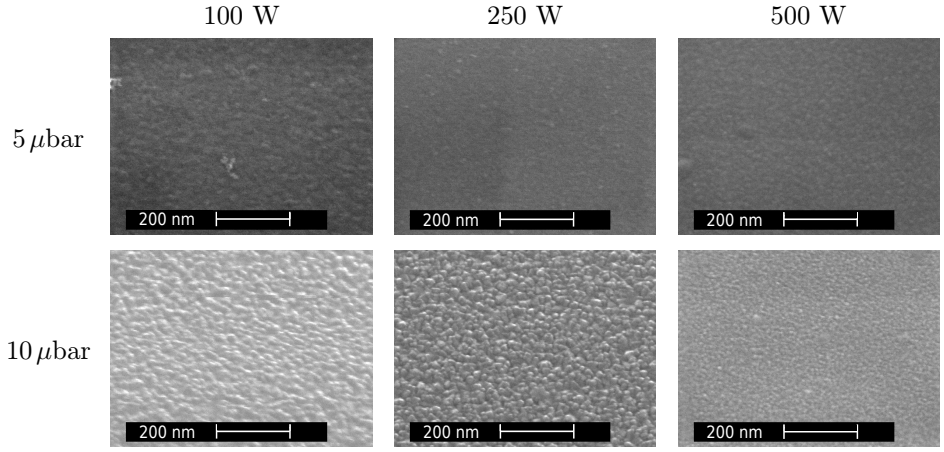

Figure 2.18. SEM images of the TiN film surfaces at a 30° tilt angle for different RF power and P_{tot}. The N_2 flow was fixed at 4 sccm.

Concerning RF power dependence of the surface morphology, we observe an increase of the roughness for lower power. For 10 μbar, samples made at 100 W and 250 W present a rough surface with clearly discernible grains, while the one made at 500 W is a lot smoother. At 5 μbar, the surfaces show less irregularities and only on the 100 W sample can we start to clearly discern the grains.

Conclusions on the sputtering parameters

While not exhaustive, this investigation leads to the conclusion that the lower total pressure of 5 μbar is suitable to obtain high value for T_C (above 5K which is, in fact, the highest value ever obtained in this optimisation). We chose a nitrogen flow rate of 4 sccm to ensure the deposition of near-stoechiometric TiN, and an RF power of 100 W to obtain a low deposition rate. Using those parameters, a T_C of 5.04K was achieved, with a resistivity of 48.84 $\mu\Omega$.cm on a 84 nm-thick sample. The BCS estimation for this film yields a sheet kinetic inductance $L_K^{\square} \approx 1.47$ pH. This value, while not high initially, is easily increased by using a lower thickness film, deposited with the same parameters. Taking advantage of our low deposition rate of ≈0.025 nm.s^{-1}, we then realised TiN thin films under 5 nm.

2.2.2.2 TiN thin films under 5 nm thickness

In those film under 5 nm, i.e. well below the electron mean free path of around 15 nm measured in thicker TiN films, we expect an increase in resistivity and a decrease of T_C. Because of those low thicknesses, it was no longer possible to use the profilometer as earlier to measure the thickness of the deposited film. We thus estimated the film thickness from the deposition time using the deposition rate of 0.0278(±0.0026) nm.s^{-1} measured on a 16 nm sample made in the same conditions. Those thin films were also deposited on 7x7 mm SiO_2 substrates and measured as the previous ones. The temperature dependence of their sheet resistance with temperature is given in figure 2.19. Below thickness of 1.95 nm, TiN becomes an insulator at low temperature. Here, the sheet resistance of a 1.67 nm sample reaches 19 $k\Omega$ at 330 mK, translating to a resistivity of around

3200 $\mu\Omega$.cm, well above the SIT of the material, theoretically expected at $R^{\square} = R_Q = \frac{\hbar}{(2e)^2} \approx 6.45\,k\Omega$ [45].

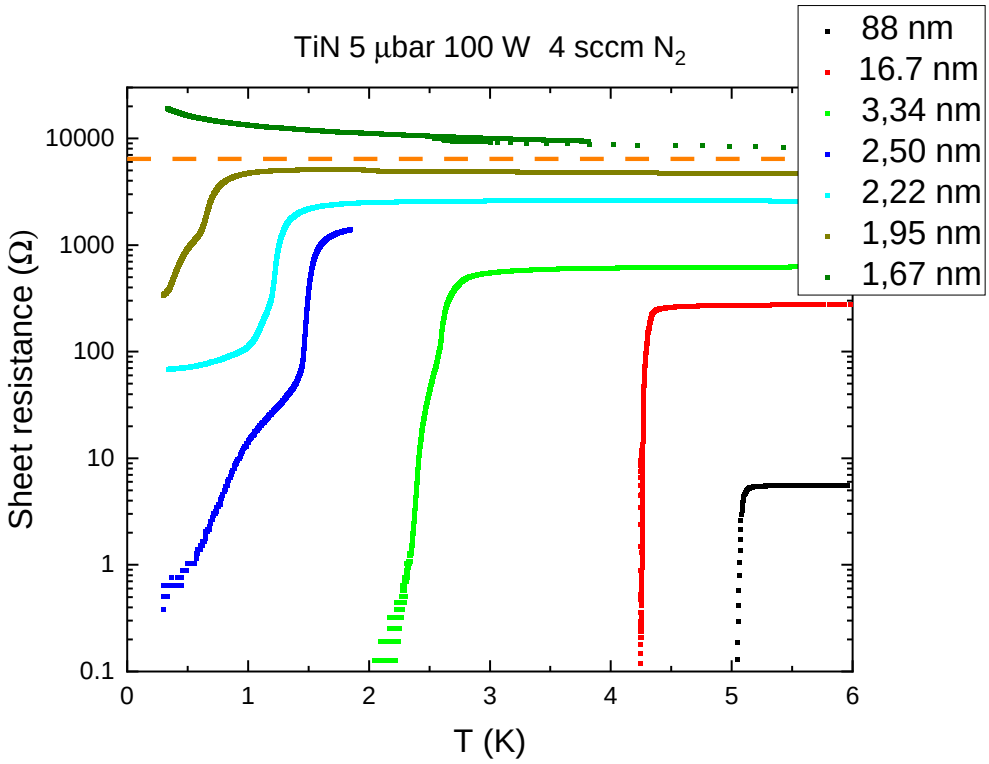

Figure 2.19. Sheet resistance versus temperature for TiN thin films of different thickness. The horizontal orange dashed line represent the theoretical value for the SIT at $R^{\square} = R_Q \approx 6.45\,k\Omega$.

Compared to the 88 nm-thick sample, the T_C of the thinner samples is lower and their normal state sheet resistance is higher, as expected. Indeed, the sheet resistance is linked to the inverse of the thickness, so it gets higher on thinner samples. However, this is not the only effect responsible for this increase in sheet resistance, as we can measured the resistivity of the film is also increasing as its thickness is reduced (see figure 2.20). As mentioned earlier, the electron mean free path in our thicker layer is of the order of 15 nm. Hence surface effects dominate the conduction in sub-10 nm

films [137], yielding a significant increase of the resistivity and a variation of the sheet resistance much stronger than simply the inverse thickness.

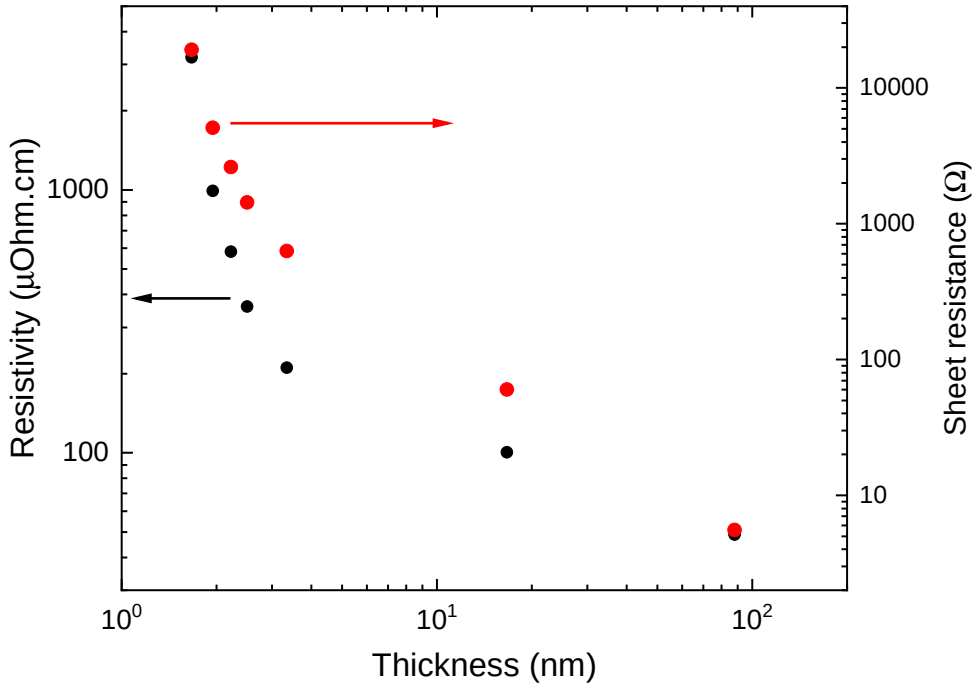

(false-color)

Figure 2.20. Resistivity (black) and sheet resistance (red) of the samples presented in figure 2.19, measured above the superconducting transition at the maximum value of the sheet resistance. For the 1.67 nm point, the resistivity and sheet resistance is measured at 330 mK.

Out of the samples presented in figure 2.19, we chose to work with the 3.34 nm-thick sample, as it provides the best compromise between a large value for T_C around 2.2 K and a high normal state sheet resistance of around 630 Ω, yielding $L_K \approx 350$ pH in the superconducting state. This sample presents two advantages:

* It enables us to performs further measurements, and especially microwave measurements, in the same 300 mK cryostat that we used here. Indeed, this base temperature is lower than the commonly used limit of $T_C/5$ for the onset of losses in superconducting circuit caused by quasiparticles.

* Unlike the thinner samples which reach a finite sheet resistance at 300 mK, this sample shows a sheet resistance that goes below the limit of our DC measurement setup under 2 K.

2.2.2.3 Impact of the substrate on sub 5 nm TiN thin films

We now discuss the effect of the substrate on our films properties. Indeed, the samples we described so far were deposited on thermally oxidised Si substrates (350 nm of SiO_2 on Si) for the sake of simplicity and cost. However, while working with superconducting circuits, we know that using high resistivity intrinsic silicon substrates with as little as possible silicon oxide is beneficial. For this reason, we used HF cleaned intrinsic silicon wafers as a substrate for the rest of our experiments, in order to get rid of the silicon oxide. Typically, a two inch high resistivity ($\approx 10\,k\Omega$.cm) intrinsic

silicon wafer is cleaned in a dilute HF acid solution before being rinsed in deionized water. This etches away the natural oxide on the surface of the wafer. It is then quickly (under 5 minutes) put into the sputtering machine and the chamber is pumped down. This reduces the oxide layer thickness from several nanometers to an individual atomic layer [94]. Titanium nitride is then sputtered using the chosen parameters and, after deposition, the wafer is transferred into a electron beam evaporation machine, in order to evaporate a 50 nm-thick aluminium film, which acts as a protection layer.

We measured the superconducting properties of a film deposited on a wafer prepared as described above with the same parameters as the 3.34 nm sample measured before (on SiO_2), and we found that the values of T_C and R_N were different. Indeed, we found $T_C \approx 1.45\,K$ (2.2 K on SiO_2) and $R_N \approx 1319\,\Omega$ (630Ω on SiO_2), as shown in figure 2.21. The deposition rates measured on 16nm thick samples were roughly the same, at $0.027\,\mathrm{nm}.s^{-1}$ on HF cleaned Si and $0.0278(\pm 0.0026)\,\mathrm{nm}.s^{-1}$ on SiO_2, and so there is only a slight variation in thickness between the previous sample on SiO_2 and this one on Si (3.34 nm and 3.24 nm respectively). We tentatively explain the discrepancy of results between those two samples by the nature of the material that makes the substrate interface with the deposited TiN. Indeed, silicon oxide is an amorphous material, while silicon is crystalline. Thus on silicon oxide, the TiN lattice is less perturbed at the substrate/TiN interface than on intrinsic silicon. Indeed, while silicon and TiN share the same cubic crystalline structure (fcc), their lattice constant are not in perfect agreement: 0.543 nm [138] for silicon and 0.425 nm [139] for TiN. This mismatch leads to strains and deformation near the Si/TiN interface, which can lead to changes in the deposited film properties. As our films are under 5 nm thick, this effect can have large consequences. To compensate for this different interface, we then deposited a slightly thicker layer of 4.86 nm under the same deposition parameters. The resulting values for T_C and $R_N^{\square}$ are 2.2 K and 530 Ω, yielding $L_K^{\square} \approx 330\,\mathrm{pH}$.

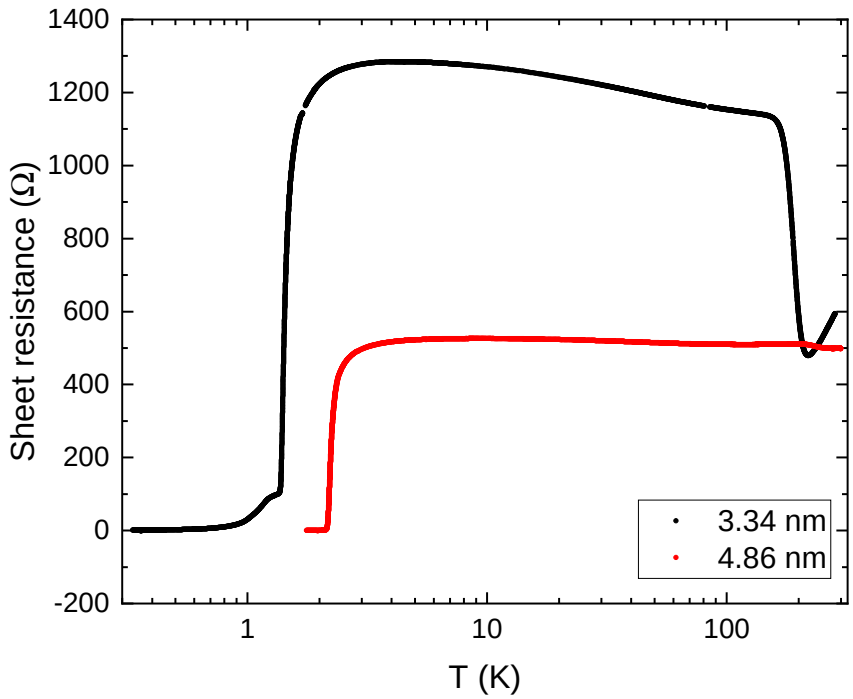

Figure 2.21. Sheet resistance measurements of two TiN thin films deposited on HF cleaned intrinsic high resistivity silicon wafers.

Film	T_C	$R_N^{\square}\,(\Omega)$	d (nm)	$\rho_N\,(\mu\Omega.\text{cm})$	$L_K^{\square}\,(\text{pH})$	l_e(nm)
A	1.45	1319	3.24	427	1256	4.21
B	2.22	530	4.86	256	330	6.99
C	2.35	20.5	16.2	33.21	12.05	54.2

Table 2.2. Summary of the characteristics for the three TiN thin films. We estimated l_e using $n \approx 5.10^{22}\,\text{cm}^{-3}$ [140].

As a result, we characterised 3 different TiN films (denoted A, B and C) deposited on high resistivity intrinsic silicon that can be used for further experiments, especially for microwave measurements. Their characteristics are summed up in table 2.2. As expected, the thicknesses are lower than the rough estimations of l_e.

2.2.2.4 Film spatial non-uniformity

TiN deposition, and more generally every physical deposition technique, suffers from non-uniformity over the scale of a wafer [127, 136]. This results in variations in the deposited layer thickness and/or its composition and characteristics [136]. In the case of TiN, the edge of the wafer presents a higher sheet resistance [127] and lower T_C [130] due to lower thickness and higher contaminants concentration [127]. To quantify this increase in our films, we deposited two wafers in the same conditions as films A and B (see table 2.2). We then cut 7x1.5 mm samples from the center of each wafer and from their edges. We measured those samples in the same way as in section 2.2.2.1. The values of those measurement are summed up in table 2.3.

		A clone	B clone
Center	$R_N^{\square}\,(\Omega)$	1770	531
	$T_C\,(K)$	1.1	2.2
	$L_K^{\square}\,(\text{pH})$	2222	333
Edge	$R_N^{\square}\,(\Omega)$	1927 (+8.9 %)	573 (+8.1 %)
	$T_C\,(K)$	0.92 (-16.4 %)	2 (-9.1 %)
	$L_K^{\square}\,(\text{pH})$	2893 (+30.2 %)	396 (+18.9 %)

Table 2.3. Measurements of the normal sheet resistance, the superconducting critical temperature and the associated BCS kinetic inductance of two TiN thin films, clone to film A and B, deposited on intrinsic Si substrate, at the center and at the edge of each wafer.

We measure an increase of the sheet resistance and a decrease of the superconducting temperature when going from the center to the edge of the wafer. The increase of the kinetic inductance ends up as 30.2 % for film A's clone and 18.9 % for film B's clone. Those values are the maximum expected variation of the kinetic inductance over the size of a wafer for our films. To mitigate this effect, we did not use the edge of the wafers for the rest of this work. We also point out that the clone of film A has an higher sheet resistance and a lower superconducting transition temperature than film A, regardless of the position within the wafer. This illustrates the limited reproducibility we can expect for this set of deposition parameter.

2.2.2.5 Effect of an oxygen plasma on TiN thin films

Such extremely thin films may be sensitive to some of the processes used during subsequent nanofabrication steps. One particular step that affects them is the plasma ashing process, i.e. the application of an oxygen plasma for resist removal. We characterised the effect of such a 100 W, 0.2 mbar and 40 sccm oxygen plasma on 3.34 and 25 nm-thick TiN samples.

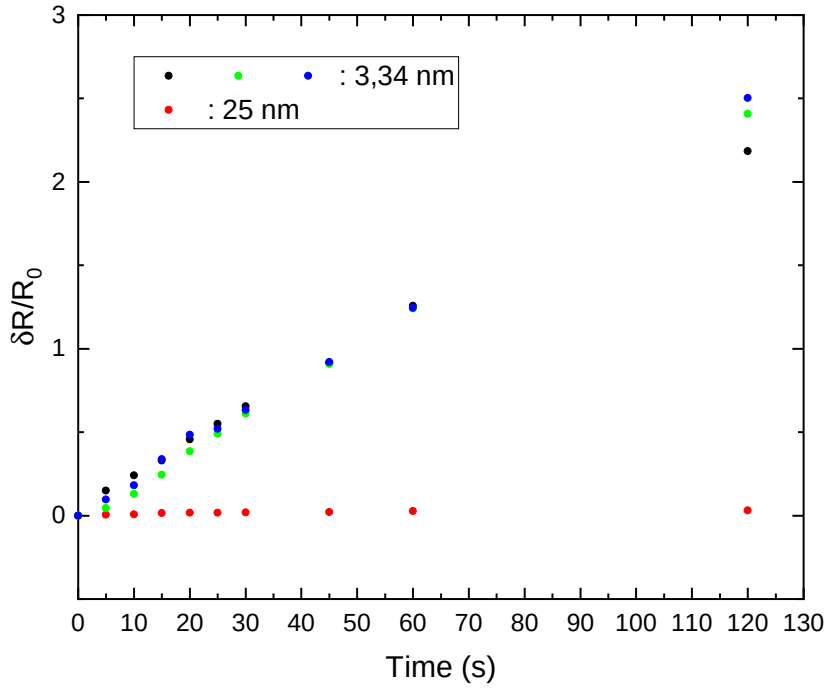

Figure 2.22. Room temperature measurements of the relative sheet resistance variations of thin TiN films deposited on SiO_2 after a time in a 100 W oxygen plasma at 200 μbar.

We measured the room temperature (300 K) sheet resistance of several samples after exposing them to this cleaning plasma for an increasing period of time (see figure 2.22). For the thinner samples, we measured a sizeable increase in sheet resistance of around 65% and 240% for a 30 and 120 seconds treatment, respectively. For the thicker sample of 25 nm, this increase reached only 3% after 120 seconds. We tentatively attribute this increase to the insertion of oxygen in the TiN films, either as a contaminant or as an oxide. Indeed, as titanium oxides are thermodynamically more stable than titanium nitride [141], it is possible to oxidise TiN under highly energetic conditions, such as in a plasma or at high temperature (>800 °C). This increase of oxygen content is only taking place at the free surface of the films, and it has limited impact on the 25 nm thick sample.

As the Residual Resistivity Ratio (RRR) of our films is just slightly below 1 (see figure 2.21 for example), we thus estimate that the normal state resistance just above T_C $R_N^{\square}$ is affected in the same manner. Moreover, as illustrated in figure 2.19, a higher sheet resistance also leads to a lower T_C. This valuable information indicates that, if we use an oxygen plasma cleaning step of 30 seconds on a sample (typical cleaning step), one can expect its normal sheet resistance to increase by about 60%. This increase, together with a probable decrease in T_C (though we did not measured T_C here), would lead to an increase of its sheet kinetic inductance by more than 60%.

It is worth noting that the effect of such oxygen plasma on our TiN thin films can be mostly reversed by a nitrogen plasma (produced in a RIE machine with low acceleration voltage and at 45 μbar). After 120 seconds in an oxygen plasma, the sheet resistance of the thin sample increased by 240%. The subsequent application of a nitrogen plasma for 60 seconds reduces the resistance to only a 30% above its value before the the O_2 plasma. This effect could be of interest as a tool to change the kinetic inductance of a superconducting device after fabrication, but we did not investigated it in more details.

2.2.2.6 Scaling of superconducting and metallic properties

As suggested by Ivry et al. [142], superconducting thin films of different materials (including TiN)

seem to follow an universal scaling:

$$d.T_C = A.R_N^{\square -B} \tag{2.11}$$

with A and B fit parameters, B being close to unity. We used this formula to fit all the data points we obtained during our sputtering optimisation, and the results are shown in figure 2.23.

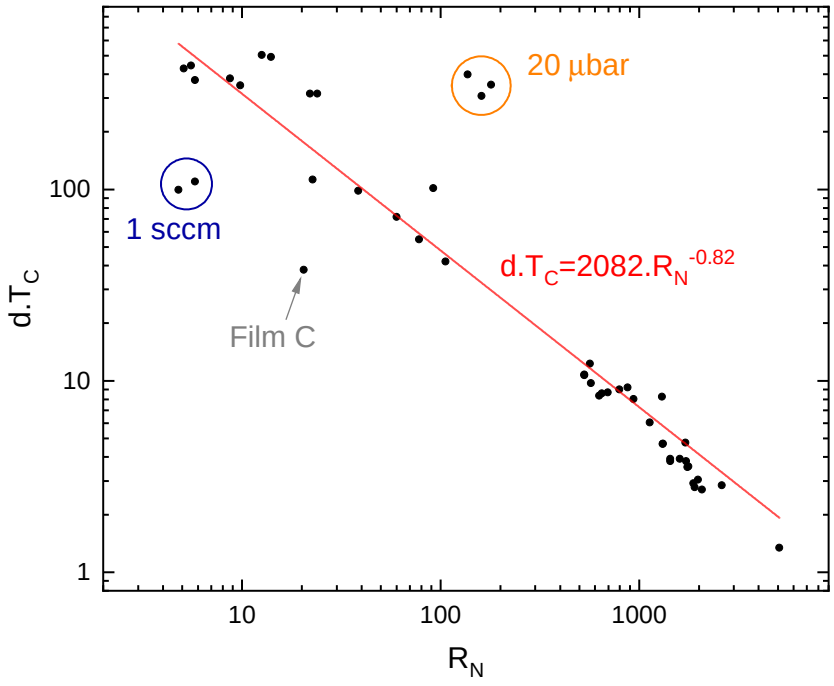

Figure 2.23. Values of the $d.T_C$ product for all the samples made during sputtering optimisation with respect to $R_N^{\square}$. Red line is a fit using formula (2.11). Deviating samples at high total pressure and low nitrogen flow rates as well as film C are highlighted, see text for more details.

We also find that most of our TiN thin films follow the scaling of (2.11), with B= 0.82 and A=2082. This result is close to those obtained in [142] for TiN thin films from different research groups. This scaling could be use to assess the superconducting characteristics of future TiN thin films. Indeed, because of their RRR close to unity (for $d \geqslant 3\,\mathrm{nm}$), a measure of their room temperature sheet resistance together with the knowledge of their thickness leads to an estimate of their T_C. The only samples that somewhat deviate from this scaling are the ones made at high P_{tot} or low N_2 flow rate and film C. The samples at high P_{tot} present some extremely high resistivity and rough surfaces, while the ones at low N_2 flow rate are probably not made of TiN anymore (see section 2.2.2.1). This suggests that samples not following this scaling strongly deviate from homogeneous TiN thin films.

2.2.3 Microwave response of sub 5 nm TiN thin films

2.2.3.1 Introduction

To explore the response of our TiN thin films in the microwave (MW) regime, we patterned CPW resonators, and measured them at low temperature to characterise their resonance. We extract the resonances frequencies f_{res}, their intrinsic quality factors Q_{int} and their coupling quality factor Q_c,

at different temperatures and power.

Resonator design and fabrication

For samples made from films A and B (see table 2.2), the resonator design is described in figure 2.24a, and the design used for the sample made from film C is depicted figure 2.24b. On each sample, several resonators (2 to 3) were coupled to the same 50Ω transmission line as so-called hanger resonators, using two different coupling geometries (see figure 2.24). The coupling length L_c was chosen in order to set the coupling factor Q_c^{sim} in the 10-60k range, using microwave simulations. The length of the CPW cavity l was adjusted to obtain a resonance frequency between 2 and 4 GHz for each resonator. On the same sample, we chose frequencies separated by at least 130 MHz, in order to measure each resonator independently. The width w of the central conductor and the gap g of the CPW resonators were maintained at 5 μm and 10 μm respectively for all samples.

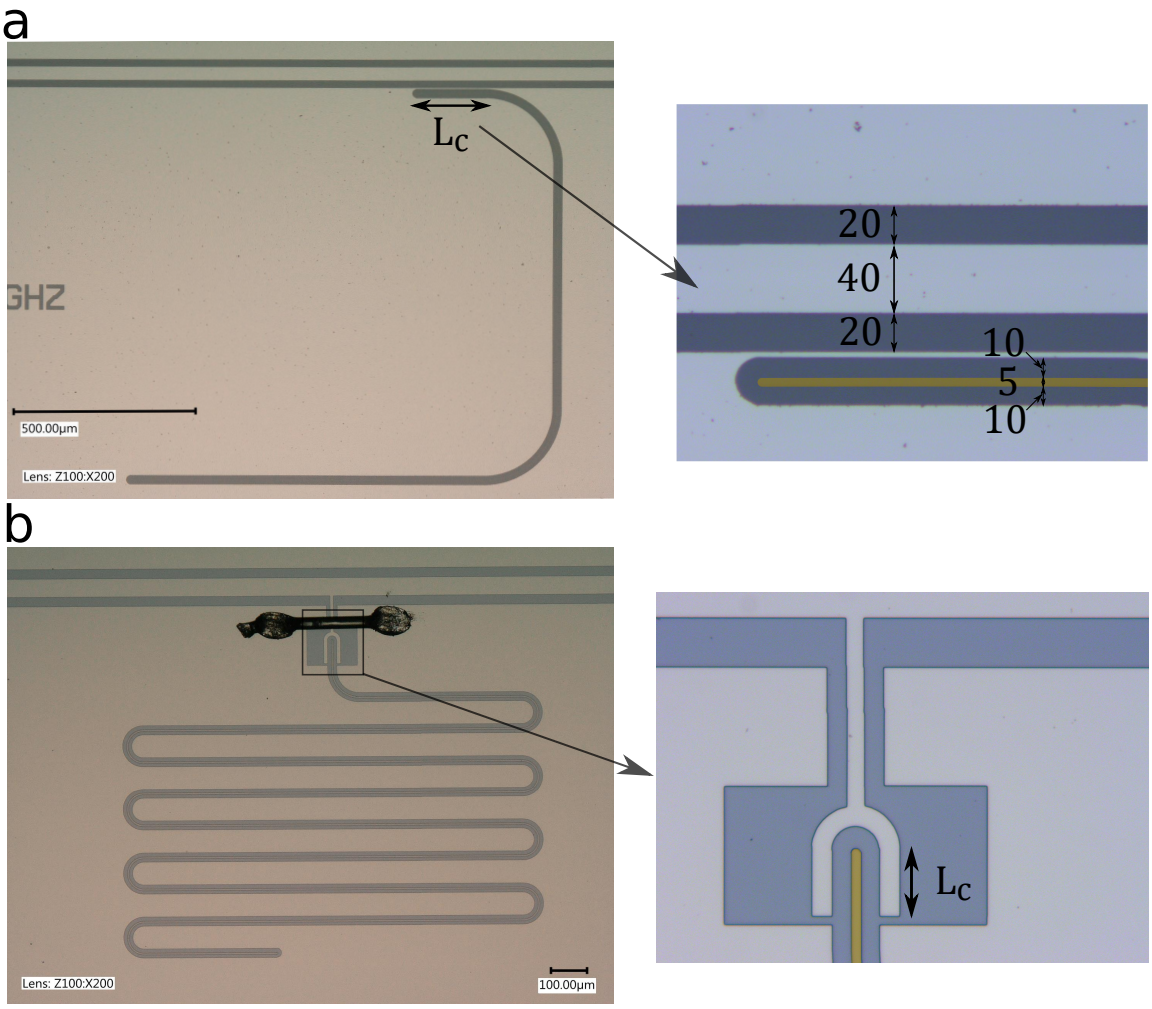

Figure 2.24. CPW TiN resonators with zoom on the coupling zone to the transmission line. Highlighted in (false-color) gold on the zoomed pictures is the CPW resonator TiN central conductors. Numerical values are in μm **a:** A resonator of sample B1, with aluminium ground plane. The ground plane width between the CPW and the transmission line is 4 μm. The coupling length L_c is the length where the CPW resonator and the transmission line are parallel. **b:** A resonator of sample C1, with niobium ground plane. The coupling length L_c is the length where the CPW central conductor is in between the two sides of the fork. The fork is made out of niobium and is galvanically connected to the transmission line.

The ground planes were realised in low $L_K^{\square}$ superconducting films such as aluminium or niobium films. Sample B1 has a ground plane made of 50 nm-thick aluminium, while all the other ones have

100 nm-thick niobium instead. A summary of the geometrical characteristics of all the resonators made is given in table 2.4. For sample B1, a $30\,s$ oxygen plasma (see section 2.2.2.5) was used to clean the surface after fabrication, a step which was not used for the other samples. Resonators on sample C1 have a slightly modified coupling design (see figure 2.24b), in order to achieve a larger coupling for the same coupling length, and thus a lower Q_c.

Sample	$l\,(\mu m)$	$w\,(\mu m)$	$g\,(\mu m)$	$L_c\,(\mu m)$	Q_c^{sim}	$f_0^{\mathrm{sim}}\,(\mathrm{GHz})$
A1	800	5	10	100	16k	3.44
	850	5	10	150	12k	3.26
	900	5	10	200	9k	3.08
B1/B2	2000	5	10	100	62k	2.66
	2500	5	10	200	28k	2.19
C1	7000	5	10	130*	14k	3.2
	9000	5	10	70*	40k	2.5
	11100	5	10	40*	91k	2.0

Table 2.4. Characteristics of the TiN resonators investigated here. The star indicates a different coupling design (see figure 2.24).

The fabrication of samples with a niobium ground plane was made of two main steps (see figure 2.25):

- The resonator central wire is patterned in an electron sensitive positive resist (PMMA A3) using an eLINE electron beam masker (a,b). After development, the resist acts as a positive mask for the deposition of a 20 nm aluminium layer (c). After lift-off (d), this layer is used as a negative mask for the RIE etching of the TiN layer, leaving only the resonator wire in the TiN layer (e).

- Niobium is then deposited using an a DC sputtering machine on the full surface of the sample (f). PMMA is applied again and patterned (f, g), to selectively etch away the ground plane material using RIE (h). The aluminium mask still on top of the resonator central wire acts as a stopping layer for the RIE. Aluminium is then removed using a basic solution based on TMAH, which attacks neither TiN nor niobium (i).

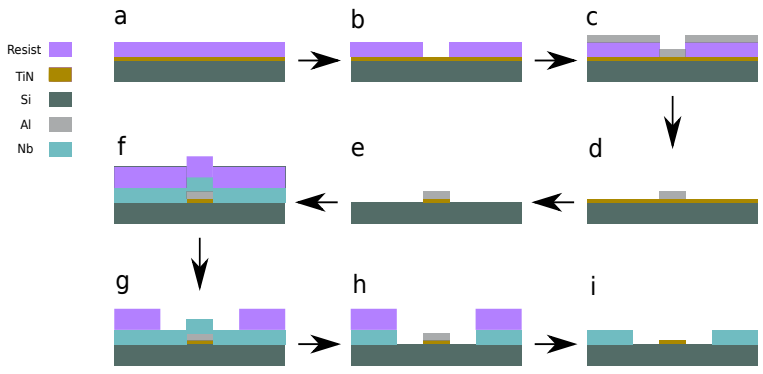

Figure 2.25. Detailed fabrication steps for samples with niobium ground plane (samples A1, B2 and C1). **a:** PMMA layer deposition on top of TiN layer. **b:** Exposition and development of the resist. **c:** Aluminium evaporation. **d:** Lift-off. **e:** RIE etching of TiN. **f:** Niobium and PMMA deposition. **g:** Exposition and development of the resist. **h:** RIE etching of the niobium. **i:** Resist removal.

Microwave measurement setup

The samples from films B and C were cooled down to 300 mK, and the one from film A to 50 mK. They were measured using a VNA from 1 to 10 GHz (see figure 2.26). Their resonances were characterized by measuring the transmission parameter S_{21} that we fitted to extract the resonance parameters [143, 144].

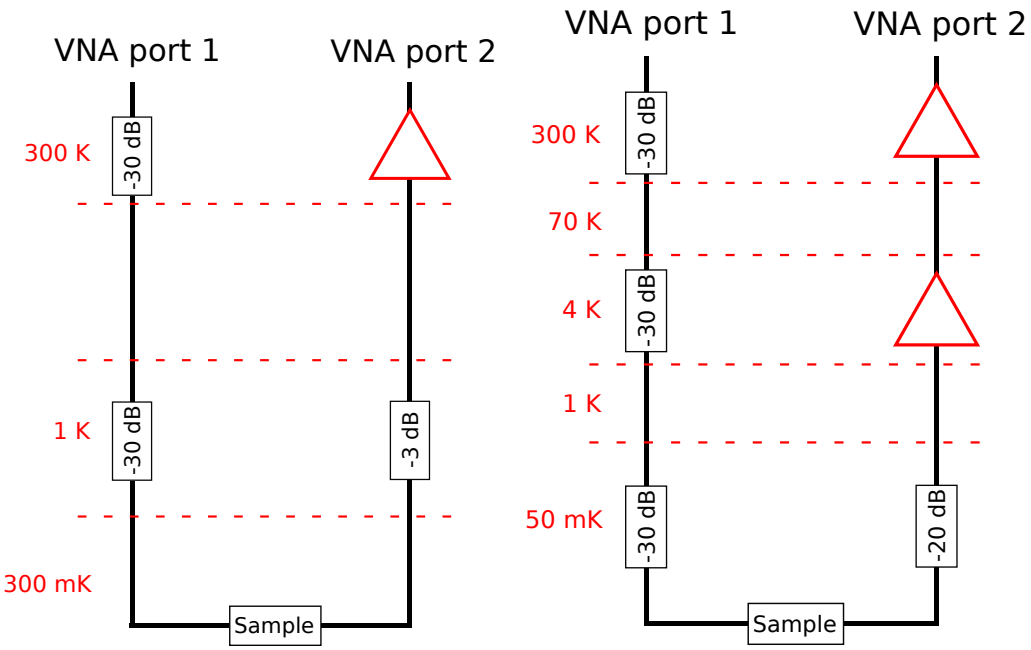

Figure 2.26. Experimental microwave setup used for sample measurement. **left:** 300 mK cryostat setup used for samples B1, B2 and C1. **right:** 50 mK setup used for sample A1.

2.2.3.2 Resonances characterisation

The values of the resonance frequency and quality factors of all the resonators are summarised in table 2.5. As Q_{int} varies with the probing power, those values are given for the power at which Q_{int} is maximum. The power dependence of Q_{int} will be discussed later on.

Sample	$l\,(\mu m)$	Q_c^{sim}	f_0^{sim} (GHz)	f_0^{meas} (GHz)	Q_c^{meas}	$Q_{\text{int}}^{\text{meas}}$	$L_K^{\square,\text{BCS}}$ (pH)	$L_K^{\square,\text{meas}}$(pH)	$Z_C(\Omega)$
A1	800	16k	3.44	3.91	10k	1700	1256	1053	≈1.3k
	850	12k	3.26	3.70	10k	1400	1256	1042	≈1.3k
	900	9k	3.08	3.55	9k	1500	1256	1009	≈1.3k
B1	2000	62k	2.66	2.03	51k	32.6k	330	601	≈1k
	2500	28k	2.19	1.65	32k	30.2k	330	621	≈1k
B2	2000	62k	2.66	3.02	33k	2.3k	330	282	≈700
	2500	28k	2.19	2.38	25k	4.4k	330	288	≈700
C1	7000	14k	3.2	2.98	18k	20k	12.05	20.8	≈180
	9000	40k	2.5	2.52	35k	43k	12.05	17.2	≈170
	11100	91k	2.0	2.15	180k	33k	12.05	15.6	≈160

Table 2.5. Summary of all the low-power value for the resonance frequency, the internal quality factor and the coupling quality factor for all the resonators. All the samples were measured at 300 mK, except A1 which was measured at 50 mK.

We extract the sheet kinetic inductance $L_K^{\square,\text{meas}}$ from the resonance frequency and compare it to the calculated value of the corresponding TiN film $L_K^{\square,\text{BCS}}$ (see section 2.2.2.3).

Sheet kinetic inductance

For sample A1 and B2, $L_K^{\square,\text{meas}}$ is lower than $L_K^{\square,\text{BCS}}$ of film A and B by 19.7% and 12.8%, respectively. If we take into account that deviation, it will not hinder future use of those TiN films.

On the other hand, sample B1 exhibits a significant 85% increase in sheet kinetic inductance from the BCS value of film B. We attribute this drastic increase to the oxygen plasma cleaning that was used during the fabrication of this sample. Indeed, as shown in section 2.2.2.5, such an oxygen plasma leads to an increase of the sheet resistance of 65% which, together with a hypothetical decrease of T_C from 2.2 to 1.95 K, perfectly explains the increase of $L_K^{\square}$ measured on this sample. Sample B2, made of the same film as sample B1, was not submitted to this oxygen plasma and indeed has an inductance closer to expectations for this film.

Internal Quality factor

We observe that the internal quality factor tends to decrease with the sheet kinetic inductance. We tentatively attribute the sizeable difference of Q_{int} between sample B1 and B2 to a different fabrication process regarding the ground plane. Indeed, the Al ground plane of sample B1 was deposited on the freshly sputtered TiN. On the other hand, the Nb ground plane of sample B2 was sputtered after the removal of the TiN layer by RIE etching. This RIE step leaves a rough surface on the sample, leading to a potentially lossy Si/Nb interface. This particular effect was not further investigated here.

2.2.3.3 Power dependence of the internal quality factor

We have measured how the properties of resonators on A1 and B1 sample evolve with the applied power (see figure 2.27). We observe variations of Q_{int} with the average number $\bar{n}$ of photons in the cavity frequently seen in superconducting resonators [145, 94, 136]: at high power, Q_{int} drops due to depairing, and, at low power, the coupling of the resonator to TLSs may decrease Q_{int} (see section 1.5). This latter effect is observed in sample B1, but not in sample A1. We also observed similar behaviour for the higher harmonics of each resonator on both samples (figure 2.27b and 2.27c).

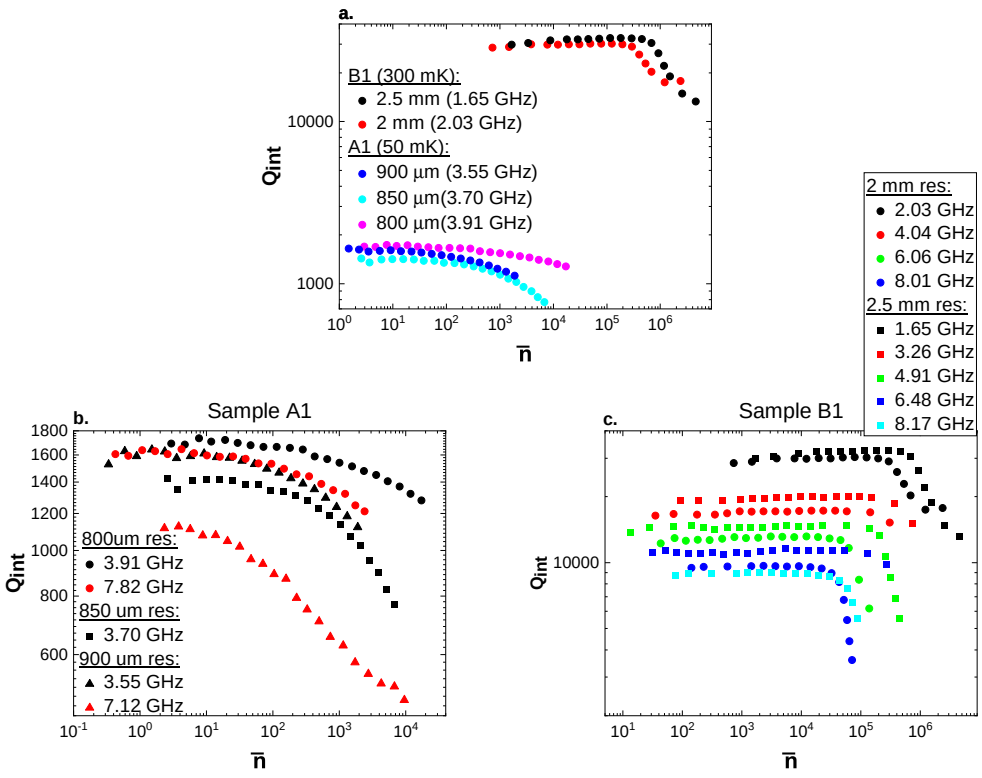

Figure 2.27. Internal quality factors Q_{int} of the resonances of samples A1 and B1. **a:** fundamental resonances of the resonators. **b:** fundamentals and higher harmonics of sample A1. **c:** fundamentals and higher harmonics of sample B1.

For sample B1, every harmonic follows this common behaviour: upon reducing the number of photons in the resonator $\bar{n}$ down to $10^5 - 10^6$ photons, Q_{int} increases , then reaches a maximum value and then slightly decreases at lower power. For sample A1, while some harmonics seem to

reach a plateau at low power, it is not the case for all of them. Indeed, some Q_{int} curves only reach the beginning of a plateau at very low power, around one photon in the resonators, and do not reach a TLS dominated regime.

2.2.3.4 Ageing process in TiN thin films

Given that the films we consider here are very thin and that Ti can react with oxygen, one can expect that exposing our samples at ambient conditions without taking any precautions could affect their properties. We already know that an O_2 plasma treatment increases film resistivity (see section 2.2.2.5 and 2.2.3.2); we now discuss the potential ageing of those films in ambient conditions. For this purpose, we measured sample B1 over several weeks, and we compared the resonance frequency and Q_{int} for the second harmonic of the 2.5 mm resonator. We chose this particular harmonic at 3.27 GHz for practical reasons, as it is the one with the most data available. Between the first and the second measurements, the sample was left roughly 3 weeks at ambient conditions. Between the 2$^{\text{nd}}$ and 3$^{\text{rd}}$ ones, the sample was left in the 300 mK cryostat at room temperature but at low helium pressure for 3 days. As depicted in figure 2.28, the storing conditions of the sample had an effect on its properties:

- The quality factor during the 2$^{\text{nd}}$ measurement was an order of magnitude lower than during the first one, but it recovered some of this loss after storage at low helium pressure. However, its variation with respect to $\bar{n}$ did not changed much: it still reaches a maximum around 10^5 photons and then slightly decreases.
- The value of the resonance frequency did not changed much (it changed by less than 10 MHz between measurements), but its variation with $\bar{n}$ did. Indeed, while the resonance frequency reached a plateau at low power during the first measurement, it decreases when lowering $\bar{n}$ below 10^4 photons during the 2$^{\text{nd}}$. Again, this decrease was nearly removed during the 3$^{\text{rd}}$ one.

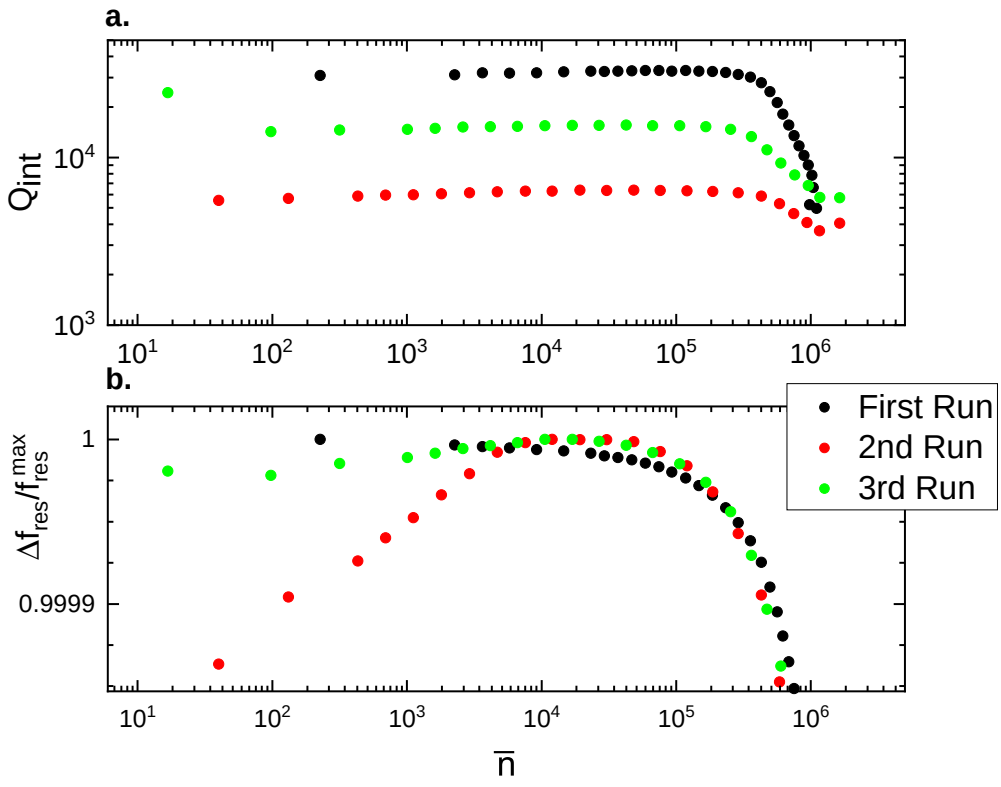

Figure 2.28. Internal quality factor Q_{int} and relative change of the resonance frequency of the second harmonic of the 2.5 mm resonator (3.26 GHz) of sample B1 versus the number of photons in its cavity. **a:** Internal quality factor; **b:** relative frequency variation.

This behaviour is compatible with an increase of the TLS density at the surface of our sample during its stay at ambient conditions. Indeed, the presence of a TLS ensemble coupled to a superconducting resonator has a negative impact on its internal quality factor and reduces its resonance frequency at low power [74, 145] (see section 1.5.3). Interestingly, those added TLS can be mostly removed by putting our sample at low helium pressure for a few days. This suggests that they are only adsorbed at the sample surface, and do not originate from chemical modification of the thin films (e.g. oxidation). For the rest of this work, we took the precaution of storing all the samples in a vacuum chamber, to avoid any uncontrolled modification of their properties during storage (even reversible).

2.2.3.5 Power dependance of the resonance frequency: Self-Kerr effect in TiN

All superconducting resonators become nonlinear at sufficiently high power, a phenomenon that manifests notably through a change of the resonance frequency. A typical power-dependence measurement for our devices is presented figure 2.29a. We identify three regions on this graph:

- In region A, the resonance frequency slightly increases at low $\bar{n}$ due to the interaction of TLS with the resonator.
- In region B, the frequency is decreasing. This is due to the Self-Kerr nonlinearity of the disordered superconductor.
- In region C, higher order non-linearities become significant and the internal quality factor collapses, thus we can no longer correctly measure the resonance.

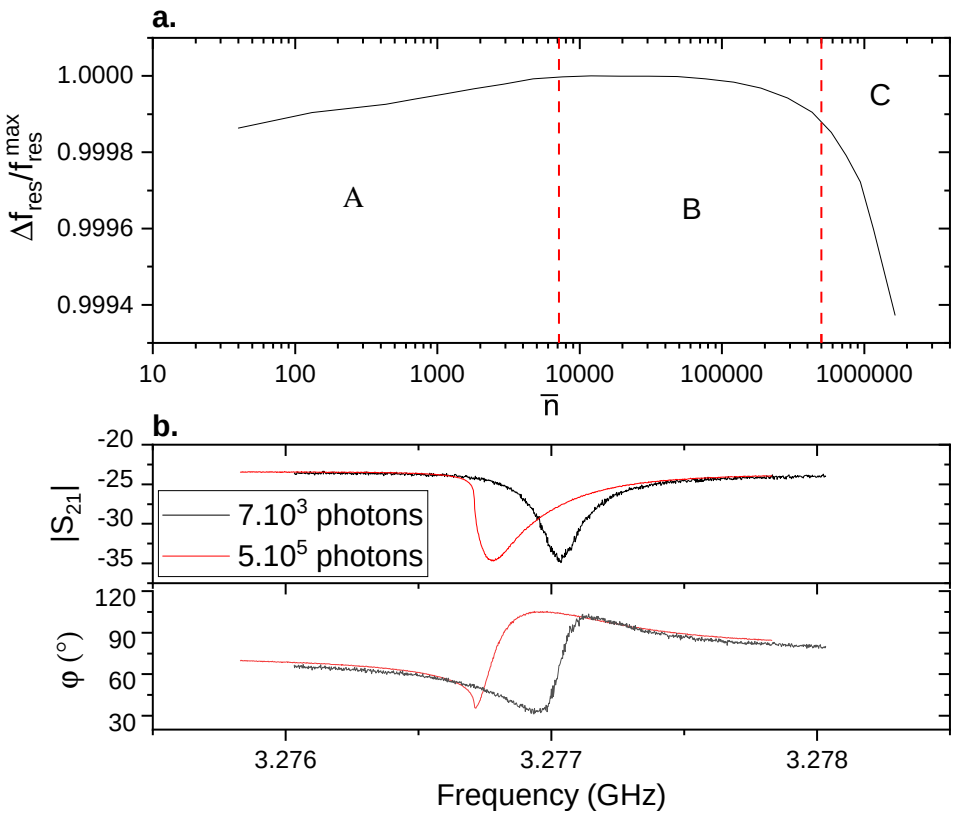

Figure 2.29. Typical power dependence of our non linear TiN CPW resonators, measured here at 3.27GHz and 300 mK. **a**: Relative variation of the frequency versus the number of photons in the resonator cavity. Red dotted lines are region separators, see main text for more details. **b**: Resonance shape at 7.10^3 (black) and at 5.10^5 (red) photons in the resonator.

We now focus on region B, in which we can apply the theory for the self-Kerr non-linearities described in section 1.4. The resonance shape in this region is shown in figure 2.29b for a small and a large probing power. At large power (red curve), the resonance shape becomes asymmetric and the resonator is approaching a bistable regime. By fitting these shapes at different power using a non-linear model and using the parameters extracted in section 2.2.3.2, we obtain the self-Kerr coefficients K_m of the resonator. We applied this procedure to the two resonators present on sample B1 for all their modes.

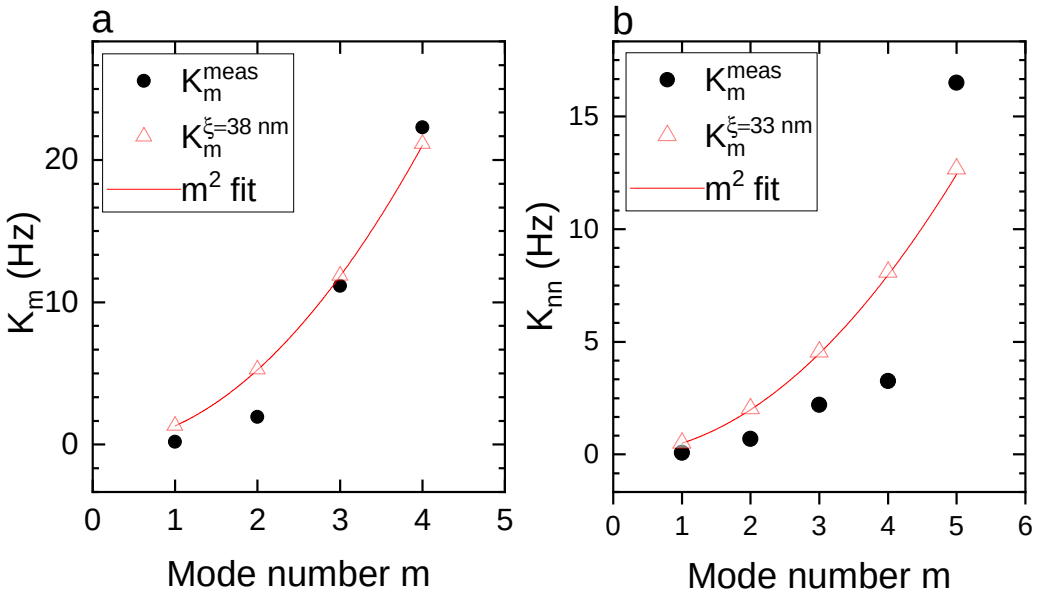

Figure 2.30. Kerr coefficients for each modes of the 2 mm resonator (**a**) and the 2.5 mm resonator (**b**) of sample B1. Black dots are measured values using non linear fits, red curve is a simple n^2 fit of the data and red triangles are calculated values using formula (1.14).

Our results for the self-Kerr coefficients of both resonators are given in figure 2.30. They are following quite loosely the m^2 fit (red curves in figure 2.30) expected for the coefficients K_m. Fitting the data using equation (1.13) yields $\xi = 38$nm and $\xi = 33$nm for the resonator lengths 2 mm and 2.5 mm, respectively. These values are larger than both the electron mean free path l_e and the thickness d of this film, thus placing it in the dirty limit ($l_e \ll \xi$) of a 2D superconductor ($d \ll \xi$). Note that sample B1 has been exposed to an oxygen plasma prior to measurement, but we expect the other samples made using this film to remain in this 2D dirty superconductor limit.

2.2.4 Conclusions on TiN

We have deposited superconducting TiN thin films with a large range of properties in a reproducible manner. Using sputtering conditions that lead to high T_C, low resistivity, good surface morphology and low deposition rates in ≈100nm thick films, we deposited ultra thin films of TiN. We have characterised those sub-5 nm films using both DC and microwave measurements. We verified that those films are still superconducting and selected 3 of them with T_C between 1.45 and 2.35 K. We used those films to pattern CPW resonators, whose measurements confirmed their high sheet kinetic inductance. We found internal quality factors ranging from 2k to 43k, with film B providing the best compromise between good internal quality factors and a large kinetic inductance. We have also measured the power dependence of resonators on sample B1, from which we extracted their self-Kerr coefficients and the value of the superconducting coherence length ξ in this film.

TiN film B is a suitable low-loss high kinetic inductance material, and we will use it in the experiments described in the following sections.

Chapter 3

Nanowire resonators

As explained in section 1.3.4, we aim at realising the QPS box proposed by Hriscu et al. [34] in order to investigate QPS physics. As far as we know, this device has not yet been experimentally investigated. We patterned several lumped 2D resonators on TiN thin film B. One of them is presented in figure 3.1, alongside its equivalent electrical circuit. These devices are based on a long ($>10\,\mu m$) nanowire inductor with a width w below 200 nm, implementing a QPS junction. The low wire width together with the large $R_N^{\square}$ of TiN thin film B naturally leads to highly inductive nanowires. The QPS energy resulting from this design is expected to be large ($E_S \propto \exp\left(-\frac{w}{R_N^{\square}}\right)$) and should allow us to probe the effect of the QPS junction: the modulation of the resonance frequency by the charge offset applied to the two ends of the wire.

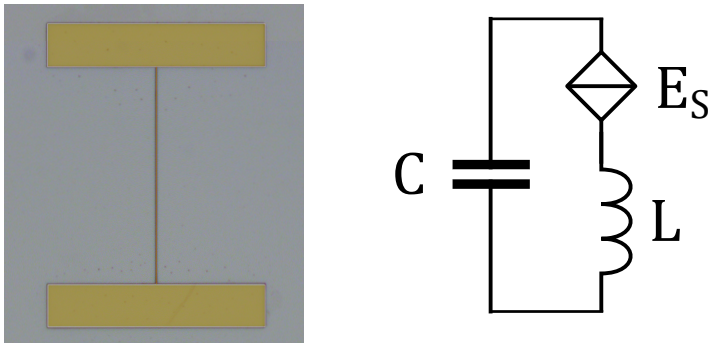

Figure 3.1. Optical photograph of a TiN nanowire lumped resonator fabricated in film B (see section 2.2.2.3) and used in this chapter. The material highlighted in (false-color) gold is TiN. On the right is the equivalent electrical circuit.

The large value of the inductance in those devices also makes their characteristic impedances $Z_C = \sqrt{L/C}$ larger than $1k\Omega$. This renders them likely to be sensitive to charge defects, such as charged dipoles. Indeed, the electrostatic coupling of such dipole to a resonator scales as $\sqrt{Z_C}$ (see

section 1.5.4.1) and induces fluctuations in the resonance frequency. Thus the observation of the QPS junction modulation could be difficult.

3.1 Sample design and fabrication

3.1.1 Design details

Our lumped TiN resonators consist of capacitor made of two pads connected by a 50 μm-long nanowire, which provides the inductance and possibly a QPS junction. One of our resonator is shown in figure 3.2, where the TiN is highlighted in gold. They are placed in a recess in the ground plane of a 50Ω niobium microwave transmission that runs close to the resonator. This line couples the resonator to the rest of the measurement circuit. We can apply a DC voltage to this transmission line, in order to apply a DC electric field in the recess, and thus on the resonator.

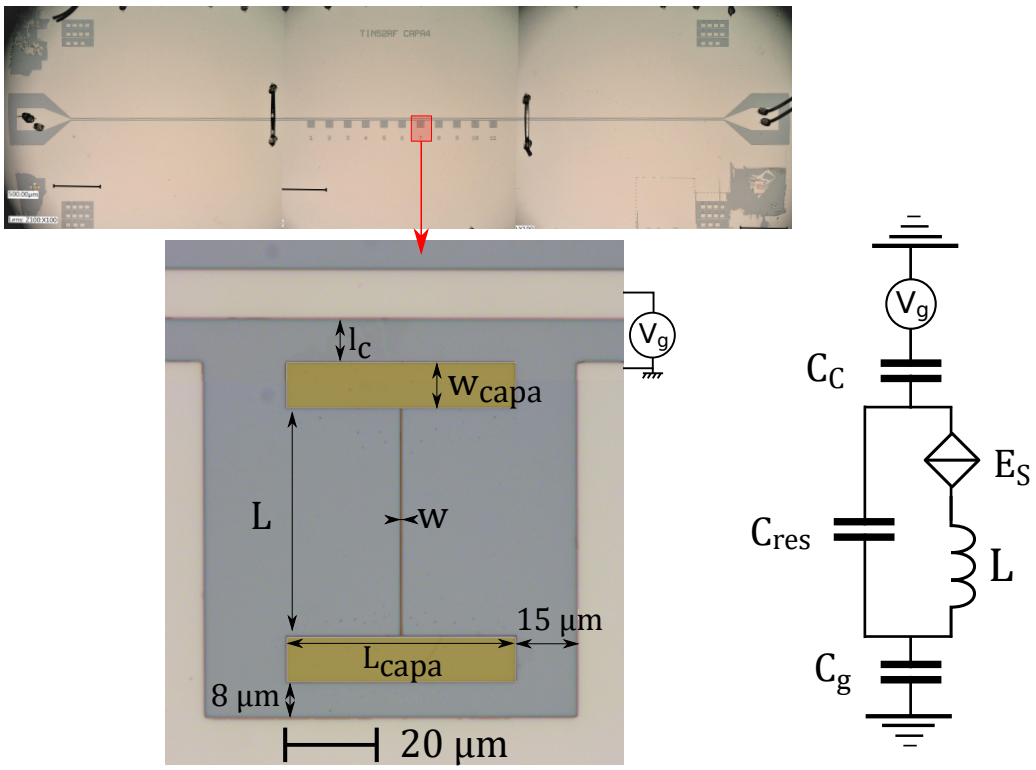

Figure 3.2. Optical photograph of a TiN nanowire lumped resonator fabricated in film B (see section 2.2.2.3) and used in this chapter. The material highlighted in gold is TiN. on the right is the equivalent electrical circuit. The central conductor of the 50Ω microwave transmission line used to couple the resonators to our measurement setup is visible on top of the bottom left picture. A DC voltage can also be applied to this conductor to generate an electric field. Here w=146 and $l_C = 8\,\mu m$, which leads to an inductance of 113nH and a resonance frequency of 7 GHz.

The dimensions defined in figure 3.2 are summed up in table 3.1. Only the wire width w and the coupling distance l_C were varied. The coupling quality factor Q_C of the resonator strongly increases with l_C, resulting in Q_C between 1000 and 10000 for the chosen range of l_C.

l	w	L_{capa}	w_{capa}	l_C
$50\,\mu m$	$40-400\,\text{nm}$	$50\,\mu m$	$10\,\mu m$	$8-24\,\mu m$

Table 3.1. Geometrical characteristics of our resonators.

Using Sonnet microwave simulations and assuming the absence of any QPS junction, we chose resonant frequencies f_{res} in the 4 to 8 GHz band for which we have a complete set of microwave components (circulators, filters, HEMT amplifiers…). Several resonators were coupled to the same measurement line. Test zones containing multiple nanowires of each chosen w were also fabricated at the periphery of the sample in order to measure their width using a SEM and estimate the reproducibility and the dispersion of w in the fabrication process.

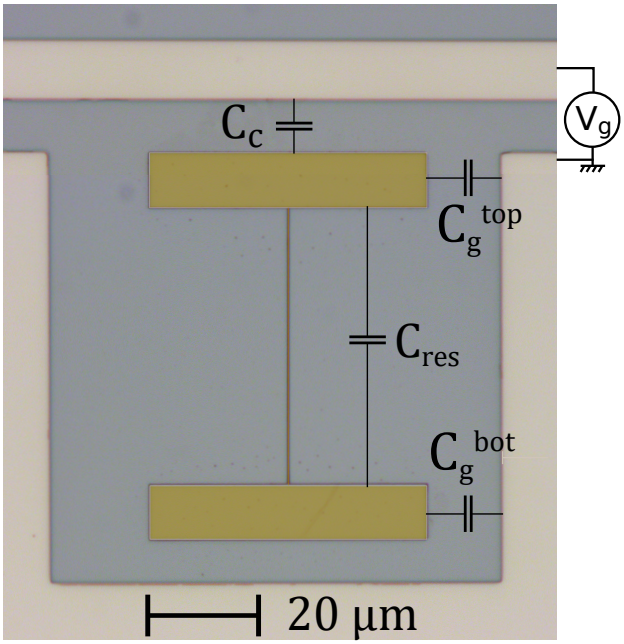

Figure 3.3.

Using electrostatic simulations, we estimated the DC capacitance of our devices, presented in figure 3.3. The values of the coupling capacitance C_c, the resonator capacitance C_{res} and the ground capacitance of each pads of the resonator C_g^{top} and C_g^{bot} are presented in table 3.2.

$C_c\,(\text{fF})$	$C_{\text{res}}\,(\text{fF})$	$C_g^{\text{top}}\,(\text{fF})$	$C_g^{\text{bot}}\,(\text{fF})$
3.3 - 1.6	0.43	2.3 - 2.9	5.3

Table 3.2. Capacitance of our devices using electrostatic simulations without taking into account the nanowire. The different values for a single capacitance correspond to $l_c = 8$ and $24\,\mu m$.

3.1.2 Resonator nanofabrication

The resonator nano-fabrication process is sketched in figure 3.4. This process, similar to the one described in section 2.2.3.1, requires two lithographic steps:

- a first e-beam lithography step of the aluminium mask used to etch away the TiN and define the resonators (a to e in figure 3.4).

- A second e-beam lithography to define the niobium transmission line and ground plane (f to i in figure 3.4).

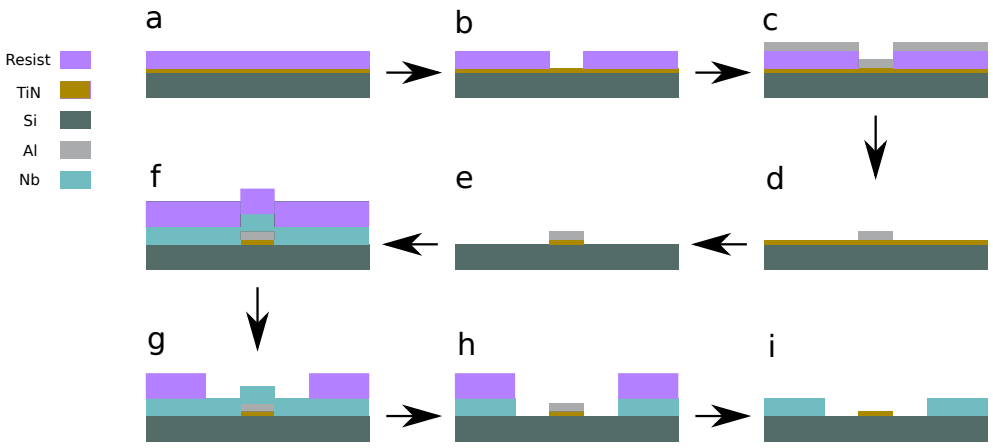

Figure 3.4. Detailed fabrication steps for our nanowire lumped resonator. **a:** PMMA layer deposition on top of TiN layer. **b:** Electron beam exposure of the resonator's pattern. **c:** Aluminium evaporation. **d:** Lift-off. **e:** RIE etching of TiN. **f:** Niobium and UV3 deposition. **g:** Exposition and development of the resist. **h:** RIE etching of the niobium. **i:** Resist removal.

After fabrication, the width of nanowires in the test zones is measured and the mean value is used to adjust the microwave simulations. We did not observe the resonator themselves with the SEM prior to measuring them, to avoid any SEM-induced contamination. The resulting resonance frequencies are shown in table 3.3 for the sample used in this chapter.

Resonator	a	b	1	2	3	4	5	6
w (nm)	45	70	78	99	122	147	169	191
l_C (μm)	8	8	8	8	8	24	24	24
$f_{\text{res}}^{\text{sim}}$ (GHz)	4.33	5.09	5.11	5.76	6.39	6.98	7.45	8.32
Q_C^{sim}	3550	3040	2550	2210	1970	6840	6480	5780

Table 3.3. Measured geometrical parameters, simulated resonance frequency and coupling quality factor for all our resonators.

Using the values of w and the characteristics of our TiN thin film, we can estimate the values of the QPS junction energy E_s for our resonators, which are presented in table 3.4.

Resonator	a	b	1	2	3	4	5	6
w (nm)	45	70	78	99	122	147	169	191
E_S/h	84 GHz	3.4 GHz	1.2 GHz	69 MHz	2.9 MHz	92 kHz	4.3 kHz	194 Hz

Table 3.4. Estimation of E_s/h using $R_N^{\square} = 530\Omega$, $T_c = 2.2$K and $\xi = 30$nm, obtained in section 1.3.4. [36]

Given that $E_S/h \gg \hbar\omega_a$ and $E_S/h \approx \hbar\omega_b$, we do not expect the measurement of resonator a and b can be easily done, if not entirely impossible.

3.2 Measurement setup

3.2.1 Cryogenic setup

We used a cryogen-free dilution refrigerator with base temperature of 50mK, fitted with microwave cryogenic lines to measure the transmission of the sample (see figure 3.5). The input line thermal noise is filtered by two 30dB attenuators and passes through a bias-tee. This bias-tee, together

with a DC-block at the sample's output, enables the application of a DC voltage to the sample. The transmitted microwave signal goes through a 4 to 8 GHz bandpass filter and an isolator, before being amplified by a 37 dB cryogenic High Electron Mobility Transistor (HEMT, LNF-LNC0.3_14A, 0.3 to 14 GHz) amplifier with a noise temperature of 4.2 K.

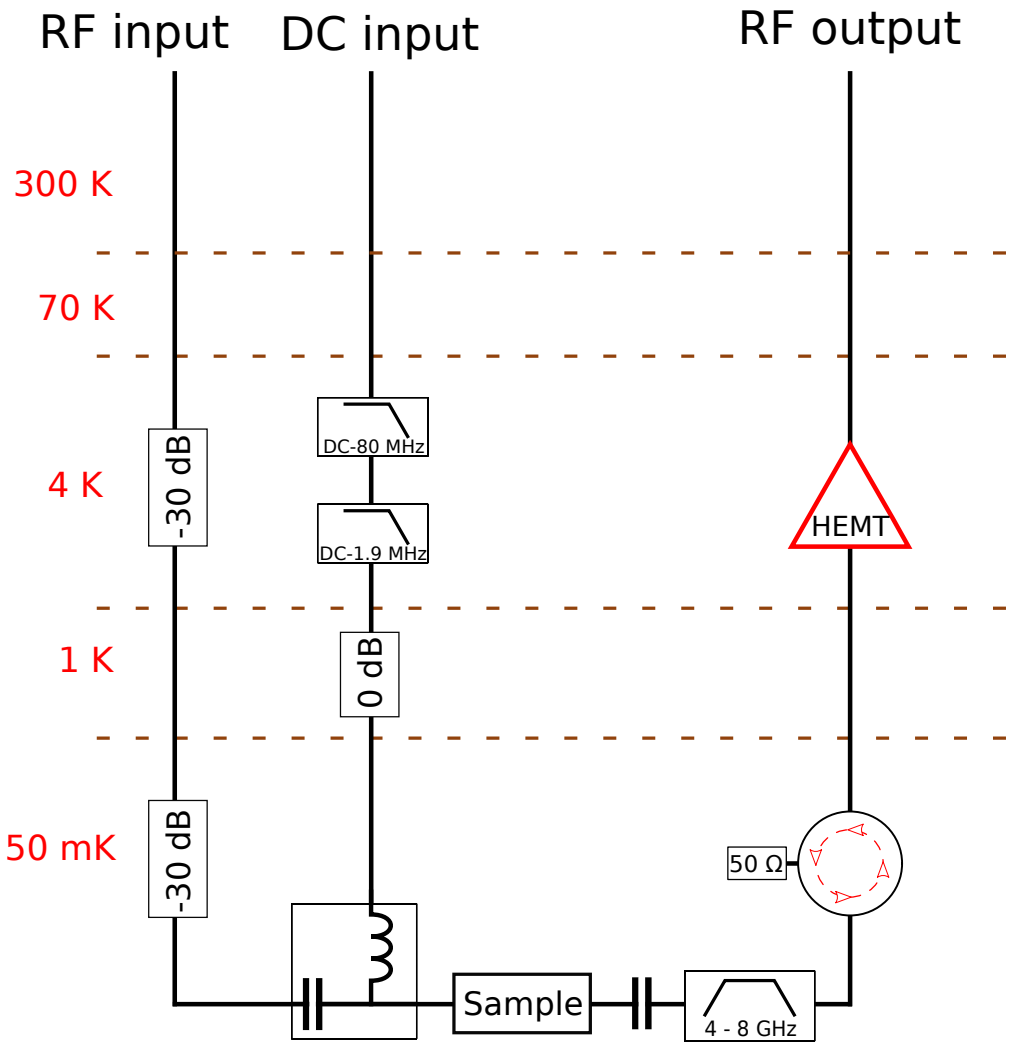

Figure 3.5. Microwave cryogenic lines used to characterise our sample.

3.2.2 Room temperature setup

In order to characterise our resonators, we used either a VNA to measure the frequency dependent-transmission of our sample, or a so-called Pound-Drever-Hall (PDH) setup to track the fast changes of the resonance frequency (without measuring the entire resonance curve).

3.2.2.1 The Pound-Drever-Hall measurement scheme

To measure shifts in the resonance frequency of a superconducting resonator, one usually measures the phase of the complex transmission S_{21} at a fixed frequency f_{vna} close to the resonance frequency f_{res}. The measured phase of S_{21} varies linearly with the small detuning $f_{\mathrm{vna}} - f_{\mathrm{res}}$, while the magnitude $|S_{21}|$ does not change. This phase measurement is very sensitive to spurious phase drifts

in the entire measurement setup, such as temperature fluctuations of the microwave components. In order to remove those large phase fluctuations that do not originate from the sample, we use a Pound Drever Hall (PDH) setup which is insensitive to global phase shifts.

The PDH technique was initially developed for laser frequency stabilisation [146, 147]. Its application to microwave superconducting resonator characterisation is illustrated in ref. [92]. It is well suited to characterise our side coupled resonators measured in transmission with a "notch" type frequency response as shown in figure 3.7. In this technique, a carrier signal at frequency $f_c \approx f_{\mathrm{res}}$, phase-modulated to add sidebands at $\pm f_m$, is used to excite the resonator. The value of f_m is chosen so that sidebands $f_c \pm f_m$ fall out of the resonance dip, but close to it. Since the frequencies f_c and $f_c \pm f_m$ are close-by, the uncontrolled phase drifts in the various cables and microwave components will be nearly the same for the carrier and its sidebands. At the output of the refrigerator, a square law power detector (typically a diode detector) is used to measure the output signal power from the resonator, which is then demodulated at f_m. This demodulated signal is insensitive to global phase shifts and is used as the error signal for a PID controller which regulates the value of f_c, keeping $f_c = f_{\mathrm{res}}$.

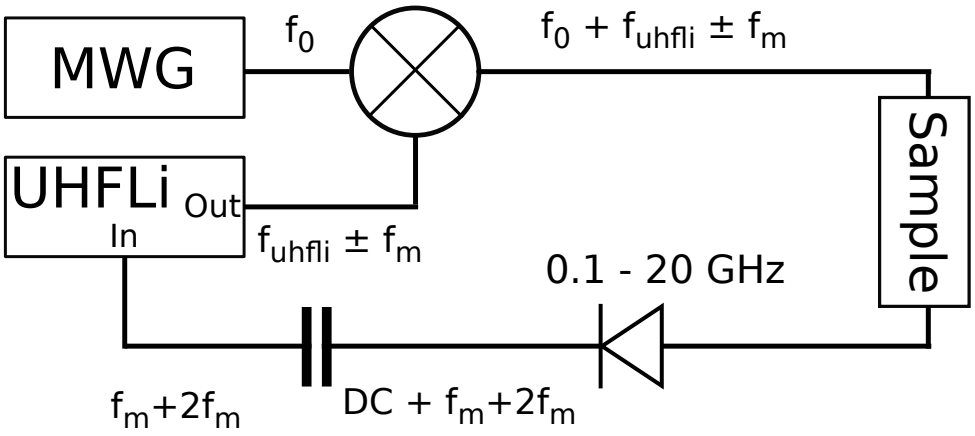

Figure 3.6. Simple view of our Pound Drever Hall room temperature measurement setup used to track and measure the resonator frequency with high accuracy. A radio frequency signal at 300 MHz from the Ultra High Frequency Lock-in (UHFLi) amplifier modulated at a frequency f_m is up-mixed with a microwave signal f_0 from a microwave generator (MWG). This up-mixed excitation is sent to the sample and the transmitted signal is detected by a diode-based RF power detector. The DC component of the detection is blocked by a DC block and the resulting signal at f_m is demodulated by the lock-in amplifier.

For implementing this measurement technique (see figure 3.6), we use a Zurich Instrument Ultra High Frequency Lock-in (UHFLi) amplifier which produces a carrier at $f_{\mathrm{uhfli}} \approx 300\,\mathrm{MHz}$ and its sidebands, demodulates the output signal from the diode and implements a PID control over f_{uhfli}. The modulated signal from the UHFLi is upconverted using a mixer and a high frequency microwave signal at f_0 up to the 4-8 GHz band. To produce the sidebands at $f_c \pm f_m$, the UHFLi uses amplitude modulation with a phase shift of π to the lower band, in order to emulate a phase modulation. The complex signal sent to the resonator is then:

$$V_{\mathrm{in}} = A\Big(e^{i\omega_c t} + \frac{m}{2}(e^{i(\delta\omega^+)t} - e^{i(\delta\omega^-)t})\Big)$$

with $\omega_c = 2\pi(f_0 + f_{\mathrm{uhfli}})$, m the modulation depth and $\delta\omega^{\pm} = \omega_c \pm \omega_m$. Assuming a perfect transmission line side-coupled to a perfect notch resonator, the output signal from the resonator writes:

$$V_{\mathrm{out}} = S_{21}(\omega_c)e^{i\omega_c t} + \frac{m}{2}(S_{21}(\omega^+)e^{i\omega^+ t} - S_{21}(\omega^-)e^{i\omega^- t})$$

with $S_{21}(\omega)$ the complex transmission of the resonator. The diode signal is:

$$S(\omega_c, t) = k\,|V_{\text{out}}|^2 \tag{3.1}$$

with k a conversion constant specific to the diode detector, hence:

$$\begin{aligned} S(\omega_c, t) \;=\; k\,A^2\Big(& |S_{21}(\omega_c)|^2 + \frac{m^2}{4}(|S_{21}(\delta\omega^+)|^2 + |S_{21}(\delta\omega^-)|^2) + \frac{m}{2}\mathrm{Im}(e^{i\omega_m t}(S_{21}(\omega_c)\overline{S_{21}(\delta\omega^-)} - \\ & \overline{S_{21}(\omega_c)}S_{21}(\delta\omega^+))) + 2\omega_m \text{ terms}\Big) \end{aligned} \tag{3.2}$$

where the overbar denotes the complex conjugate. The DC terms are blocked by a DC block and the $2\omega_m$ terms are of no interest for us. The PID error signal is obtained by demodulation of the ω_m component of $S(\omega_c, t)$ at ω_m:

$$kA^2\frac{m}{2}\mathrm{Im}(e^{i\omega_m t}(S_{21}(\omega_c)\overline{S_{21}(\delta\omega^-)} - \overline{S_{21}(\omega_c)}S_{21}(\delta\omega^+)))$$

This signal is present along two quadratures and, given a correct choice of the demodulation phase (empirically found for each resonator), they have a typical shape presented in figure 3.7. The error signal for the PID controller is finally the in phase x quadrature that vanishes at $f_c = f_{\text{res}}$ and varies linearly with small detuning $f_c - f_{\text{res}}$.

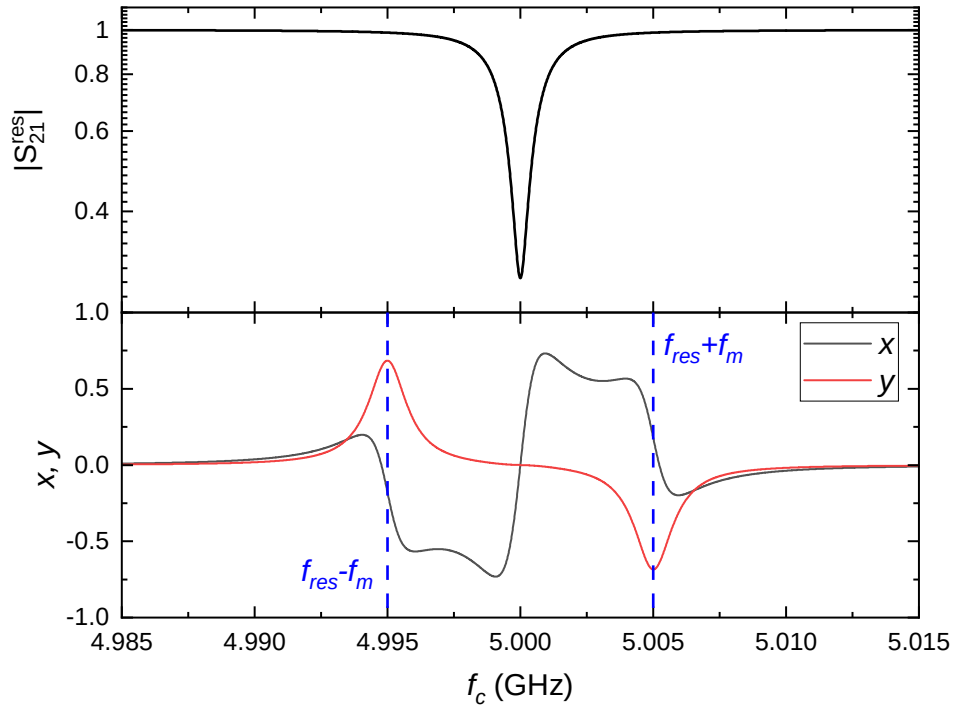

Figure 3.7. top: Magnitude of the complex transmission S_{21} of a perfect 5 GHz notch resonator, with $Q_{\text{int}} = 10000$ and $Q_c = 2000$. **bottom:** In phase (x) and out of phase (y) quadratures of the signal demodulated at ω_m from $\tilde{S}$ (3.2), with $\tilde{S}(\omega_c, t) = \frac{2\,S(\omega_c, t)}{m\,A^2}$ and $f_m = 5$ MHz. The dashed lines represent frequencies at $f_{\text{res}} \pm f_m$.

Any small global phase fluctuations will only result in the slope $\left.\frac{\mathrm{dx}}{\mathrm{df_c}}\right|_{f_c = f_{\text{res}}}$ to slightly change, which does not hinder the operation of the PID controller and thus the measurement of f_c.

3.2.2.2 Room temperature setup: PDH and VNA

The complete room temperature setup we use in this chapter is shown in figure 3.8. Using microwave switches, we can connect either a VNA or a PDH setup to our dilution refrigerator. This allows us to consecutively characterise our resonators using the VNA (to obtain their resonance frequencies and quality factors) and perform faster experiments using the PDH, e.g. for measuring the resonance frequency noise.

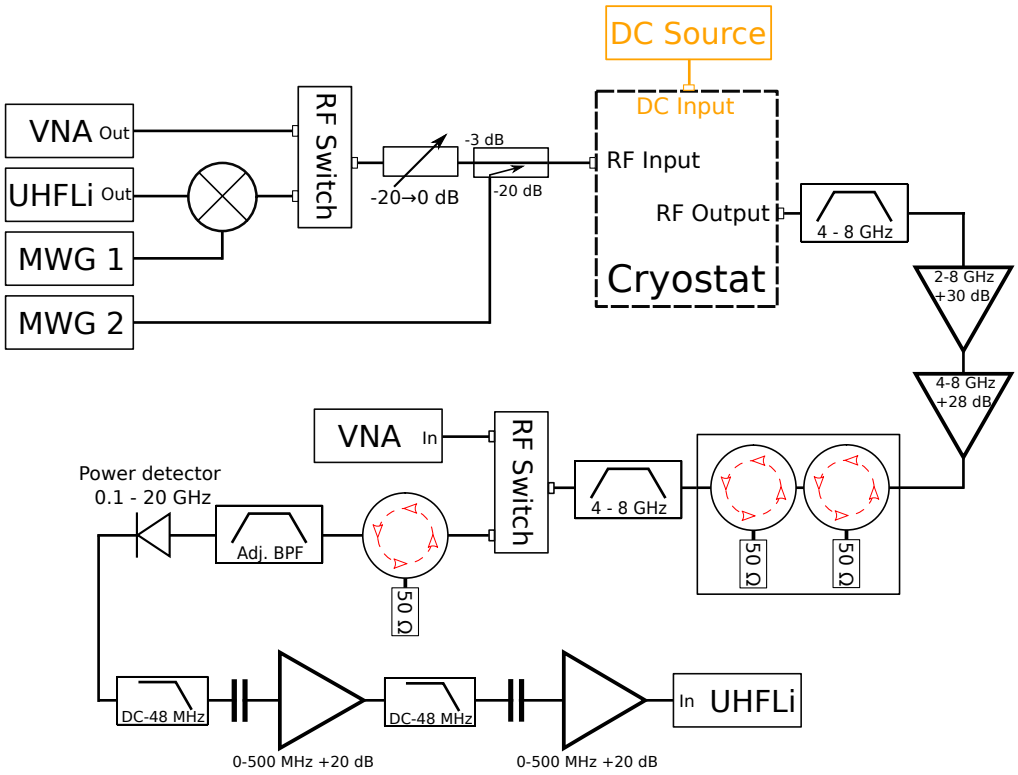

Figure 3.8. Microwave room temperature setup used to measure our resonators. RF switches allow us to alternate between measurements with PDH or VNA. A voltage-controlled attenuator is inserted before the refrigerator to finely tune the injected power. A -20dB coupler is used to inject a second microwave tone. Several 4-8 GHz bandpass filters and isolators are present to reduce noise and spurious reflections in the setup. We use two microwave amplifiers with a total gain of 58dB, and two low frequency amplifiers with a total gain of 40dB after the Schottky diode detector.

We have several microwave components in the common path of both setups. After the input microwave switch, there is a voltage controlled attenuator and a -20dB coupler. These enable the fine adjustment of the input power and the addition of a second RF signal for two-tone measurements (coming from MWG 2), respectively. At the RF output of the refrigerator, and before the second microwave switch, we placed several bandpass filters, low-noise microwave amplifiers and isolator, all working within the 4-8 GHz band. This is to amplify the RF signal coming out of the refrigerator while filtering any spurious signal outside our selected band of frequencies. The isolators remove any waves reflected by the bandpass filter.

The PDH setup contains additional components, aside from the common ones described above and those described in figure 3.6. Those are an adjustable bandpass filter (and its associated isolator) before the diode detector and two low-noise low frequency ($<$500 MHz) amplifiers, each with their lowpass filter, before the UHFLi input. The adjustable filter is a YIG bandpass filter tunable from 2 to 8 GHz, with a bandwidth of 30 MHz. We use this filter to remove as much unwanted signal as possible before the diode detection, in order to keep the best sensibility of the

detector, and its adjustability enables us to measure all our resonators. The lowpass filters and the low frequency amplifiers amplify the signal at the modulation frequency (<5 MHz) before its demodulation by the UHFLi.

3.3 Experimental results

We measured our sample during several cooldowns. Some results, like the resonance frequencies and the quality factors, changed over the course of those cooldowns spanning several weeks, similar to what we measured in section 2.2.3.4. However, the noise measurements, the gate dependence, etc. was qualitatively reproducible at each cooldown. The results presented in this section are thus representative of all our cooldowns. The temperature of the sample during the measurements was 50mK, unless specified otherwise.

3.3.1 Resonators characterisation

3.3.1.1 Resonance frequencies and quality factors

After each cooldown, we first measure the transmission of the sample using the VNA, in order to characterise each resonance. By fitting the obtained S_{21} for each resonator we extract the resonance frequencies and their quality factors. The values for the first cooldown are presented in table 3.5. The measured values of f_{res} and Q_c qualitatively agree with the ones simulated without considering the presence of QPS junctions. The designed increase in Q_C between resonator 3 and 4 is well apparent in the results.

Resonator	a	b	1	2	3	4	5	6
$w\,(\text{nm})$	45	70	78	99	122	147	169	191
$l_C\,(\mu m)$	8	8	8	8	8	24	24	24
$f_{\text{res}}^{\text{sim}}\,(\text{GHz})$	4.33	5.09	5.11	5.76	6.39	6.98	7.45	8.32
Q_C^{sim}			2550	2210	1970	6840	6480	5780
$f_{\text{res}}\,(\text{GHz})$			4.529	5.644	6.492	7.223	7.495	8.21
Q_C			2200	1630	2300	5800	5800	6800
Q_{int}			10000	6250	14500	9000	3300	4200
$Z_C\,(\Omega)$			6020	5910	5517	5094	4598	4456

Table 3.5. Resonance parameters measured during the first cooldown of our 6 resonator samples. The values of the characteristic impedance Z_C are calculated using $Z_C = L\omega_{\text{res}}$ and the theoretical value of the total inductance L from the wire width w.

The values of f_0 and Q_{int} present some fluctuations over the course of the different cooldowns. Indeed, similar to the results in section 2.2.3.4, both values tend to decrease when we thermally cycle the sample. However, the values of Q_{int} were always sufficient for proper measurement of f_0 with our PDH setup (i.e. $Q_{\text{int}} > 1000$), and the shift in f_0 did not exceed 300 MHz.

We did not measure any traces of either resonator a or b. We can explain this in two ways: either their nanowire suffered damage during fabrication, or the value of E_S corresponding to those two devices was too high. In the latter case, the description given in section 1.3.4 is not valid, the resulting devices are not resonators with a gate dependence but rather fall in the Coulomb blockade category. The non-linearities are so high that only their ground state is accessible, and we can not measure them using the same techniques as the other resonators. We decided to concentrate on the visible resonances for the rest of this work.

3.3.1.2 Power dependence of the resonances

We measured the power dependence of the resonance frequency f_{res} and the internal quality factor Q_{int}, and the results are shown in figure 3.9 for the first cooldown. As expected, f_{res} decreases with the approximate average number of photons $\bar{n}'$ due to the self-Kerr effect (see section 1.4), and Q_{int} follows the same trend. Note that we use here the approximate value $\bar{n}'$ instead of the average number of photons in the resonator $\bar{n}$ because we do not know precisely the spurious attenuation along our cryogenic lines (usually several dB). Thus the value $\bar{n}'$ is calculated using the resonance fit considering perfect cryogenic lines, and we have $\bar{n} \lessapprox \bar{n}'$.

For $\bar{n}' < 1000$ the value of Q_{int} stays above 1000 for all our resonators, the lowest being resonator 5 at around 1500. Those $Q_{\mathrm{int}} > 1000$ are sufficient to allow us to measure the resonance either via the VNA or PDH setup. Most of our measurement were done with $\bar{n} \approx 100$.

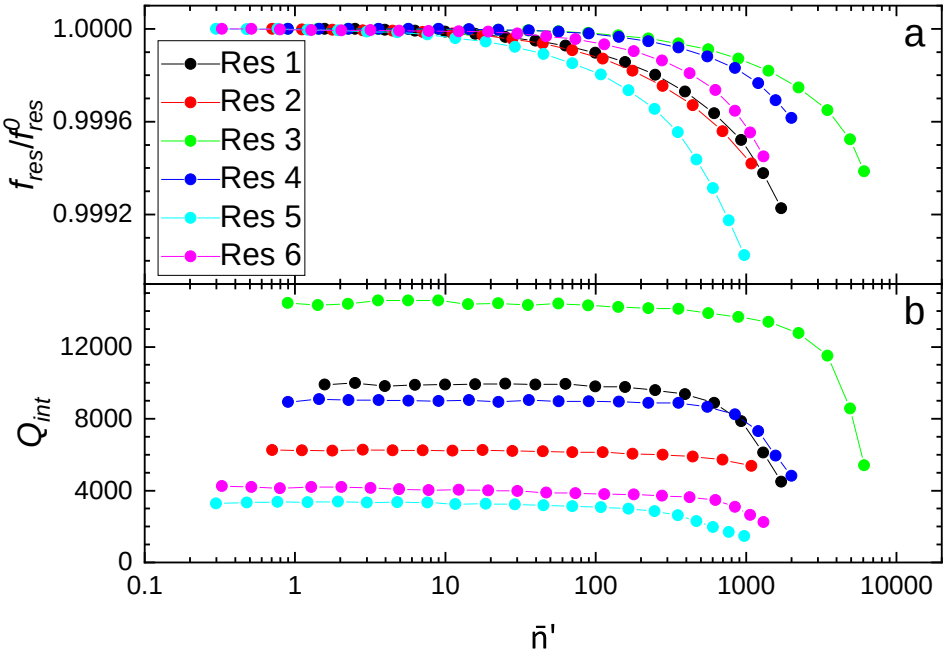

Figure 3.9. Power dependence of the relative variations of f_{res} and internal quality factors Q_{int} of our resonators during the first cooldown. Note here that $\bar{n}'$ is the estimated number of photons in the resonators assuming perfect cryogenic transmission lines.

We do not observe any significant decrease of f_{res} or Q_{int} when $\bar{n}'$ is reduced towards 1. This behaviour is different from the preliminary measurements we made on TiN CPW resonators (see section 2.2.3), where the central conductor was much larger than the nanowire, the charactyeristic impedance much lower, and where both f_{res} and Q_{int} were lower at $\bar{n} \approx 1$ than at intermediate power ($\bar{n} \approx 100$), as explained by the GTM model [74] (see Sec. 1.5).

3.3.1.3 Estimation of $\bar{n}$ using the self-Kerr effect

In order to obtain an independent and more precise estimation of $\bar{n}$, we used the non linear behaviour of our resonators described by their theoretical self-Kerr coefficients presented in section 1.4:

$$K \approx \frac{3\pi}{4} \alpha r \frac{Z_C}{R_Q} \left(\frac{\xi}{l} \right)^2 \hbar w_{\mathrm{res}}$$

From the preliminary measurement on our TiN thin film, we have an estimation of $\xi \approx 35\,\mathrm{nm}$, leading to $K \approx 5\,\mathrm{kHz}$ for our resonators. With those values and the measurement of the resonance frequency at a very low measurement power f_{res}^{0} , we can estimate the number of photons present in its cavity, as:

$$\bar{n} \approx \left(\frac{f_{\mathrm{res}} - f_{\mathrm{res}}^{0}}{K} \right)$$

This method has two main sources of errors:

- to estimate the coefficients K, we used the value of Z_C from the first cooldown. During the subsequent cooldowns, Z_C changed slightly, with $\delta Z_C \approx \pm 2\,10^{-2}\,Z_C$.

- And we assume that the resonance frequency reaches a plateau at low power, which is sometimes not exactly the case due to TLS influence on our devices. During some cooldowns, the f_{res} presents an initial increase with $\bar{n}$. In those cases, the determination of $\bar{n}$ is not possible before the maximum of f_{res} is reached, and after this maximum the estimation is impacted by the constant frequency error $\delta f_{\mathrm{res}}^{0} = f_{\mathrm{res}}^{0,\mathrm{real}} - f_{\mathrm{res}}^{0,\mathrm{meas}}$. We estimate that $\delta f_{\mathrm{res}}^{0} \leqslant 400\,\mathrm{kHz}$, which translates into an error on the number of photons $\delta\bar{n} \leqslant 80$.

However, most of our measurement were done at relatively high power, with $\bar{n} > 100$. The potential errors due to Z_C and f_{res}^{0} imprecisions are thus not significant. As expected, we find values for $\bar{n}$ using this method that are smaller than $\bar{n}'$. These values are in quantitative agreement with $\bar{n}'$ corrected by spurious 3 to 10 dB losses between the refrigerator input and the sample.

3.3.2 Gate dependence of f_{res}

Hriscu and Nazarov have predicted that whenever quantum coherent phase slips occur in the nanowire inductor of our resonators, their resonance frequency should be modulated periodically with the DC charge present on the electrode of the capacitance, with a $2e$ period [34] (see section 3.1.1). Given the estimate of the gate capacitances (see section 3.1.1), we calculate the corresponding period for the gate voltage for the potential QPS junction modulation of $\approx$1.46 and 2.46 mV, for $l_c = 8$ and $24\,\mu m$, respectively.

We have thus systematically investigated the gate voltage dependence of the resonance frequencies, using the PDH setup. Unfortunately, we have not found any repeatable modulating signal in those gate measurement, whatever the resonator.

3.3.2.1 Lack of gate modulation

During the first cooldown, we confirmed the lack of observable, stable, periodic gate dependence of f_{res}, at any voltage scales. From this lack of modulation, we discuss several point regarding the QPS in this system.

The QPS energy E_S could be too low to measure any modulation in our devices, but given the estimations in table 3.4, $E_S^{\mathrm{res}\,1} \approx 1\,\mathrm{GHz}$ and $E_S^{\mathrm{res}\,2} \approx 70\,\mathrm{MHz}$, we should observe a significant charge modulation in resonator 1 and 2. At higher E_S, such as in resonators a and b, the resulting device is not measureable. For resonators 3 and up, E_S decreases rapidly below $\approx$1 MHz, and we did not expect to observe any modulation, as $E_S \ll \hbar\Gamma \approx 1\,\mathrm{MHz}$ the linewidth of our resonators. As we mentioned before, estimating E_S can lead to significant error, due to the exponential dependence on not so well defined constant of order one. Thus our estimations could be some order of magnitude higher than the actual values.

We can also explain the lack of modulation in resonator 1 and 2 by the chosen measurement parameters, and especially by the number of photons $\bar{n}$ in the resonator. We have seen that

such QPS box devices are highly nonlinear and that the charge modulation amplitude is itself modulated by $\bar{n}$ (see figure 1.6) and decreases for high $\bar{n}$. During our measurements, $\bar{n}$ may have happened to be at a value resulting in a low charge modulation amplitude. Indeed, during our measurement we mainly used $200 \leqslant \bar{n} < 1000$, and we have seen in section 1.3.4 that one needs to have $E_S \geqslant \hbar\Gamma n^{3/4} \approx 50$ to 180 MHz to observe a significant effect of the QPS modulation. Adding this effect to the uncertainty in estimating E_S, this could explain the lack of charge modulation. The simple solution, however, would be to reduce $\bar{n}$. But we now come to the main reason, in our opinion, that we did not observed charge effect: frequency noise and fluctuations of f_{res}.

Indeed, at low values of $\bar{n}$, our measurement of f_{res} was plagued by large fluctuations and large noise. We decided to focus our efforts on understanding and controlling those fluctuations before going any further in exploring the QPS physics of our devices.

3.3.2.2 Global linear shift

We first observe that the resonance frequency of our resonators present a small linear shift with the gate voltage, as illustrated figure 3.10. The slope $p = \frac{\mathrm{df_{res}}}{\mathrm{dV_g}}$ is different between resonators and varies slightly between cooldowns around $p \approx 10\,\mathrm{kHz}.V^{-1}$. This value leads to a small relative frequency shift $\tilde{p} = p/f^0_{\mathrm{res}} \approx 2.10^{-6} V^{-1}$ for large electric fields up to $10^4 - 10^5\, V.m^{-1}$. We tentatively attribute this small shift to the variations of the capacitances with the large electric fields applied in the substrate.

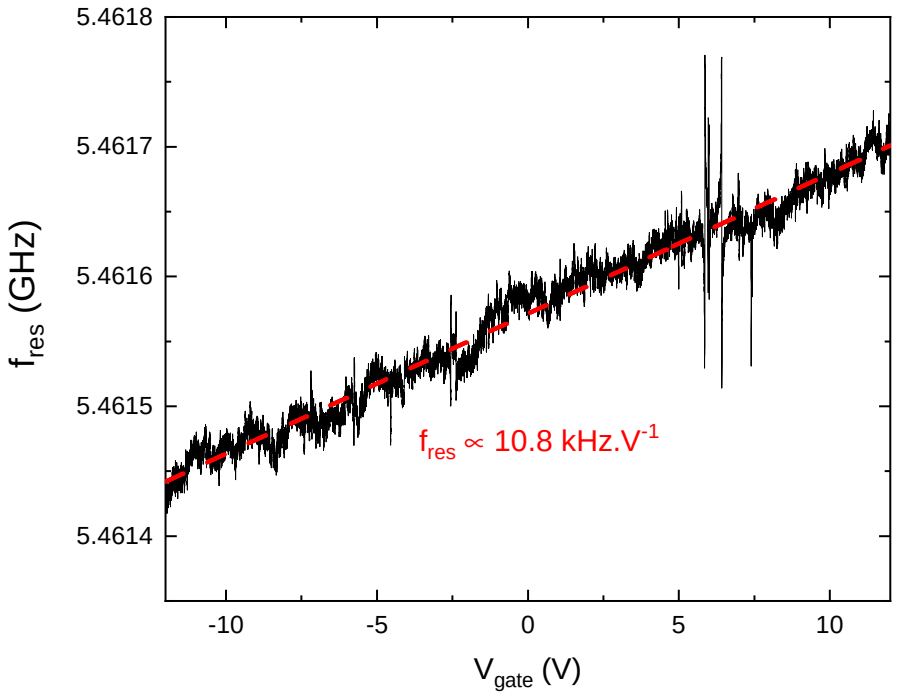

Figure 3.10. Gate dependence of the resonance frequency of Res2. The dashed red line is a linear fit with a slope of $10.8\,\mathrm{kHz}/V$.

Indeed, when using doped semiconductors, electric fields can be used to interact with the dopants and tune the conductivity of electronic devices such as in Metal Oxide Semiconductors (MOS) field effect transistors. In the case of very low dopants concentration, these effects of

accumulation or depletion of charge carriers lead to change in the permittivity ε_r of the substrate, which affects the capacitance of the devices used (see [148] for an illustration based on low doped BDD MOS capacitors). In the case of p-type semiconductors, the capacitance of MOS devices decrease when a positive gate voltage is applied due to depletion of charge carriers, which would result in an increase of f_{res}.

3.3.2.3 Coupling to TLS: presence of anticrossings

A striking feature of those gate sweeps is the presence of clear, reproducible, sharp peaks in the resonance frequency (see inset of figure 3.11) at specific gate voltages. The shape of these peaks is characteristic of an anticrossing between the resonator and a charged TLS whose energy gap ε_{tls} varies with the gate voltage (see section 1.5.1.1). This energy gap $\varepsilon_{\text{tls}}(V_g)$ takes the form: $\varepsilon_{\text{tls}}(V_g) = \sqrt{\varepsilon_0^2 + \gamma^2(V_g - V_0)^2}$ [149], where ε_0 is the energy minimum at V_0 of the TLS and γ is the strength of its coupling with V_g. When the energy of the TLS matches that of the resonator, the two systems hybridize, causing the appearance of an avoided crossing, or anticrossing, in the energy levels of the coupled system. Experimentally, this manifests as what is shown in the inset of figure 3.11: two symmetric anticrossings for each TLS. Note that two TLS anticrossings are visible in this inset, with a narrow one nested in a wider one.

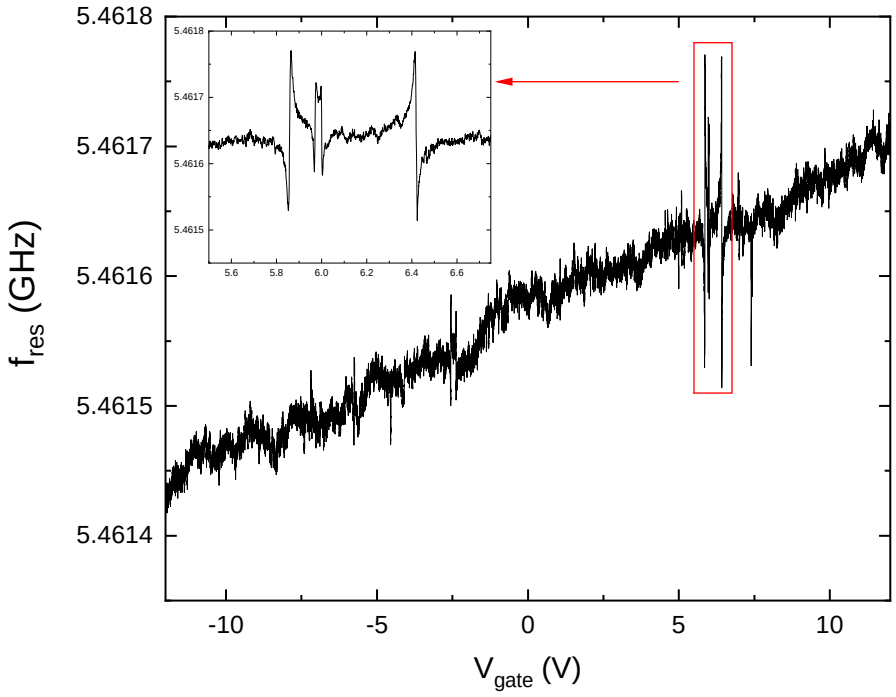

Figure 3.11. Gate dependence of the resonance frequency of resonator 2. Highlighted in red and presented in the inset is two of the ≈6 TLS anticrossings visible on this resonator during this run. The inset shows a small TLS anticrossing within a larger one.

We always find TLS anticrossings during large gate voltage sweeps, their number ranging from 2 to 30. The exact number and position of those TLS anticrossings changed between each cooldown, and sometimes even while during a cooldown. In most cases however, they were stable enough for measurement.

3.3.2.4 TLS parameters extraction

From the Jaynes-Cummings description of a TLS dispersively coupled to a resonator (see section 1.5.3.1), we have the frequencies f^+ and f^- for the upper branch and lower branch of the TLS anticrossings, respectively:

$$f^{\pm} = \frac{f_{\text{res}} + f_{\text{tls}}}{2} \pm \sqrt{\left(\frac{f_{\text{res}} - f_{\text{tls}}}{2}\right)^2 + \left(\frac{g}{2\pi}\right)^2} \tag{3.3}$$

with the TLS frequency in a static electric field $f_{\text{tls}} = \frac{\varepsilon_{\text{tls}}}{h} = \sqrt{(f^0_{\text{tls}})^2 + \left(\frac{\gamma}{h}(V_g - V_0)\right)^2}$, the TLS minimum frequency $f^0_{\text{tls}} = \frac{\varepsilon_0}{h}$ and the coupling strength g from the Jaynes-Cummings Hamiltonian. For simplicity, we dropped the factor 2π in $g/2\pi$ and express g directly in Hz. Using this model, we can fit the obtained TLS anticrossings by using the frequency of the branch closest to the one of the resonator:

$$f_{\text{fit}} = \begin{cases} f^+ \text{ if } \delta f^+ < \delta f^- \\ f^- \text{ if } \delta f^+ > \delta f^- \end{cases} \text{with } \delta f^{\pm} = |f^{\pm} - f_{\text{res}}| \tag{3.4}$$

Those fits provide the characteristics of the coupled TLS such as its coupling strength g and its minimum frequency $f^0_{\text{TLS}} = \varepsilon_0/h$ (see figure 3.12 for examples).

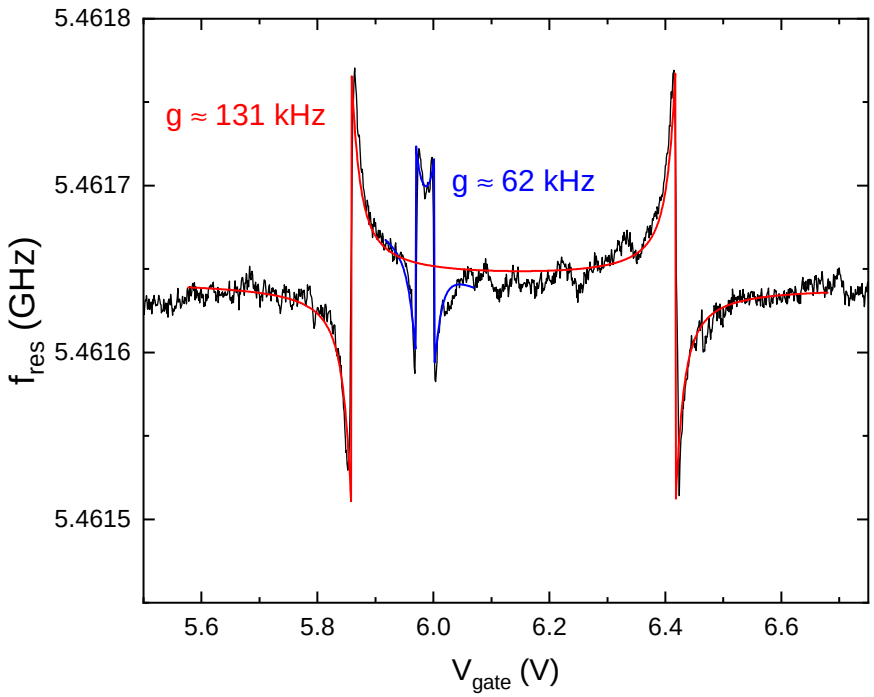

Figure 3.12. Example of two TLS anticrossing fitted on the gate dependence of the resonance frequency of resonator 2.

We applied this fit to all the clearly visible anticrossings measured during our different cooldowns, and the distribution of the resulting coupling strength g is shown in figure 3.13 for each resonator.

The lower limit on g is set by the standard deviation of our resonance frequency measurement, around 10 kHz. The red lines on the histograms represent the capacitive coupling $g_{10D} = 10 e a_0 E_{\mathrm{zpf}}/h$ of a 10 Debye dipole to the resonator, with $E_{\mathrm{zpf}} = \frac{\hbar\omega_{\mathrm{res}}}{el}\sqrt{\frac{\pi Z_C}{4R_Q}}$ the characteristic amplitude of the zero point fluctuating electric field in the resonator. While the majority of the measured g fall under these lines, several anticrossings have values of g well above them; resonator 6 even has one TLS anticrossing with $g \approx 4\, g_{10D}$.

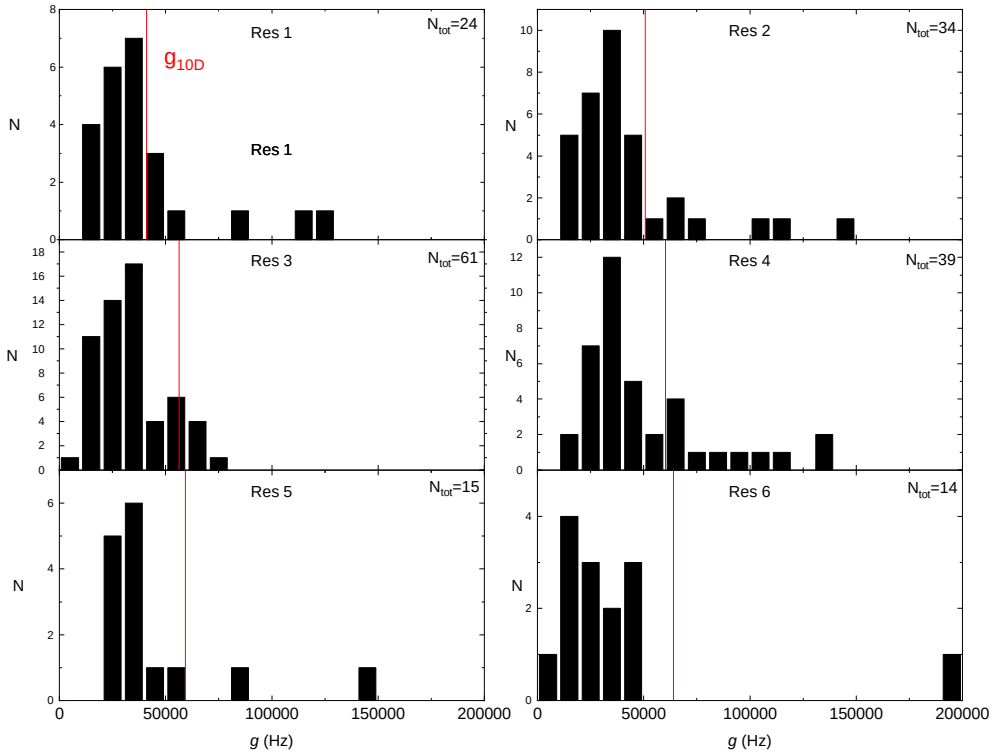

Figure 3.13. Distribution of the coupling factors g for all the resonators and all the detected TLS anticrossings during all our cooldowns. Red lines are the values of $g_{10D} = 10.e.a_0.E_{\mathrm{ZPF}}$ corresponding to the electric coupling of a 10 Debye dipole to the resonators.

3.3.2.5 Two Level System anticrossing power dependence

For one TLS anticrossing on resonator 1, we measured its dependence with the measurement power. Gate sweeps at different power are presented in figure 3.14. We first observe that the

resonance frequency of the resonator f_{res} decreases with $\bar{n}$ due to the self-Kerr effect. This frequency variation provides a spectroscopy of the TLS anticrossing. The TLS anticrossing switches between two discrete positions in V_g over time (-0.6829 and $-0.7429\,V$), but we were able to measure it nonetheless. We fitted the TLS anticrossing at $\bar{n} \approx 190$ using the model presented in 3.3.2.4, and the resulting parameters ($f^0_{\text{tls}} = 4.4622\,\text{GHz}$, $\gamma = 3.291.10^9\,\text{Hz}/V$ and $g \approx 76\,\text{kHz}$) gave us the the value of $f_{\text{tls}}(V_g)$, which is the red hyperbola in figure 3.14.

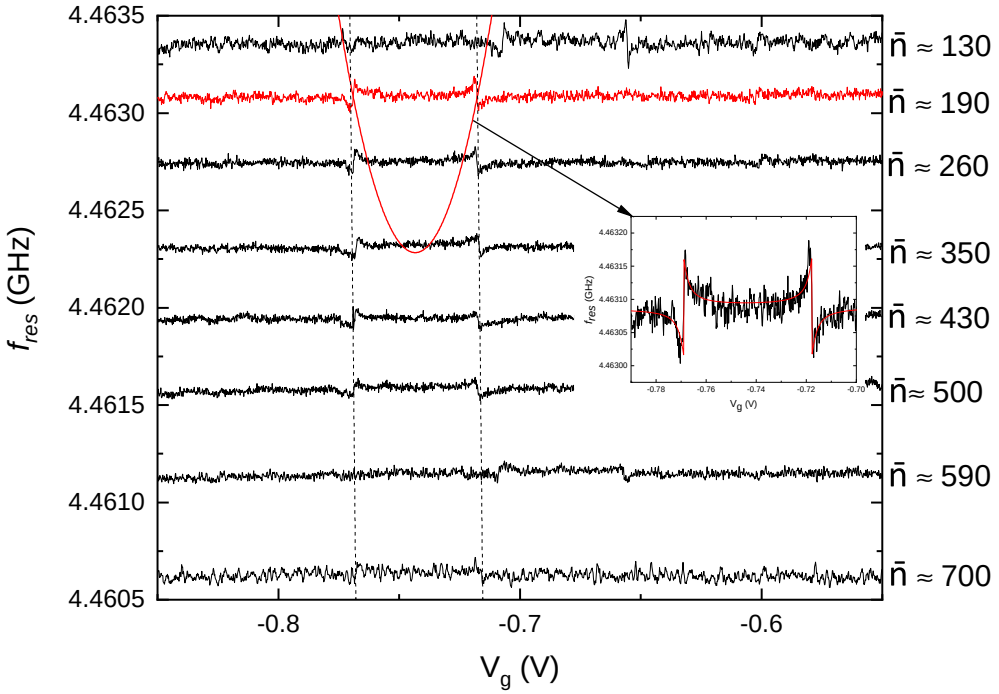

Figure 3.14. Spectroscopy of a TLS anticrossing coupled to resonator 1. The number of photons in the resonator $\bar{n}$ is increased which reduces f_{res} and thus allow us to probe lower frequencies.. The position of this TLS anticrossing in gate voltage is fluctuating between two discrete values with time, but it still remains in the measurement window. The red data curve is corresponding to $\bar{n} \approx 190$. The red hyperbola is the TLS frequency with $f^0_{\text{tls}} = 4.4622\,\text{GHz}$, $\gamma = 3.291.10^9\,\text{Hz}/V$ and $V_0 = -0.743\,V$. Those parameters were extracted using a fit of the TLS anticrossing (see inset), which also gave $g \approx 76\,\text{kHz}$.

Interestingly, the measured width of the TLS anticrossings at higher power do not follow the expected width of the hyperbola of $f_{\text{tls}}(V_g)$, extracted from $\bar{n} \approx 190$. Indeed, assuming the TLS parameters were independent of $\bar{n}$, the TLS anticrossing should be located on the red hyperbola for all $\bar{n}$. Thus the TLS anticrossing should become narrower at higher $\bar{n}$ and disappear above $\bar{n} \approx 350$, i.e. when $f_{\text{res}} < f^0_{\text{tls}}$. This is not the case in our measurement, where a TLS anticrossing happens at all powers with similar width.

We performed the fit of the TLS anticrossing for all the measured $\bar{n}$, and the results are presented in figure 3.15 and 3.16. To obtain accurate results, we performed brute force global minimisation fits, because non-linear least square minimisation did not provide good results on this TLS anticrossing, unlike the fits presented in figure 3.12. The 3 explored parameters were g, γ and f^0_{tls}; we fixed V_0 and f_{res} for each values of $\bar{n}$ as the center of the TLS anticrossing and the mean value of the resonance in the measurement window, respectively. The steps of the parameters were 1.4 kHz, 90 MHz$/V$ and 30 kHz for g, γ and f^0_{tls} respectively, and we took a grid of 100 steps per parameters, resulting in 10^6 candidate fits. We took the mean of the parameters over the first

100 best fit candidates as their final values, and the standard deviation of the same set of fits as the error estimation.

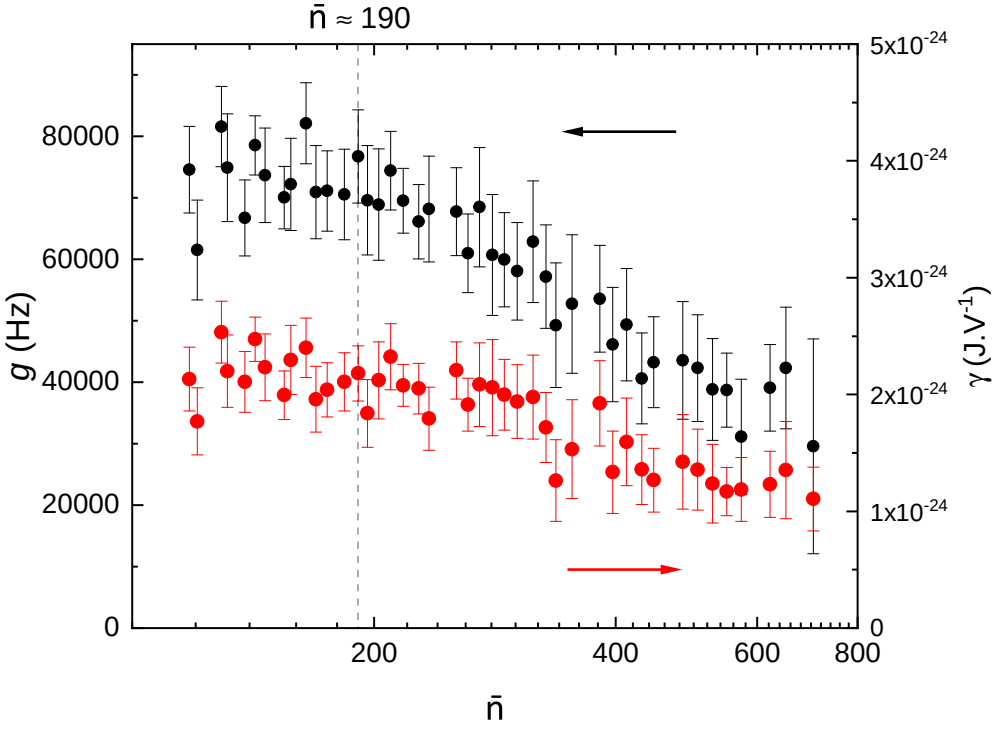

Figure 3.15. The coupling factor g in Hz (black) and the sensitivity γ (red) extracted from the TLS anticrossing fit at different number of photons in the resonator $\bar{n}$. The vertical dashed line corresponds to $n \approx 190$.

The values of g and γ decrease roughly by a factor 2 from $\bar{n} \approx 130$ to $\bar{n} \approx 700$, as is shown in figure 3.15. The dependence of $f^0_{\mathrm{TLS}} = \frac{\varepsilon_0}{h}$ with power is presented in figure 3.16 along with the resonator frequency f_{res}. The TLS minimum frequency f^0_{TLS} decreases alongside f_{res} with $\bar{n}$, and nearly at the same rate for $\bar{n} > 400$. This nearly linear relationship between f_{res} and f^0_{TLS} (see inset of figure 3.16) seems to indicate that the energy of the TLS ε_0 is linked to the same superconducting

properties responsible for the self-Kerr effect as the resonator itself.

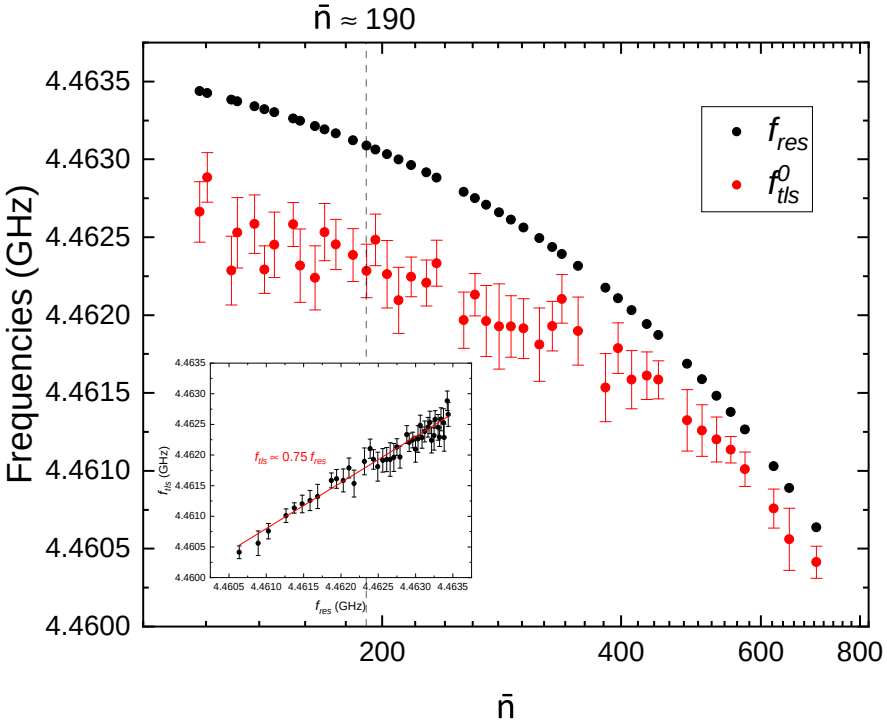

Figure 3.16. Resonance frequency f_{res} and TLS minimum frequency f^0_{tls} extracted from the TLS anti-crossing fits as a function of the number of photons n in the resonator. The vertical dashed line corresponds to $n \approx 190$. The inset respresent f^0_{tls} as a function of f_{res}, with a linear fit of slope 0.75 in red.

While the present common view on TLS coupled to superconducting resonator describes the TLS as weakly coupled and independent from the resonator itself, this behaviour has also been observed by S. E. de Graaf et al. [149] on NbN resonators. In this work, the authors attribute the observed TLS to quasiparticles trapped by the superconducting gap fluctuations. Those quasiparticles occupy a few bound states, thus creating TLSs, named qTLS. Those qTLS are dependent on the superconducting gap Δ of the material, and their frequency decreases when Δ is reduced (e.g. with a magnetic field). Moreover, the distribution of qTLS energy would be different from the STM description. Indeed, given the nature of qTLS, the authors expect their DOS to be peaked just below the value of Δ, in contrast with the constant distribution of the STM.

We measured the same behaviour on several different TLS anticrossings, on different resonators. However, one has to keep in mind that our model for the fitting of the TLS anticrossings does not take into account the effect of the number of photons in the resonator. It could be possible that this introduces a bias in the obtained values of g and f^0_{tls}, and that the actual values are different (higher for g and lower for f^0_{tls}). To confirm those results, we would need to realise two-tone spectroscopy of the TLS in order to obtain its frequency parabola. Unfortunately, due to time constraint, we did not yet realise two tone spectroscopy measurement when changing the measurement power.

3.3.2.6 Two-tone spectroscopy of a TLS anticrossing

In order to directly measure the TLS frequency hyperbola, we performed 2-tone spectroscopy of some of the TLS anticrossings. We use the $-20\,\mathrm{dB}$ coupler to inject a second microwave signal

alongside the main measurement excitation, and we measure the variation of the resonance frequency (with the PDH) or the phase of the signal (with the VNA). When the 2nd tone excites the TLS, the resonator frequency or the phase of the signal shifts, producing a 2D spectroscopic map, as shown in figure 3.17 for a VNA spectroscopy.

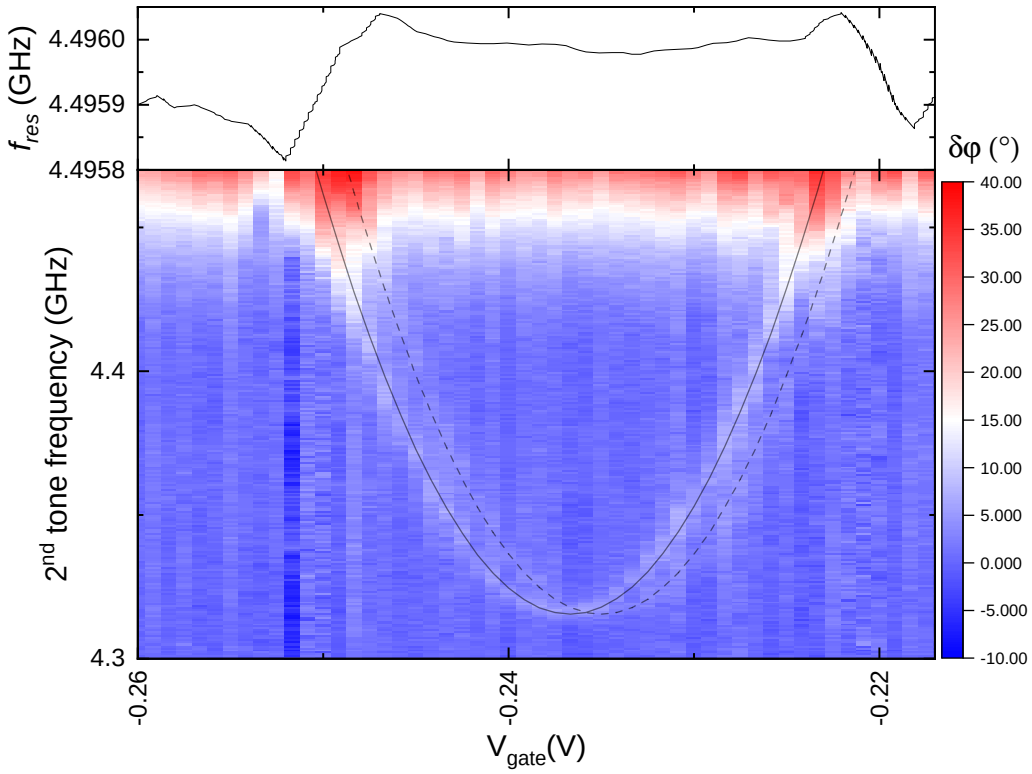

Figure 3.17. Two tone phase spectroscopy of resonator 1 done using a VNA in continuous wave mode, set at the unperturbed resonator frequency of 4.4959 GHz with $\bar{n} \approx 30$. The plain line is the frequency of a TLS $f_{\mathrm{tls}}(V_g) = \frac{\varepsilon_{\mathrm{tls}}(V_g)}{h}$ with $f^0_{\mathrm{tls}} = \frac{\varepsilon_0}{h} = 4.316\,\mathrm{GHz}$, $\gamma = 5.64\,10^{-23}\,J/V$ and $V_0 = -0.2367 V$. The dashed hyperbola equals the plain hyperbola shifted by 1.7 mV. This duplication of a TLS signal is the sign that this particular TLS is not only strongly coupled to the resonator, but also to another TLS with different frequency (which is higher than the measurement bandwidth).

The plain line in figure 3.17 represents the TLS frequency $f_{\mathrm{tls}}(V_g) = \frac{\varepsilon_{\mathrm{tls}}(V_g)}{h}$ which forms a hyperbola with $f^0_{\mathrm{tls}} = \frac{\varepsilon_0}{h} = 4.316\,\mathrm{GHz}$, $\gamma = 5.64\,10^{-23}\,\mathrm{Hz}/V$ and $V_0 = -0.2367 V$. The dashed line is the same hyperbola, but shifted by 1.7 mV. We interpret presence of this shifted hyperbola as the indication that this TLS, while being strongly coupled to our resonator, is also strongly coupled to another slower TLS [86]. This second TLS randomly produces a shift in the first TLS electromagnetic environment, which moves the first TLS V_0 between two values, hence the two shifted hyperbolas. Those two-tone measurements, while of great interest, did not usually

result in a visible hyperbola, unlike the one shown in figure 3.17, and we did not performed them systematically on all TLS anticrossings.

3.3.3 Noise measurements

The resonance frequencies f_{res} of our resonators present significant fluctuations over time. To characterise them, we obtain the frequency noise of our devices from the error signal of the PDH setup without activating the PID controller. This error signal almost linearly follows the resonance frequency shift (see section 3.2.2.1).

Using the fractional frequency fluctuations $y(t) = \frac{f_{\text{res}}(t) - f_{\text{res}}^0}{f_{\text{res}}^0}$, we calculate the Power Spectral Density (PSD) $S_y(f)$ using Welch's method [150], from which we subtract a background signal measured 10 to 40 MHz away from the resonance. We also calculate the Overlapping Allan Deviation (OADEV, see [151, 152] for exact definitions) $\sigma_y(\tau)$, which gives the RMS value of the relative frequency fluctuation over a given timescale τ. Typical noise results can be seen in figure 3.18 and 3.20. At low frequency and for all our resonators, we observe roughly a $1/f$ behaviour for $S_y(f)$ and a plateau for $\sigma_y(\tau)$, similar to what is expected for TLS-induced noise (see section 1.5.3.2).

3.3.3.1 Low frequency $1/f$ noise

The measured $S_y(f)$ (figure 3.18) of all our resonators follow a linear trend on the log-log plot up to the 10 Hz measurement bandwidth, above which $S_y(f)$ is reduced by the UHFLi input filter.

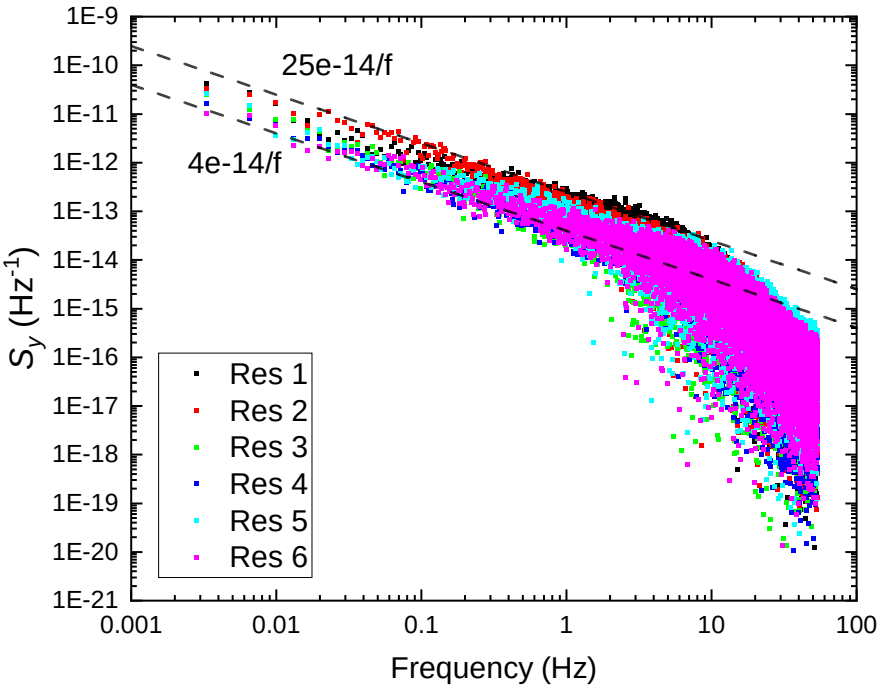

Figure 3.18. Power spectral density of the fractional frequency fluctuations of our resonators at $V_g = 0\,V$ and for $18 < \bar{n} < 235$, depending on the resonator, with $N_{\text{pts}} = 3.10^5$ and a sampling rate of 107 Hz. The dashed black line is the PSD of a flicker frequency noise, i.e. a $\frac{\alpha}{f}$ line on the log-log plot.

We fitted the linear part of these log-log plots with the function A/f^{α} to obtain the values of the dimensionless amplitude A and the slope α of the noise. The extracted values are presented in figure 3.19 for each resonator, and we have afitted value of $\alpha \approx 1.01$. We thus identify this signal with a $1/f$ noise, which is the noise type expected for TLS-induced noise in the STM. We also obtain $A \approx 5\,\text{to}\,15.10^{-14}$, with resonators 1 and 2 displaying higher values than the other resonators.

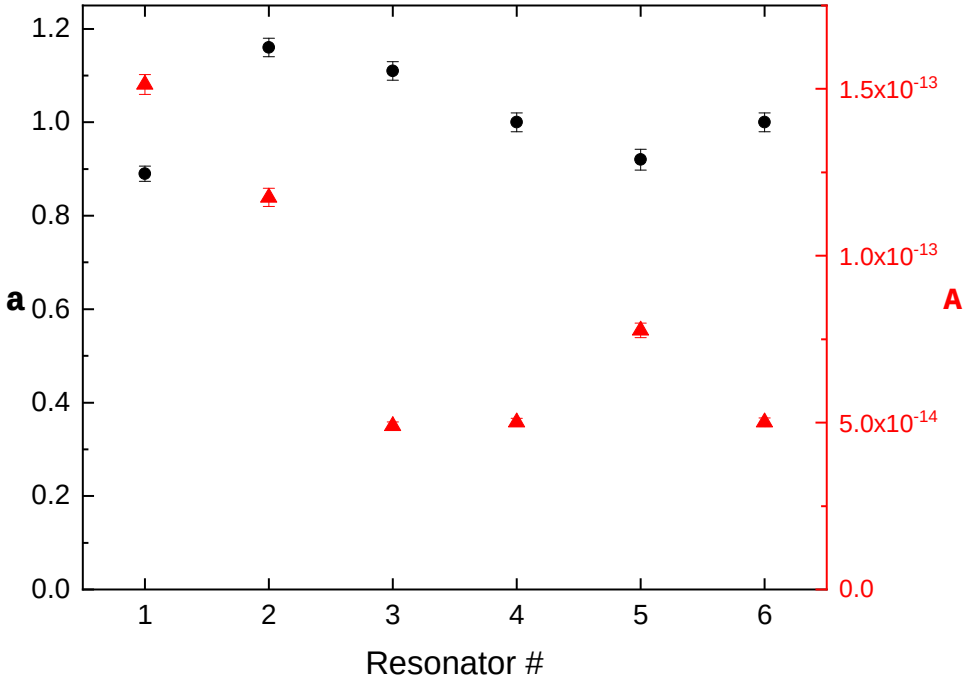

Figure 3.19. Amplitude A and slope α of the PSD presented in figure 3.18 fitted with A/f^{α}.

For the OADEV (figure 3.20) there is an initial increase at low τ due to the measurement filter at 10 Hz, and then all curves stay roughly stable on a plateau. The high τ parts of these curves (corresponding to the low frequency components in the PSD) suffer from low precision, due to the

finite number of data samples acquired. Nonetheless, the values of the plateaus $B \approx 3$ to 7.10^{-7} are in good agreement with the measured coefficients A on the PSD. Indeed, the theoretical [152] relation between those two coefficients is in the case of a perfectly $1/f$ noise is:

$$B/\sqrt{A} = \sqrt{2\ln(2)} \approx 1.18$$

which gives, using $A \approx 5$ to 15.10^{-14}, $B/10^{-7} \approx 2.64$ to 4.6. Those noise amplitudes are one order of magnitude higher than those reported in low impedance Nb resonator [153].

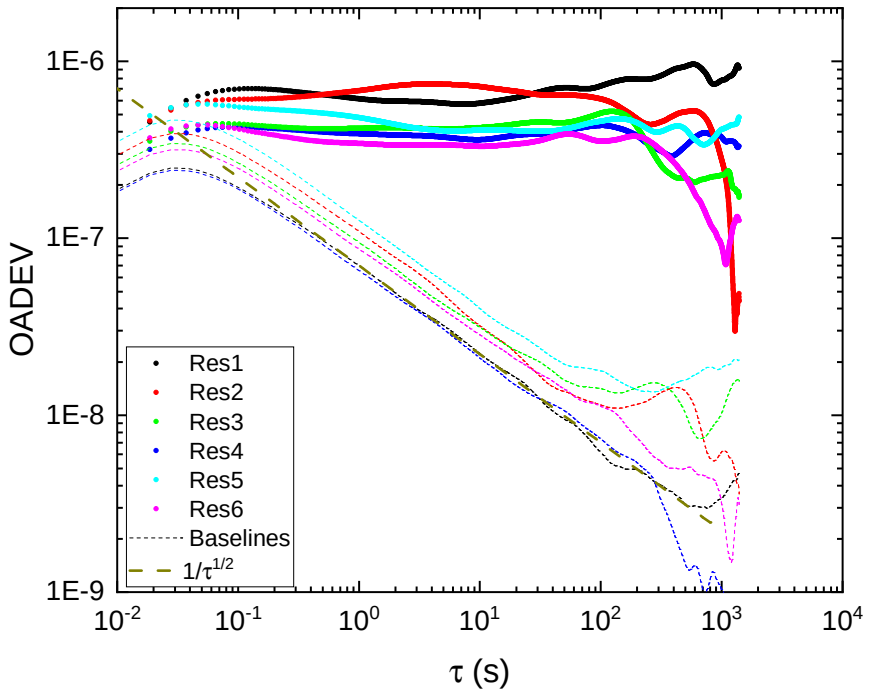

Figure 3.20. Overlapping Allan Deviation (OADEV) of the fractional frequency fluctuations of our resonators at $V_g = 0\,V$ and for $18 < \bar{n} < 235$, depending on the resonator, with $N_{\text{pts}} = 3.10^5$ and a sampling rate of 107 Hz. The thin dashed lines represent the baseline's OADEV measured next to the resonators (40 MHz shift). The thick dashed line is the OADEV of white noise, i.e. a $\frac{\alpha}{\sqrt{\tau}}$ line on the log-log plot.

As described in section, the STM model for an ensemble of uniformly distributed TLS weakly coupled to a microwave resonator yields a $1/f$ dependence for the PSD $S_y(f)$ [86, 149]. This translates into a plateau for the OADEV $\sigma_y(\tau)$ [152], which describes well our results. The amplitude of

this $1/f$ noise is predicted to depend on temperature and measurement power following equation (1.26).

3.3.3.2 Power dependence of the noise

We measured the PSD of resonator 3 at different probing power, and we fitted the linear part of the PSD (on a log-log plot) of the low frequency noise in the same way as in previous section. The results are presented in figure 3.21. At lower $\bar{n}$, the white noise coming from the measurement loop becomes dominant, reducing the crossover frequency to white noise. Thus fits at lower $\bar{n}$ present higher uncertainties, but overall, we find $\alpha \approx 1$. We do not observe any significant change of A with $\bar{n}$. The value of A stays around 7.10^{-14} for $\bar{n} \in [200, 460]$, which is similar to the value presented in figure 3.19 corresponding to a different cooldown.

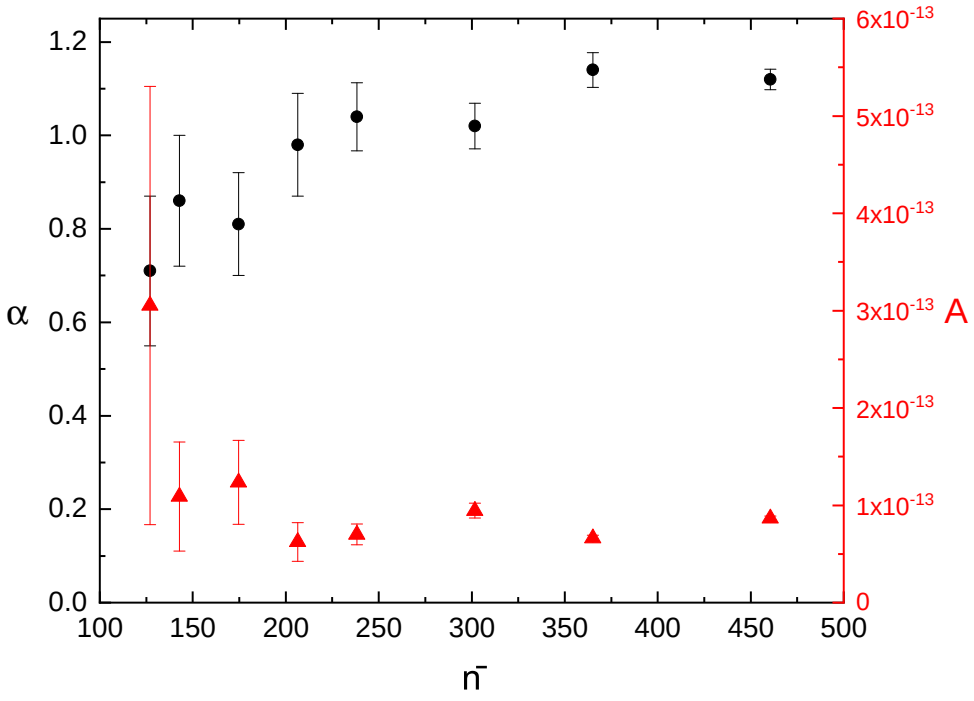

Figure 3.21. Amplitude A and slope α of the low frequency PSD of resonator 3 fitted with A/f^{α} at different $\bar{n}$.

The STM predicts that the $1/f$ noise should decrease at higher probing power, due to the saturation of the coherent TLS coupled to the resonator. This effect is not observed in our case, where the amplitude A reach a plateau at higher power. One explanation for this would be that the critical number of photons in equation (1.26) $n_c \gg 400$. Considering that at $\bar{n} \approx 400$ strong effects like non-linearities (see figure 3.9) start to become significant, we do not find this explanation satisfactory.

3.3.3.3 Temperature dependence of the noise

Similarly, we repeated the noise measurement for resonator 3 at different temperatures, from 60 to 300mK with $\bar{n} \approx 200$ (see figure 3.22). Up to 200 mK, we find $\alpha \approx 1$ and $A \approx 7.10^{-14}$. At 300mK, we

observe an increase of A to $\approx 14.10^{-14}$. These observations are also in conflict with the STM, which predicts a reduction of A caused by the thermal saturation of coherent TLS. Indeed, given that $k_b T \approx \hbar\omega_{\text{res}}$ at 300mK, we would expect a significant saturation of the coherent TLS bath up to f_{res}.

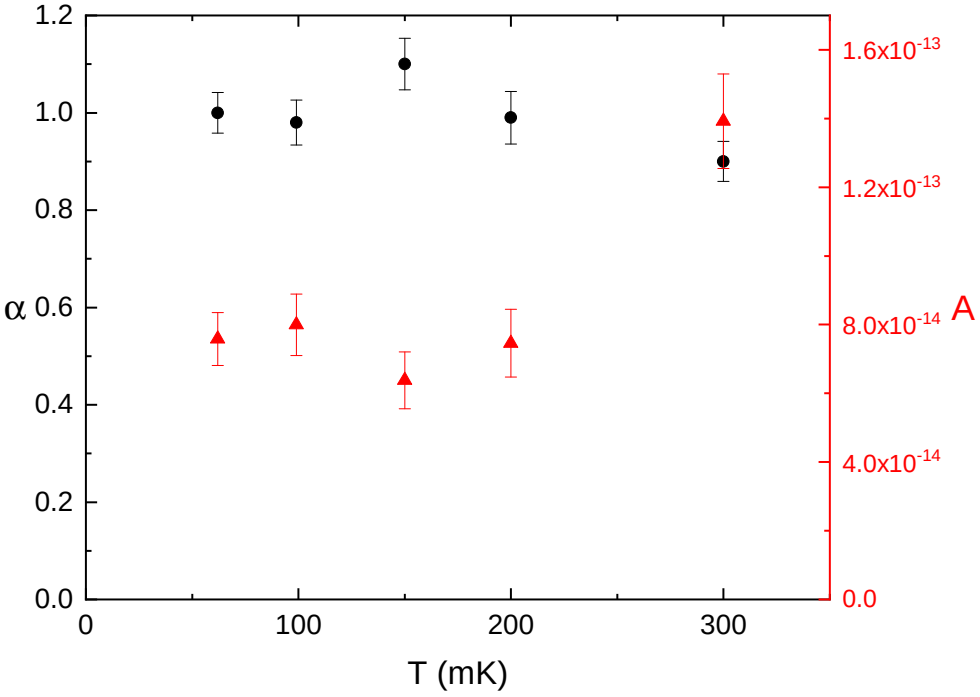

Figure 3.22. Amplitude A and slope α of the low frequency PSD of resonator 3 fitted with A/f^{α} for $\bar{n} \approx 200$ and at different temperatures.

3.3.3.4 Added TLS noise at a TLS anticrossing

We measured the noise of resonator 2 at specific values of V_g corresponding to the position of a TLS anticrossing. In figure 3.23, two consecutive V_g sweeps, separated by ≈100 s, of this anticrossing are shown. Like in in section 3.3.2.6, this particular TLS appears to be also strongly coupled to

another slower random fluctuators, leading to V_0 jumps between two discrete values. We measure the PSD of the resonance frequency shift with V_g ranging from $1.19V$ to $1.64V$ (see figure 3.24).

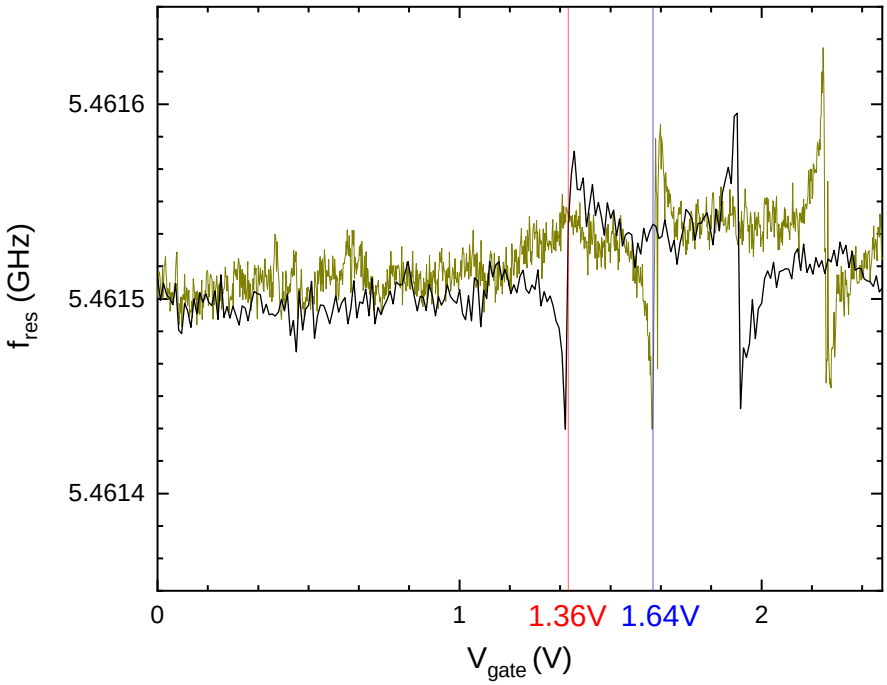

Figure 3.23. Gate voltage dependence of the resonance frequency of resonator 2 measured prior to the noise measurement at different gate voltage measured at $\bar{n} \approx 87$. The two curves were taken with a slight wait time between them. An anticrossing is present around 1.6 V and seems to alternate between two positions with a low frequency. This behaviour is similar to the one presented in section 3.3.2.6, except here the second TLS coupled to the one visible here switches less frequently.

When V_g is far from the anticrossing (e.g. $V_g = 1.19V$), we found the same type of PSD than in figure 3.18. However, when V_g is close to one of the spike of the TLS anticrossing (i.e. when the TLS is strongly interacting with the resonator) the noise increases. This increase is particularly visible at $V_g = 1.36$ and $1.64V$, which corresponds to the two discrete values for the left side of the TLS anticrossing. At $V_g = 1.36V$ the PSD shows a typical response for a Random Telegraph Signal (RTS) superposed with the $1/f$ noise coming from our resonator. This RTS like PSD is due to the random switching of this TLS during the measurement window, bringing the TLS anticrossing either on or away from the fixed value of V_g, and it induces an excess noise:

$$S_y^{\mathrm{RTS}}(f) = \frac{4C^2\tau_0}{1+(2\pi f\tau_0)^2} \tag{3.5}$$

with C the RTS amplitude and τ_0 its time constant. For $V_g = 1.3V$, this RTS noise contribution

dominates the resonance frequency noise between 1 and 100 Hz.

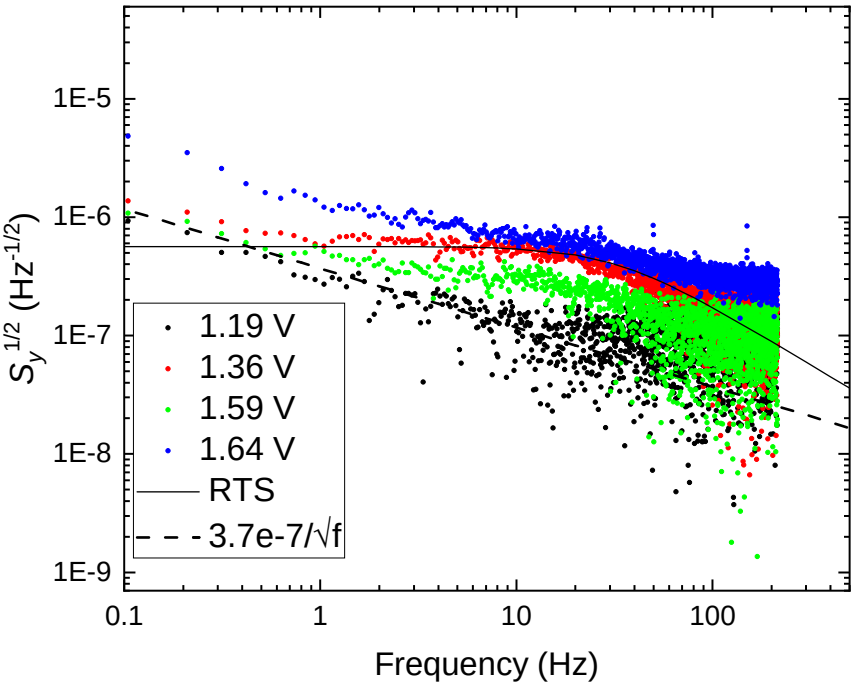

Figure 3.24. Power Spectral Density of the fractional frequency fluctuations of resonator 2 at different gate voltage around a TLS anticrossing (see figure 3.23) measured at $\bar{n} \approx 87$, with $N_{\text{pts}} = 2.10^5$ and a sampling rate of 429 Hz. The dashed black line is the PSD of a flicker frequency noise, i.e. a $\frac{\alpha}{f}$ line on the log-log plot. The plain line is the noise PSD of a Random Telegraph Signal (see formula (3.5)), with $C = 4\,10^{-6}$ and $\tau_0 = 5\,10^{-3}$ seconds.

The value $\tau_0 = 5.10^{-3}$ s extracted from the fit of the PSD with formula (3.5) translate into a characteristic frequency of 200 Hz for the considered fluctuators. This 200 Hz fluctuator cannot be identified as the slow TLS producing the variations presented in figure 3.23. Indeed, the period of the fluctuations present in figure 3.23 are of the order of 100 s. This places the RTS like noise added by this slow fluctuator outside of the accessible range of frequencies in this measurement. This shows that several individual slow incoherent TLSs can dominate the low frequency noise of our resonators at specific gate voltage.

3.4 Discussion

While we did not observe any gate modulation of the resonance frequency of our devices, we measured the presence of a large low frequency noise that could mask a weak modulation. To describe this noise, we made some comparisons along the way between our results and the STM presented in section 1.5 (and depicted again in figure 3.25 for reference). Some of our results are in agreement with this model, while others do not match its prediction. We now summarise and discuss the main similarities and difference between our results and this theory on the TLS in superconducting devices.

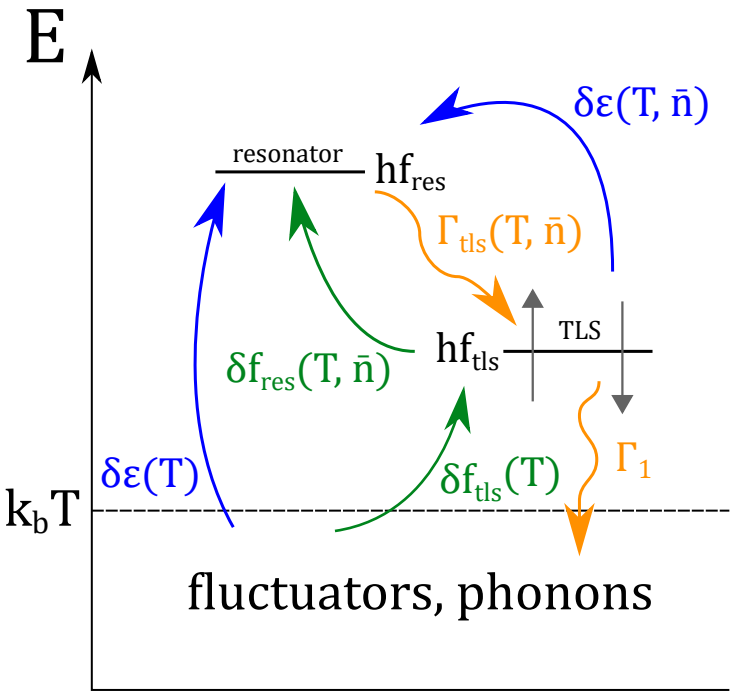

Figure 3.25. Overview of the effects described by the STM of a bath of coherent and incoherent (thermal fluctuators) TLS on a superconducting resonator. The orange paths represent energy transfers from the resonator to a coherent TLS of dissipation rate Γ_1 and then to the environment (fluctuators, phonons). The blue arrows depict the mean contribution of the TLSs increasing the dielectric constant. The green arrows stand for the time dependent fluctuations of the coherent TLS frequency which in turn induce fluctuations in the resonance frequency of the resonator.

TLS coupling strength

As described by the STM, we find that our resonators are coupled to a set of coherent TLS, some of which we can bring to strong resonant coupling using the gate-induced electric field. The resulting TLS anticrossings are well fitted by the Jaynes-Cummings Hamiltonian describing the electrostatic coupling of a TLS with a resonator in the dispersive regime. However, the values we extract for the coupling strength g of those TLSs are, for some of them, require surprisingly large electric dipoles. While this fact alone is not sufficient to rebute the STM, it raises the question of how to achieve such large couplings.

One way to explain those would be to consider that the fluctuating vacuum electric field $\vec{E}_{\text{zpf}}$ is not constant in our devices, and presents larger values due to geometrical effects. Another explanation would be the presence of dipoles with moments larger than 10 Debyes. We think that both those explanation are not suited for our experiments, as we now explain. Indeed, most of the naturally occurring dipoles in a laboratory environment have moments up to 3 or 4 Debyes (e.g. $|\vec{p}_{H_2O}| \approx 2$). Such dipoles moments are known to exist in superconducting devices [154], and dipoles of 10 Debyes is already the maximum value attainable in solids. Using a reference of 10 Debyes, as we did here, is then a safe estimation for the maximum value for the dipoles of the defects in our devices. If we consider dipoles of 3 or 4 D, the large value of 10 D somehow also encompasses a potential increase of E_{zpf} by geometrical factors of up to 3 times. Moreover, as our TiN thin film is highly inductive, we also expect the penetration depth of the microwave fields to be large ($\approx 1\,\mu m$ [128]), reducing any AC charge accumulations at the edges of our devices. This should prevent any strong increase of $\vec{E}_{\text{zpf}}$ by geometrical factors.

As a result, it seems likely that some of the TLS we observe are not coupled to the resonator only through the resonant electric field, usually considered within the STM. An additional coupling mechanism could come from TLS coupling directly to the conduction channels in our resonators,

as described in section 1.5.4.2. While we do not yet have a direct proof of that alternative coupling mechanism, we obtain several other results concerning the applicability of the STM and, more importantly, the electrostatic coupling of the TLSs in our experiment.

TLS-TLS interaction

We measure several TLS anticrossings that present clear signature of TLS-TLS interaction. Indeed, the double parabola in figure 3.17 and the anticrossings shifts in figures 3.14 and 3.23 arise from the coupling of the observed coherent TLS to at least one other incoherent fluctuator. This behaviour is considered in an extension of the STM, in the so-called Generalised Tunneling Model (GTM) [74]. These interactions of coherent TLS with incoherent fluctuators are responsible for the low frequency noise we observe in our resonators. Indeed, in some cases we observed a clear signature of a random telegraph noise in the low frequency PSD of our resonators, as can be seen in figure 3.24.

Low frequency noise and TLS saturation

We found a $1/f$ dependency of the low frequency PSD of the resonance frequency of our resonators. This result is perfectly described by the STM and an electrostatic coupling, and we found such results whatever the measurement conditions. This seems to indicate that the low frequency behaviour of the frequency noise is dominated by the TLS interacting with our resonators. However, while probing for the temperature or power dependence of this $1/f$ noise, we found no clear variation, in contradiction with the predictions. Indeed, the STM, together with an electrostatic coupling, predicts that the saturation effect of the coherent TLS, through thermal or resonant excitations, would reduce their impact on the host device (see section 1.5.3.2). We find no such effects in the low frequency PSD of our resonators.

Moreover, this saturation effect should also impact the resonance frequencies and internal quality factors. We measured this impact during preliminary measurement on TiN (section 2.2.3, but it was much less pronounced on our nanowire resonators.

Altogether, this tends to indicate that the impact of coherent TLSs on our devices is negligeable compared to the bath of incoherent fluctuators (except for coherent TLSs in strong interaction at specific gate voltage). As we described earlier, direct non-resonant interaction of fluctuators with the conduction channels in the nanowires can also be taken into account. This would explain the lack of power and temperature dependence of the noise in our devices.

3.5 Conclusions and perspectives

During this work, we investigated the behaviour of microwave resonators based on nanowire of an highly disordered superconductor, titanium nitride. While these nanowires and devices were supposed to implement the dual of the Josephson junction and of RF-SQUID, respectively, we found no evidence of this duality. More precisely, we did not observed the predicted charge modulation of the resonance frequency with the voltage applied to a local gate in our devices. This lack of observation is not, however, sufficient to conclude the absence of this duality. Indeed, results by other authors [61, 37, 62] seem to indicate that ultra-thin nanowires do exhibit a behaviour dual to the Josephson junction.

We found that, in our devices, resonance frequency fluctuations were larger than expected if they were caused by conventional coupling to electric dipoles and we observed an overwhelming low frequency noise caused by spurious Two-Level Systems. The impact of those two-level systems could not be entirely described by the Standard Tunneling Model or its extensions when using an electrostatic coupling. We discussed a novel description for the coupling of two-level systems to the electrons in the conduction channels of highly inductive nanowires, which could explain the large coupling observed in our devices. However, we could not obtain a clear answer as to which coupling scheme was dominant. We nonetheless expect that both coupling mechanism coexist, and that in any highly inductive nanowire both should be considered.

In order to realise quantum phase slip devices of the same quality as state of the art JJ based Qubits, one would then need to reduce drastically the impact of TLS. This issue is also becoming a concern in low impedance devices containing JJs as their quality factors increase. While special steps can be taken in the fabrication process to reduce the TLS density, it is improbable that this density will ever come close to zero. Using special design considerations could also decrease the number of TLS coupled to the nanowires. For example, one could use short constriction in relatively thick wires in order to implement QPS junctions, instead of a long continuous nanowire like we did here. This is the design considered in succesful works by other authors [37, 61], however we think that the poor coherence obtained in those works can be explained by the extra impact of the TLS bath on the conduction channels we describe.

Altogether, our results highlight the dire need for investigations in the field of highly disordered superconductors and their application in highly impedant quantum devices.

Bibliography

[1] H. Kamerlingh Onnes. *Further Experiments with Liquid Helium. C. On the Change of Electric Resistance of Pure Metals at Very Low Temperatures Etc. IV. The Resistance of Pure Mercury at Helium Temperatures*, volume 124, pages 261–263. Springer Netherlands, Dordrecht, 1991.

[2] J. Bardeen, L. N. Cooper, and J. R. Schrieffer. Microscopic Theory of Superconductivity. *Physical Review*, 106(1):162–164, apr 1957.

[3] B. D. Josephson. Possible new effects in superconductive tunnelling. *Physics Letters*, 1(7):251–253, jul 1962.

[4] D. Drung, C. Abmann, J. Beyer, A. Kirste, M. Peters, F. Ruede, and T. Schurig. Highly Sensitive and Easy-to-Use SQUID Sensors. *IEEE Transactions on Applied Superconductivity*, 17(2):699–704, jun 2007.

[5] B. Jeanneret and S. P. Benz. Application of the Josephson effect in electrical metrology. *The European Physical Journal Special Topics*, 172(1):181–206, jun 2009.

[6] A. J. Leggett. Macroscopic Quantum Systems and the Quantum Theory of Measurement. *Progress of Theoretical Physics Supplement*, 69:80–100, mar 1980.

[7] John M. Martinis, Michel H. Devoret, and John Clarke. Energy-Level Quantization in the Zero-Voltage State of a Current-Biased Josephson Junction. *Physical Review Letters*, 55(15):1543–1546, oct 1985.

[8] Michel H. Devoret, John M. Martinis, Daniel Esteve, and John Clarke. Resonant Activation from the Zero-Voltage State of a Current-Biased Josephson Junction. *Physical Review Letters*, 53(13):1260–1263, sep 1984.

[9] John Clarke, Andrew N. Cleland, Michel H. Devoret, Daniel Esteve, and John M. Martinis. Quantum Mechanics of a Macroscopic Variable: The Phase Difference of a Josephson Junction. *Science*, 239(4843):992–997, feb 1988.

[10] Y. Nakamura, Yu. A. Pashkin, and J. S. Tsai. Coherent control of macroscopic quantum states in a single-Cooper-Pair box. *Nature*, 398(6730):786–788, apr 1999.

[11] D. Vion, A. Aassime, A. Cottet, P. Joyez, H. Pothier, C. Urbina, D. Esteve, and M. H. Devoret. Manipulating the Quantum State of an Electrical Circuit. *Science*, 296(5569):886–889, may 2002.

[12] J. E. Mooij and Yu V. Nazarov. Superconducting nanowires as quantum phase-slip junctions. *Nature Physics*, 2(3):169, mar 2006.

[13] Albert Schmid. Diffusion and Localization in a Dissipative Quantum System. *Physical Review Letters*, 51(17):1506–1509, oct 1983.

[14] S. A. Bulgadaev. Phase diagram of a dissipative quantum system. *JETP Lett*, 39(6):264–267, 1984.

[15] A. Murani, N. Bourlet, H. le Sueur, F. Portier, C. Altimiras, D. Esteve, H. Grabert, J. Stockburger, J. Ankerhold, and P. Joyez. Absence of a Dissipative Quantum Phase Transition in Josephson Junctions. *Physical Review X*, 10(2):21003, apr 2020.

[16] F. Nguyen, N. Boulant, G. Ithier, P. Bertet, H. Pothier, D. Vion, and D. Esteve. Current to Frequency Conversion in a Josephson Circuit. *Physical Review Letters*, 99(18):187005, nov 2007.

[17] A. Grimm, F. Blanchet, R. Albert, J. Leppäkangas, S. Jebari, D. Hazra, F. Gustavo, J.-L. Thomassin, E. Dupont-Ferrier, F. Portier, and M. Hofheinz. Bright On-Demand Source of Antibunched Microwave Photons Based on Inelastic Cooper Pair Tunneling. *Physical Review X*, 9(2):21016, apr 2019.

[18] A. M. Hriscu and Yu. V. Nazarov. Model of a Proposed Superconducting Phase Slip Oscillator: A Method for Obtaining Few-Photon Nonlinearities. *Physical Review Letters*, 106(7):77004, feb 2011.

[19] Michael Tinkham. *Introduction to Superconductivity*. Courier Corporation, jan 2004.

[20] Frank Arute, Kunal Arya, Ryan Babbush, Dave Bacon, Joseph C. Bardin, Rami Barends, Rupak Biswas, Sergio Boixo, Fernando G. S. L. Brandao, David A. Buell, Brian Burkett, Yu Chen, Zijun Chen, Ben Chiaro, Roberto Collins, William Courtney, Andrew Dunsworth, Edward Farhi, Brooks Foxen, Austin Fowler, Craig Gidney, Marissa Giustina, Rob Graff, Keith Guerin, Steve Habegger, Matthew P. Harrigan, Michael J. Hartmann, Alan Ho, Markus Hoffmann, Trent Huang, Travis S. Humble, Sergei V. Isakov, Evan Jeffrey, Zhang Jiang, Dvir Kafri, Kostyantyn Kechedzhi, Julian Kelly, Paul V. Klimov, Sergey Knysh, Alexander Korotkov, Fedor Kostritsa, David Landhuis, Mike Lindmark, Erik Lucero, Dmitry Lyakh, Salvatore Mandrà, Jarrod R. McClean, Matthew McEwen, Anthony Megrant, Xiao Mi, Kristel Michielsen, Masoud Mohseni, Josh Mutus, Ofer Naaman, Matthew Neeley, Charles Neill, Murphy Yuezhen Niu, Eric Ostby, Andre Petukhov, John C. Platt, Chris Quintana, Eleanor G. Rieffel, Pedram Roushan, Nicholas C. Rubin, Daniel Sank, Kevin J. Satzinger, Vadim Smelyanskiy, Kevin J. Sung, Matthew D. Trevithick, Amit Vainsencher, Benjamin Villalonga, Theodore White, Z. Jamie Yao, Ping Yeh, Adam Zalcman, Hartmut Neven, and John M. Martinis. Quantum supremacy using a programmable superconducting processor. *Nature*, 574(7779):505–510, oct 2019.

[21] U. Alvarez-Rodriguez, M. Sanz, L. Lamata, and E. Solano. Quantum Artificial Life in an IBM Quantum Computer. *Scientific Reports*, 8(1):14793, oct 2018.

[22] P. G. De Gennes. *Superconductivity Of Metals And Alloys*. Avalon Publishing, mar 1999.

[23] Sophie Gueron and Quantronics Group. *Quasiparticles in a Diffusive Conductor: Interaction and Pairing*. PhD thesis.

[24] Venkat Chandrasekhar. An introduction to the quasiclassical theory of superconductivity for diffusive proximity-coupled systems. *ArXiv:cond-mat/0312507*, nov 2004.

[25] J. Rammer and H. Smith. Quantum field-theoretical methods in transport theory of metals. *Reviews of Modern Physics*, 58(2):323–359, apr 1986.

[26] Albert Schmid. Diffusion and Localization in a Dissipative Quantum System. *Physical Review Letters*, 51(17):1506–1509, oct 1983.

[27] S.A Bulgadaev. Phase diagram of a dissipative quantum system.

[28] V. Bouchiat, D. Vion, P. Joyez, D. Esteve, and M. H. Devoret. Quantum coherence with a single Cooper pair. *Physica Scripta*, 1998(T76):165, 1998.

[29] Anil Murani, Nicolas Bourlet, Hélène le Sueur, Fabien Portier, Carles Altimiras, Daniel Esteve, Hermann Grabert, Jürgen Stockburger, Joachim Ankerhold, and Philippe Joyez. Absence of a dissipative quantum phase transition in Josephson junctions. *Physical Review X*, 10(2):21003, apr 2020.

[30] B. D. Josephson. The discovery of tunnelling supercurrents. *Reviews of Modern Physics*, 46(2):251–254, apr 1974.

[31] R. Landauer. Spatial Variation of Currents and Fields Due to Localized Scatterers in Metallic Conduction. *IBM Journal of Research and Development*, 1(3):223–231, jul 1957.

[32] Jens Koch, Terri M. Yu, Jay Gambetta, A. A. Houck, D. I. Schuster, J. Majer, Alexandre Blais, M. H. Devoret, S. M. Girvin, and R. J. Schoelkopf. Charge-insensitive qubit design derived from the Cooper pair box. *Physical Review A*, 76(4):42319, oct 2007.

[33] Anton Frisk Kockum and Franco Nori. Quantum bits with Josephson junctions. *ArXiv:1908.09558 [cond-mat, physics:quant-ph]*, aug 2019.

[34] A. M. Hriscu and Yu. V. Nazarov. Coulomb blockade due to quantum phase slips illustrated with devices. *Physical Review B*, 83(17):174511, may 2011.

[35] Peter K. Day, Henry G. LeDuc, Benjamin A. Mazin, Anastasios Vayonakis, and Jonas Zmuidzinas. A broadband superconducting detector suitable for use in large arrays. *Nature*, 425(6960):817–821, oct 2003.

[36] S. E. de Graaf, R. Shaikhaidarov, T. Lindström, A. Ya. Tzalenchuk, and O. V. Astafiev. Charge control of blockade of Cooper pair tunneling in highly disordered TiN nanowires in an inductive environment. *Physical Review B*, 99(20):205115, may 2019.

[37] O. V. Astafiev, L. B. Ioffe, S. Kafanov, Yu A. Pashkin, K. Yu Arutyunov, D. Shahar, O. Cohen, and J. S. Tsai. Coherent quantum phase slip. *Nature*, 484(7394):355, apr 2012.

[38] Jiahao Kang, Yuji Matsumoto, Xiang Li, Junkai Jiang, Xuejun Xie, Keisuke Kawamoto, Munehiro Kenmoku, Jae Hwan Chu, Wei Liu, Junfa Mao, Kazuyoshi Ueno, and Kaustav Banerjee. On-chip intercalated-graphene inductors for next-generation radio frequency electronics. *Nature Electronics*, 1(1):46–51, jan 2018.

[39] Yen-Hsiang Lin, J. Nelson, and A. M. Goldman. Superconductivity of very thin films: The superconductor-insulator transition. *Physica C: Superconductivity and its Applications*, 514:130–141, jul 2015.

[40] Vsevolod F. Gantmakher and Valery T. Dolgopolov. Superconductor-insulator quantum phase transition. *Physics-Uspekhi*, 53(1):1, 2010.

[41] A. Frydman. The superconductor insulator transition in systems of ultrasmall grains. *ArXiv:cond-mat/0102067*, feb 2001.

[42] Yongguang Qin, Carlos L. Vicente, and Jongsoo Yoon. Magnetically induced metallic phase in superconducting tantalum films. *Physical Review B*, 73(10):100505, mar 2006.

[43] K. H. Sarwa B. Tan, Kevin A. Parendo, and A. M. Goldman. Evidence of spatially inhomogeneous pairing on the insulating side of a disorder-tuned superconductor-insulator transition. *Physical Review B*, 78(1):14506, jul 2008.

[44] M. R. Beasley, J. E. Mooij, and T. P. Orlando. Possibility of Vortex-Antivortex Pair Dissociation in Two-Dimensional Superconductors. *Physical Review Letters*, 42(17):1165–1168, apr 1979.

[45] T. I. Baturina, S. V. Postolova, A. Yu Mironov, A. Glatz, M. R. Baklanov, and V. M. Vinokur. Superconducting phase transitions in ultrathin TiN films. *EPL (Europhysics Letters)*, 97(1):17012, 2012.

[46] K. Yu. Arutyunov, D. S. Golubev, and A. D. Zaikin. Superconductivity in one dimension. *Physics Reports*, 464(1):1–70, jul 2008.

[47] R. S. Newbower, M. R. Beasley, and M. Tinkham. Fluctuation Effects on the Superconducting Transition of Tin Whisker Crystals. *Physical Review B*, 5(3):864–868, feb 1972.

[48] J. S. Langer and Vinay Ambegaokar. Intrinsic Resistive Transition in Narrow Superconducting Channels. *Physical Review*, 164(2):498–510, dec 1967.

[49] X. S. Ling, J. D. McCambridge, N. D. Rizzo, J. W. Sleight, D. E. Prober, L. R. Motowidlo, and B. A. Zeitlin. Fluctuation Effects on a Strongly Pinned Vortex Lattice in a Thin Type-II Superconducting Wire. *Physical Review Letters*, 74(5):805–808, jan 1995.

[50] F. Sharifi, A. V. Herzog, and R. C. Dynes. Crossover from two to one dimension in in situ grown wires of Pb. *Physical Review Letters*, 71(3):428–431, jul 1993.

[51] N. Giordano. Evidence for Macroscopic Quantum Tunneling in One-Dimensional Superconductors. *Physical Review Letters*, 61(18):2137–2140, oct 1988.

[52] Andrei D. Zaikin, Dmitrii S. Golubev, Anne van Otterlo, and Gergely T. Zimányi. Quantum Phase Slips and Transport in Ultrathin Superconducting Wires. *Physical Review Letters*, 78(8):1552–1555, feb 1997.

[53] A. Bezryadin, C. N. Lau, and M. Tinkham. Quantum suppression of superconductivity in ultrathin nanowires. *Nature*, 404(6781):971, apr 2000.

[54] J. E. Mooij and C. J. P. M. Harmans. Phase-slip flux qubits. *New Journal of Physics*, 7(1):219, 2005.

[55] Audrey Cottet. *Implémentation d'un bit quantique dans un circuit supraconducteur / Implementation of a quantum bit in a superconducting circuit*. PhD thesis, Université Pierre et Marie Curie - Paris VI, sep 2002.

[56] A. O Caldeira and A. J Leggett. Quantum tunnelling in a dissipative system. *Annals of Physics*, 149(2):374–456, sep 1983.

[57] Mihajlo Vanević and Yuli V. Nazarov. Quantum Phase Slips in Superconducting Wires with Weak Inhomogeneities. *Physical Review Letters*, 108(18):187002, may 2012.

[58] J. T. Peltonen, O. V. Astafiev, Yu. P. Korneeva, B. M. Voronov, A. A. Korneev, I. M. Charaev, A. V. Semenov, G. N. Golt'sman, L. B. Ioffe, T. M. Klapwijk, and J. S. Tsai. Coherent flux tunneling through NbN nanowires. *Physical Review B*, 88(22):220506, dec 2013.

[59] J. T. Peltonen, Z. H. Peng, Yu. P. Korneeva, B. M. Voronov, A. A. Korneev, A. V. Semenov, G. N. Gol'tsman, J. S. Tsai, and O. V. Astafiev. Coherent dynamics and decoherence in a superconducting weak link. *Physical Review B*, 94(18):180508, nov 2016.

[60] Morten Kjaergaard, Mollie E. Schwartz, Jochen Braumüller, Philip Krantz, Joel I.-Jan Wang, Simon Gustavsson, and William D. Oliver. Superconducting Qubits: Current State of Play. *Annual Review of Condensed Matter Physics*, 11(1):369–395, mar 2020.

[61] S. E. de Graaf, S. T. Skacel, T. Hönigl-Decrinis, R. Shaikhaidarov, H. Rotzinger, S. Linzen, M. Ziegler, U. Hübner, H.-G. Meyer, V. Antonov, E. Il'ichev, A. V. Ustinov, A. Ya Tzalenchuk, and O. V. Astafiev. Charge quantum interference device. *Nature Physics*, 14(6):590–594, jun 2018.

[62] JANNE LEHTINEN. *QUANTUM FLUCTUATIONS IN SUPERCONDUCTING NANOSTRUCTURES*. PhD thesis, University of Jyväskylä, 2014.

[63] A. Anthore, H. Pothier, and D. Esteve. Density of States in a Superconductor Carrying a Supercurrent. *Physical Review Letters*, 90(12):127001, mar 2003.

[64] P Joyez. Nonlinearity in superconducting resonators. *Unpublished*.

[65] W. A. Phillips. Tunneling states in amorphous solids. *Journal of Low Temperature Physics*, 7(3):351–360, may 1972.

[66] P. w Anderson, B. I. Halperin, and c M. Varma. Anomalous low-temperature thermal properties of glasses and spin glasses. *The Philosophical Magazine: A Journal of Theoretical Experimental and Applied Physics*, 25(1):1–9, jan 1972.

[67] Clemens Müller, Jared H. Cole, and Jürgen Lisenfeld. Towards understanding two-level-systems in amorphous solids – Insights from quantum circuits. *Reports on Progress in Physics*, 82(12):124501, dec 2019.

[68] W. Woods, G. Calusine, A. Melville, A. Sevi, E. Golden, D.K. Kim, D. Rosenberg, J.L. Yoder, and W.D. Oliver. Determining Interface Dielectric Losses in Superconducting Coplanar-Waveguide Resonators. *Physical Review Applied*, 12(1):14012, jul 2019.

[69] M. Steffen, M. Sandberg, and S. Srinivasan. Recent research trends for high coherence quantum circuits. *Superconductor Science and Technology*, 30(3):30301, jan 2017.

[70] P. Dutta and P. M. Horn. Low-frequency fluctuations in solids: $\frac{1}{f}$ noise. *Reviews of Modern Physics*, 53(3):497–516, jul 1981.

[71] J. L. Black and B. I. Halperin. Spectral diffusion, phonon echoes, and saturation recovery in glasses at low temperatures. *Physical Review B*, 16(6):2879–2895, sep 1977.

[72] Grigorij J. Grabovskij, Torben Peichl, Jürgen Lisenfeld, Georg Weiss, and Alexey V. Ustinov. Strain Tuning of Individual Atomic Tunneling Systems Detected by a Superconducting Qubit. *Science*, 338(6104):232–234, oct 2012.

[73] Jürgen Lisenfeld, Grigorij J. Grabovskij, Clemens Müller, Jared H. Cole, Georg Weiss, and Alexey V. Ustinov. Observation of directly interacting coherent two-level systems in an amorphous material. *Nature Communications*, 6, feb 2015.

[74] Lara Faoro and Lev B. Ioffe. Generalized Tunneling Model for TLS in amorphous materials and its predictions for their dephasing and the noise in superconducting microresonators. *Physical Review B*, 91(1):14201, jan 2015.

[75] Anthony J. Leggett and Dervis C. Vural. "Tunneling Two-Level Systems" Model of the Low-Temperature Properties of Glasses: Are "Smoking-Gun" Tests Possible? *The Journal of Physical Chemistry B*, 117(42):12966–12971, oct 2013.

[76] Clare C. Yu. Why Study Noise Due to Two Level Systems: A Suggestion for Experimentalists. *Journal of Low Temperature Physics*, 137(3):251–265, nov 2004.

[77] Kartiek Agarwal, Ivar Martin, Mikhail D. Lukin, and Eugene Demler. Polaronic model of two-level systems in amorphous solids. *Physical Review B*, 87(14):144201, apr 2013.

[78] SangKook Choi, Dung-Hai Lee, Steven G. Louie, and John Clarke. Localization of Metal-Induced Gap States at the Metal-Insulator Interface: Origin of Flux Noise in SQUIDs and Superconducting Qubits. *Physical Review Letters*, 103(19):197001, nov 2009.

[79] S. E. de Graaf, L. Faoro, J. Burnett, A. A. Adamyan, A. Ya Tzalenchuk, S. E. Kubatkin, T. Lindström, and A. V. Danilov. Suppression of low-frequency charge noise in superconducting resonators by surface spin desorption. *Nature Communications*, 9(1):1143, mar 2018.

[80] Wayne Woods, Greg Calusine, Alexander Melville, Arjan Sevi, Evan Golden, David K. Kim, Danna Rosenberg, Jonilyn L. Yoder, and William D. Oliver. Determining interface dielectric losses in superconducting coplanar waveguide resonators. *Physical Review Applied*, 12(1):14012, jul 2019.

[81] E.T. Jaynes and F.W. Cummings. Comparison of quantum and semiclassical radiation theories with application to the beam maser. *Proceedings of the IEEE*, 51(1):89–109, jan 1963.

[82] Camille Janvier. *Coherent Manipulation of Andreev Bound States in an Atomic Contact*. These de doctorat, Université Paris-Saclay (ComUE), sep 2016.

[83] Serge Haroche and Jean-Michel Raimond. *Exploring the Quantum: Atoms, Cavities, and Photons*. OUP Oxford, aug 2006.

[84] H. Wang, M. Hofheinz, J. Wenner, M. Ansmann, R. C. Bialczak, M. Lenander, Erik Lucero, M. Neeley, A. D. O'Connell, D. Sank, M. Weides, A. N. Cleland, and John M. Martinis. Improving the coherence time of superconducting coplanar resonators. *Applied Physics Letters*, 95(23):233508, dec 2009.

[85] W. A. Phillips. Two-level states in glasses. *Reports on Progress in Physics*, 50(12):1657–1708, dec 1987.

[86] J. Burnett, L. Faoro, and T. Lindström. Analysis of high quality superconducting resonators: consequences for TLS properties in amorphous oxides. *Superconductor Science and Technology*, 29(4):44008, mar 2016.

[87] Lara Faoro and Lev B. Ioffe. Internal Loss of Superconducting Resonators Induced by Interacting Two-Level Systems. *Physical Review Letters*, 109(15):157005, oct 2012.

[88] Lara Faoro and Lev B. Ioffe. Interacting tunneling model for two-level systems in amorphous materials and its predictions for their dephasing and noise in superconducting microresonators. *Physical Review B*, 91(1):14201, jan 2015.

[89] Shwetank Kumar, Jiansong Gao, Jonas Zmuidzinas, Benjamin A. Mazin, Henry G. LeDuc, and Peter K. Day. Temperature dependence of the frequency and noise of superconducting coplanar waveguide resonators. *Applied Physics Letters*, 92(12):123503, mar 2008.

[90] T. Lindström, J. E. Healey, M. S. Colclough, C. M. Muirhead, and A. Ya. Tzalenchuk. Properties of superconducting planar resonators at millikelvin temperatures. *Physical Review B*, 80(13):132501, oct 2009.

[91] J. Burnett, L. Faoro, I. Wisby, V. L. Gurtovoi, A. V. Chernykh, G. M. Mikhailov, V. A. Tulin, R. Shaikhaidarov, V. Antonov, P. J. Meeson, A. Ya Tzalenchuk, and T. Lindström. Evidence for interacting two-level systems from the 1/ f noise of a superconducting resonator. *Nature Communications*, 5(1):4119, jun 2014.

[92] T. Lindström, J. Burnett, M. Oxborrow, and A Ya. Tzalenchuk. Pound-locking for characterization of superconducting microresonators. *Review of Scientific Instruments*, 82(10):104706, oct 2011.

[93] Hélène le Sueur, Artis Svilans, Nicolas Bourlet, Anil Murani, Laurent Bergé, Louis Dumoulin, and Philippe Joyez. Microscopic charged fluctuators as a limit to the coherence of disordered superconductor devices. *ArXiv:1810.12801 [cond-mat]*, oct 2018.

[94] M. R. Vissers, J. Gao, D. S. Wisbey, D. A. Hite, C. C. Tsuei, A. D. Corcoles, M. Steffen, and D. P. Pappas. Low loss superconducting titanium nitride coplanar waveguide resonators. *Applied Physics Letters*, 97(23):232509, dec 2010.

[95] P. C. J. J. Coumou, M. R. Zuiddam, E. F. C. Driessen, P. J. de Visser, J. J. A. Baselmans, and T. M. Klapwijk. Microwave Properties of Superconducting Atomic-Layer Deposited TiN Films. *IEEE Transactions on Applied Superconductivity*, 23(3):7500404–7500404, jun 2013.

[96] Amanda S. Barnard. *The Diamond Formula: Diamond Synthesis–a Gemmological Perspective*. Butterworth-Heinemann, 2000.

[97] Jessica Bousquet. *Propriétés optiques et électroniques du diamant fortement dopé au bore*. PhD thesis, Université Grenoble Alpes, jul 2015.

[98] Naoji Fujimori, Hideaki Nakahata, and Takahiro Imai. Properties of Boron-Doped Epitaxial Diamond Films. *Japanese Journal of Applied Physics*, 29(Part 1, No. 5):824–827, may 1990.

[99] M. Werner and R. Locher. Growth and application of undoped and doped diamond films. *Reports on Progress in Physics*, 61(12):1665–1710, dec 1998.

[100] X. Blase. Quasiparticle band structure and screening in silicon and carbon clathrates. *Physical Review B*, 67(3):35211, jan 2003.

[101] T. Klein, P. Achatz, J. Kacmarcik, C. Marcenat, F. Gustafsson, J. Marcus, E. Bustarret, J. Pernot, F. Omnes, Bo E. Sernelius, C. Persson, A. Ferreira da Silva, and C. Cytermann. Metal-insulator transition and superconductivity in boron-doped diamond. *Physical Review B*, 75(16):165313, apr 2007.

[102] E. A. Ekimov, V. A. Sidorov, E. D. Bauer, N. N. Mel'nik, N. J. Curro, J. D. Thompson, and S. M. Stishov. Superconductivity in diamond. *Nature*, 428(6982):542–545, apr 2004.

[103] Y. Takano, M. Nagao, K. Kobayashi, H. Umezawa, I. Sakaguchi, M. Tachiki, T. Hatano, and H. Kawarada. Superconductivity in CVD Diamond Thin Film Well-Above Liquid Helium Temperature. *Applied Physics Letters*, 85(14):2851–2853, oct 2004.

[104] M. Hoesch, T. Fukuda, T. Takenouchi, J. P. Sutter, S. Tsutsui, A. Q. R. Baron, M. Nagao, Y. Takano, H. Kawarada, and J. Mizuki. Acoustic and optical phonons in metallic diamond. *Science and Technology of Advanced Materials*, 7:0, aug 2006.

[105] E. Bustarret, J. Kačmarčik, C. Marcenat, E. Gheeraert, C. Cytermann, J. Marcus, and T. Klein. Dependence of the Superconducting Transition Temperature on the Doping Level in Single-Crystalline Diamond Films. *Physical Review Letters*, 93(23):237005, dec 2004.

[106] V. A. Sidorov, E. A. Ekimov, S. M. Stishov, E. D. Bauer, and J. D. Thompson. Superconducting and normal-state properties of heavily hole-doped diamond. *Physical Review B*, 71(6):60502, feb 2005.

[107] E Bustarret, P Achatz, B Sacépé, C Chapelier, C Marcenat, L Ortéga, and T Klein. Metal-to-insulator transition and superconductivity in boron-doped diamond. *Philosophical Transactions of the Royal Society A: Mathematical, Physical and Engineering Sciences*, 366(1863):267–279, jan 2008.

[108] Akihiro Kawano, Hitoshi Ishiwata, Shingo Iriyama, Ryosuke Okada, Takahide Yamaguchi, Yoshihiko Takano, and Hiroshi Kawarada. Superconductor-to-insulator transition in boron-doped diamond films grown using chemical vapor deposition. *Physical Review B*, 82(8):85318, aug 2010.

[109] Jonathan E. Moussa and Marvin L. Cohen. Constraints on ${T}_{c}$ for superconductivity in heavily boron-doped diamond. *Physical Review B*, 77(6):64518, feb 2008.

[110] Yuki Sakai, James R. Chelikowsky, and Marvin L. Cohen. Heavy boron doping in superconducting carbon materials. *Physical Review Materials*, 4(5):54801, may 2020.

[111] Philipp Achatz. *Superconductivity in Diamond and Related Materials*. PhD thesis, Université Joseph-Fourier - Grenoble I, nov 2008.

[112] D. C. Mattis and J. Bardeen. Theory of the Anomalous Skin Effect in Normal and Superconducting Metals. *Physical Review*, 111(2):412–417, jul 1958.

[113] Gufei Zhang, Monika Zeleznik, Johan Vanacken, Paul W. May, and Victor V. Moshchalkov. Metal–Bosonic Insulator–Superconductor Transition in Boron-Doped Granular Diamond. *Physical Review Letters*, 110(7):77001, feb 2013.

[114] Gufei Zhang, Tomas Samuely, Jozef Kačmarčík, Evgeny A. Ekimov, Jun Li, Johan Vanacken, Pavol Szabó, Junwei Huang, Paulo J. Pereira, Dorin Cerbu, and Victor V. Moshchalkov. Bosonic Anomalies in Boron-Doped Polycrystalline Diamond. *Physical Review Applied*, 6(6):64011, dec 2016.

[115] C. Coleman, F. Mazhandu, S. J. Reddhi, T. Aslan, D. Wei, C. Huynh, P. Gnauck, and S. Bhattacharyya. Superconducting Diamond as a platform for quantum technologies. *Journal of Physics: Conference Series*, 1461:12014, mar 2020.

[116] Gufei Zhang, Stuart Turner, Evgeny A. Ekimov, Johan Vanacken, Matias Timmermans, Tomás Samuely, Vladimir A. Sidorov, Sergei M. Stishov, Yinggang Lu, Bart Deloof, Bart Goderis, Gustaaf Van Tendeloo, Joris Van de Vondel, and Victor V. Moshchalkov. Global and Local Superconductivity in Boron-Doped Granular Diamond. *Advanced Materials*, 26(13):2034–2040, apr 2014.

[117] B. L. Willems, V. H. Dao-, J. Vanacken, L. F. Chibotaru, V. V. Moshchalkov, I. Guillamón, H. Suderow, S. Vieira, S. D. Janssens, O. A. Williams, K. Haenen, and P. Wagner. Intrinsic granularity in nanocrystalline boron-doped diamond films measured by scanning tunneling microscopy. *Physical Review B*, 80(22):224518, dec 2009.

[118] François Couëdo. *Transitions de Phase Quantiques Dans Les Systèmes Désordonnés de Basse Dimension*. PhD thesis, 2014.

[119] David M.Pozar. *Microwave Engineering, 3Rd Ed*. Wiley India Pvt. Limited, sep 2009.

[120] D. E. Oates, Alfredo C. Anderson, C. C. Chin, J. S. Derov, G. Dresselhaus, and M. S. Dresselhaus. Surface-impedance measurements of superconducting NbN films. *Physical Review B*, 43(10):7655–7663, apr 1991.

[121] Gufei Zhang, Tomas Samuely, Naoya Iwahara, Jozef Kačmarčík, Changan Wang, Paul W. May, Johanna K. Jochum, Oleksandr Onufriienko, Pavol Szabó, Shengqiang Zhou, Peter Samuely, Victor V. Moshchalkov, Liviu F. Chibotaru, and Horst-Günter Rubahn. Yu-Shiba-Rusinov bands in ferromagnetic superconducting diamond. *Science Advances*, 6(20):0, may 2020.

[122] Gufei Zhang, Tomas Samuely, Zheng Xu, Johanna K. Jochum, Alexander Volodin, Shengqiang Zhou, Paul W. May, Oleksandr Onufriienko, Jozef Kačmarčík, Julian A. Steele, Jun Li, Johan Vanacken, Jiri Vacík, Pavol Szabó, Haifeng Yuan, Maarten B. J. Roeffaers, Dorin Cerbu, Peter Samuely, Johan Hofkens, and Victor V. Moshchalkov. Superconducting Ferromagnetic Nanodiamond. *ACS Nano*, 11(6):5358–5366, jun 2017.

[123] W. Meissner and H. Franz. Messungen mit Hilfe von flüssigem Helium. IX. Supraleitfähigkeit von Carbiden und Nitriden. *Zeitschrift für Physik*, 65(1):30–54, nov 1930.

[124] W. Spengler, R. Kaiser, A. N. Christensen, and G. Müller-Vogt. Raman scattering, superconductivity, and phonon density of states of stoichiometric and nonstoichiometric TiN. *Physical Review B*, 17(3):1095–1101, feb 1978.

[125] R. Sun, K. Makise, W. Qiu, H. Terai, and Z. Wang. Fabrication of (200)-Oriented TiN Films on Si (100) Substrates by DC Magnetron Sputtering. *IEEE Transactions on Applied Superconductivity*, 25(3):1–4, jun 2015.

[126] A. Torgovkin, S. Chaudhuri, A. Ruhtinas, M. Lahtinen, T. Sajavaara, and I. J. Maasilta. High quality superconducting titanium nitride thin film growth using infrared pulsed laser deposition. *Superconductor Science and Technology*, 31(5):55017, 2018.

[127] S. Ohya, B. Chiaro, A. Megrant, C. Neill, R. Barends, Y. Chen, J. Kelly, D. Low, J. Mutus, P. J. J. O'Malley, P. Roushan, D Sank, A. Vainsencher, J. Wenner, T. C. White, Y. Yin, B. D. Schultz, C. J. Palmstrøm, B. A. Mazin, A. N. Cleland, and John M. Martinis. Room temperature deposition of sputtered TiN films for superconducting coplanar waveguide resonators. *Superconductor Science and Technology*, 27(1):15009, 2014.

[128] Uwe S. Pracht, Marc Scheffler, Martin Dressel, David F. Kalok, Christoph Strunk, and Tatyana I. Baturina. Direct observation of the superconducting gap in a thin film of titanium nitride using terahertz spectroscopy. *Physical Review B*, 86(18):184503, nov 2012.

[129] B. Sacépé, C. Chapelier, T. I. Baturina, V. M. Vinokur, M. R. Baklanov, and M. Sanquer. Disorder-Induced Inhomogeneities of the Superconducting State Close to the Superconductor-Insulator Transition. *Physical Review Letters*, 101(15):157006, oct 2008.

[130] Michael R. Vissers, Jiansong Gao, Martin Sandberg, Shannon M. Duff, David S. Wisbey, Kent D. Irwin, and David P. Pappas. Proximity-coupled Ti/TiN multilayers for use in kinetic inductance detectors. *Applied Physics Letters*, 102(23):232603, jun 2013.

[131] Josephine B. Chang, Michael R. Vissers, Antonio D. Córcoles, Martin Sandberg, Jiansong Gao, David W. Abraham, Jerry M. Chow, Jay M. Gambetta, Mary Beth Rothwell, George A. Keefe, Matthias Steffen, and David P. Pappas. Improved superconducting qubit coherence using titanium nitride. *Applied*

Physics Letters, 103(1):12602, jul 2013.

[132] Martin Sandberg, Michael R. Vissers, Jeffrey S. Kline, Martin Weides, Jiansong Gao, David S. Wisbey, and David P. Pappas. Etch induced microwave losses in titanium nitride superconducting resonators. *Applied Physics Letters*, 100(26):262605, jun 2012.

[133] J. Gao, M. R. Vissers, M. O. Sandberg, F. C. S. da Silva, S. W. Nam, D. P. Pappas, D. S. Wisbey, E. C. Langman, S. R. Meeker, B. A. Mazin, H. G. Leduc, J. Zmuidzinas, and K. D. Irwin. A titanium-nitride near-infrared kinetic inductance photon-counting detector and its anomalous electrodynamics. *Applied Physics Letters*, 101(14):142602, oct 2012.

[134] F. Vaz, J. Ferreira, E. Ribeiro, L. Rebouta, S. Lanceros-Méndez, J. A. Mendes, E. Alves, Ph. Goudeau, J. P. Rivière, F. Ribeiro, I. Moutinho, K. Pischow, and J. de Rijk. Influence of nitrogen content on the structural, mechanical and electrical properties of TiN thin films. *Surface and Coatings Technology*, 191(2):317–323, feb 2005.

[135] T. S. Radhakrishnan, Y. Hariharan, M. C. Valsakumar, D. Sundararaman, and V. S. Raghunathan. Enhanced superconductivity in titanium on nitriding. *Physica B+C*, 107(1):649–650, aug 1981.

[136] Michael R. Vissers, Jiansong Gao, Jeffrey S. Kline, Martin Sandberg, Martin P. Weides, David S. Wisbey, and David P. Pappas. Characterization and in-situ monitoring of sub-stoichiometric adjustable superconducting critical temperature titanium nitride growth. *Thin Solid Films*, 548:485–488, dec 2013.

[137] E. H. Sondheimer. The mean free path of electrons in metals. *Advances in Physics*, 50(6):499–537, sep 2001.

[138] CODATA Value: lattice parameter of silicon. https://physics.nist.gov/cgi-bin/cuu/Value?asil.

[139] Yoshiharu Krockenberger, Shin-ichi Karimoto, Hideki Yamamoto, and Kouich Semba. Coherent growth of superconducting TiN thin films by plasma enhanced molecular beam epitaxy. *Journal of Applied Physics*, 112(8):83920, oct 2012.

[140] J. S. Chawla, X. Y. Zhang, and D. Gall. Effective electron mean free path in TiN(001). *Journal of Applied Physics*, 113(6):63704, feb 2013.

[141] WebElements Periodic Table » Titanium » properties of compounds. https://www.webelements.com/titanium/compound_properties.html.

[142] Yachin Ivry, Chung-Soo Kim, Andrew E. Dane, Domenico De Fazio, Adam N. McCaughan, Kristen A. Sunter, Qingyuan Zhao, and Karl K. Berggren. Universal scaling of the critical temperature for thin films near the superconducting-to-insulating transition. *Physical Review B*, 90(21):214515, dec 2014.

[143] Corey Rae Harrington McRae, Haozhi Wang, Jiansong Gao, Michael Vissers, Teresa Brecht, Andrew Dunsworth, David Pappas, and Josh Mutus. Materials loss measurements using superconducting microwave resonators. *ArXiv:2006.04718 [physics, physics:quant-ph]*, jun 2020.

[144] Paul J. Petersan and Steven M. Anlage. Measurement of Resonant Frequency and Quality Factor of Microwave Resonators: Comparison of Methods. *Journal of Applied Physics*, 84(6):3392–3402, sep 1998.

[145] D. P. Pappas, M. R. Vissers, D. S. Wisbey, J. S. Kline, and J. Gao. Two Level System Loss in Superconducting Microwave Resonators. *IEEE Transactions on Applied Superconductivity*, 21(3):871–874, jun 2011.

[146] R. W. P. Drever, J. L. Hall, F. V. Kowalski, J. Hough, G. M. Ford, A. J. Munley, and H. Ward. Laser phase and frequency stabilization using an optical resonator. *Applied Physics B*, 31(2):97–105, jun 1983.

[147] Eric D. Black. An introduction to Pound-Drever-Hall laser frequency stabilization. *American Journal of Physics*, 69(1):79–87, dec 2000.

[148] Gauthier Chicot. Field effect in boron doped diamond. Page 181.

[149] S. E. de Graaf, L. Faoro, L. B. Ioffe, S. Mahashabde, J. J. Burnett, T. Lindström, S. E. Kubatkin, A. V. Danilov, and A. Ya Tzalenchuk. Two-level systems in superconducting quantum devices due to trapped quasiparticles. *ArXiv:2004.02485 [cond-mat, physics:quant-ph]*, apr 2020.

[150] P. Welch. The use of fast Fourier transform for the estimation of power spectra: A method based on time averaging over short, modified periodograms. *IEEE Transactions on Audio and Electroacoustics*, 15(2):70–73, jun 1967.

[151] D.W. Allan. Statistics of atomic frequency standards. *Proceedings of the IEEE*, 54(2):221–230, 1966.

[152] W J Riley. Handbook of Frequency Stability Analysis. Page 136.

[153] J. Burnett, T. Lindström, M. Oxborrow, Y. Harada, Y. Sekine, P. Meeson, and A. Ya. Tzalenchuk. Slow noise processes in superconducting resonators. *Physical Review B*, 87(14):140501, apr 2013.

[154] Alexander Bilmes, Anthony Megrant, Paul Klimov, Georg Weiss, John M. Martinis, Alexey V. Ustinov, and Jürgen Lisenfeld. Resolving the positions of defects in superconducting quantum bits. *Scientific Reports*, 10(1):3090, dec 2020.

université PARIS-SACLAY | ÉCOLE DOCTORALE Physique en l'Île-de-France (PIF)

Titre : Transition de phase dissipative et dualité de la jonction Josephson

Mots clés : supraconducteurs, jonction Josephson, sauts de phase, système à deux niveaux

Résumé : Plus d'un siècle après sa découverte, la supraconductivité est aujourd'hui utilisée dans de nombreuses applications. Une de ces applications est l'électronique supraconductrice, et un des blocs de base de celle-ci est la jonction Josephson. Cet élément a permis la réalisation de circuits électroniques dans le régime quantique et il a aidé à redéfinir la valeur du Volt dans le Système International d'unité à partir d'effets quantiques. Ces dernières années, beaucoup de temps et d'efforts sont dépensés pour améliorer ce composant et les circuits l'intégrant dans l'objectif de réaliser de meilleurs circuits à bit quantique pour l'informatique quantique. Il est donc normal de se demander si l'existence de ces circuits de pointe contenant des jonctions Josephson et des supraconducteurs conventionnels indique une maîtrise parfaite de ceux-ci. Dans ce travail de thèse, nous montrons que cela n'est pas entièrement le cas via l'exploration de deux circuits quantiques supraconducteurs pour lesquels des études plus approfondies sont nécessaires. Le premier concerne la jonction Josephson elle-même et son comportement lorsqu'elle est mise en présence d'un environnement électromagnétique.

En effet, il a été prédit il y a presque 40 ans qu'une jonction Josephson deviendrait isolante lorsqu'elle est connectée à une résistance plus grande que $R_Q = \frac{h}{4e^2} \sim 6.45\ k\Omega$. Nous ne trouvons aucunes traces de cet état isolant dans nos expériences qui mesurent l'admittance de jonctions Josephson connectées en parallèle de résistance de valeur $R > R_Q$. Le deuxième circuit explore le composant supposé dual de la jonction Josephson, la jonction à sauts de phase quantique, qui consiste en un nanofil de supraconducteur fortement inductif. Dans ces nanofils, des sauts de 2π de la phase supraconductrice sont censés produire les effets duals des paires de Cooper passant par effet tunnel dans la jonction Josephson. La maîtrise de ces effets duals permettrait la réalisation d'une nouvelle classe de circuits supraconducteurs quantiques. Nous avons fabriqué des résonateurs micro-ondes à partir de couches minces de supraconducteur fortement inductif. Nous ne trouvons aucune signature de l'effet des sauts de phase quantiques dans nos dispositifs. Cependant, nous mesurons un fort bruit basse fréquence causé par des systèmes à deux niveaux, et nous explorons ses implications dans ce type de résonateur.

Title : Dissipative phase transition and duality of the Josephson junction

Keywords : superconductors, Josephson junction, phase slips, two level systems

Abstract : More than a century after its discovery, superconductivity is used today in many applications. One of those is in superconducting electronics, of which the Josephson junction is a basic building block. This element has enabled the realisation of electronic circuits in the quantum regime, and it has helped redefining the Volt in the SI system around quantum effects. Nowadays, a lot of time and efforts are spent in order to improve Josephson junction based circuits to realise state of the art Quantum-bits for quantum computing. One may think that those highly sensitive experiments involving Josephson junctions and conventional superconductivity imply an exquisite understanding of the component and its behaviour. We show in this thesis work that this is not entirely the case, and we explore two types of superconducting quantum circuits that are in need of clarification. The first one concerns the Josephson junction itself, and a subtle issue regarding its interaction with its electromagnetic environment.

Indeed, it has been predicted 40 years ago that a Josephson junction would become insulating when connected to a resistance larger than $R_Q = \frac{h}{4e^2} \sim 6.45\ k\Omega$. We find no traces of such insulating state in our experiments which measure the admittance of a Josephson junction connected in parallel to a resistance $R > R_Q$. The second circuit we explore is the supposedly dual circuit to the Josephson junction, the quantum phase slip junction, which consists of a nanowire made of a highly inductive superconductor. Slips of the superconducting phase in those nanowires should produce the dual effects of the Cooper-pairs tunneling in Josephson junctions. The control of such an effect would then permit the realisation of a new class of superconducting quantum devices. We measured microwaves resonators patterned in a thin film of an highly inductive superconductor. We find no clear signal revealing the presence of quantum phase slips in our devices. However, we find a clear signature of two-level system noise, and we explore its implication in this kind of devices.

Maison du doctorat de l'Université Paris-Saclay
2ème étage aile ouest, Ecole normale supérieure Paris-Saclay
4 avenue des Sciences,
91190 Gif sur Yvette, France